John Hock Lye Pang

Lead Free Solder

Mechanics and Reliability

Springer

Lead Free Solder

John Hock Lye Pang

Lead Free Solder

Mechanics and Reliability

Springer

John Hock Lye Pang
School of Mechanical and Aerospace Engineering
Nanyang Technological University
50 Nanyang Avenue
Singapore 639798
Singapore
jhlpang@gmail.com

ISBN 978-1-4614-0462-0 e-ISBN 978-1-4614-0463-7
DOI 10.1007/978-1-4614-0463-7
Springer New York Dordrecht Heildelberg London

Library of Congress Control Number: 2011937228

Printed on acid-free paper

Springer is part of Springer Science+Business Media (www.springer.com)

Preface

Green electronic products require the use of lead-free (Pb-free) solder materials for soldering. Semiconductor packaging and electronics manufacturing employ Pb-free solder for silicon chip interconnection and surface mount assembly of integrated circuit (IC) components on a printed circuit board (PCB). Design and reliability evaluation of Pb-free soldered assemblies involves multidisciplinary knowledge in Pb-free solder material, it's mechanical properties, manufacturing compatibility with IC components and PCB materials, quality of soldering process and solder joint reliability performance in service.

The global electronics manufacturing industry has made a critical shift to Pb-free solder materials and soldering technology after more than 40 years of use of tin–lead (Sn–Pb) solders. Since July 2006, the European Commission Directives on "Waste Electrical and Electronic Equipment (WEEE)" and on the "Restriction of the use of certain Hazardous Substances (RoHS)" in electrical and electronics equipment has resulted in a global shift to RoHS compliant Pb-free electronic products. The electronic manufacturing industry has since sucessfully implemented Pb-free solder technology. In America, the National Electronics Manufacturing Initiative (NEMI) organization recommended the use of Pb-free, tin–silver–copper (95.5Sn–3.9Ag–0.6Cu) solder alloy for solder reflow process and tin–copper (99.3Sn–0.7Cu) solder alloy for wave soldering. However, it is now common practice to use different variations of tin–silver–copper (SAC) solder alloys, namely SAC305, SAC387, and SAC405, respectively.

This book on "*Lead Free Solder: Mechanics and Reliability*" provides a comprehensive knowledge base for Pb-free solder mechanical properties, materials constitutive models, fatigue life prediction models, finite element modeling, and simulation of reliability test results. Application of Pb-free solders requires advance mechanics of materials characterizations, computational modeling and simulation of reliability tests subject to thermal cycling test, vibration fatigue test,

and board-level drop impact test conditions. The tensile, creep, and fatigue properties for 95.5Sn–3.8Ag–0.7Cu (SAC387) and 99.3Sn–0.7Cu solder materials are covered in detail and compared to other solder alloys. Mechanical properties and constitutive models were derived for use in finite element analysis to predict solder joint reliability in a design-for-reliability (DFR) methodology.

John Hock Lye Pang, PhD, ASME Fellow

Contents

Chapter 1
Introduction

Abstract Chapter 1 provides an introduction on the use and application of lead- free solders in the semiconductor packaging and electronics manufacturing industry. The importance of solder joint reliability testing and assessments is described within a framework of a DFR methodology. This DFR methodology provides a systematic approach to understanding the mechanics of deformation of solder materials, characterizing the mechanical properties, constitutive models for creep and viscoplastic analysis, fatigue life prediction models, which are then employed in a finite element modeling and simulation analysis to assess the solder joint reliability performance.

Lead-free solder alloys, soldering, and surface mount technology play a critical role in the semiconductor packaging and electronics manufacturing industry. Solder joints in electronic products are used as interconnection materials for enabling electrical, thermal, and mechanical function in electronic packaging design and manufacturing of Integrated Circuit (IC) devices and surface mount assembly of electronic components on printed circuit board (PCB) products.

Since July 2006, European legislations [1, 2] on Waste Electrical and Electronic Equipment (WEEE) and on the Restriction of the use of Hazardous Substances (RoHS), had a major impact on the electronics manufacturing industry where cooperative efforts have seen the industry made a smooth transition from tin–lead (Sn–Pb) to lead-free tin–silver–copper (Sn–Ag–Cu) solder alloys. Great efforts have been achieved to restrict the use of Pb-based solders and replace it with Pb-free solders in consumer electronic products. Pb-free solder applications in the risk adversed electronic products sectors like in the medical, military, automotive, and high perfomance computers industry requires extensive knowledge in mechanics and reliability performance of Pb-free soldered assemblies.

Lead-free solder technology involves multidisciplinary knowledge in solder alloy materials, properties, soldering, manufacturing, quality, and long-term solder joint reliability in service. Ternary, tin–silver–copper (Sn–Ag–Cu) solder alloys have been

J.H.L. Pang, *Lead Free Solder: Mechanics and Reliability*,
DOI 10.1007/978-1-4614-0463-7_1,

deployed for solder reflow assembly process [3]. Eutectic 99.3Sn–0.7Cu solder alloy is more commonly used for wave soldering process. Eutectic 96.5Sn–3.5Ag solder alloy is often employed in solder-bumped, flip chip wafer-level packaging processes.

Typically for Sn–xAg–yCu solder alloys [4], the range of silver, x, is 3–4% wt. and copper, y, is 0.5–0.7% wt. Three lead-free solder alloy compositions used for solder reflow assembly process are Sn–3Ag–0.5Cu (SAC305), Sn–3.8Ag–0.7Cu (SAC387) , and Sn–4Ag–0.5Cu (SAC405) respectively. Lead-free Sn–Ag–Cu solder alloys (with notations: SAC305, SAC387, and SAC405) have been rigorously evaluated for its material properties, its soldering compatibility with IC components and PCB materials in surface mount assembly, and solder joint reliability assessments.

Lead-free solder materials application requires mechanics characterization of the mechanical properties and constitutive models. Robust reliability evaluation of solder joint assemblies subject to accelerated test requirements for thermal cycling, mechanical cycling, vibration, and drop impact loading test conditions [5].

Quality and reliability are two important product attributes that contribute to the success of electronic product operations in service [6]. A design-built-test approach in quality and reliability testing of soldered IC and PCB assemblies is often supported by a Design-for-Reliability (DFR) approach by modeling and simulation of lead-free solder joint performance [7–9].

The DFR methodology, which provides a knowledge base for lead-free solder alloys and their material constitutive models, fatigue life prediction models, finite element modeling, and simulation of reliability test methods, is shown in Fig. 1.1.

The middle column in Fig. 1.1 shows the accelerated temperature cycling (ATC) reliability test results for thermal cycling (TC) and thermal shock (TS) given in a Weibull plot. The Mean-Time-To-Failure (MTTF) for different TC and TS test results can be correlated by a scale factor (SF) or an acceleration factor (AF).

The right column in Fig. 1.1 shows the finite element analysis (FEA) modeling requirements which involves numerical modeling details for 3D geometry and load history, material properties, temperature, and strain-rate dependent constitutive model. The output from the FEA result will provide the fatigue damage driving force parameter for a strain-range or plastic work based fatigue life prediction model.

The left column of the DFR methodology shown in Fig. 1.1 is the fatigue life prediction analysis procedure using low cycle fatigue models based on strain-range or energy-based fatigue models.

The above DFR methodology applies to solder joint reliability evaluation for both lead-free and tin–lead electronic solders. This requires extensive materials characterization [10, 11], fatigue life prediction test and modeling [12–16], FEA modeling and simulation [17–20], and reliability tests for conducting a DFR assessment as illustrated in Fig. 1.2. Various 2D and 3D FEA models have been developed for a Plastic Ball Grid Array (PBGA) component assembly to a PCB as shown in Fig. 1.3.

This book on *Lead-Free Solder: Mechanics and Reliability* will report on the extensive research work done on mechanics of materials characterization of Sn–3.8Ag–0.7Cu and Sn–0.7Cu solders, finite element modeling of solder joint reliability correlated to thermal cycling, vibration, and drop impact tests for lead-free solders.

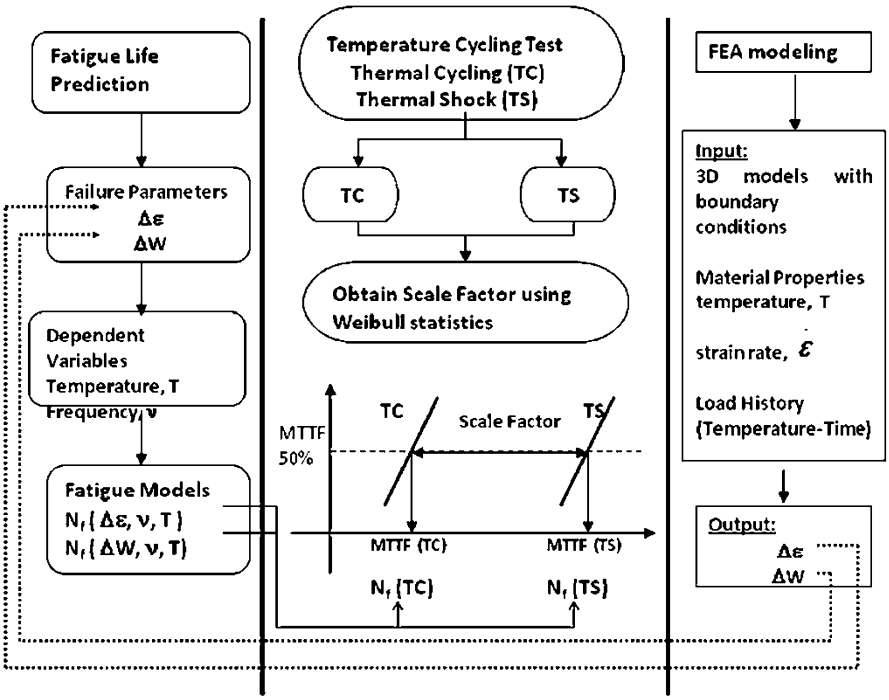

Fig. 1.1 DFR methodology for solder joint reliability assessments

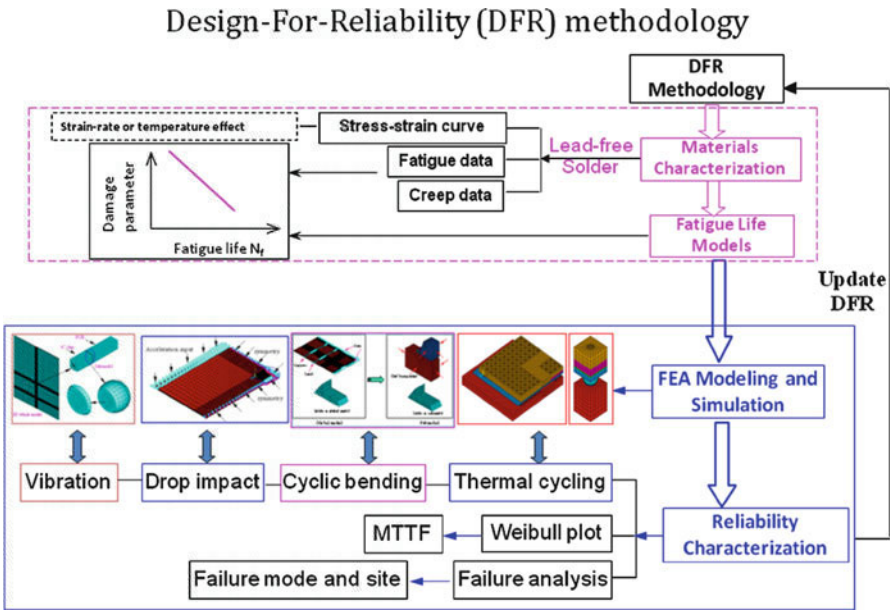

Fig. 1.2 DFR approach for FEA modeling and fatigue analysis

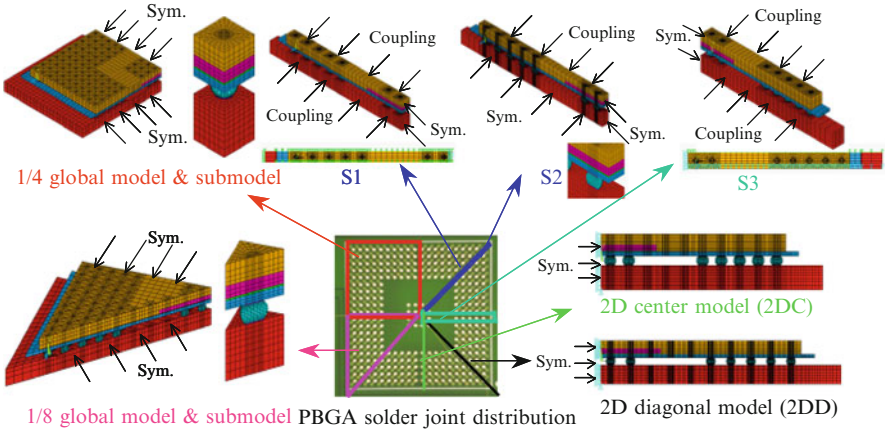

Fig. 1.3 Finite element models (2D and 3D) for a PBGA component

References

1. European Parliament (2003) Directive 2002/95/EC on the restriction of the use of certain hazardous substances in electrical and electronic equipment. Official J Eur Union, pp L37/19–L37/23
2. European Parliament (2003) Directive 2002/96/EC on waste of electrical and electronic equipment. Official J Eur Union, pp L37/24-L37/38
3. NEMI, National Electronics Manufacturers Initiative. (http://www.nemi.org)
4. Schubert A, Pang JHL (2002) Lead free solder materials and reliability performance. Short course notes at 4th electronics packaging technology conference, lead-free workshop, 10 Dec 2002
5. Pang JHL, Wong SCK, Wang ZP, Guest Editors (2002) Lead-free and lead-bearing solders. Soldering Surface Mount Technol 14(3)
6. Pang JHL, Dudek R (2005) Lead free solder materials and reliability performance. Short course notes at 7th electronics packaging technology conference, 6 Dec 2005
7. Pang JHL (2007) Lead-free solder materials: design for reliability. In: Suhir E, Lee YC, Wong CP (eds) Micro- and opto-electronic materials and structures: physics, mechanics, design, reliability, packaging, vol 1, Materials physics/materials mechanics. Springer, New York
8. Pang JHL, Low TH, Xiong BS, Che FX (2003) Design for reliability (DFR) methodology for electronic packaging assemblies. Proceedings of 2003 electronics packaging technology conference, pp 470–478
9. Sitaraman SK, Pang JHL (2001) Fundamentals of design for reliability, chapter 5. In: Tummala RR (ed) Fundamentals of microsystems packaging. Mc Graw Hill, New York
10. Pang JHL, Xiong BS (2005) Mechanical properties for 95.5Sn-3.8Ag-0.7Cu lead free solder alloy. IEEE Trans Components Packaging Technol 28(4):830–840
11. Pang HLJ, Xiong BS, Neo CC, Zhang XR, Low TH (2003) Bulk solder and solder joint properties for lead free 95.5Sn-3.8Ag-0.7Cu solder alloy. Proceedings of 53rd electronic components and technology conference, New Orleans, Louisiana, USA, 27–30 May 2003, pp 673–679
12. John PHL, Xiong BS, Low TH (2004) Low cycle fatigue models for lead free solders. Thin Solid Film 462–463:408–412
13. Pang HLJ, Xiong BS, Low TH (2004) Creep and fatigue properties of lead free Sn-3.8Ag-0.7Cu solder. Proceedings of 54th ECTC, Las Vegas, vol 2, 1–4 June 2004, pp 1333–1337

14. Pang JHL, Xiong BS, Low TH (2004) Low cycle fatigue of lead-free 99.3Sn-0.7Cu solder alloy. Int J Fatigue 26:865–872
15. Pang JHL, Xiong BS, Low TH (2004) Comprehensive mechanics characterization of lead-free 95.5Sn-3.8Ag-0.7Cu solder. Micromater Nanomater 3:86–93
16. Pang JHL, Xiong BS, Che FX (2004) Modeling stress strain curves for lead-free Sn-3.8Ag-0.7Cu solder. IEEE proceedings of EuroSime 2004 conference, Belgium, 9–12 May
17. Che FX, Pang JHL et al (2005) Lead free solder joint reliability characterization for PBGA, PQFP and TSSOP assemblies. Proceedings of 2005 electronic components and technology conference, 55th ECTC, pp 916–921
18. Pang JHL, Che FX, Low TH (2004) Vibration fatigue analysis for FCOB solder joints. Proceedings of IEEE, 2004 electronic components and technology conference, 54th ECTC, vol 1, pp 1055–1061
19. Pang JHL, Patrick, Low TH, Xiong BS (2004) Lead-free 95.5Sn-3.8Ag-0.7Cu solder joint reliability analysis for micro-BGA assembly. Proceedings of IEEE, 2004 inter society conference on thermal phenomena, ITherm 2004, vol 2, pp 131–136
20. Pang JHL, Yeo A, Low TH, Che FX (2004) Lead-free 96.5Sn-3.5Ag flip chip solder joint reliability analysis. Proceedings of IEEE, 2004 inter society conference on thermal phenomena, ITherm 2004, vol 2, pp 160–164

Chapter 2
Theory on Mechanics of Solder Materials

Abstract Chapter 2 reviews the fundamental theory on mechanics of solder materials. As solder materials are subject to high operating temperatures relative to their melting point, the thermo-mechanical deformation response of the solder is dependent on both temperature and strain-rate conditions. Hence, the theory on mechanics of solder materials will focus on elastic-plastic-creep and viscoplastic models for describing the thermo-mechanical deformation response of lead-free solder materials operating over a wide range of temperatures (−40°C to +125°C) and strain rates (0.0001–1,000 s^{-1}).

Solder materials in electronic packaging assemblies are subjected to thermo-mechanical loads during accelerated reliability tests and in service operation. Accelerated Thermal Cycling (ATC) tests subject the solder joints to extreme temperatures; for example from −40°C to +125°C. Such cyclic thermo-mechanical induced deformations in the package assembly cause the solder material to develop severe cyclic inelastic strains and cumulative fatigue damage resulting in failure of the solder joints [1, 2].

The stress, strain, and strain energy density components in solder materials can be computed numerically, if the governing material constitutive model has been developed from mechanics of materials tests. Materials testing and characterization of the elastic and inelastic deformation behavior are needed to derive the constitutive models to describe the solder deformation behavior in an elastic-plastic-creep model or a viscoplastic model approach [3].

Thermo-mechanical fatigue analysis in solder joints of electronic assemblies will require a stress and strain analysis approach and this often involves 2D and 3D modeling of the package assembly subject to the design or reliability test condition [4–6]. Fatigue damage driving force parameters such as stress-range, strain-range,

The original version of this chapter was revised. An erratum to this chapter can be found at https://doi.org/10.1007/978-1-4614-0463-7_9

DOI 10.1007/978-1-4614-0463-7_2,

and inelastic strain energy density per cycle can be computed and used in fatigue life prediction models.

2.1 Thermo-Mechanical Stress and Strain Analysis

An electronic package assembly is made up of different deformable materials joined by solder materials that undergo extensive amounts of deformations when subject to cyclic thermal loading. It is essential to understand the basic governing equations of thermo-mechanical strain in solder joints induced by mismatch in thermo-mechanical deformations [1, 2]. For a simple case, it can be assumed that the package is stress-free at a uniform temperature where there are no external or residual forces present. It is also assumed that the velocity and displacement of every element in the package at the instantaneous reference state is assumed to be small and the fundamental strain–displacement relation is given by,

$$\varepsilon_{ij} = \frac{1}{2}\left(\frac{\partial u_i}{\partial x_j} + \frac{\partial u_j}{\partial x_i}\right). \tag{2.1}$$

Hence, the governing equations for the isotropic thermal stresses for electronic packaging structure with steady-state heat flow condition ($\partial T/\partial t = 0$) are given by,

$$\delta_{ij}\frac{\partial}{\partial x_i}\left(\frac{\partial T}{\partial x_j}\right) = 0 \tag{2.2}$$

$$\sigma_{ij} = \lambda\varepsilon_{kk}\delta_{ij} + 2G\varepsilon_{ij} - \beta\delta_{ij}(T - T_0) \tag{2.3}$$

with the multi-axial strain components in a solid element given by,

$$\varepsilon_x = \frac{\partial u}{\partial x}, \quad \varepsilon_y = \frac{\partial v}{\partial y}, \quad \varepsilon_z = \frac{\partial w}{\partial z} \tag{2.4}$$

$$\gamma_{xy} = \frac{\partial u}{\partial y} + \frac{\partial v}{\partial x}, \quad \gamma_{yz} = \frac{\partial v}{\partial z} + \frac{\partial w}{\partial y}, \quad \gamma_{xz} = \frac{\partial w}{\partial x} + \frac{\partial u}{\partial z} \tag{2.5}$$

In three-dimensional analysis, a solid is subjected to multi-axial states of stresses and strains. The principal stresses and strains in the three principal planes, 1, 2, and 3 can be computed from a mechanics of materials analysis or by a numerical modeling approach employing a finite element analysis (FEA) method.

$$\sigma_1 > \sigma_2 > \sigma_3 \text{ and } \varepsilon_1 > \varepsilon_2 > \varepsilon_3,$$

where σ_1, σ_2, and σ_3 are the principal stresses, and ε_1, ε_2, and ε_3 are the principal strains at an element.

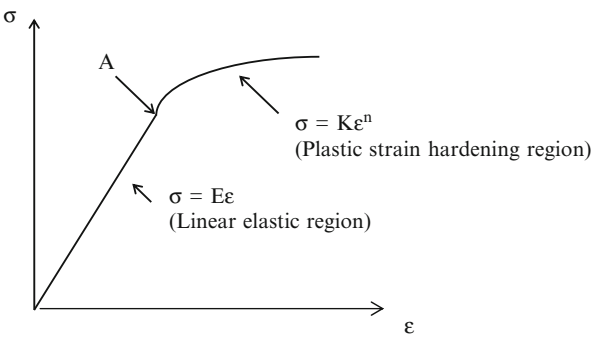

Fig. 2.1 Elastic-plastic stress–strain curve plot

The equivalent *von Mises* stress equation is a yield criterion and is used to determine if the Yield stress state at the onset of plastic yielding has occurred in a solid element.

$$\sigma^{\mathrm{e}} = \frac{1}{\sqrt{2}}\left[(\sigma_1 - \sigma_2)^2 + (\sigma_2 - \sigma_3)^2 + (\sigma_3 - \sigma_1)^2\right]^{1/2} \tag{2.6}$$

Similarly, the equivalent *von Mises* strain equation is used to compute the corresponding equivalent strain at the onset of plastic yielding and beyond.

$$\varepsilon^{e} = \frac{\sqrt{2}}{3}\left[(\varepsilon_1 - \varepsilon_2)^2 + (\varepsilon_2 - \varepsilon_3)^2 + (\varepsilon_3 - \varepsilon_1)^2\right]^{1/2} \tag{2.7}$$

In soldered electronic assemblies, the shear strain components are particularly important due to thermal expansion mismatch shear deformations in solder joints. The effective shear stress and shear strain can be derived from the equivalent *von Mises* stress and strain by:
effective shear stress,

$$\tau^{*} = \frac{1}{\sqrt{3}}\sigma^{\mathrm{e}} \tag{2.8}$$

and effective shear strain,

$$\gamma^{*} = \sqrt{3}\varepsilon^{e}. \tag{2.9}$$

The multi-axial stress and strain state at any point in a three-dimensional solid element can be resolved down to an equivalent stress and strain state using the *von Mises* stress–strain equation. This can then be related to the tensile test stress and strain response for modeling the elastic-plastic stress–strain curve behavior of a ductile material shown in Fig. 2.1.

The linear elastic region can be modeled by Hooke's law where stress (σ) and strain (ε) is related by Young's Modulus (E).

$$\sigma = E\varepsilon \tag{2.10}$$

The plastic strain hardening region can be modeled by a time-independent non-linear stress–strain relationship,

$$\sigma = K\varepsilon^n \tag{2.11}$$

The plastic strain hardening region can be modeled as an isotropic or kinematic hardening material. Isotropic hardening assumes that the origin of the *von Mises* yield surface remains stationary in the stress space and the size of its yield surface expand resulting from strain hardening. In kinematic hardening, the *von Mises* yield surface does not change in size, but the origin of the yield surface is allowed to translate in the stress space to model strain hardening effects of increasing plastic flow stress. For solder materials, the tensile stress and strain curves are dependent on the test temperature and strain rate. The elastic modulus, yield strength, and ultimate tensile strength (UTS) properties vary with temperature and strain rate.

For a typical thermal cycling test from −40°C to 125°C, these mechanical properties reduce with the increase in temperature [7]. At −40°C to 125°C, a lead-free SAC solder material has a homologous temperature range of 0.5–0.8 of its melting point temperature of 217°C or 490 K. Creep deformation behavior in a solder material is highly dependent on the stress and temperature state. An elastic-plastic-creep constitutive model or viscoplastic constitutive model is needed to facilitate finite element modeling and simulation of solder joint reliability subject to thermal cycling tests [8].

2.2 Elastic-Plastic-Creep Model

Elastic-plastic-creep analysis [8] treats the total strain as the sum of the phenomenological components of elastic strain, time-independent plastic strain and time-dependent creep strain as shown below.

$$\varepsilon_{ij} = \varepsilon_{ij}^{\mathrm{e}} + \varepsilon_{ij}^{\mathrm{p}} + \varepsilon_{ij}^{\mathrm{c}} \tag{2.12}$$

where ε_{ij}, $\varepsilon_{ij}^{\mathrm{e}}$, $\varepsilon_{ij}^{\mathrm{p}}$, and $\varepsilon_{ij}^{\mathrm{c}}$ are total, elastic, time-independent plastic and time-dependent creep strain tensors, respectively.

The total strain can be divided into an elastic component, $\varepsilon_{\mathrm{el}}$, a time-independent plastic component, $\varepsilon_{\mathrm{pl}}$, and a time-dependent creep component, $\varepsilon_{\mathrm{cr}}$. The secant modulus can be expressed as:

$$\frac{1}{E_{\mathrm{sec}}} = \frac{\varepsilon_{\mathrm{tot}}}{\sigma} = \frac{\varepsilon_{\mathrm{el}}}{\sigma} + \frac{\varepsilon_{\mathrm{pl}}}{\sigma} + \frac{\varepsilon_{\mathrm{cr}}}{\sigma} = \frac{1}{E_{\mathrm{el}}} + \frac{1}{E_{\mathrm{pl}}} + \frac{1}{E_{\mathrm{cr}}} \tag{2.13}$$

From (2.13), it is noted that by increasing the strain rate, the contribution of the time dependent creep strain decreases such that for an infinite strain rate, ε_{cr} and $1/E_{cr}$ tend towards zero. Similarly, by decreasing the stress level of taking the slope on the stress–strain curve to calculate secant modulus, the contribution of the time-independent plastic strain decreases so that at a stress level small enough, any plastic effects can be eliminated, such that ε_{pl} and $1/E_{pl}$ tend towards zero. Therefore, only the elastic component is left and this results in giving the true Elastic modulus.

2.2.1 Temperature and Strain-Rate Dependent Elastic Modulus

The constitutive model [9, 10] for the apparent Elastic modulus can be written as

$$E(T,\dot{\varepsilon}) = (a_0 T + a_1)\log(\dot{\varepsilon}) + (a_2 T + a_3) + \delta, \tag{2.14}$$

where $\dot{\varepsilon}$ is the strain rate; T is the temperature; $a_0,\ a_1,\ a_2,$ and $a_3$are constants; $\delta$is the error term, which is introduced to account for any experimental error.

For constant temperature, two temperature-dependent constants $\alpha(T) = a_0 T + a_1$ and $\beta(T) = a_2 T + a_3$, can be introduced.

Equation (2.14) can then be written as

$$E = \alpha(T)\log(\dot{\varepsilon}) + \beta(T) + \delta \tag{2.15}$$

From (2.15), we can get the linear estimator equation:

$$\widehat{E} = \widehat{\alpha}\log(\dot{\varepsilon}) + \widehat{\beta}, \tag{2.16}$$

where $\widehat{E},\ \widehat{\alpha},\ \widehat{\beta}$ are estimated values of $E,\ \alpha,$ and $\beta,$ respectively.

It is necessary to rewrite (2.16) in matrix notation in the form

$$Y = X \times C \tag{2.17}$$

and apply multiple linear regression with,

$$Y = \begin{bmatrix} E_1 \\ E_2 \\ \vdots \\ E_n \end{bmatrix} \quad X = \begin{bmatrix} \log(\dot{\varepsilon}_1) & 1 \\ \log(\dot{\varepsilon}_2) & 1 \\ \vdots & \vdots \\ \log(\dot{\varepsilon}_n) & 1 \end{bmatrix} \quad C = \begin{bmatrix} \alpha \\ \beta \end{bmatrix} \tag{2.18}$$

Using the experimental data, the temperature-dependent constants can be derived from calculus, where the estimated coefficient matrix, $\widehat{C}$, can be found from (2.19)

$$\widehat{C} = (X^{\mathrm{T}}X)^{-1}X^{\mathrm{T}}Y, \tag{2.19}$$

where $\widehat{C} = \begin{bmatrix} \widehat{a} \\ \widehat{\beta} \end{bmatrix}$. Then the temperature-dependent constants α, β also can be expressed by the matrix notation forms

$$\begin{cases} Y_1 = X_1 \times C_1 \\ Y_2 = X_2 \times C_2 \end{cases}, \tag{2.20}$$

where

$$Y_1 = \begin{bmatrix} \alpha_1 \\ \alpha_2 \\ \alpha_3 \end{bmatrix} \quad X_1 = \begin{bmatrix} T_1 & 1 \\ T_2 & 1 \\ T_3 & 1 \end{bmatrix} \quad C_1 = \begin{bmatrix} a_0 \\ a_1 \end{bmatrix}$$

$$Y_2 = \begin{bmatrix} \beta_1 \\ \beta_2 \\ \beta_3 \end{bmatrix} \quad X_2 = \begin{bmatrix} T_1 & 1 \\ T_2 & 1 \\ T_3 & 1 \end{bmatrix} \quad C_2 = \begin{bmatrix} a_2 \\ a_3 \end{bmatrix}$$

Thus, the constants a_0, a_1, a_2, and a_3 can be determined from calculus that estimated coefficient matrix, $\widehat{C}_1$, $\widehat{C}_2$, are calculated as

$$\begin{aligned} \widehat{C}_1 &= (X_1{}^{\mathrm{T}} X_1)^{-1} X_1{}^{\mathrm{T}} Y_1 \\ \widehat{C}_2 &= (X_2{}^{\mathrm{T}} X_2)^{-1} X_2{}^{\mathrm{T}} Y_2, \end{aligned} \tag{2.21}$$

where

$$\widehat{C}_1 = \begin{bmatrix} \widehat{a}_0 \\ \widehat{a}_1 \end{bmatrix}, \quad \widehat{C}_2 = \begin{bmatrix} \widehat{a}_2 \\ \widehat{a}_3 \end{bmatrix} \tag{2.22}$$

By solving (2.19), (2.21), and (2.22) and substituting the solution of constants of a_0, a_1, a_2, and a_3 into (2.14), the apparent Elastic modulus for 95.5Sn–3.8Ag–0.7 Cu is obtained [7] as follows:

$$E(T, \dot{\varepsilon})_{\mathrm{SnAgCu}} = (-0.0005T + 6.4625)\log(\dot{\varepsilon}) + (-0.2512T + 71.123) \tag{2.23}$$

2.2.2 *Temperature and Strain-Rate Dependent Yield Stress and Ultimate Tensile Stress*

The yield stress and UTS were established and expressed individually as follows:

$$\sigma_y(T, \dot{\varepsilon}) = \alpha(T)(\dot{\varepsilon})^{\beta(T)}, \tag{2.24}$$

where $\dot{\varepsilon}$ is the strain rate, T is the temperature, and

$$\begin{cases} \alpha(T) = b_0 T + b_1 \\ \beta(T) = b_2 T + b_3 \end{cases}$$

here $b_0,\ b_1,\ b_2,$ and b_3 are curve-fitted constants.

$$\mathrm{UTS}(T, \dot{\varepsilon}) = \alpha(T)(\dot{\varepsilon})^{\beta(T)}, \tag{2.25}$$

where $\dot{\varepsilon}$ is the strain rate, T is the temperature, and

$$\begin{cases} \alpha(T) = c_0 T + c_1 \\ \beta(T) = c_2 T + c_3 \end{cases}$$

here $c_0,\ c_1,\ c_2,$ and c_3 are unknown constants.

Employing the same evolution procedure to determine the apparent Elastic modulus, the constants for yield stress and UTS can be determined [7] as follows:

$$\sigma_y(T, \dot{\varepsilon})_{\mathrm{SnAgCu}} = (-0.2314T + 68.37)(\dot{\varepsilon})^{(2.29\times10^{-4}T + 0.0724)} \tag{2.26}$$

$$\mathrm{UTS}(T, \dot{\varepsilon})_{\mathrm{SnAgCu}} = (-0.2337T + 75.98)(\dot{\varepsilon})^{(2.5\times10^{-4}T + 0.0707)}. \tag{2.27}$$

The elastic modulus, yield stress, and UTS properties of solder materials are dependent on the temperature and strain rate of loading in a tensile test. Strain-rate hardening effects cause these properties to increase with the increase in strain rate from 10^{-5} s^{-1} to 10^{-1} s^{-1} [7, 11].

2.2.3 *Ramberg-Osgood Model for Elastic-Plastic Stress–Strain Curve*

One of the major goals of thermo-mechanical analysis in the electronics industry is to be able to model the stress–strain response in the solder joint and predict its reliability performance in design and in service.

A Ramberg-Osgood model describes the elastic-plastic behavior of solder materials very well and can be used to describe the stress–strain curve of solder tensile test results given by

$$\varepsilon = \frac{\sigma}{E} + \alpha\left(\frac{\sigma}{\sigma_0}\right)^n, \tag{2.28}$$

where n is the hardening exponent, α and σ_0 are material constants.

However for solder materials, the stress–strain curve is dependent on temperature and strain rate. Hence, a Modified Ramberg-Osgood model can be developed to include the temperature and strain-rate dependent effects.

2.2.4 Temperature and Strain-Rate Dependent Modified Ramberg-Osgood Model

The Ramberg-Osgood model hardening exponent n and stress coefficient σ_0 are modified to be temperature and strain-rate dependent for solder materials. The temperature and strain-rate dependent Modified Ramberg-Osgood model can be described as

$$\varepsilon(T,\dot{\varepsilon}) = \frac{\sigma}{E} + \alpha\left(\frac{\sigma}{\sigma_0(T,\dot{\varepsilon})}\right)^{n(T,\dot{\varepsilon})}. \tag{2.29}$$

From the tensile test result, the mechanical properties have a linear relationship with temperature and logarithmic relationship with strain rate. So formation of temperature and strain-rate dependent n and σ_0 can be written as

$$\sigma_0(T,\dot{\varepsilon}) = \sigma_0 + aT^* + b\dot{\varepsilon}^* \tag{2.30}$$

$$n(T,\dot{\varepsilon}) = n + cT^* + d\dot{\varepsilon}^* \tag{2.31}$$

where $T^* = \frac{T-T_\mathrm{r}}{T_\mathrm{m}-T_\mathrm{r}}$, $\dot{\varepsilon}^* = \ln\left(\frac{\dot{\varepsilon}}{\dot{\varepsilon}_r}\right)$, a and c are temperature coefficients, b and d are strain-rate coefficients. T_r and $\dot{\varepsilon}_r$ are reference temperature and strain rate, respectively. T_m is the melting temperature of Sn–3.8Ag–0.7Cu (217°C), n and σ_0 are hardening exponent and stress coefficient at the reference temperature and strain rate.

2.3 Creep Constitutive Models

Creep of a solder material is often characterized by its steady-state creep strain rate, $\dot{\varepsilon}_{ss}$, which can be simply expressed as power law relationship,

$$\dot{\varepsilon} = A\sigma^n e^{\frac{-Q}{KT}}, \tag{2.32}$$

where A is material constant, σ is applied stress, n is stress exponent, Q is creep activation energy, K is Boltzmann's constant, and T is absolute temperature. The activation energy, Q, and the stress exponent, n, change with the dominant creep mechanism and may have different values for different regimes of the applied stress.

By taking the natural logarithm, (2.32) can be rewritten as,

$$\ln\ \dot{\varepsilon} = \ln A + n\ \ln\ \sigma - \frac{Q}{K}\frac{1}{T} \tag{2.33}$$

It can be seen from (2.33) that for the creep process under the controlling constant stress, the creep deformation mechanism does not change at small temperature range. Therefore, the activation energy, Q, could be determined from the slope of the, ln ε versus $1/T$ plot.

To describe the steady-state creep strain rate over a wider regime of stresses and temperatures, a hyperbolic-sine creep model is often used for solder materials [11]. The steady-state creep strain rate for intermediate to high stress power law breakdown regime is:

$$\dot{\varepsilon} = C[\sin\ h(\alpha\sigma)]^n \exp\left(-\frac{Q}{KT}\right), \tag{2.34}$$

where $\dot{\varepsilon}_c$ = equivalent creep strain rate (s^{-1}), σ = equivalent *von Mises* stress (N/mm^2), T = absolute temperature (kelvin), C is a constant, α is the stress level at which the power law dependence breaks down, n is the stress exponent for dislocation glide-controlled kinetics, Q is the activation energy for creep deformation process, and K is the Boltzmann's constant.

The elastic-plastic-creep approach is a phenomenological way to describe the constitutive behavior of solder alloy, since the elastic, plastic and creep strains represent different deformation. For thermo-mechanical cyclic loading, the time-independent plastic strain and time-dependent creep strain can be readily computed from an elastic-plastic-creep analysis using FEA modeling and simulation [12, 13]. Another useful method from a state variable approach of inelastic strain is the viscoplastic strain analysis approach. This method combines the creep and plastic strain components as a unified state variable inelastic strain.

2.4 Viscoplastic Constitutive Model

The viscoplastic model approach follows the materials perspective that dislocation motion is the cause of both creep and plastic deformation [8, 13], and combined them into inelastic strain. A viscoplastic model that has been used for modeling rate-dependent deformation behavior of ductile metals is the Anand viscoplastic model, which was originally reported by Anand [14] and Brown et al. [15]. The Anand viscoplastic model was applied to tin–lead solder joints subject to thermal cycling loading by Darveaux [16]. The Anand viscoplastic model was curve fitted for lead-free tin–silver (Sn–3.5Ag) and tin–silver–copper (SAC387) solder alloys, respectively [12, 17].

The total strain is expressed as,

$$\varepsilon_{ij} = \varepsilon_{ij}^{\mathrm{e}} + \varepsilon_{ij}^{\mathrm{in}}, \tag{2.35}$$

where $\varepsilon_{ij}^{\mathrm{in}}$ is the inelastic strain tensor.

The Anand model consists of two coupled differential equations that relate the inelastic strain rate to the rate of deformation resistance.

The strain rate equation is represented by,

$$\frac{\mathrm{d}\varepsilon_{\mathrm{in}}}{\mathrm{d}t} = A\left[\sin\ h\left(\xi\frac{\sigma}{s}\right)\right]^{\frac{1}{m}} \exp\ (-Q/RT) \tag{2.36}$$

The rate of deformation resistance is given by

$$\dot{s} = \left\{h_0(|B|)^{\alpha}\frac{B}{|B|}\right\}\frac{\mathrm{d}\varepsilon_{\mathrm{p}}}{\mathrm{d}t} \tag{2.37}$$

$$B = 1 - \frac{s}{s^*} \tag{2.38}$$

$$s^* = \hat{s}\left[\frac{1}{A}\frac{\mathrm{d}\varepsilon_p}{\mathrm{d}t}\exp\ (-Q/RT)\right], \tag{2.39}$$

where $\mathrm{d}\varepsilon_{\mathrm{in}}/\mathrm{d}t$ is the effective inelastic strain rate, σ is effective true stress, s is the deformation resistance, T is the absolute temperature, A is pre-exponential factor, ξ is stress multiplier, m is strain rate sensitivity of stress, Q is activation energy, R is universal gas constant, h_0 is hardening/softening constant, $\hat{s}$ is coefficient for deformation resistance saturation value, n is strain-rate sensitivity of saturation value, and α is strain-rate sensitivity of hardening or softening.

In the Anand model, (2.36) deals with the relationship between saturation stress and strain rate under certain temperatures. Equations (2.37)–(2.39) deal with the hardening and softening flow response where the relationship between strain and stress can be computed over a range of strain rate and temperature.

The saturation stress in (2.40) can be derived from (2.36) as follows:

$$\sigma^* = \frac{\hat{s}}{\xi}\left(\frac{\dot{\varepsilon}_{\mathrm{p}}}{A}e^{Q/RT}\right)^n \sin\ h^{-1}\left[\left(\frac{\dot{\varepsilon}_{\mathrm{p}}}{A}e^{Q/RT}\right)^m\right], \tag{2.40}$$

where $\dot{\varepsilon}_p$ and T denote strain rate and temperature, respectively.

The parameters Q/R, A, $\hat{s}/\xi$, m, and n can be determined by a nonlinear fitting method to steady-state creep strain rate test data.

The relationship between the viscoplastic stress and inelastic strain is given by,

$$\sigma = \sigma^* - [(\sigma^* - cs_0)^{(1-a)} + (a-1)ch_0\sigma^{*(-a)}\varepsilon_{\mathrm{p}}]^{1/(1-a)}. \tag{2.41}$$

Table 2.1 Anand model parameters for 63Sn–37Pb solder

	A	Q/R	ξ	m	$\hat{s}$	n	h_0	a	s_0
63Sn-37Pb	26.0	5,797	10	0.256	83.1	0.043	92148	1.24	38.0

The variable ε_p is the nonlinear strain, and a, s_0 and h_0 are parameters to be determined, where c is a function of strain rate and temperature given in (2.42).

$$c \equiv \frac{1}{\xi} \sin\ h^{-1}\left[\left(\frac{\dot{\varepsilon}_p}{A} e^{Q/RT}\right)^m\right] \quad c<1. \tag{2.42}$$

The values of the nine material parameters Q, A, $\hat{s}$, ξ, m, n, a, s_0, and h_0 for any given solder alloy can be determined by the curve-fitting procedures given below:

1. Determination of the saturation stress σ^* under a series of strain rate and temperature by creep test.
2. Curve fitting of parameters Q/R, A, $\hat{s}/\xi$, m, and n in (2.40).
3. Determination of ξ and $\hat{s}$. For value of $\hat{s}/\xi$ has been determined in step (2), value of ξ should be estimated such that the value of c will match condition: $c < 1$. And then the value of $\hat{s}$ can be derived from $\hat{s}/\xi$ and the estimate of ξ.
4. Curve fitting of a, s_0, and h_0 in (2.41).

For example, the above curve-fitting method for the Anand viscoplastic model was applied to tensile and creep test data for 63Sn–37Pb solder alloy. Tensile test data for three different temperatures, 25°C, 75°C, and 125°C, and three states of strain rate, 5.6E−2, 5.6E−3, and 5.6E−4, were used. Table 2.1 shows the result of the nine parameters of the Anand viscoplastic model for 63Sn–67Pb solder.

2.5 Fatigue Life Prediction Models for Solder Materials

Thermo-mechanical fatigue failure in solder joints subject to thermal cycling tend to fail in the Low Cycle Fatigue (LCF) range where the fatigue life to failure falls between 100 and 10,000 thermal cycles. The fatigue life prediction models to be used depends on the fatigue test condition and fatigue damage parameters used. The fatigue damage driving force parameters such as the plastic strain-range, creep strain range and inelastic strain energy density per cycle can be used in different fatigue life prediction models.

The LCF approach can be based on the strain or energy parameter used to characterize the fatigue failure process [18–20]. These parameters are (a) plastic strain range, (b) creep strain range and (c) inelastic energy. The strain range-based fatigue approach employs low cycle strain-controlled fatigue test method. The inelastic strain comprises of the plastic strain range and creep strain range. The plastic shear strain deformation is represented by the time-independent plastic

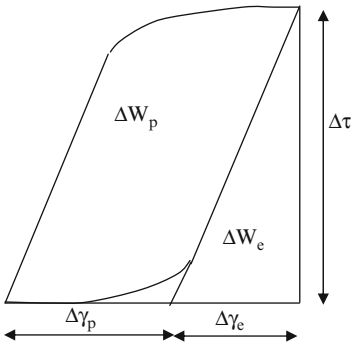

Fig. 2.2 Cyclic stress–strain hysteresis loop

strain component, while the creep strain component contributes to the time-dependent inelastic strain included in the plastic shear strain ($\Delta\gamma_p$) component as shown in Fig. 2.2. The energy-based fatigue model employs the cyclic stress–strain hysteresis loop to compute the elastic strain energy density (ΔW_e) and inelastic dissipated energy or plastic work per cycle (ΔW_p).

2.5.1 Plastic Strain Range Fatigue Models

The Coffin–Manson fatigue model [18] is perhaps the best-known and most widely used approach for LCF analysis. The total number of cycles to failure, $N_{f,}$ is dependent on the plastic strain range, $\Delta\varepsilon_{p,}$ the fatigue ductility coefficient, ε_f', and the fatigue ductility exponent, c, given in the expression below:

$$\frac{\Delta\varepsilon_p}{2} = \varepsilon_f'(2N_f)^c. \tag{2.43}$$

The fatigue ductility coefficient, ε_f', is approximately equal to the true fracture ductility, ε_f. The fatigue ductility exponent, c, varies between -0.5 and -0.7 [21], and experimental data are required to determine the constants.

Solomon's LCF model [22] relates the plastic shear strain range to fatigue life cycles is given below:

$$\Delta\gamma_p N_p^{\alpha} = \theta \tag{2.44}$$

$\Delta\gamma_p$ is the plastic shear strain range. N_p is the number of cycles to failure, θ is the inverse of the fatigue ductility coefficient, and α is a material constant.

2.5.2 Creep Strain Range Fatigue Models

Creep strain range fatigue models account strictly for the cyclic creep deformation in the solder joints. Early attempts at modeling creep were made by isolating the elastic and plastic deformation mechanisms. Creep, as mentioned previously, can be separated into two possible mechanisms, matrix and grain boundary creep. Knecht and Fox [23] proposed a simple matrix creep fatigue model relating the solder microstructure and the matrix creep shear strain range given below,

$$N_{\mathrm{f}} = \frac{C}{\Delta\gamma_{\mathrm{mc}}} \tag{2.45}$$

The number of cycles to failure, N_{f}, is related to a constant C, which is dependent on failure criteria and solder microstructure. $\Delta\gamma_{\mathrm{mc}}$ is the strain range due to matrix creep.

2.5.3 Creep-Fatigue Interaction Model

By applying Miner's linear superposition principal, both plastic and creep strain can be accounted for in strain-based fatigue model [24]. This model combines the Solomon fatigue model with the Knecht and Fox creep model and is given below:

$$\frac{1}{N_{\mathrm{f}}} = \frac{1}{N_{\mathrm{p}}} + \frac{1}{N_{\mathrm{c}}}, \tag{2.46}$$

where N_{p} refers to the number of cycles to failure due to plastic fatigue and is obtained directly from the Solomon's fatigue model, N_{c} refers to the number of cycles to failure due to the creep fatigue and is obtained from the Knecht and Fox's creep fatigue model.

2.5.4 Frequency Modified Plastic Strain Range Method

The constants in the Coffin–Manson model are dependent on temperature and cyclic frequency. The modified Coffin–Manson model [25] given below:

$$\left[N_{\mathrm{f}} v^{(k-1)}\right]^{m} \Delta\varepsilon_{\mathrm{p}} = C, \tag{2.47}$$

where

$$v^{(k-1)} = \begin{cases} v^{(k_1-1)} & \text{for } 1\ \text{Hz} \geq v \geq 10^{-3}\text{Hz} \\ \left[\dfrac{v}{10^{-3}}\right]^{(k_2-1)} \left(10^{-3}\right)^{(k_1-1)} & \text{for } 10^{-3}\text{Hz} > v \geq 10^{-4}\text{Hz} \end{cases}$$

and, k_1, k_2, m, and C are dependent on temperature and frequency. The frequency effect was compensated by this frequency-modified model. However, the temperature effect of LCF behavior is still a problem.

2.5.5 *Energy-Based Models*

Energy-based fatigue models form the largest group of models. These models are used to predict fatigue failure based on a hysteresis energy term or type of volume-weighted average stress–strain history.

A modified energy-based LCF model [26], is given below,

$$\left[N_{\mathrm{f}} v^{(k-1)}\right]^m \frac{W_{\mathrm{p}}}{2\sigma_{\mathrm{f}}} = C, \tag{2.48}$$

where

$$v^{(k-1)} = \begin{cases} v^{(k_1-1)} & \text{for } 1\ \text{Hz} \geq v \geq 10^{-3}\text{Hz} \\ \left[\dfrac{v}{10^{-3}}\right]^{(k_2-1)} \left(10^{-3}\right)^{(k_1-1)} & \text{for } 10^{-3}\text{Hz} > v \geq 10^{-4}\text{Hz} \end{cases}$$

and, k_1, k_2, m, and C are dependent on temperature and frequency.

An empirical plastic work model was developed by Darveaux [2, 16] for solder joint subject to thermal cycling tests and is used to predict the crack initiation and crack growth behavior using the equations given below:

$$N_0 = K_1 \Delta W^{K_2} \tag{2.49}$$

$$\frac{\mathrm{d}a}{\mathrm{d}N} = K_3 \Delta W^{K_4}, \tag{2.50}$$

where ΔW is the plastic work, a is the area of the solder joint where a fatigue crack will grow till failure, K_1, K_2, K_3, and K_4 are constants fitted to the test data. This model must be used with a calibrated FEA model with a specific element size and volume.

The plastic work, ΔW, calculated must be normalized by the volume of the solder elements used for fatigue analysis.

$$\Delta W_{\text{ave}} = \frac{\sum \Delta W \cdot V}{\sum V}, \tag{2.51}$$

where ΔW_{ave} is the average plastic work and V is the volume of each element selected for analysis.

References

1. Lau JH (1993) Thermal stress strain in microelectronics packaging. New York: Van Nostrand Reinhold
2. Lau JH (1991) Solder joint reliability, theory and application. New York, Van Nostrand Reinhold
3. Pang HLJ (2007) Lead-free solder materials: design for reliability, Chapter 12. In: Suhir E, Lee YC, Wong CP (eds) Micro- and opto-electronic materials and structures: physics, mechanics, design, reliability, packaging, vol 7, Materials physics/materials mechanics. Springer, New York
4. Pang JHL, Chong DYR (2001) Flip chip on board solder joint reliability analysis using 2-D and 3-D FEA models. IEEE Trans Adv Packag 24(4):499–506
5. Pang JHL, Chong DYR, Low TH (2001) Thermal cycling analysis of flip-chip solder joint reliability. IEEE Trans Components Packag Technol 24(4):705–712
6. Pang JHL, Low TH, Xiong BS, Che FX (2003) Design for reliability (DFR) methodology for electronic Packaging assemblies. Proceedings of IEEE, 2003 Electronics Packaging Technology Conference, pp 470–478
7. Pang JHL, Xiong BS (2005) Mechanical properties for 95.5Sn-3.8Ag-0.7Cu lead-free solder alloy. IEEE Trans Components Packag Technol 28(4):830–840
8. Yeo A, Lee C, Pang HLJ (2006) Flip chip solder joint reliability analysis using viscoplastic and elastic-plastic-creep analysis. IEEE Trans Components Packag Technol 29(2):355–363
9. Shi XQ, Pang HLJ, Zhou W, Wang ZP (1999) Temperature and strain rate effects on mechanical properties of 63Sn/37Pb solder alloy. Advances in Electronic Packaging 1999, Proceedings of InterPACK'99, pp 551–557
10. Shi XQ, Zhou W, Pang HLJ et al (1999) Effect of temperature and strain rate on mechanical properties of 63Sn/37Pb solder alloy. ASME J Electron Packag 121(3):179–185
11. Pang JHL, Xiong BS, Low TH (2004) Creep and fatigue characterization of lead free 95.5Sn-3.8Ag-0.7Cu solder. Proceedings of IEEE, 2004 Electronic Components and Technology Conference, 54th ECTC, vol 2, pp 1333–1337
12. Pang JHL, Yeo A, Low TH, Che FX (2004) Lead-free 96.5Sn-3.5Ag flip chip solder joint reliability analysis. Proceedings of IEEE, 2004 Inter Society Conference on Thermal Phenomena, ITherm 2004, vol 2, pp 160–164
13. Che FX,Pang JHL (2004) Thermal fatigue reliability analysis for PBGA with Sn-3.8Ag-0.7Cu solder joints. 2004 Proceedings of Electronics Packaging Technology Conference, pp 787–792
14. Anand L (1985) Constitutive equations for hot working of metals. J Plasticity 1:213–231
15. Brown SB, Kwon HK, Anand L (1989) An internal variable constitutive model for hot working of metals. Int J Plastic 5:95–130
16. Darveaux R (2000) Effect of simulation methodology on solder joint crack growth correlation. Electronic Components and Technology Conference, 2000 IEEE, pp 158–169

17. Che FX, Pang JHL, Xiong BS, Xu L, Low TH (2005) Lead free solder joint reliability characterization for PBGA, PQFP and TSSOP assemblies. 2005 Proceedings of 55th Electronic Components and Technology Conference, pp 916–921
18. Coffin LF (1954) A study of the effects of cyclic thermal stresses on a ductile metal. Trans ASME 76:931
19. Manson SS (1965) Fatigue a complex subject-some simple approximations. Exp Mech 5 (7):193–226
20. Morrow JD (1964) Cyclic plastic strain energy and fatigue of metals. ASTM STP 378, American Society for Testing and Materials, Philadelphia, PA, p 45
21. Kilinski TJ, Lesniak JR, Sandor BI (1991) Modern approaches to fatigue life prediction of SMT solder joints. In: Lau JH (ed) Solder joint reliability theory and applications. Van Nostrand Reinhold, New York
22. Solomon HD (1991) Predicting thermal and mechanical fatigue lives from isothermal low cycle data, Chapter 14. In: Lau JH (ed) Solder joint reliability. Van Nostrand Reinhold, New York
23. Knecht S, Fox R (1990) Constitutive relationship and creep-fatigue life model for eutectic tin-lead solder. IEEE Trans Components, Hybrids, and Manufacturing Technol 13(2):424–433
24. Pang JHL, Seetoh CW, Wang ZP (2000) CBGA solder joint reliability evaluation based on elastic-plastic-creep analysis. J Electron Packag 122:255–261
25. Shi XQ, Pang HLJ, Zhou W, Wang ZP (2000) Low cycle fatigue analysis of temperature and frequency effects in eutectic solder alloy. Int J Fatigue 22:217–228
26. Shi XQ, Pang HLJ, Zhou W, Wang ZP (1999) A modified energy-based low cycle fatigue model for eutectic solder alloy. Scr Mater 41(3):289–296

Chapter 3
Mechanical Properties and Constitutive Models

Abstract Chapter 3 reports on experimental tests to characterize the mechanical properties for the apparent elastic modulus, yield stress, and ultimate tensile strength. These mechanical properties are highly dependent on test temperature and test strain rate. For high strain-rate test conditions, a Split-Hopkinson pressure bar (SHPB) test method was employed for measuring strain-rate influence on the yield stress of lead-free solder material. Comparisons of these mechanical properties were made for Sn–Ag–Cu, Sn–Cu, and Sn–Pb solder alloys. Strain rate and temperature-dependent mechanics of material models were curve-fitted for the range of temperatures (−40°C to +125°C) and strain-rates (0.0001–1,000 s^{-1}) tested. Creep tests results are presented in steady state creep models. A rate dependent viscoplastic deformation model by Anand, was fitted to the test data from the creep test and tensile test of Sn–Ag–Cu, Sn–Cu, and Sn–Pb solder alloys.

In this chapter, the mechanical properties for bulk solder materials specifically for 95.5Sn–3.8Ag–0.7Cu and 99.3Sn–0.7Cu lead-free solder alloys will be reported in detail. This will include temperature and strain rate-dependent tensile tests, high strain rate tension test by the Split-Hopkinson pressure bar, and creep tests. Constitutive models for steady state creep deformation behavior and rate-dependent viscoplastic deformation models were derived from the tensile and creep test results.

3.1 Tensile Tests

The tensile test method was employed to measure the mechanical properties of 95.5Sn–3.8Ag–0.7Cu and 99.3Sn–0.7Cu solder alloys. Dog bone-shaped bulk solder specimens for the uniaxial tensile test were machined from solder bar. The specimen has a total length of 65 mm, a gauge length of 15 mm, and a diameter of 3 mm (shown in Fig. 3.1) following the ASTM standard [1]. The tensile tests were

J.H.L. Pang, *Lead Free Solder: Mechanics and Reliability*,
DOI 10.1007/978-1-4614-0463-7_3,

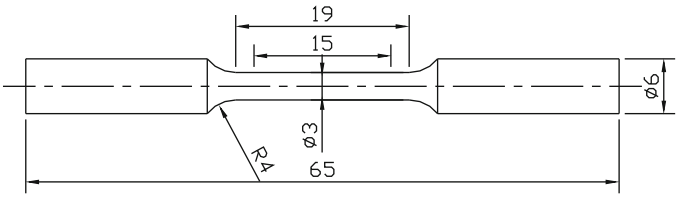

Fig. 3.1 Tensile and creep specimen (in mm)

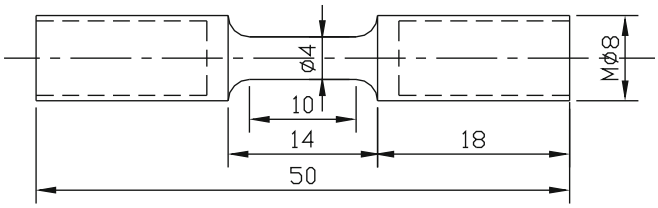

Fig. 3.2 Split Hopkinson pressure bar specimen (in mm)

carried out on a universal testing machine, at four different temperatures (−40°C, 25°C, 75°C, and 125°C). At each temperature, three different displacement rates were used (0.5, 5, and 50 mm/min).

3.2 High Strain Rate Tests

A Split Hopkinson Pressure Bar (SHPB) test method was employed to test the mechanical properties of 95.5Sn–3.8Ag–0.7Cu and 99.3Sn–0.7Cu solder alloys at high strain rates. Dog bone-shaped bulk solder specimens for tensile SHPB test were prepared by machining from bars. The specimen has a total length of 50 mm, a gauge length of 10 mm, and a diameter of 4 mm as shown in Fig. 3.2. The specimen was threaded at both ends and screwed to the test system.

The SHPB is based on the theory of wave propagation in elastic bar and interaction between a stress pulse and the specimen of different impedance. A schematic of SHPB and recording system is shown in Fig. 3.3. There is a data acquisition system to collect and analyze the output waveforms from the SHPB test method.

3.3 Creep Tests

Creep tests were conducted for 95.5Sn–3.8Ag–0.7Cu and 99.3Sn–0.7Cu solder alloys using the bulk solder specimen shown in Fig. 3.1. Creep tests were carried out on a universal testing machine under constant load creep test conditions at isothermal test temperatures in a thermal chamber. Creep tests were carried out at

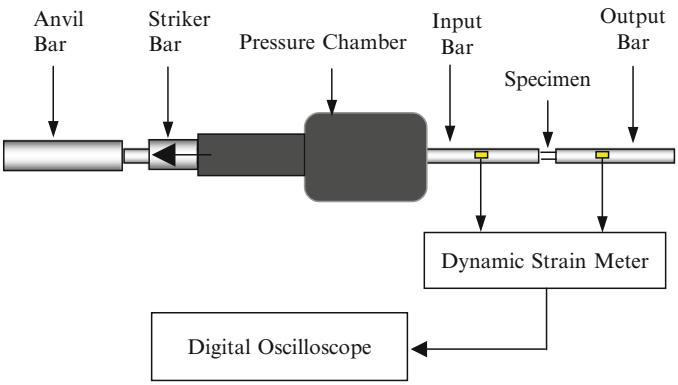

Fig. 3.3 High strain rate tension test using SHPB test system

four different isothermal temperatures (−40°C, 25°C, 75°C, and 125°C) with the stress set at 11 different values (3, 4, 5, 7, 10, 15, 20, 25, 30, 35, 40, 50, 60, and 70 MPa).

3.4 Tensile Test Results

3.4.1 95.5Sn–3.8Ag–0.7Cu Solder Alloy

The effects of strain rate and temperature on the 95.5Sn–3.8Ag–0.7Cu tensile properties were evaluated and the stress–strain curves for the three different strain rates at a constant temperature of 25°C are shown in Fig. 3.4. The test result for the three strain rate conditions at a temperature of 125°C is given in Fig. 3.5. It can be seen that the mechanical properties of 95.5Sn–3.8Ag–0.7Cu is dependent on the test temperature and strain rate parameters [2, 3].

The result of the effect of temperature on elastic modulus is shown in Fig. 3.6. It can be seen that the curves demonstrate linear relationship between the elastic modulus and the temperature and it is noted that elastic modulus decreases at higher temperatures. The effect of strain rate on elastic modulus was presented by plotting the graph of elastic modulus versus strain rate as shown in Fig. 3.7. The plot shows approximately straight lines with a constant slope for the temperature tested. This is expected as the elastic modulus has a linear function of logarithmic strain rate and elastic modulus increase with the strain rate.

The yield stress was computed from the stress–strain curve at 0.2% plastic strain. The effects of test temperature and strain rate on the yield stress are shown in Figs. 3.8 and 3.9. There is a linear relationship between the yield stress and temperature, and the trend shows a decrease in yield stress at higher temperatures. The yield stress versus logarithmic strain rate plot also shows a linear relationship and it is noted that yield stress increases with faster strain rate.

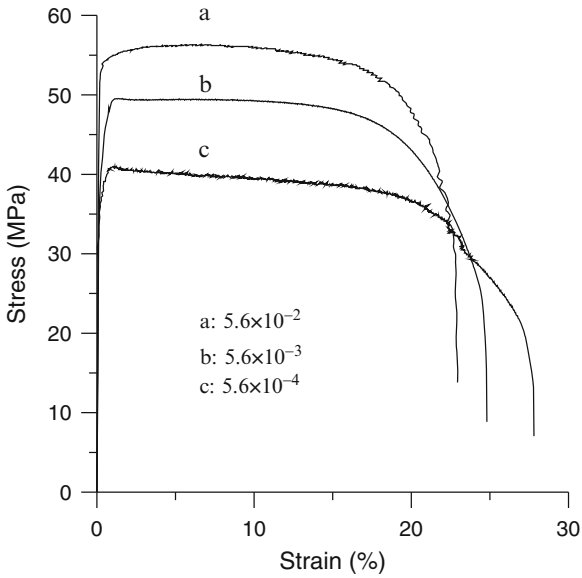

Fig. 3.4 Tensile test results at 25°C

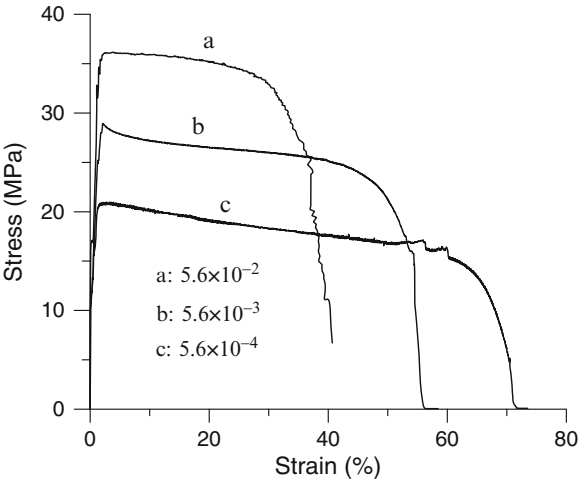

Fig. 3.5 Tensile test results at 125°C

The corresponding results for the ultimate tensile stress (UTS) are shown in Figs. 3.10 and 3.11, respectively. The UTS results have a similar trend to the yield stress results. The UTS increases with increase in strain rate and decreases with increase in temperature.

The temperature- and strain rate-dependent elastic modulus, yield stress, and UTS for the bulk 95.5Sn–3.8Ag–0.7Cu solder tensile test results were given in Table 3.1.

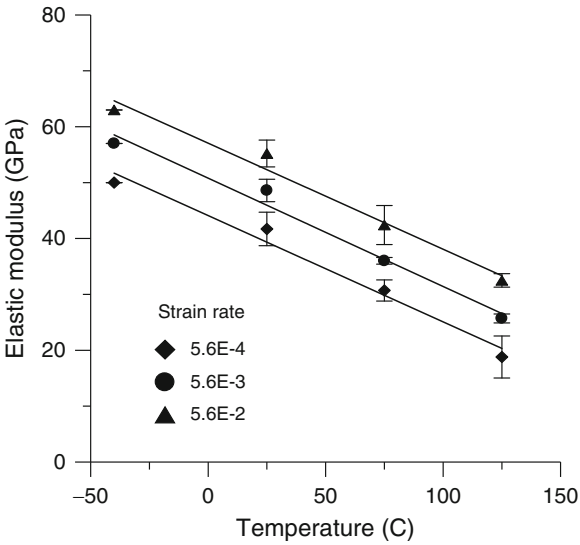

Fig. 3.6 Effect of temperature on elastic modulus

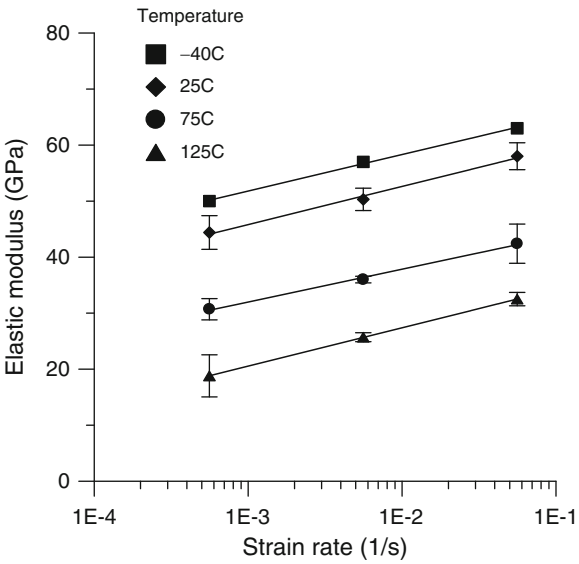

Fig. 3.7 Effect of strain rate on elastic modulus

3.4.2 99.3Sn–0.7Cu Solder Alloy

The mechanical properties of 99.3Sn–0.7Cu solder alloy have similar trend with Sn–3.8Ag–0.7Cu solder alloy, the elastic modulus, yield stress, and UTS will increase with strain rate and decrease with temperature. But it is noted that

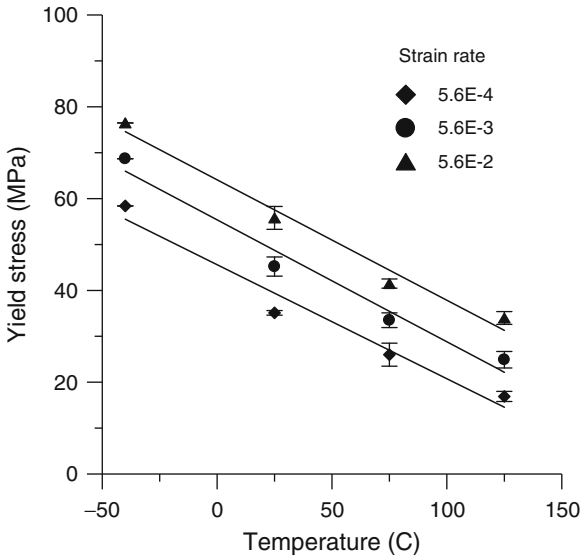

Fig. 3.8 Effect of temperature on yield stress

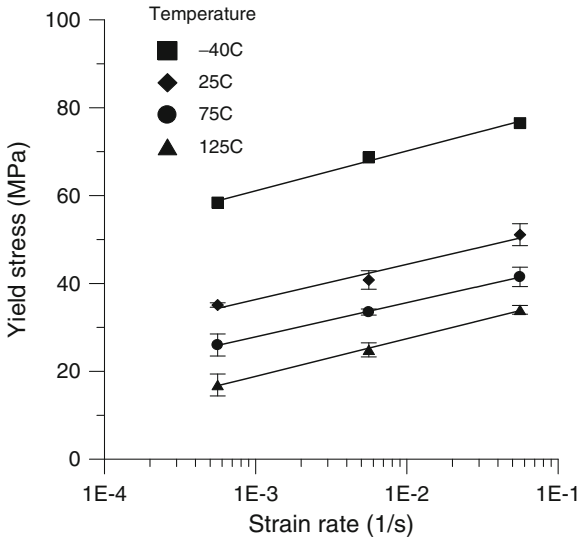

Fig. 3.9 Effect of strain rate on yield stress

Sn–0.7Cu solder has lower yield stress and UTS properties compared to 95.5Sn–3.8Ag–0.7Cu solder alloy. The temperature- and strain rate-dependent elastic modulus, yield stress, and UTS for the bulk 99.3Sn–0.7Cu solder tensile test results were given in Table 3.2.

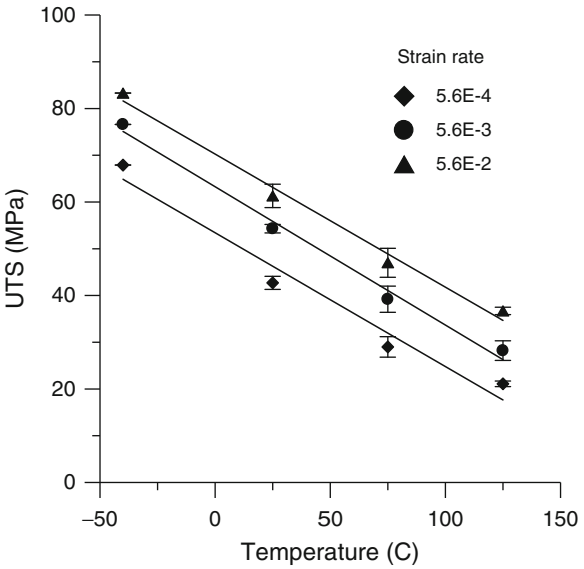

Fig. 3.10 Effect of temperature on UTS

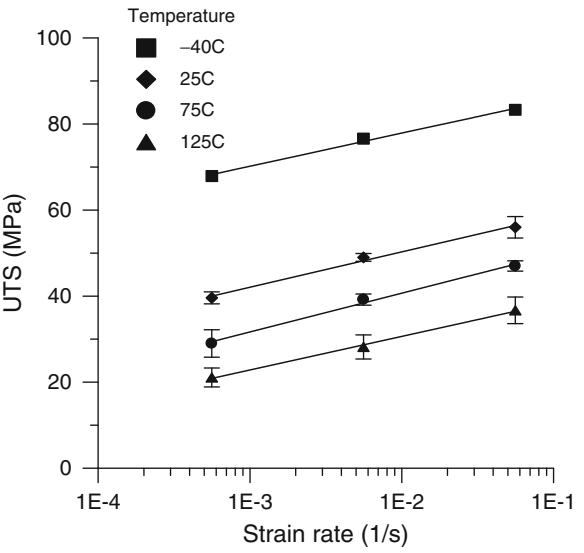

Fig. 3.11 Effect of strain rate on UTS

Table 3.1 Tensile test results for Sn–3.8Ag–0.7Cu solder

	E (GPa)	Yield (MPa)	UTS (MPa)
25°C			
5.6×10^{-4}	41.8	35.1	40.6
5.6×10^{-3}	48.3	42.9	49.0
5.6×10^{-2}	55.1	52.8	58.0
75°C			
5.6×10^{-4}	30.7	25.6	29.0
5.6×10^{-3}	36.0	33.5	38.8
5.6×10^{-2}	42.4	41.5	47.0
125°C			
5.6×10^{-4}	18.8	16.7	19.7
5.6×10^{-3}	26.1	23.9	27.2
5.6×10^{-2}	32.5	34.0	39.7
−40°C			
5.6×10^{-4}	51	58.4	67.9
5.6×10^{-3}	57	68.7	76.6
5.6×10^{-2}	63	76.5	83.3

Table 3.2 Summary of tensile test results for Sn–0.7Cu solder

	E (GPa)	Yield (MPa)	UTS (MPa)
25°C			
5.6×10^{-4}	20.2	31.1	35.8
5.6×10^{-3}	25.6	36.5	45.0
5.6×10^{-2}	32	47.8	52.0
75°C			
5.6×10^{-4}	15.6	22.8	26.1
5.6×10^{-3}	18.9	30.4	34.2
5.6×10^{-2}	23.3	35.8	42.0
125°C			
5.6×10^{-4}	11.6	16.5	18.2
5.6×10^{-3}	15.0	21.4	26.1
5.6×10^{-2}	18.9	29.5	38.2

3.4.3 Comparison on Tin-Lead and Lead-Free Solder Properties

The mechanical properties for 63Sn–37Pb solder at different temperatures and strain rates were reported by Shi et al. [4]. The comparison of elastic modulus, yield stress, and UTS for Sn–3.8Ag–0.7Cu (SAC387), 99.3Sn–0.7Cu (Sn–0.7Cu), and 63Sn–37Pb (Sn–37Pb) at room temperature and high temperature are shown in Figs. 3.12, 3.13, and 3.14, respectively. It can be seen that SAC387 has the highest mechanical properties among the three solders. Sn–0.7Cu solder has similar mechanical properties as Sn–37Pb solder. The differences in elastic modulus are significant for three solders.

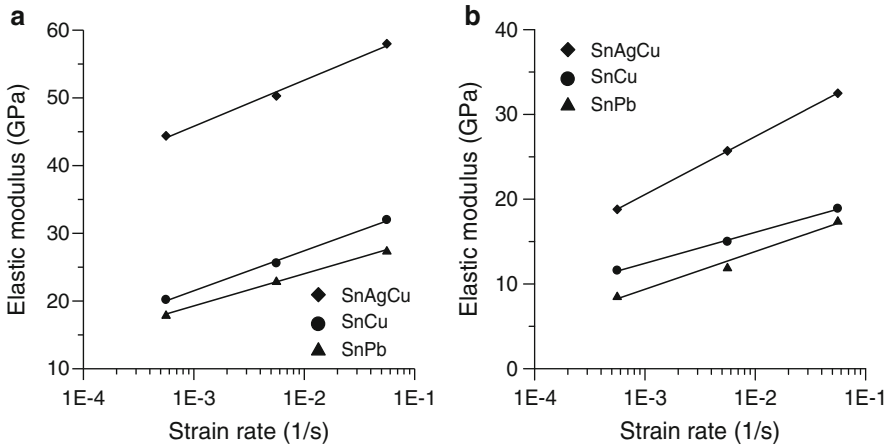

Fig. 3.12 (**a**) Comparison of elastic modulus at 25°C. (**b**) Comparison of elastic modulus at 125°C

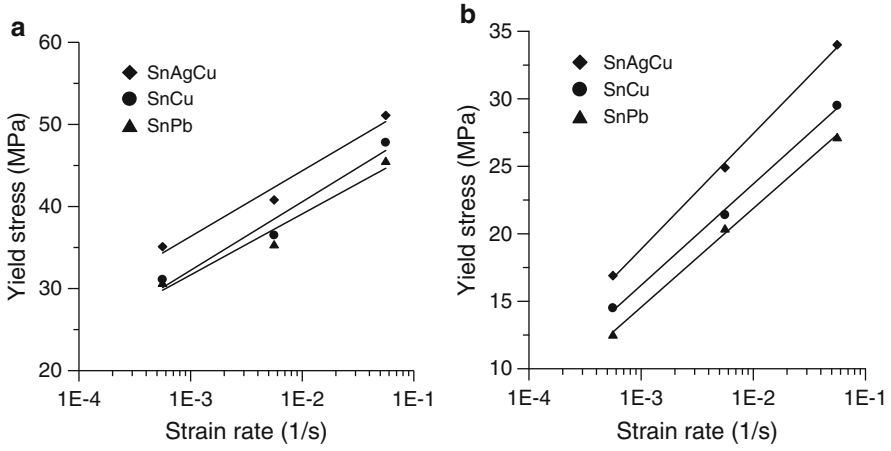

Fig. 3.13 (**a**) Comparison of yield stress at 25°C. (**b**) Comparison of yield stress at 125°C

At room temperature, SAC387 has a modulus of 50 GPa, compared to around 30 GPa for Sn–0.7Cu and Sn–37Pb solder alloys. However, the difference in yield stress and UTS is not as significant as elastic modulus, and the differences for three solders are within 15 MPa for all test conditions.

Comparisons were made with reported [5–10] tensile properties for Sn–Ag–Cu and Sn–Cu lead-free solders. The comparison of elastic modulus and tensile

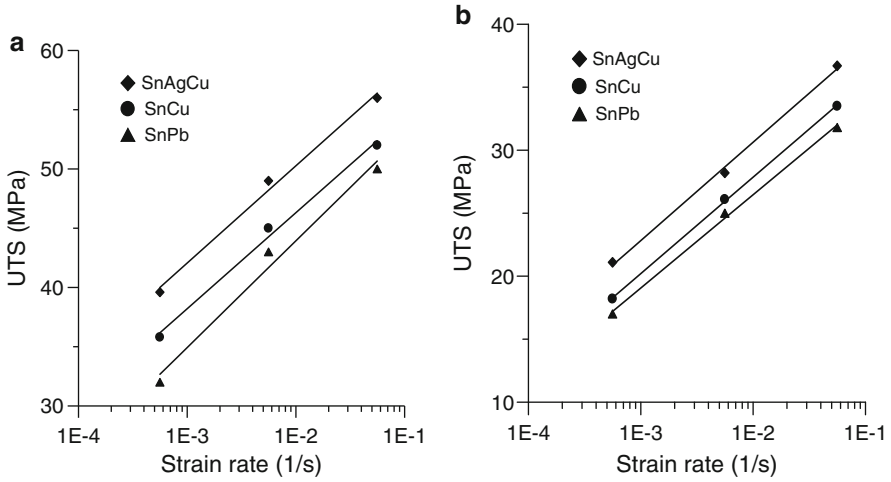

Fig. 3.14 (**a**) Comparison of UTS at 25°C. (**b**) Comparison of UTS at 125°C

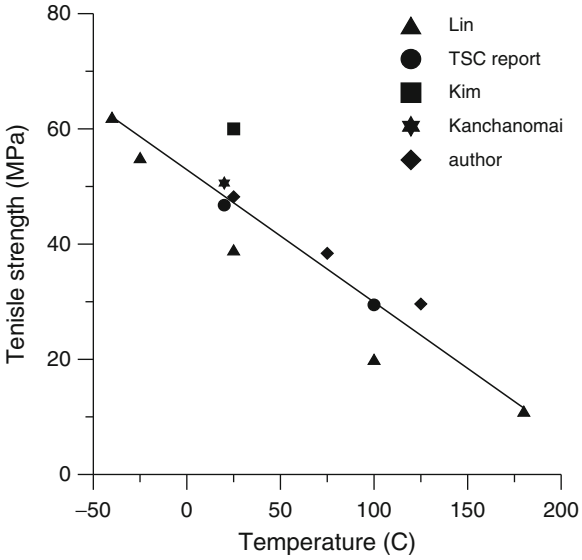

Fig. 3.15 Tensile strength for Sn–Ag–Cu

strength at different temperatures for Sn–Ag–Cu and Sn–Cu solders is shown in Figs. 3.15 and 3.16, respectively. It is noted that there are typical variations in the tensile strength results, as there are experimental differences in material and specimen preparation, and test conditions.

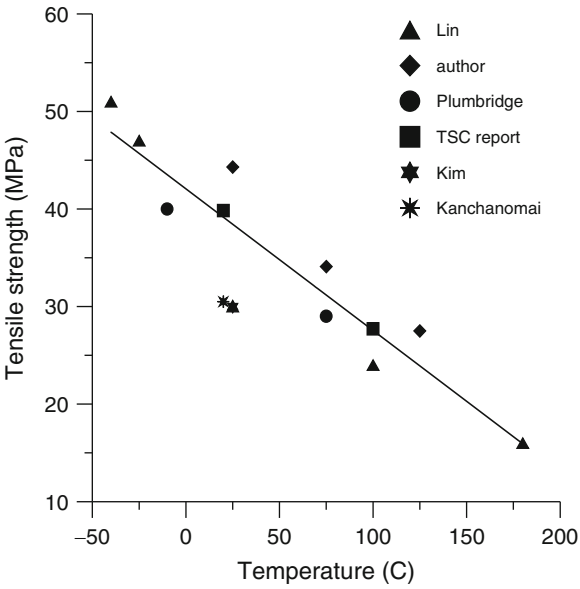

Fig. 3.16 Tensile strength for Sn–Cu

3.5 Split Hopkinson Pressure Bar Tensile Test Result

Split Hopkinson pressure bar (SHPB) tests were conducted with a SHPB, so the stress and strain could be measured and calculated [11, 12]. Upon the incident pulse hitting the specimen, it is split into reflected and transmitted pulse. Based on the strain gauge readings of incident, reflected, and transmitted pulses, stress and strain during the impact tests can be determined. Typical pulse shape and relationship among incident, reflected, and transmitted pulses are shown in Figs. 3.17 and 3.18.

By plotting all stress–strain curves into one graph, the effect of strain on the Sn–3.8Ag–0.7Cu and 99.3Sn–0.7Cu solders tensile properties of impact tests could be evaluated and compared. The stress–strain curves of Sn–3.8Ag–0.7Cu at room temperature and different strain rates (7×10^2, 9×10^2, and 1.3×10^3 s^{-1}) were shown at Fig. 3.19. The strain rate-dependent stress–strain curves at four different strain rates of Sn–0.7Cu solder were shown in Fig. 3.20. The elastic modulus and yield stress at different strain rates are summarized in Table 3.3. Sn–3.8Ag–0.7Cu has higher mechanical properties than Sn–0.7Cu at high strain rates [12].

3.5.1 Strain Rate- and Temperature-Dependent Tensile Properties

The mechanical properties of Sn–3.8Ag–0.7Cu and Sn–0.7Cu are strongly dependent on temperature and strain rate. Hence, a statistical method incorporating linear

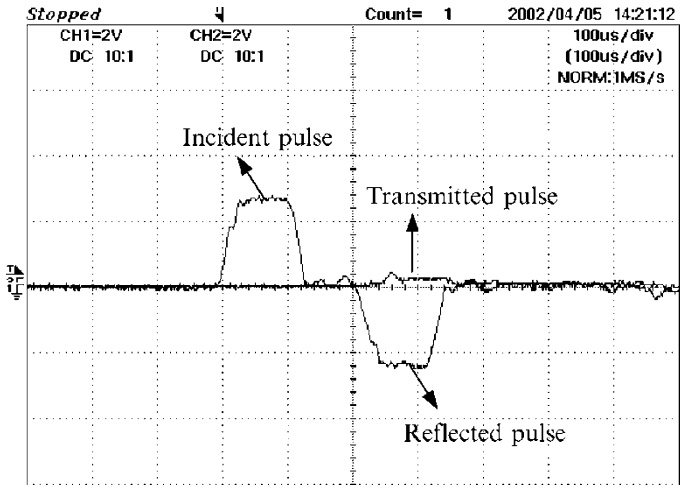

Fig. 3.17 Typical pulse shape of SHPB test

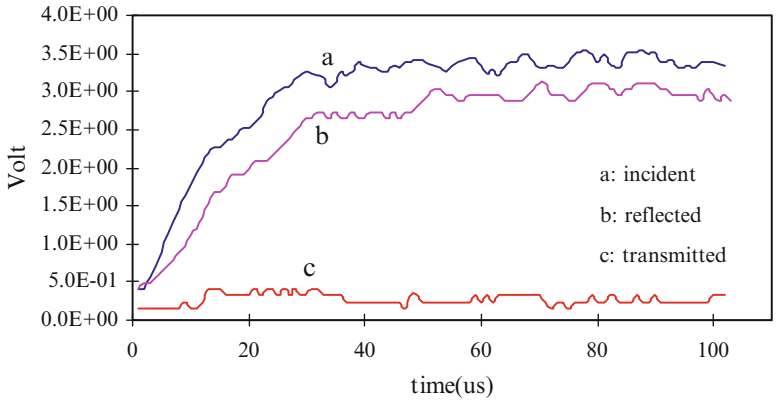

Fig. 3.18 Typical relationship among incident, reflected, and transmitted pulse

regression was employed to quantify the temperature- and strain rate-dependent mechanical properties of 95.5Sn–3.8Ag–0.7Cu and 99.3Sn–0.7Cu lead-free solders.

The Young's modulus of 95.5Sn–3.8Ag–0.7Cu and 99.3Sn–0.7Cu is as follows:

$$E(T,\dot{\varepsilon})_{\mathrm{SnAgCu}} = (0.00074T + 6.44)\log(\dot{\varepsilon}) + (-0.1932T + 65.935) \tag{3.1}$$

$$E(T,\dot{\varepsilon})_{\mathrm{SnCu}} = (-0.0235T + 6.396)\log(\dot{\varepsilon}) + (-0.157T + 42.1) \tag{3.2}$$

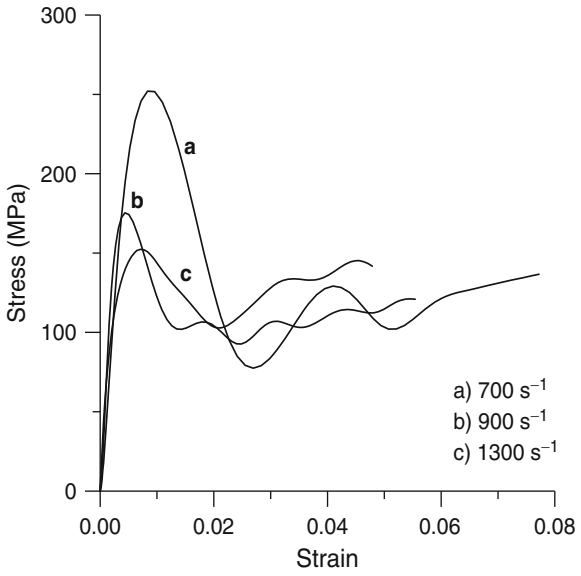

Fig. 3.19 Impact results for Sn–3.8Ag–0.7Cu

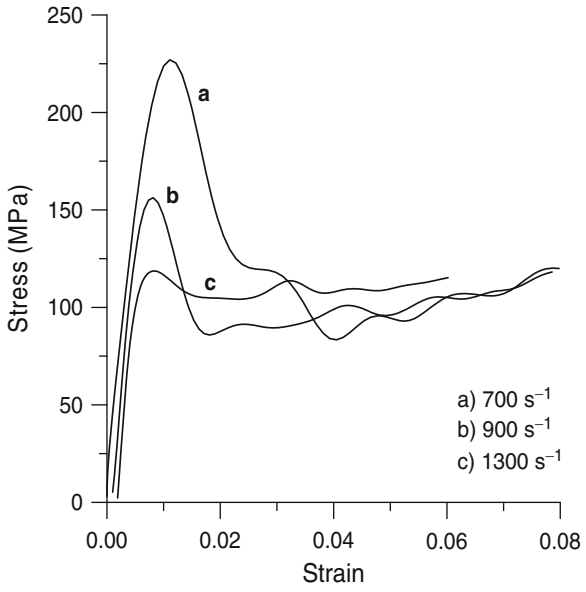

Fig. 3.20 Impact results for Sn–0.7Cu

The yield stress and UTS were derived from fitting to the test data and are expressed individually as follows:

$$\sigma_y(T,\dot{\varepsilon})_{\mathrm{SnAgCu}} = (-0.2053T + 76.61)(\dot{\varepsilon})^{(6.54\times10^{-4}T+0.074)} \tag{3.3}$$

Table 3.3 SHPB test results of Sn–3.8Ag–0.7Cu and Sn–0.7Cu solders

	Sn–3.8Ag–0.7Cu		Sn–0.7Cu	
	E (GPa)	Yield (MPa)	*E* (GPa)	Yield (MPa)
7×10^2	52.8	129	12.89	111
9×10^2	53.3	175	13.64	129
1.3×10^3	54.0	300	29.8	203

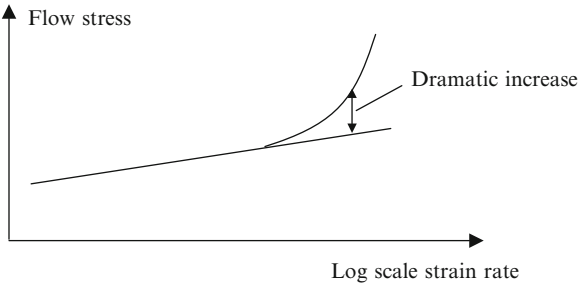

Fig. 3.21 Schematic of strain rate-dependent flow stress

$$\sigma_y(T,\dot{\varepsilon})_{\text{SnCu}} = (-0.199T + 65.1)(\dot{\varepsilon})^{(2.87\times10^{-4}T+0.08254)} \tag{3.4}$$

$$\text{UTS}(T,\dot{\varepsilon})_{SnAgCu} = (-0.2161T + 81.32)(\dot{\varepsilon})^{(6.27\times10^{-4}T+0.0619)} \tag{3.5}$$

$$\text{UTS}(T,\dot{\varepsilon})_{\text{SnCu}} = (-0.062T + 65.8)(\dot{\varepsilon})^{(7.9\times10^{-4}T+0.0545)} \tag{3.6}$$

The above equations (3.1)–(3.6) for elastic modulus, yield stress and UTS are within 5% of the tensile test results for the range of temperature and strain rate tested. Hence the curve-fitted equations (3.1)–(3.6) are recommended for use to model the temperature (−40°C to +125°C) and strain rate- (10^{-4} to 10^{-1} s^{-1}) dependent mechanical properties for 95.5Sn–3.8Ag–0.7Cu and 99.3Sn–0.7Cu lead-free solders respectively.

The strain rate-dependent flow stress (or yield stress) of the lead-free solders at high strain rates (such as impact tests) are highly dependent on strain rates as well. The flow or yield stress equations in (3.3) and (3.4) should be used for conventional tensile test conditions at low strain rate conditions. If the strain rate is as high as in the impact test conditions (10^2 s^{-1} to 10^3 s^{-1}), (3.3) and (3.4) are no longer able to model the strain rate effects adequately. There is a dramatic difference between the flow or yield stress behavior at higher strain rate conditions. Most ductile metals, exhibit strain rate sensitivity effects, where the flow stress will experience a dramatic increase at high strain rates (10^2 s^{-1} to 10^3 s^{-1}) due to strain rate hardening behavior [13]. The strain rate dependent on flow stress in Fig. 3.21 shows a linear increase when plotted with logarithmic strain rate. Above a high strain rate regime (10^2 s^{-1} to 10^3 s^{-1}) a dramatic increase in flow stress is expected due to strain rate hardening response.

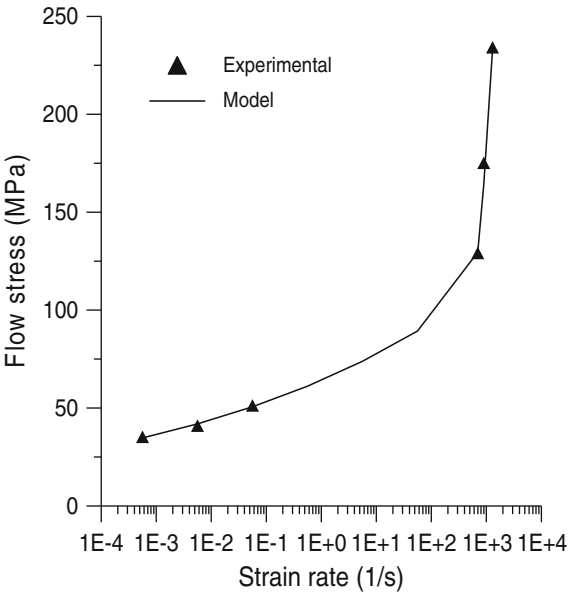

Fig. 3.22 Flow stress versus strain rate for SAC387

Equations (3.3) and (3.4) can be used to predict the flow stress for slower strain rates. But this linear relationship could not be used to describe the flow stress over a wider range of strain rate (10^{-4} s^{-1} to 10^{3} s^{-1}). The flow stress will increase dramatically when the strain rate is at a higher level (10^{2} s^{-1} to 10^{3} s^{-1}). This higher strain rate part can be modeled by (3.7).

$$\sigma_{increase} = B\dot{\varepsilon}^{m}\dot{\varepsilon} \geq 10^{2} \tag{3.7}$$

By combining (3.3) and (3.4) with (3.7), the constitutive model to predict the strain rate-dependent flow stress over a wider range of strain rate can be developed.

Based on the SHPB test result at room temperature for three different strain rates, the values of constant B and exponent m in (3.7) can be derived. Hence, combining (3.3) and (3.4) with the result from (3.7), the strain rate-dependent flow stress at room temperature over a wide range of strain rates (10^{-4} s^{-1} to 10^{3} s^{-1}) for Sn–3.8Ag–0.7Cu and Sn–0.7Cu is now given in (3.8) and (3.9), respectively.

$$\sigma_{flow}(\dot{\varepsilon})_{\mathrm{SnAgCu}} = \begin{cases} 64.1\dot{\varepsilon}^{0.082} & 10^{-4} \leq \dot{\varepsilon} < 10^{2} \\ 64.1\dot{\varepsilon}^{0.082} + 1.44 \times 10^{-5}\dot{\varepsilon}^{2.22} & \dot{\varepsilon} \geq 10^{2} \end{cases} \tag{3.8}$$

$$\sigma_{\mathrm{flow}}(\dot{\varepsilon})_{SnCu} = \begin{cases} 60.1\dot{\varepsilon}^{0.09} & 10^{-4} \leq \dot{\varepsilon} < 10^{2} \\ 60.1\dot{\varepsilon}^{0.091} + 1.64 \times 10^{-6}\dot{\varepsilon}^{2.46} & \dot{\varepsilon} \geq 10^{2} \end{cases} \tag{3.9}$$

A plot of the experimental flow stress test data from SHPB and the predicted flow stress model result show good agreement for SAC387 solder in Fig. 3.22 and for Sn–0.7Cu solder in Fig. 3.23 respectively.

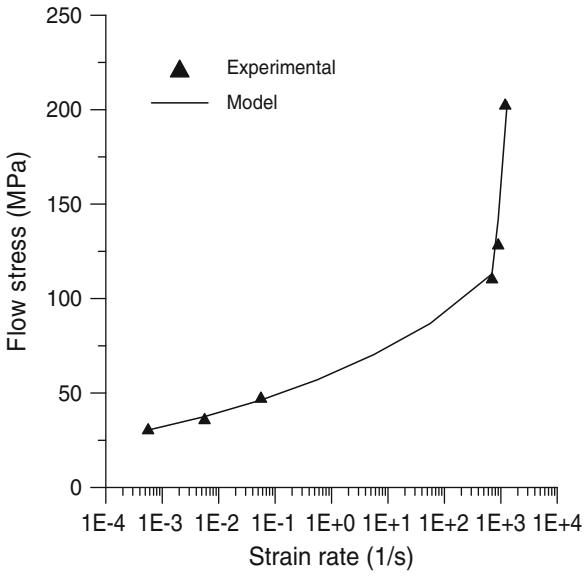

Fig. 3.23 Flow stress versus strain rate for Sn–0.7Cu

3.6 Creep Test Result

3.6.1 Steady State Creep Strain Rate for Lead-Free Solders

The steady state creep strain rates are plotted against the applied stress in Fig. 3.24 for SAC387 and in Fig. 3.25 for Sn–0.7Cu solder alloys. It can be seen that at a constant temperature and increasing applied stress, the steady state creep strain rate will increase with increasing stress level. At higher temperature test conditions, it is clear that the steady state creep strain rate test data increases significantly in orders of magnitude. By comparing the creep properties for SAC387 versus Sn–0.7Cu solder, it can be seen that SAC387 solder has lower creep strain rates at the same condition of stress and temperature. It can be concluded that SAC387 has lower creep strain rate resistance compared to Sn–0.7Cu solder alloy [14].

3.6.2 Comparison with Reported Tin–Lead and Lead-Free Solder Results

3.6.2.1 Comparison with Tin–Lead Solder

The creep properties for 63Sn–37Pb solder at different temperatures and stress levels was reported earlier by Shi et al. [4]. The comparison of steady state creep strain rate for Sn–3.8Ag–0.7Cu, Sn–0.7Cu, and 63Sn–37Pb at room temperature (25°C) and at high temperature (125°C) are shown in Figs. 3.26 and 3.27,

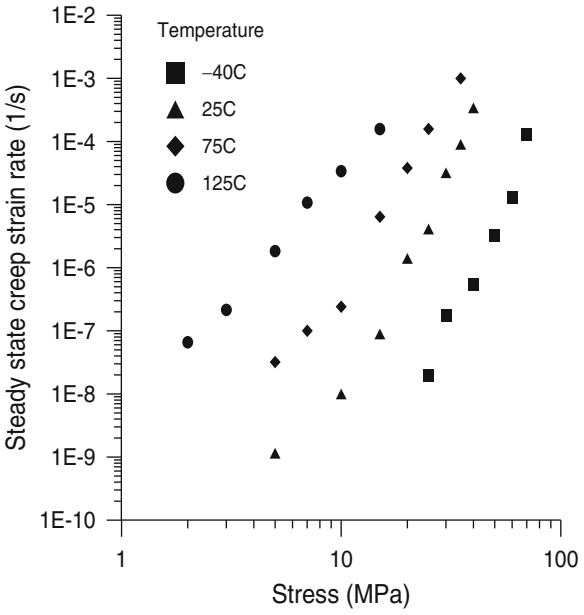

Fig. 3.24 Steady state creep behavior of Sn–Ag–Cu

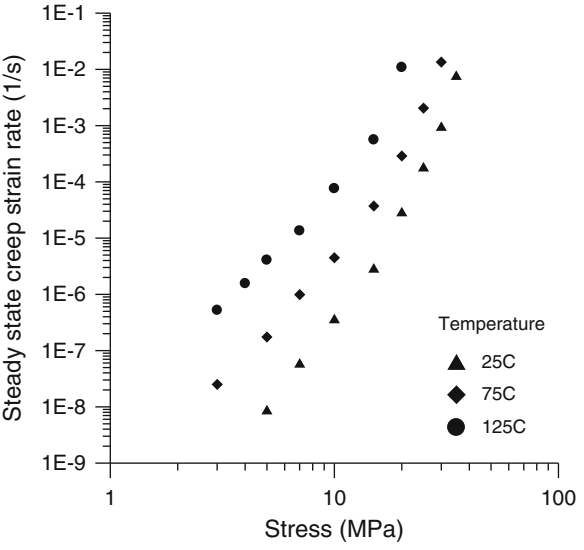

Fig. 3.25 Steady state creep behavior of Sn–Cu

respectively. It can be seen that both lead-free solder alloys (SAC387 and Sn–0.7Cu) have better creep resistance compared to tin–lead solder (Sn–37Pb). Between the two lead-free solders, SAC387 has better creep resistance compared to Sn–0.7Cu solder.

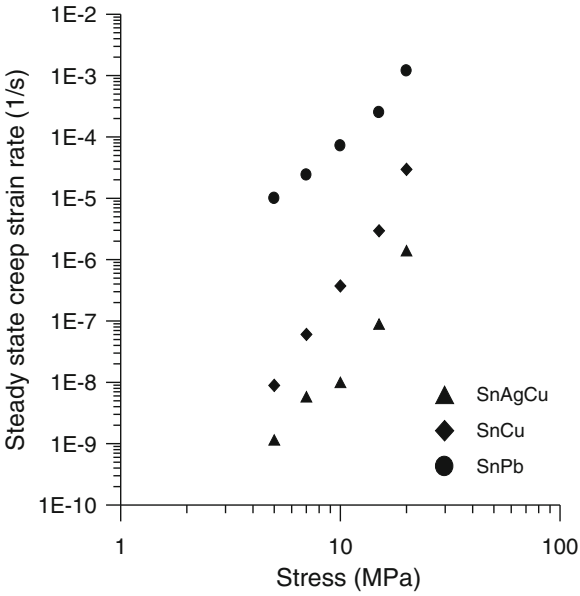

Fig. 3.26 Comparison of creep resistance at 25°C

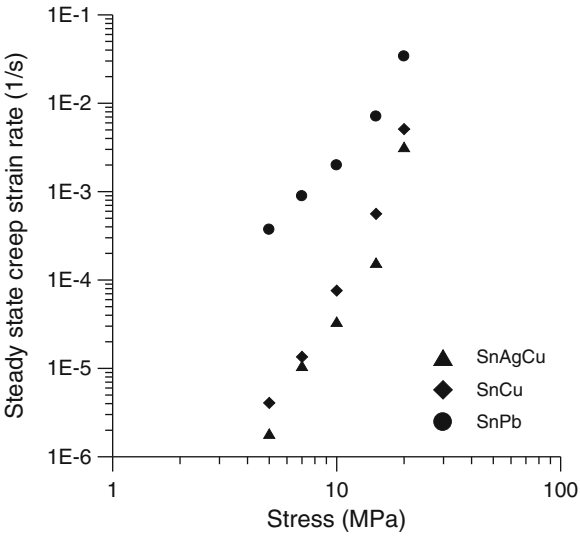

Fig. 3.27 Comparison of creep resistance at 125°C

3.6.2.2 Comparison with Reported Lead-Free Solder Results

Some reported creep test results [15–18] for Sn–3.8Ag–0.7Cu and Sn–0.7Cu solder alloys were reviewed and compared to the author's creep test data. Figure 3.28 shows the comparison with Sn–Ag–Cu creep test data from Morris et al. [15].

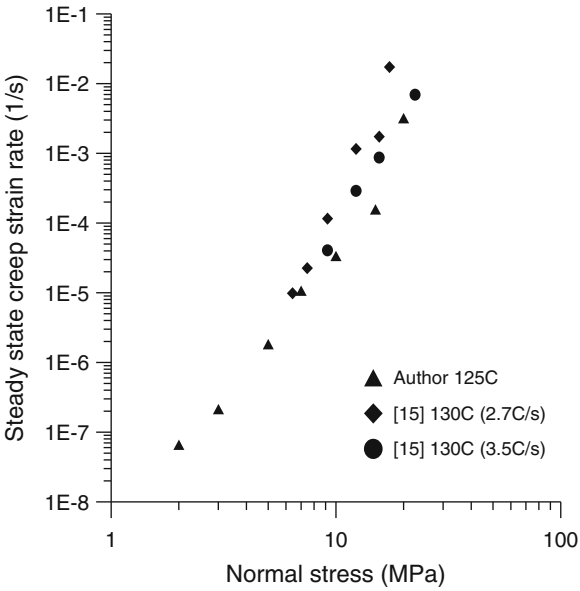

Fig. 3.28 Creep properties for Sn–Ag–Cu

Solder joint specimens were used in Fay's lap-shear test samples with a solder joint height of 160 μm. Their samples were cooled at two cooling rates of 2.7°C/s and 3.5°C/s, respectively. It was found that steady state creep strain rates for the author's bulk solder data and the solder joint creep test results by Morris et al. [15] were comparable at high temperature [19, 20] as shown in Fig. 3.28. The Sn–Ag–Cu creep data comparison at room temperature between Dusek [16] and author's result are also acceptable. Few creep data for Sn–0.7Cu solder was reported, the author's Sn–0.7Cu data was compared with results reported by Plumbridge [17] at 75°C, and good comparison is noted in Fig. 3.29.

3.6.3 Creep Models

Creep of a material is often characterized by its steady state creep strain rate $\dot{\varepsilon}_{ss}$, which can be simply expressed as power law relationship

$$\dot{\varepsilon} = A\sigma^n e^{\frac{-Q}{kT}}, \tag{3.10}$$

where A is material constant, σ is applied stress, n is stress exponent, Q is creep activation energy, k is Boltzmann's constant, and T is absolute temperature. The activation energy, Q, and the stress exponent, n, change with the dominant creep mechanism, and may have different values at different regimes of the applied stress.

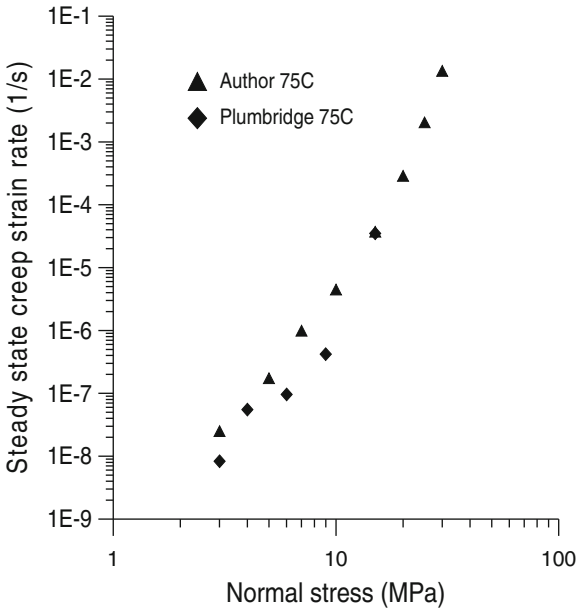

Fig. 3.29 Creep properties for Sn–Cu

To describe the steady state creep strain rate at different regimes of stress and temperature, hyperbolic-sine model is widely used. The expression of the models is,

$$\dot{\varepsilon} = C[\sinh(\alpha\sigma)]^n \exp\left(-\frac{Q}{kT}\right) \tag{3.11}$$

Then the results of steady state creep strain rate dependent on normal stress and temperature for 95.5Sn–3.8Ag–0.7Cu and 99.3Sn–0.7Cu lead-free solders were use to curve fit to the model described in (3.11). Figures 3.30 and 3.31 show the comparison of calculated steady strain rates with the experimental ones at different temperatures. The separated points in the figures express the experimental results obtained in this study; the solid lines in the figure denote the steady strain rate curves with the values of parameters obtained in curve-fitting. It is recognized that calculated results based on (3.11) show fairly good agreement with experimental results.

After curve-fitting, the parameters for Sn–3.8Ag–0.7Cu and Sn–0.7Cu solder can be determined, and were shown as,

$$\dot{\varepsilon}_{\mathrm{SnAgCu}} = 501.3[\sinh(0.0316\sigma)]^{4.96} \exp\left(-\frac{5433.5}{T}\right) \tag{3.12}$$

$$\dot{\varepsilon}_{SnCu} = 4.35[\sinh(0.096\sigma)]^{3.7} \exp\left(-\frac{4835.2}{T}\right) \tag{3.13}$$

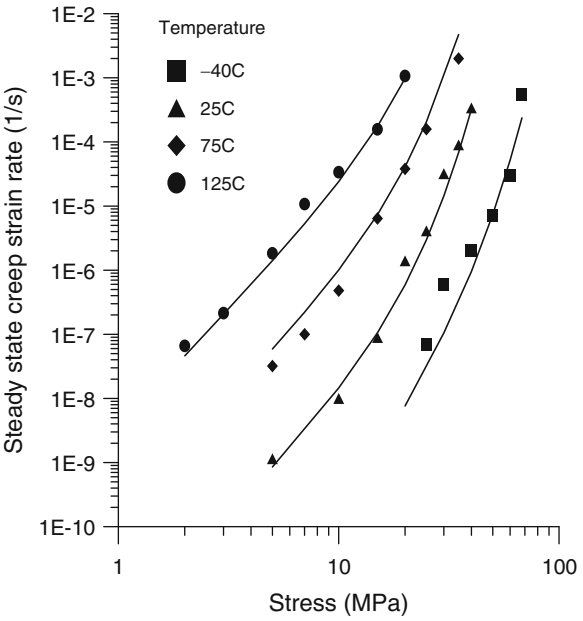

Fig. 3.30 Hyperbolic-sine model of Sn–Ag–Cu

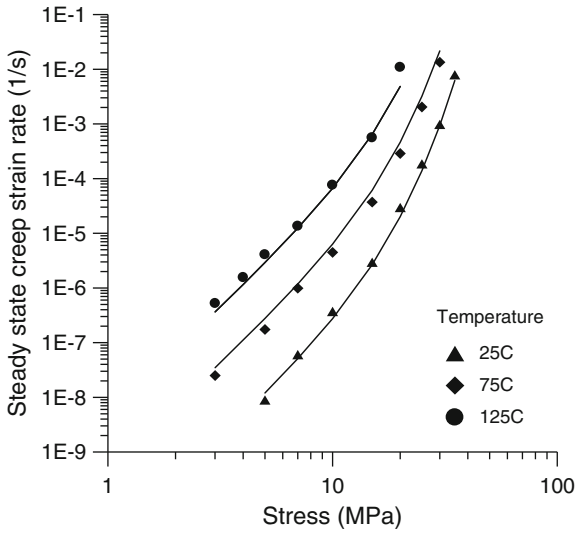

Fig. 3.31 Hyperbolic-sine model of Sn–Cu

Table 3.4 Comparison of creep test data for Sn–Ag–Cu solder alloy

	Material	Specimen	Stress exponent n	Active energy Q (KJ/mol)
Pang [21]	95.5Sn3.8Ag0.7Cu	Cylindrical bulk specimen with gauge diameter of 3 mm and gauge length of 15 mm	4.96	45.2
Lau [19]	96.5Sn3.9Ag0.6Cu	Compression specimen with diameter of 10 mm and length of 19 mm	4.2	45
Schubert [20]	95.5Sn3.8Ag0.7Cu	Flat bulk specimen with 3 × 3 mm cross section and gauge length of 30 mm	6.4	54

Lau [19] and Schubert [20] also reported their creep tests data for Sn–Ag–Cu solder, their curve-fitted results for the hyperbolic-sine creep model are shown below [21],

$$\text{Lau}_{(95.5Sn-3.9Ag-0.6Cu)} \quad \dot{\varepsilon} = 4.41 \times 10^5 [\sinh(0.005\sigma)]^{4.2} \exp(-5412/T) \tag{3.14}$$

$$\text{Schubert}_{(95.5\text{Sn}-3.8\text{Ag}-0.7\text{Cu})} \quad \dot{\varepsilon} = 2.78 \times 10^5 [\sinh(0.02447\sigma)]^{6.41} \exp(-6496/T) \tag{3.15}$$

A comparison of the Sn–Ag–Cu solder material, specimen type, stress exponent and activation energy from Lau Schubert and the Pang's creep test result is given in Table 3.4. It was noted that the stress exponent n varies from 4.2 to 6.4, while the activation energy, Q, varies from 45 to 54 KJ/mol. A comparison of the steady state creep model using the (3.12), (3.14) and (3.15) are shown in Fig. 3.32. From the figure, it can be seen that the author's creep data agree well with data reported by Lau [19]. Satisfactory agreement with Schubert's data [20] was seen at low stresses, but some difference is noted at higher stresses above 10 MPa.

3.7 Viscoplastic Constitutive Models

The Anand model has been used to model thermal cycling deformation analysis of soldered assemblies [22]. Tensile and creep test results for the two lead-free solders (SAC387 and Sn–0.7Cu) were curve-fitted to Anand model first reported by Anand [23] and Brown and Anand [24], and used by Darveaux [22] for solder alloy materials. The nine material constants for the Anand model will be presented for the SAC387 and Sn–0.7Cu lead-free solder in the section below.

The Anand model includes two kinds of equations, the first one deals with relationship between saturation stress and strain rate under certain temperature, while the second one deals with relationship between strain and stress under certain strain rate and temperature. They are as following equations (3.16) and (3.17):

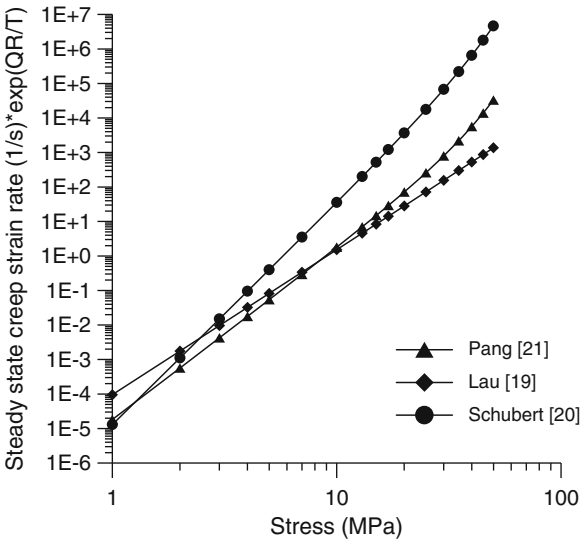

Fig. 3.32 Comparison of steady-state creep data for Sn–Ag–Cu solder alloy

Table 3.5 Parameters in Anand model for Sn–3.8Ag–0.7Cu and Sn–0.7Cu

	A	Q/R	ξ	m	$\hat{s}$	n	h_0	a	s_0
Sn–3.8Ag–0.7Cu	65.92	6,656	8	0.346	80.8	0.0002	86442.8	1.29	37.1
Sn–0.7Cu	9,875	5,276	2	0.176	65.2	0.003	61987.3	1.03	33.8

$$\sigma* = \frac{\hat{s}}{\xi}\left(\frac{\dot{\varepsilon}_p}{A}e^{Q/RT}\right)^n \sinh^{-1}\left[\left(\frac{\dot{\varepsilon}_p}{A}e^{Q/RT}\right)^m\right], \tag{3.16}$$

where variables $\dot{\varepsilon}_p$ and T denote strain rate and temperature, respectively. And parameters Q/R, A, $\hat{s}/\xi$, m, and n can be determined by a nonlinear fitting method.

$$\sigma = \sigma * -[(\sigma * -cs_0)^{(1-a)} + (a-1)ch_0\sigma*^{(-a)}\varepsilon_p]^{1/(1-a)}, \tag{3.17}$$

where variable ε_p denotes the nonlinear strain, a, s_0, and $h_0$are parameters to be determined, and c is a function of strain rate and temperature:

$$c \equiv \frac{1}{\xi}\sinh^{-1}\left[\left(\frac{\dot{\varepsilon}_p}{A}e^{Q/RT}\right)^m\right] \quad c < 1 \tag{3.18}$$

Based on the tensile and creep test of Sn–3.8Ag–0.7Cu and Sn–0.7Cu solder at different temperatures, strain rates or stress levels, nine constants in Anand model can be determined, as shown in Table 3.5.

The comparison of model prediction and the raw data for Sn–3.8Ag–0.7Cu lead-free solder is shown in Figs. 3.33 and 3.34. The separated points in the figures express the experiment results, and the solid lines in the figures denote the calculated

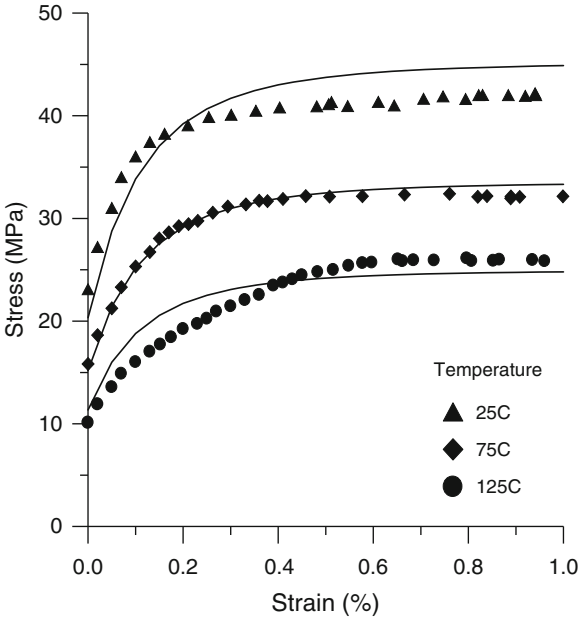

Fig. 3.33 Anand model at strain rate of $5.6 \times 10^{-4}\ s^{-1}$

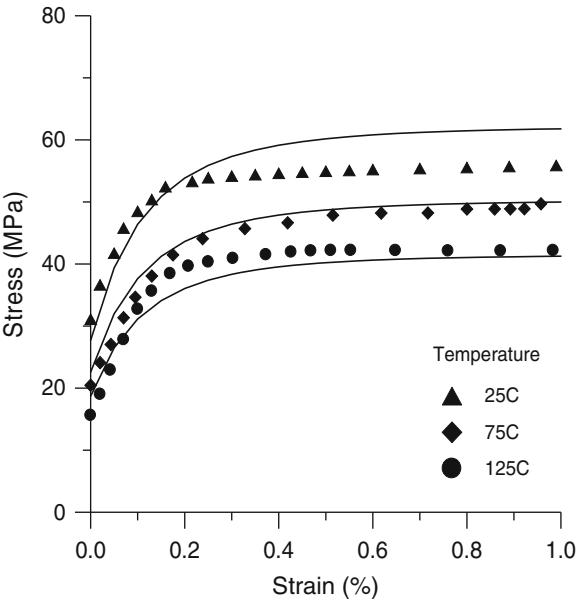

Fig. 3.34 Anand model at strain rate of $5.6 \times 10^{-2}\ s^{-1}$

stress–strain curves with the values of parameters obtained in Anand model curve-fitting. It is recognized that calculated results can predict the tensile stress–strain curves well [22].

References

1. ASTM Standards (1998) ASTM E8M: standard test methods for tension testing of metallic materials [metric], vol 03.01. The American Society for Testing and Materials, Philadelphia, PA
2. Pang HLJ, Xiong BS, Kurniawijaya H (2002) Mechanical strength of lead-free solders. GlobalTRONICS technology conference, 2002, Singapore EXPO, 3–5 Sept, pp 113–118
3. Pang HLJ, Xiong BS, Neo CC, Zhang XR, Low TH (2003) Bulk solder and solder joint properties for lead-free solder 95.5Sn-3.8Ag-0.7Cu solder alloy. IEEE proceedings of 2003 electronic components and technology conference, 2003, pp 673–679
4. Shi XQ, Zhou W, Pang HLJ, Wang ZP (1999) Effect of temperature and strain rate on mechanical properties of 63Sn/37Pb solder alloy. J Electron Packaging 121:179–185
5. Lin JK, Silva AD, Frear D, Guo Y, Jang JW, Li L, Mitchell D, Yeung B, Zhang C (2001) Characterization of lead-free solders and under bump merallurgies for flip-chip package. 2001 Electronic components and technology conference, pp 455–462
6. Kim KS, Huh SH, Suganuma K (2002) Effects of cooling speed on microstructure and tensile properties of Sn-Ag-Cu alloys. Mater Sci Eng A333:106–114
7. Kanchanomai C, Miyashita Y, Mutoh Y (2002) Low cycle fatigue behavior of Sn-Ag, Sn-Ag-Cu and Sn-Ag-Cu-Bi lead-free solders. J Electron Mater 31:456
8. Harrison MR, Vincent JH, Steen HAH (2001) Lead-free reflow soldering for electronic assembly. Soldering & Surface Mount Technol 13(3):21–38
9. Plumbridge WJ, Gagg CR (2001) The mechanical properties of lead-containing and lead-free solders meeting the environmental challenge. Proc Instn Mech Engrs 214 (Part L):153–161
10. Technical reports for the lead free solder project: properties reports: room temperature tensile properties of lead-free solder alloys (1998) Lead Free Solder CD-ROM, Project 170502, 6/99, National Center for Manufacturing (NCMS). http://www.ncms.org/index.php/programs/collaborative-projects/ncms-final-reports-test/
11. Lan Hong D, Shi-Wei RL (2001) Characterization of strain rate-dependent behavior of 63Sn-37Pb solder alloy. Proceedings of IPACK'01 The Pacific Rim/ASME international electronic packaging technical conference and exhibition, Kauai, Hawaii, July 8–13 2001, pp 1–7
12. Pang HLJ, Xiong BS, Low TH (2004) Comprehensive mechanics characterization of lead-free 95.5Sn-3.8Ag-0.7Cu solder. Micro Material and Nano Material, Issue 3
13. Tanimura S, Mimura K, Zhu WH (2000) Practical constitutive models covering wide ranges of strain rates, strains and temperature. Key Eng Mater 177–180:189–200
14. Pang HLJ, Xiong BS, Low TH (2004) Creep and fatigue properties of lead free Sn-3.8Ag-0.7Cu solder. Proceedings of 54th ECTC, Las Vegas, vol 2, June 1–4 2004, pp 1333–1337
15. Morris JW Jr, Song HG, Fay H (2003) Creep properties of Sn-rich joints. Electronic components and technology conference, pp 54–57
16. Dusek M, Hunt C (2003) Do we know enough about lead-free solders? IPC/JEDEDC, October 2003, http://www.npl.co.uk/ei/
17. Plumbridge WJ, Gagg CR, Peters S (2001) The creep of lead-free solders at elevated temperature. J Electron Mater 30(9):1178–1183
18. Pang JHL, Xiong BS, Low TH (2003) Constitutive model for lead-free 95.5Sn-3.8Ag-0.7Cu solder alloy. ICMAT, Singapore, 2003
19. Lau J, Dauksher W, Vianco P (2003) Acceleration models, constitutive equations, and reliability of lead-free solders and joints. IEEE proceedings of 2003 electronic components and technology conference, pp 229–236

20. Pang J, Schubert A (2002) Lead free solder materials and reliability performance. Short course notes at 4th electronics packaging technology conference, lead-free workshop, 10 Dec 2002
21. Pang JHL, Xiong BS (2005) Mechanical properties for 95.5Sn-3.8Ag-0.7Cu Lead free solder alloy. IEEE Trans Components Packaging Technol 28(4):830–840
22. Pang JHL, Xiong BS, Che FX (2004) Modeling stress strain curves for lead-free Sn-3.8Ag-0.7Cu solder. IEEE proceedings of EuroSime 2004 conference, Belgium, 9–12 May
23. Anand L (1985) Constitutive equations for hot working of metals. J Plasticity 1:213–231
24. Brown SB, Kwon HK, Anand L (1989) An internal variable constitutive model for hot working of metals. Int J Plastic 5:95–130

Chapter 4
Fatigue Life Prediction Models

Abstract Chapter 4 deals with low cycle fatigue tests and derivation of fatigue life prediction models curve-fitted to the fatigue test data for Sn–Ag–Cu and Sn–Cu solder alloys. The fatigue tests were conducted under low cycle fatigue test conditions over a wide range of isothermal temperatures (−40°C to +125°C) and frequencies. Both the strain-range and energy-based low cycle fatigue models were used. The fatigue life prediction model constants are presented in tables and closed-form equations for easy use to predict the solder joint fatigue life when the inelastic strain range or inelastic strain energy density fatigue driving force parameter is obtained from an FEA result.

The low cycle fatigue test specimens for 95.5Sn–3.8Ag–0.7Cu and 99.3Sn–0.7Cu solder alloy were machined from the solder bar. The configuration of the specimens has a diameter of 6 mm at the two ends, a center diameter of 3 mm, and a gauge length of 4.5 mm with a radius of curvature of 50 mm to reduce stress concentration effects due to sharp corners. The geometry of the specimen is following the ASTM standard [1] and is shown in Fig. 4.1.

The low cycle fatigue tests were conducted on a micro-force materials test system. The sine waveform was employed for all fatigue tests. The total strain was calculated from the crosshead displacement divided by the gauge length. The tests were carried out at three different frequencies (10^{-3}, 10^{-2}, and 1 Hz) and at three different temperatures (25°C, 75°C, and 125°C) with total strain set at four different values (2, 3.5, 5, and 7.5%). The fatigue failure was defined as 50% reduction of maximum tensile load.

J.H.L. Pang, *Lead Free Solder: Mechanics and Reliability*,
DOI 10.1007/978-1-4614-0463-7_4,

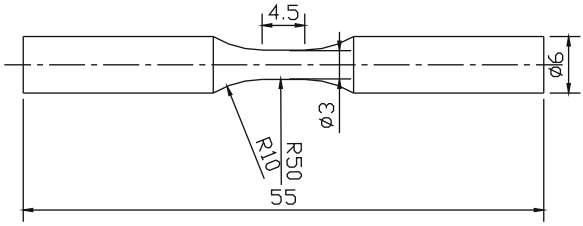

Fig. 4.1 Fatigue test specimen (in mm)

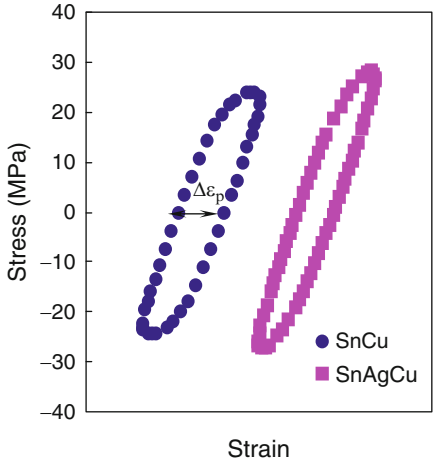

Fig. 4.2 Cyclic stress-strain hysteresis loops

4.1 Low Cycle Fatigue Test Result

4.1.1 Cyclic Stress–Strain Behavior

After calculating cyclic stress and strain in each cycle, stress–strain hysteresis loop of Sn–0.7Cu and Sn–3.8Ag–0.7Cu solders at the tenth cycle for 2% total strain range at temperature of 125°C and frequency of 1 Hz are shown in Fig. 4.2. For the same total strain range, Sn–0.7Cu solder has larger plastic range and smaller stress range than Sn–3.8Ag–0.7Cu solder. The plastic range increased with the applied total strain range, and will increase slightly with the number of cycles, as shown in Fig. 4.3.

The relationship between stress amplitude (one-half of the stress range) and number of cycles for Sn–0.7Cu and Sn–3.8Ag–0.7Cu solders for different total strain ranges at 125°C and 1 Hz are shown in Fig. 4.4. Cyclic softening was observed for both lead-free solders. At the beginning of the fatigue test, stress amplitude reduces rapidly, which may be due to the crack initiation.

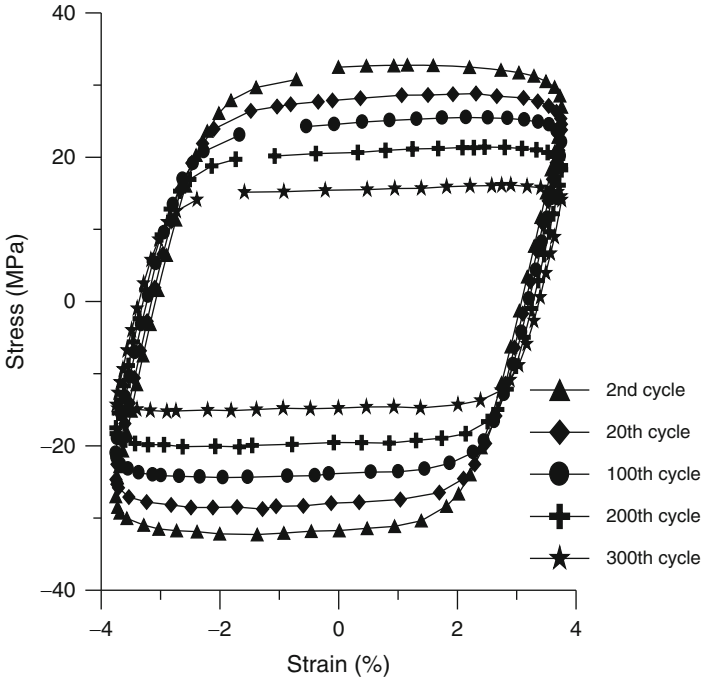

Fig. 4.3 Hysteresis loop at various cycles Sn–0.7Cu

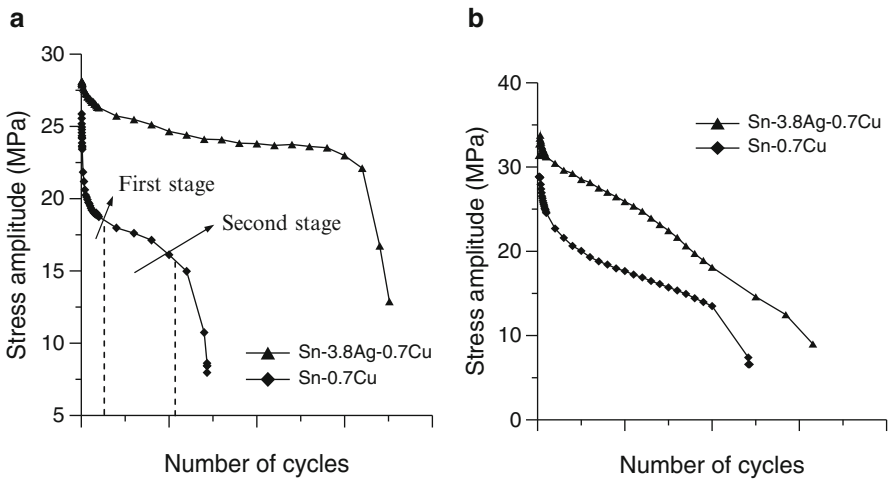

Fig. 4.4 (**a**) Relationship between stress amplitude and number of cycles at 2%, 125°C and 1 Hz. (**b**) Relationship between stress amplitude and number of cycles at 7.5%, 125°C and 1 Hz

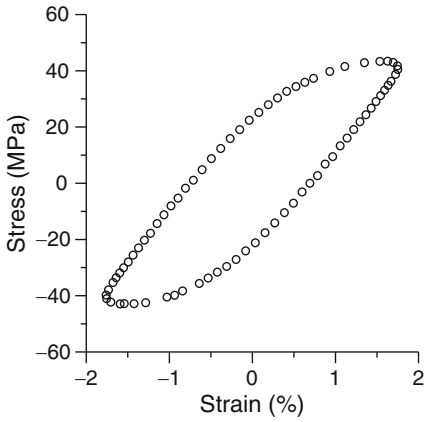

Fig. 4.5 Hysteresis loop for Sn–Cu at 1 Hz and strain range of 3.5%, at 25°C

After the crack initiation, the cracks will propagate with an increasing number of cycles. This propagation mechanism caused slow reduction of stress amplitude, which was defined as the second stage of the fatigue test. It is also noticed that the decrease rate of stress amplitude at the secondary stage will increase with the total strain range, which can be compared in Fig. 4.4a, b.

4.1.2 Effect of Temperature on Low Cycle Fatigue Behavior

Test result of Sn–0.7Cu solder at different temperatures will show the effect of temperature on low cycle fatigue. By plotting the hysteresis loop of different temperatures at strain range of 3.5% and frequency of 1 Hz, the material response at different temperatures was evaluated and compared in Figs. 4.5–4.7. The Sn–3.8Ag–0.7Cu solder has the similar trends with Sn–0.7Cu solder [2, 3].

The relationship between the fatigue life and plastic strain obtained from tests of 0.01 Hz at three different temperatures (25°C, 75°C, and 125°C) is presented in Fig. 4.6. The fatigue life versus inelastic strain energy density plot was given in Fig. 4.7.

From Figs. 4.6 and 4.7, the values of constants for Coffin–Manson model and Morrow's energy-based model can be determined for different temperatures by taking the slope and the interception of the plastic strain (inelastic strain energy density) axis. It was found that the value of m and C in Coffin–Manson model decreases with increasing temperature. For energy-based Morrow model, the same trend is noted for the constants n and A.

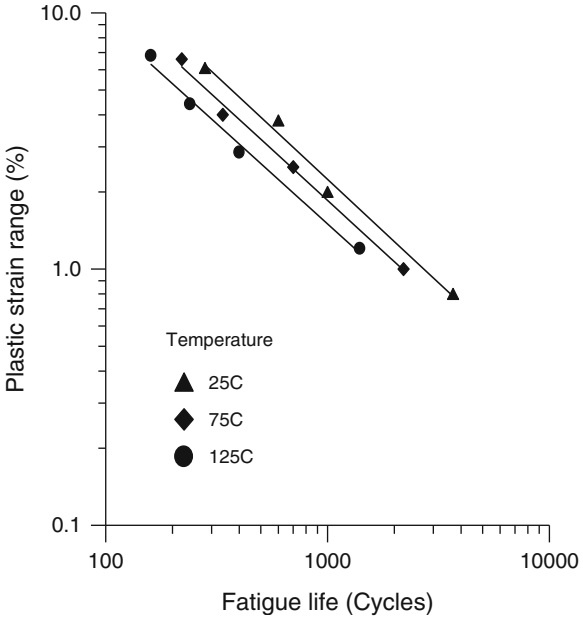

Fig. 4.6 Plastic strain versus fatigue life at 0.01 Hz for different temperatures

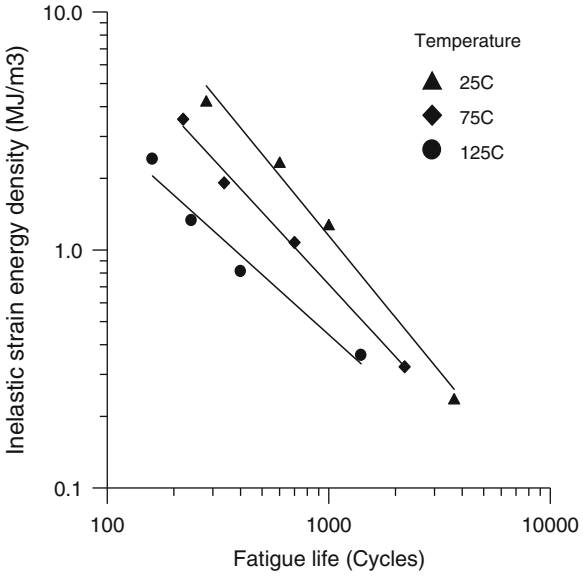

Fig. 4.7 Inelastic strain energy density versus fatigue life at 0.01 Hz for different temperatures

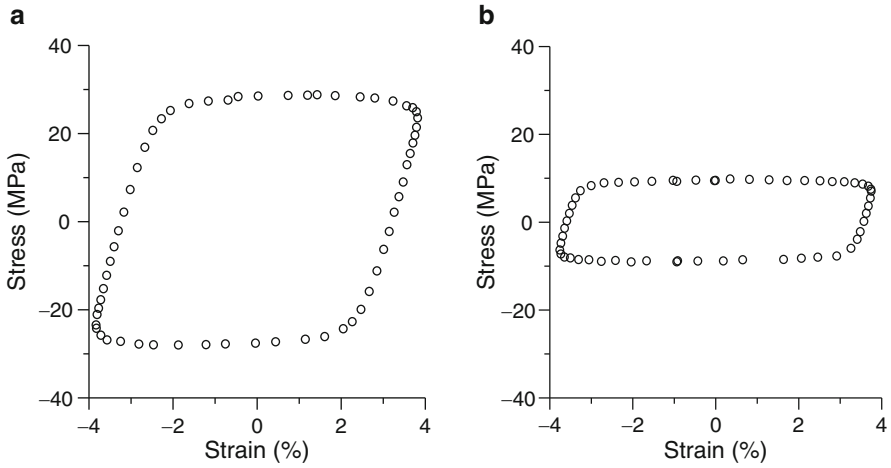

Fig. 4.8 Hysteresis loop for Sn–Cu at 125°C and strain range of 7.5%. (**a**) 1 Hz. (**b**) 0.001 Hz

4.1.3 Effect of Frequency on Low Cycle Fatigue Behavior

The fatigue test result of Sn–0.7Cu solder will show the frequency on low cycle fatigue. By plotting the hysteresis loop of different frequency at 125°C and strain range of 7.5%, the material response at different temperatures was evaluated and compared in Fig. 4.8 [2]. Sn–3.8Ag–0.7Cu solder has a similar trend.

After conducting tests at the same temperature and total strain but at different frequencies, the fatigue life of lead free solder was found to decrease with decreasing frequency. This characteristic of fatigue life can be attributed to accumulate creep damage during fatigue testing. As the frequency decreases, the time to failure increases, and this allows more time for creep to develop and thus leads to lower fatigue life in terms of cycles to failure.

As can be seen from Figs. 4.9 and 4.10, the Coffin–Manson model and energy-based model can be used to describe the fatigue behavior of lead free solder for any given frequency. However, the fatigue results have some difference at different frequencies, the value of fatigue exponent m and ductility coefficient C changes as frequency changes. It was found that, for both models, the m value decreases with frequency, but the frequency dependent is small. However, the C value decreases significantly as the frequency decreases, and is strongly frequency dependent.

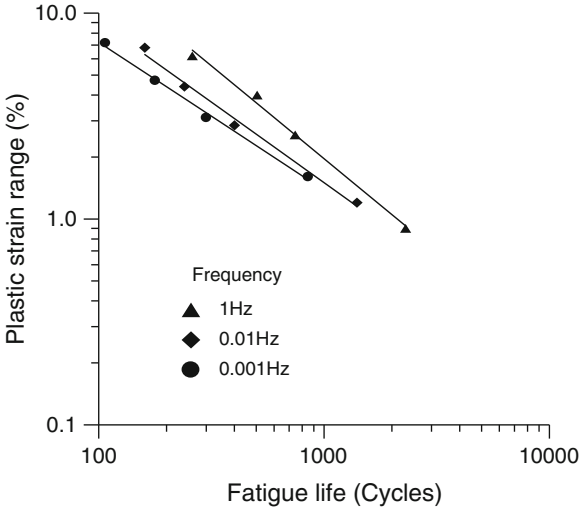

Fig. 4.9 Plastic strain versus fatigue life at 125°C for different frequencies

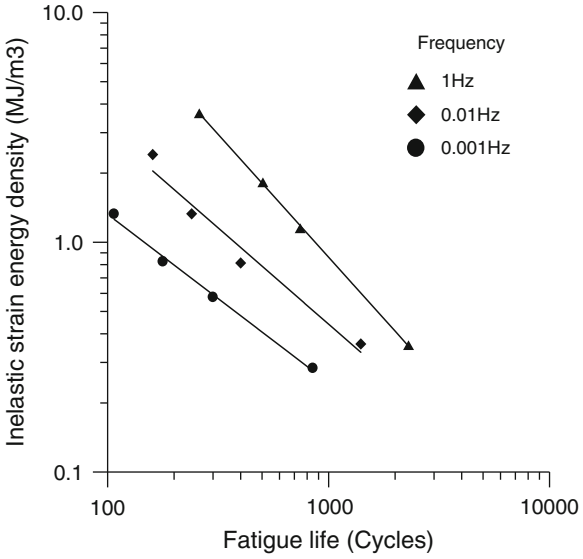

Fig. 4.10 Inelastic strain energy density versus fatigue life at 125°C for different frequencies

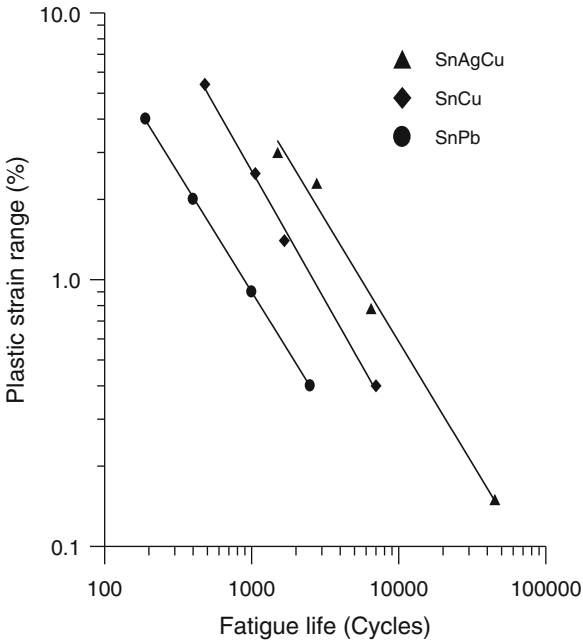

Fig. 4.11 Fatigue data at 25°C and 1 Hz

4.2 Comparison with Tin–Lead and Lead Free Solder Results

4.2.1 Comparison with Tin–Lead Solder

The fatigue properties for 63Sn–37Pb solder at different temperatures and frequencies were reported earlier by Shi [4]. The comparison of fatigue resistance for Sn–3.8Ag–0.7Cu, Sn–0.7Cu, and 63Sn–37Pb at room temperature and high frequency, and high temperature and low frequency are shown in Figs. 4.11 and 4.12, respectively. It can be seen that lead free solder has better fatigue resistance than tin–lead solder. The fatigue performance of Sn–Ag–Cu is better than Sn–Cu solder.

4.2.2 Comparison with Lead Free Solder Data

Reported studies [5–8] have found that the low cycle fatigue behavior of lead free and lead bearing solder alloys. Figure 4.13 shows the fatigue test result at room temperature and 1 Hz of different reported data of lead free and lead bearing solder alloys. The fatigue failure was defined as 50% reduction of maximum tensile load. From Fig. 4.14, it can be noticed that the conventional tin–lead solder has the lowest

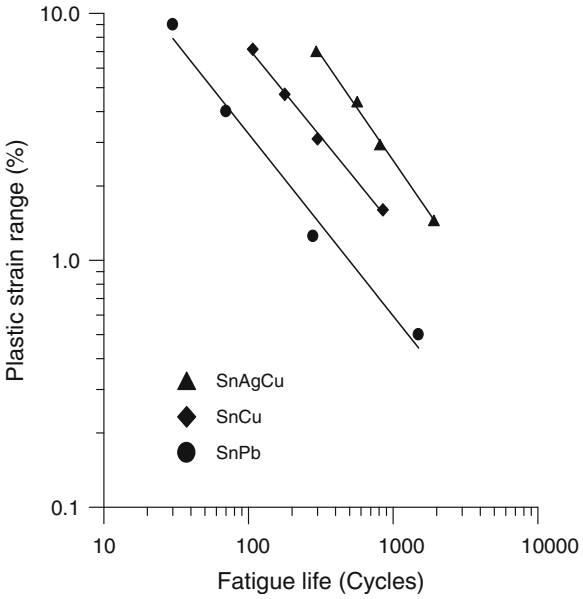

Fig. 4.12 Fatigue data at 125°C and 10^{-3} Hz

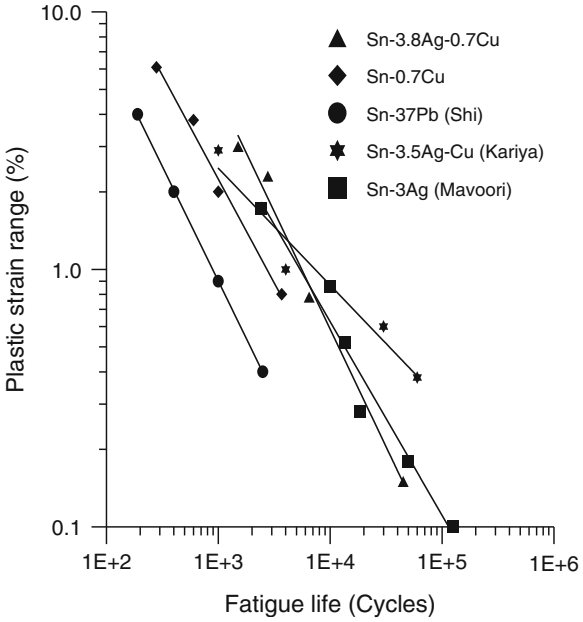

Fig. 4.13 Fatigue data for tin-lead and lead-free solders at 25°C and 1 Hz

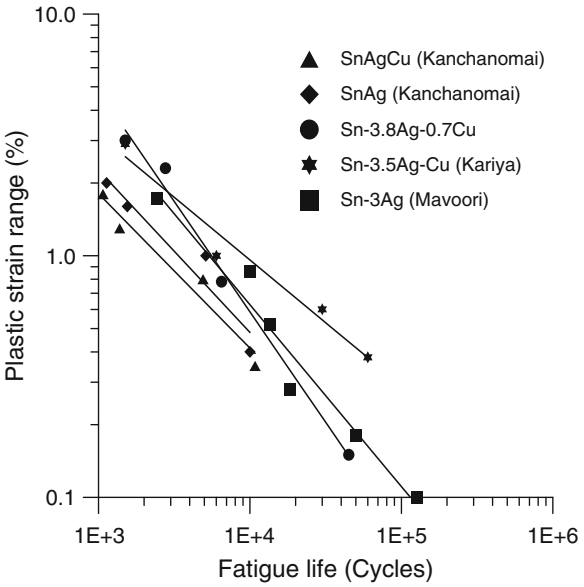

Fig. 4.14 Fatigue data for lead-free solders

fatigue life at the same test condition, three types of lead free solder: 99.3Sn–0.7Cu, 97Sn–3Ag ,and 95.5Sn–3.8Ag–0.7Cu solder all have better fatigue property than 63Sn–37Pb solder at room temperature and 1 Hz. However, in lead free solder alloys, the fatigue life of 99.3Sn–0.7Cu is lower than the other two lead free solder alloys, while 97Sn–3Ag and 95.5Sn–3.8Ag–0.7Cu solders have similar fatigue life [9, 10].

Isothermal LCF test data for Sn–Ag and SnAgCu lead free solders at 0.1 Hz and room temperature were reported by Kanchanomai et al. [5, 6]. Their failure criteria were defined at the 25% load drop of the stress amplitude. Comparison with other LCF data by Mavoori [7] and Kariya [8] at 1 Hz and room temperature, is shown in Fig. 4.14. It can be seen that at the same test condition, SnAg and SnAgCu have comparable fatigue life. However, the fatigue life data from Kanchanomai, at 0.1 Hz and with a failure definition of 25% load drop, is lower than the result by Mavoori and Kariya and the author's data.

4.3 Low Cycle Fatigue Models

The Coffin–Manson model [11, 12] has been widely used to relate low cycle fatigue life (N_f) of metallic materials with the plastic strain range ($\Delta\varepsilon_p$), as shown below:

$$N_f^m \Delta\varepsilon_p = C, \tag{4.1}$$

where m and C are material constants.

Table 4.1 m and C for Coffin–Manson model of Sn–3.8Ag–0.7Cu

	m			C		
	25°C	75°C	125°C	25°C	75°C	125°C
1 Hz	0.913	0.896	0.889	26.3	19.8	16.0
0.01 Hz	0.904	0.889	0.871	20.7	16.0	12.1
0.001 Hz	0.891	0.876	0.853	13.9	11.5	9.2

Table 4.2 n and A for Morrow's model of Sn–3.8Ag–0.7Cu

	n			A		
	25°C	75°C	125°C	25°C	75°C	125°C
1 Hz	1.103	1.079	0.953	14,865	6,208.3	1,492.8
0.01 Hz	0.973	0.944	0.926	1426.2	1,144.3	578.9
0.001 Hz	0.935	0.914	0.897	1144.4	666.9	311.7

Table 4.3 m and C for Coffin–Manson model of Sn–0.7Cu

	m			C		
	25°C	75°C	125°C	25°C	75°C	125°C
1 Hz	0.9734	0.9227	0.9022	21.27	12.51	9.98
0.01 Hz	0.8067	0.7938	0.7825	5.89	4.46	3.33
0.001 Hz	–	–	0.7192	–	–	1.98

Table 4.4 m and C for Morrow's model of Sn–0.7Cu

	n			A		
	25°C	75°C	125°C	25°C	75°C	125°C
1 Hz	1.2157	1.1406	1.1064	9,542.9	2,864.8	1,387.8
0.01 Hz	1.1396	1.0084	0.8379	1,524.8	559.46	143.71
0.001 Hz	–	–	0.7328	–	–	38.64

The Morrow's energy-based model [13] was also used to predict low cycle fatigue lives. The model predicts fatigue life in terms of inelastic strain energy density (W_p), given below:

$$N_f^n W_p = A, \tag{4.2}$$

where n is fatigue exponent and A is material ductility coefficient.

The inelastic strain energy density was determined from the area surrounded by a stable hysteresis loop.

Based on the low cycle fatigue test result at different temperatures and frequencies, the m, C, n, and A at different conditions can be determined for 95.5Sn–3.8Ag–0.7Cu and 99.3Sn–0.7Cu lead free solders. The results were summarized in Tables 4.1–4.4.

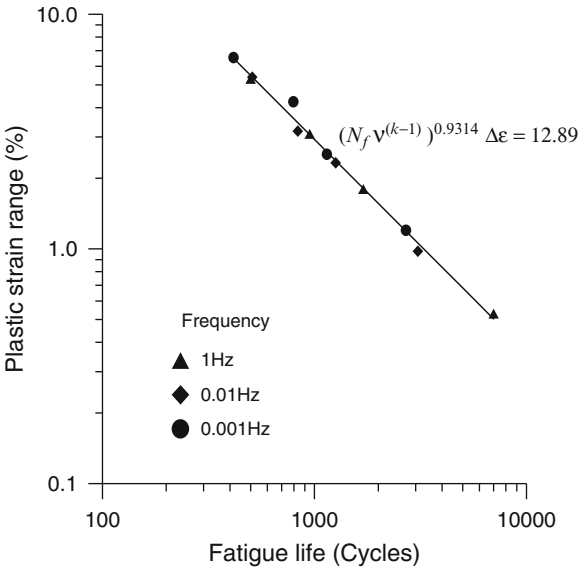

Fig. 4.15 Plastic strain versus frequency-modified fatigue life at 125°C for Sn–Ag–Cu ($k = 0.95$)

To model frequency-dependent low cycle fatigue behavior of Sn–3.8Ag–0.7Cu and Sn–0.7Cu lead free solders, the frequency-modified Coffin–Manson relationship [4] can be introduced to describe the low cycle fatigue behavior of Sn–0.7Cu solder, given below.

$$\left[N_f v^{(k-1)}\right]^m \Delta\varepsilon_p = C, \tag{4.3}$$

where v is frequency and k is frequency exponent.

Based on the fatigue test results at different frequencies at 125°C, the frequency exponent, k, can be determined to be 0.95 and 0.91 for Sn–3.8Ag–0.7Cu and Sn–0.7Cu solder, respectively. Then the frequency modified fatigue life $N_f v^{(k-1)}$can be calculated. When the plastic strain was plotted against the frequency-modified fatigue life, all the fatigue life data obtained at different frequencies were found to fit well into a single line, as shown in Figs. 4.15 and 4.16. This means that the frequency-modified Coffin–Manson model can be used to model the effect of frequency for the low cycle fatigue behavior of Sn–3.8Ag–0.7Cu and Sn–0.7Cu solder.

Similarly, the frequency-modified Morrow model can be used to model the frequency effect, as given below:

$$\left[N_f v^{(h-1)}\right]^n W_p = A, \tag{4.4}$$

where v is the frequency and h is the frequency exponent.

Based on fatigue test of Sn–3.8Ag–0.7Cu and Sn–0.7Cu solder at different frequencies, the frequency exponent, h, can be determined to be 0.82 and 0.762, respectively. Figures 4.17 and 4.18 show the inelastic strain energy density plotted

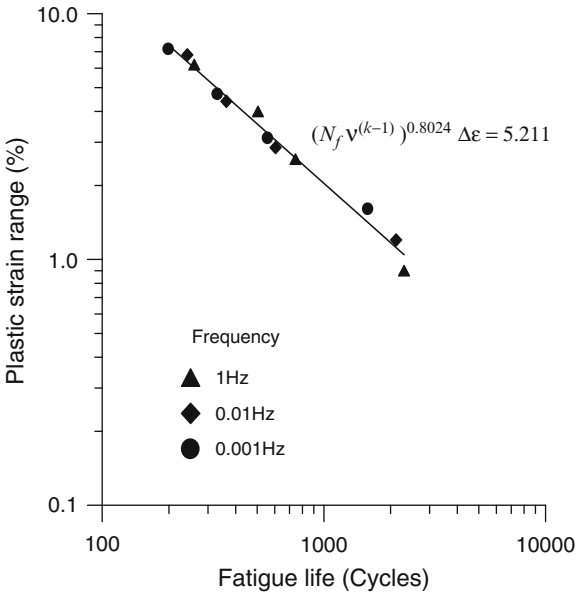

Fig. 4.16 Plastic strain versus frequency-modified fatigue life at 125°C for Sn–Cu ($k = 0.91$)

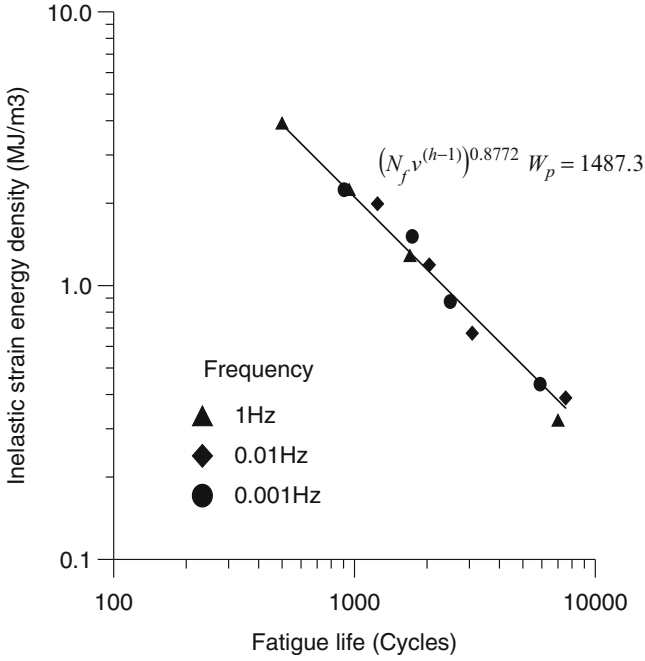

Fig. 4.17 Inelastic strain energy density versus frequency-modified fatigue life at 125°C for Sn–Ag–Cu ($h = 0.82$)

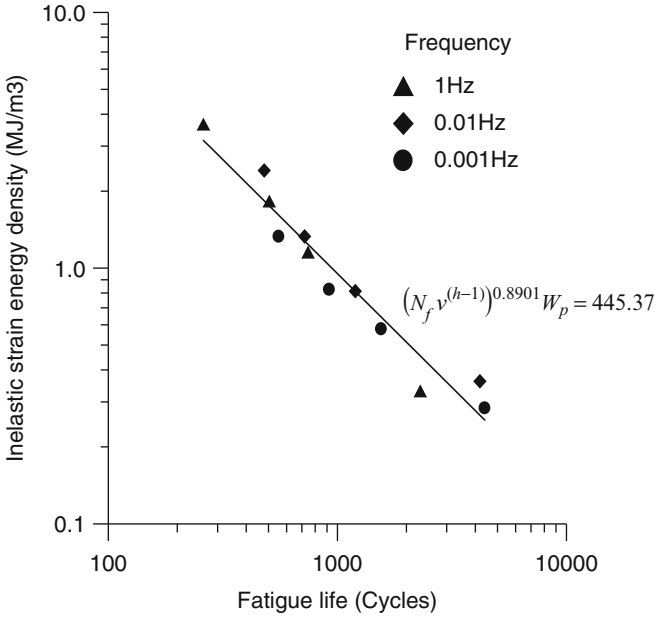

Fig. 4.18 Inelastic strain energy density versus frequency-modified fatigue life at 125 C for Sn–Cu ($h = 0.762$)

against the frequency-modified fatigue life at 125°C. It can be seen that all fatigue life data at different frequencies fall on a single line. Hence, the frequency-modified Morrow model can be used to model the effect of frequency for the low cycle fatigue behavior of lead free Sn–Ag–Cu and Sn–Cu solder.

References

1. ASTM Standards (1998) ASTM E606: standard practice for strain-controlled fatigue testing, vol 03.01. The American Society for Testing and Materials, Philadelphia, PA
2. Pang HLJ, Xiong BS, Low TH (2004) Low cycle fatigue models for lead free solders. Thin Solid Film 462–463:408–412
3. John HLP, Xiong BS, Low TH (2004) Low cycle fatigue of lead-free 99.3Sn-0.7Cu solder alloy. Int J Fatigue 26:865–872
4. Shi XQ, Pang HLJ, Zhou W, Wang ZP (2000) Low cycle fatigue analysis of temperature and frequency effects in eutectic solder alloy. Int J Fatigue 22:217–228
5. Kanchanomai C, Miyashita Y, Mutoh Y (2002) Low cycle fatigue behavior of lead-free solder 96.5Sn/3.5Ag. J Electron Mater 31:142
6. Kanchanomai C, Miyashita Y, Mutoh Y (2002) Low cycle fatigue behavior of Sn-Ag, Sn-Ag-Cu and Sn-Ag-Cu-Bi lead-free solders. J Electron Mater 31:456
7. Mavoori H, Vaynman S, Chin J, Moran B, Fine ME (1994) Isothermal fatigue life prediction of solder materials. In: Mechanics and materials for electronic packaging. ASME, New York, pp 165–179

8. Kariya Y, Otsuka M (1998) Mechanical fatigue characteristics of Sn-3.5Ag-X(X = Bi, Cu, Zn and in) solder alloys. J Electron Mater 27:1229
9. Pang JHL, Xiong BS (2004) Comparison of 5.5Sn-3.8Ag-0.7Cu solder joint and bulk solder properties. TMS 2004, 133rd annual meeting and exhibition, Charlotte, North Carolina, USA, 14–18 March 2004
10. Pang HLJ, Xiong BS, Low TH (2004) Creep and fatigue properties of lead free Sn-3.8Ag-0.7Cu solder. Proceedings of 54th ECTC, vol 2, Las Vegas, 1–4 June 2004, pp 1333–1337
11. Coffin LF (1954) A study of the effects of cyclic thermal stresses on a ductile metal. Trans ASME 76:931
12. Manson SS (1965) Fatigue a complex subject-some simple approximations. Exp Mech 5:193–226
13. Morrow JD (1964) Cyclic plastic strain energy and fatigue of metals, ASTM STP 378. American Society for Testing and Materials, Philadelphia, PA, p 45

Chapter 5
Finite Element Analysis and Design-for-Reliability

Abstract Chapter 5 reports on the application of FEA modeling and simulation techniques used for design of package assembly design for reliability. FEA modeling techniques have been developed for three-dimensional models, sub-modeling, and global–local modeling techniques. The global–local 3D modeling techniques like sub-modeling and Global–Local-Beam (GLB) methods, were applied to model solder joint reliability behavior for various test cases of thermal cycling, vibration, and impact drop tests. Implementation of the nonlinear mechanics of materials models have been integrated to the ANSYS finite element analysis program.

Finite element analysis (FEA) plays an important role in the design-for-reliability (DFR) methodology for modeling and simulation of lead-free solder joint reliability in electronic packaging assemblies. FEA modeling and simulation of solder joint reliability tests provide a physics of failure-based life prediction tool that can be used in a design-for-reliability. This can minimize excessive and time-consuming experimental test programs, particularly, where a wide range of design-of-experiment parameters are to be investigated. Applying DFR strategies with FEA modeling helps to save product development time and costs, increase product reliability, and better understanding of product design limits.

Different FEA models, for 2D, 3D slice, 3D one-eighth, and 3D quarter model have been investigated for varying levels of complexity in analysis. Global–Local modeling techniques were developed to reduce the computational effort compared to 3D quarter model. FEA modeling results for lead-free 95.5Sn–3.8Ag–0.7Cu and 99.3Sn–0.7Cu solders were compared to other lead-based and lead-free solders. Comparison of the solder joint fatigue life prediction results using the Anand viscoplastic material constants and the energy-based fatigue models respectively.

J.H.L. Pang, *Lead Free Solder: Mechanics and Reliability*,
DOI 10.1007/978-1-4614-0463-7_5,

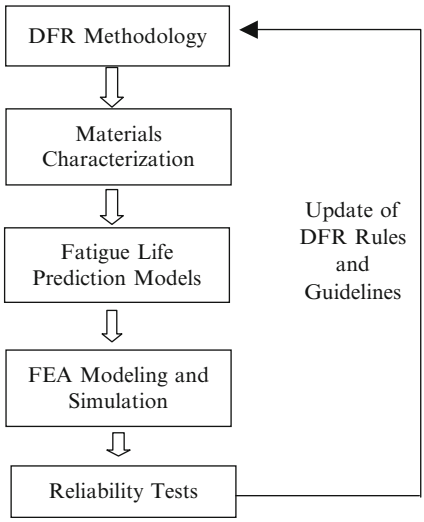

Fig. 5.1 Design for reliability (DFR) methodology

5.1 Finite Element Analysis

The finite element method developed from advances in computational structural analysis [1]. The finite element model is a representation of a structure or assembly formed by subdivisions of structural elements. These elements are connected at nodes or nodal joints. Mathematical shape functions are used to approximate the variation of the displacements over a finite element. A stiffness matrix connects all elements into a numerical model, which approximates the force–displacement relations externally at loading and boundary conditions and internally for determining the stress–strain distributions in each element.

The variational principle of mechanics, such as the principle of minimum potential energy, is often used to obtain the equilibrium conditions [2]. The equilibrium equations of the entire body are then obtained by combining the equations for the individual elements in such a way that continuity of displacements is preserved at the interconnecting nodes. These equations are modified for the given displacement boundary conditions and then solved to obtain the unknown displacements. When the displacements are known, the strain and stress can be calculated.

The FEA procedure involves the following steps:

1. Modeling elements to fit the body of the structure or assembly;
2. Specify the loading and boundary displacement conditions;
3. Derivation of each element type stiffness matrix;
4. Assembly of equations for the overall finite element model stiffness matrix;
5. Iterative solutions for all unknown nodal displacements;
6. Calculation of the element strains and stresses from the nodal displacements.

A schematic illustration of the design-for-reliability methodology for solder joint reliability analysis is shown in Fig. 5.1. FEA modeling and simulation is an important tool in the DFR evaluation of solder joint reliability in electronic

packaging assemblies. Application of the DFR method with FEA requires materials characterization of the nonlinear constitutive models, fatigue life prediction models, and validation by comparing to reliability test results.

The advantage of using the DFR procedures includes savings in reliability test time and cost. The physics of failure approach allows parametric studies to be made on material properties, geometric sizes, thicknesses, and different loading profiles. The DFR procedure can be implemented on most commercial FEA software such as ANSYS, ABAQUS, LS-DYNA, MSC-NASTRAN, and MSC-MARC. The FEA modeling and simulation work reported here were conducted using the ANSYS software [3].

The ANSYS FEA procedures consist of three steps.

1. Preprocessing:
   Create geometric model, elements and mesh, input material properties.
2. Solution Process:
   Apply loads and boundary condition, output control, load step control, selecting proper solver, obtaining the solution.
3. Postprocessing:
   Review the result, list the result, contour map, result animation.

For dynamic modeling of drop impact problems, an explicit finite element program may be used. ANSYS LS-DYNA combines the pre- and postprocessing capabilities of the ANSYS program with the explicit solver in LS-DYNA. The explicit method of solution used by LS-DYNA provides fast solutions for short-time, large deformation dynamics, quasistatic problems with large deformations and multiple nonlinear conditions, and complex contact/impact problems.

5.2 2D and 3D FEA Modeling

The electronic packaging trend is towards further miniaturization of interconnection feature size, high I/O counts within a more compact utilization IC package size and PCB mounting space. FEA techniques can be used to model physical effects like decreasing package interconnection feature sizes and this will require increasing requirements for high performance computing, higher speed, larger memory size, and hard-disk storage space. These requirements can limit the application FEA modeling on a single PC workstation, hence different levels of simplification in FEA modeling needs to be calibrated against full 3D modeling results. In this chapter, solder joint reliability analysis of thermal cycling loading on 2D model and 3D FEA models are presented. It is convenient to use the symmetry boundary conditions afforded by the nature of thermal expansion loading in electronic packaging assemblies subject to thermal cycling loading.

For thermal loading, the symmetric model is often used. A 2D model is simple and requires much fewer elements, hence less computing source compared to a 3D model. Figure 5.2 shows a 2D Plain Strain model for a Flip Chip On Board (FCOB)

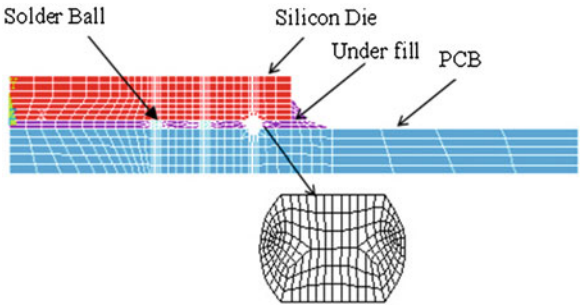

Fig. 5.2 2-D FEA model for FCOB assembly

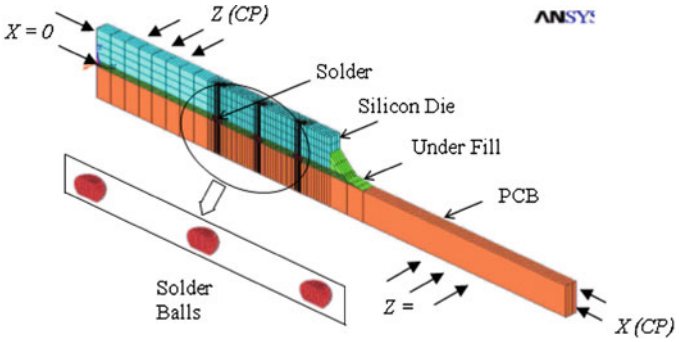

Fig. 5.3 3D Slice FEA model

assembly. For some special cases, 2D model can provide reasonable approximation to 3D model results. However, 2D model does not capture the full 3D effect of geometry and deformations, material properties variation, loading, and boundary conditions. Therefore, 3D modeling is often needed for most electronic packaging reliability simulation problems.

Another method is to reduce the full 3D FEA model to an approximate simplified 3D slice model [4, 5], technique as shown in Fig. 5.3. This can be compared to a symmetrical one-eighth 3D model [6–8], which is often the preferred model used as shown in Fig. 5.4. Some trade-off in accuracy is expected in these simplified 3D slice models as they cannot capture the full 3D effect of the package assembly. Hence, FEA model calibration work [9] is needed to quantify the comparative accuracy expected in these simplified model techniques. It was noted that the 2D-Plane Strain and 2D-Plane Stress models gave the highest and lowest solder joint strains range respectively. The 3D-Strip model and 3D-1/8th symmetry model results fall in between the 2D-Plane Strain and 2D-Plane Stress model results. The 3D-1/8th symmetry model agrees closer with the 2D-Plane Strain model, while the 3D-Strip model results are closer to the 2D-Plane Stress model results.

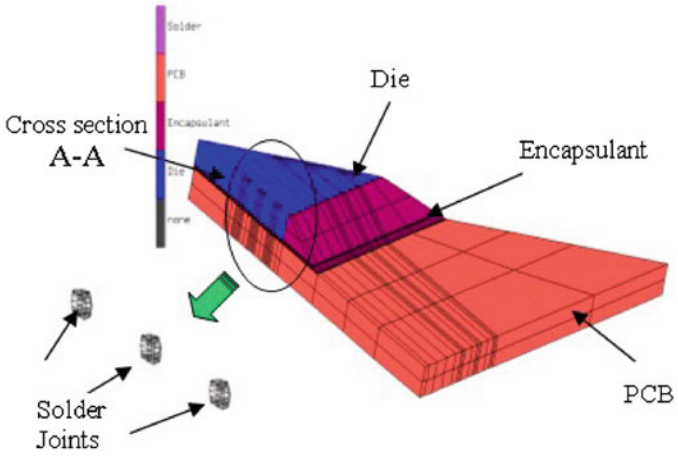

Fig. 5.4 3D FEA 1/8th octant model

5.3 3D Submodeling Technique

Global–Local modeling technique is needed when the 3D model is too large to solve or when the loading on the assembly does not have any axes of symmetry and a full 3D model is needed. The method employs a coarser global model, which is able to capture the 3D effect of deformations on a selected local submodel assembly. Transfer of the corresponding elastic deformations to a finer local submodel is used to perform a detailed nonlinear strain analysis in a solder joint. Cheng et al. [10] proposed a typical three-dimensional local model with equivalent beam for ball grid array (BGA) packaging. An effective finite element method was proposed by Yu et al. [11] to analyze the stress of the leads and the solder joints in the surface-mount assembly (SMA). The global–local modeling method is also called the submodeling technique [12–15], and has been used to simulate thermal or mechanical loadings in soldered assemblies. A simplified global–local model uses a beam element [16, 17] to model the solder connections with an effective beam stiffness. Both the submodeling and global–local beam modeling techniques will be reported in this chapter. The results from global–local model simulation were compared to those from full 3D model simulation.

5.3.1 Submodeling Procedure

Submodeling is a FEA modeling technique used to get more efficient results in a local region of model. Often the global model finite element mesh may be coarser to produce satisfactory results at the boundary surrounding a stress concentration region in a structure. To obtain more accurate results in such case, there are two

options: (a) reanalyze the entire model with greater mesh refinement but this can be too large and costly to solve, (b) use submodeling technique to generate an independent submodel in region of interest and transfer the effective loading from the global to the local part of the model.

Submodeling is also known as the cut boundary displacement method or the specified boundary displacement method. The cut boundary is the boundary of the submodel, which represents a cut through the coarse model. Displacements calculated on the cut boundary of the coarse model are transferred as boundary conditions to the fine submodel.

Submodeling technology is based on St. Venant's principle, which states that if an actual distribution of forces is replaced by a statically equivalent system, the distribution of stress and strain is altered only near the regions of load application. This implies that stress concentration effects are localized around the concentration; therefore, if the boundaries of the submodel are far enough away from the stress concentration, reasonably accurate results can be calculated within the submodel region. Aside from the obvious benefit of giving more accurate results in a region of model, the submodeling technique can reduce, or even eliminate, the need for complicated transition regions in solid finite element models.

The procedure for submodeling consists of the following steps:

1. Create and analyze the coarse model for the entire structure. This does not mean that the mesh has to be coarse, only that it is relatively coarse compared to the submodel.
2. Create the submodel for the region of interest. The location of the submodel must be the same as the corresponding portion of the coarse entire model with respect to the global origin.
3. Perform cut boundary interpolation. This is the key step in submodeling. The nodes along the cut boundaries firstly are identified and then the program calculates the degree of freedom (DOF) values at those nodes by interpolating results from the full (coarse) model. For each node of the submodel along the cut boundary, the program uses the appropriate element from the coarse mesh to determine the DOF values. These values are interpolated onto the cut boundary nodes using the element shape functions.
4. Analyze the submodel. In this step, define the analysis type and analysis options, apply the interpolated DOF values, define other loads and boundary conditions, specify load step options, and obtain the submodel solution.
5. Verify that the distance between the cut boundaries and the stress concentration is adequate.

5.3.2 Cut Boundary Selection

A calibration example was conducted to study the accuracy of the submodeling as well as the appropriate cut boundary. The selected FCOB specimen is shown schematically in Fig. 5.5. The silicon die is connected to the PCB by four solder balls at four corners. The specimen with and without underfill encapsulation was

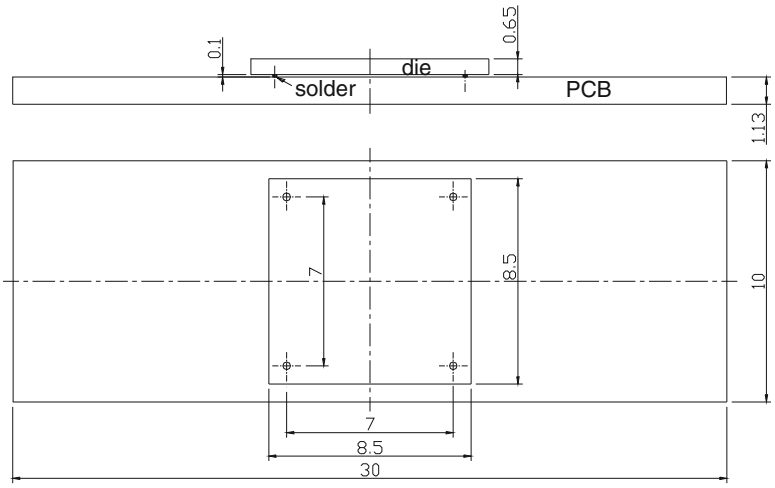

Fig. 5.5 Geometry size of the FCOB (unit in mm)

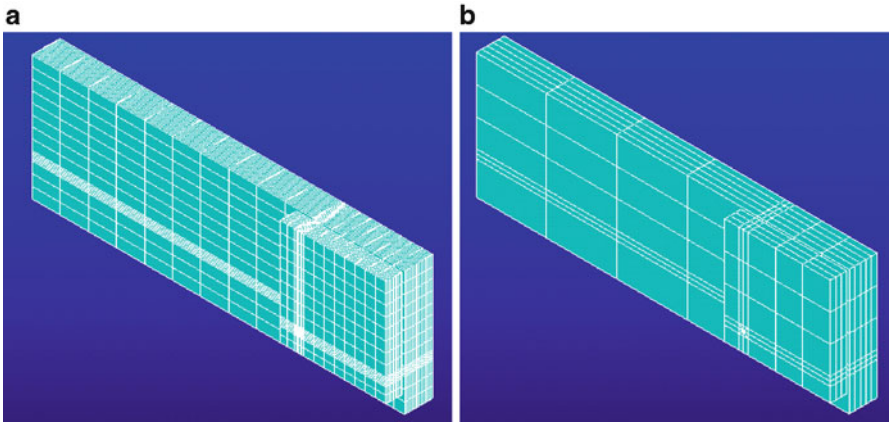

Fig. 5.6 (**a**) Fine model. (**b**) Coarse model

investigated. The size of the silicon die is 8.5 m by 8.5 mm, with a thickness of 0.65 mm. The solder joint has a solder standoff height of 0.1 mm. The PCB is made of FR-4, with a selected area of 30 mm by 10 mm and a thickness of 1.13 mm.

Initially, a thermal loading increment of 20°C was applied to this FCOB assembly to study the appropriate grid size and cut boundary condition. Due to the symmetry, only the quarter part of the assembly was modeled. The 3D quarter model meshed for fine and coarse models are shown in Fig. 5.6. Two types of boundary condition shown in Figs. 5.7 and 5.8 are conducted to determine the reasonable cut boundary. Figure 5.9 shows the maximum von Mises stress of

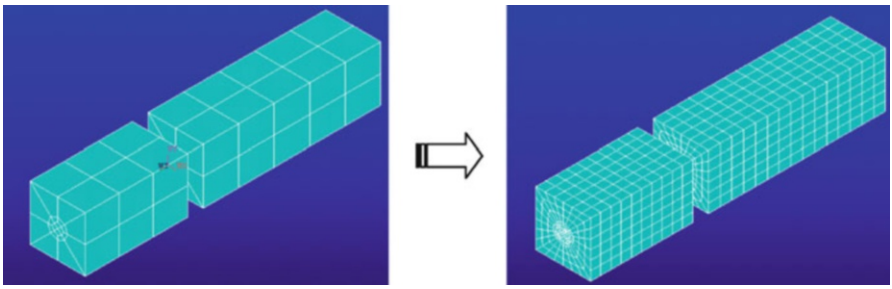

Fig. 5.7 Cut boundary for submodel (cb1)

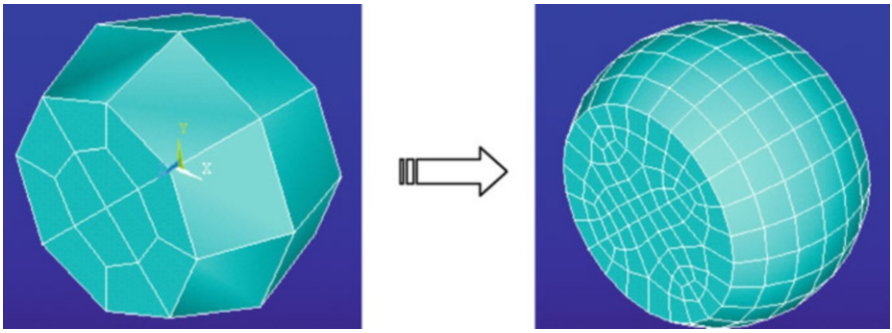

Fig. 5.8 Cut boundary for submodel (cb2)

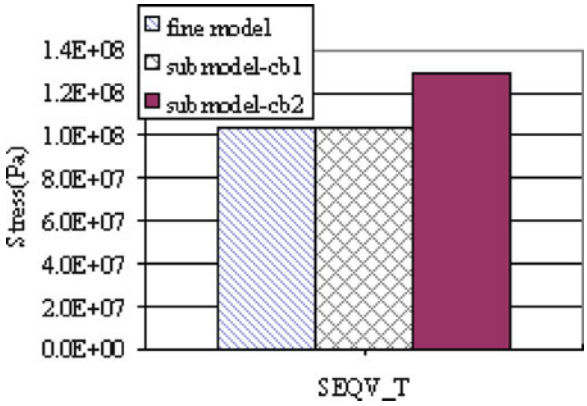

Fig. 5.9 Von Mises stress for different models

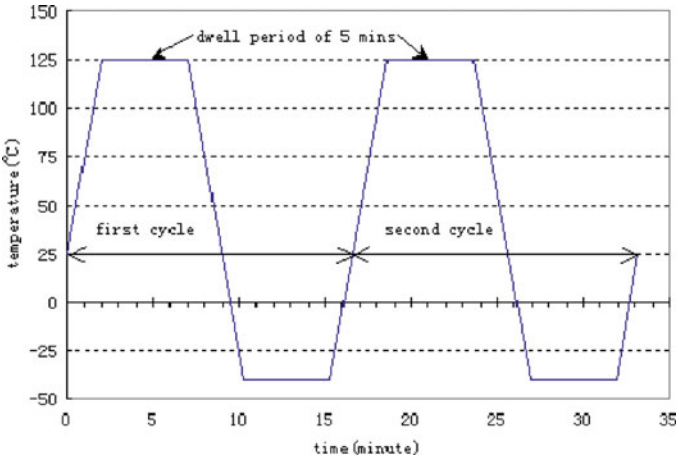

Fig. 5.10 Thermal cycling loading profile

solder/die interface comparison between fine-model and submodel with two different cut boundaries. It can be seen that the first cut boundary has more accurate result than second one compared to fine model result. The cut boundary, including die, IC chip, and PCB, was selected as suitable to take the simulation when FCOB specimen was subjected to thermal cycling loading.

5.3.3 Comparison of Submodel to Full 3D Model Results

Two cases were considered, that is, FCOB without underfill case and FCOB with underfill case. The thermal cycling loading profile (−40°C to +125°C) used is shown in Fig. 5.10. For solder joint, Anand's model was used in the FEA simulation. The plastic work density is a very important parameter in the life prediction of solder joint when it is assumed to exhibit the viscoplastic behavior when subjecting to the thermal cycling loading. The plastic work density is a very important parameter in the life prediction of solder joint when it is assumed to exhibit the viscoplastic behavior when subjecting to the thermal cycling loading. Therefore, the plastic work density was used for comparison shown in Fig. 5.11 for nonunderfill case and Fig. 5.12 for underfill case. It can be seen that the submodeling can give accurate result compared to fine 3D model, especially for FCOB without underfill case.

The submodel technique can be used in FEA simulation for reliability analysis of SMT technology without loss of accuracy. The advantages of submodel technique include reduction in computational time, hard disk space, smaller virtual memory requirements with less elements used as shown in Table 5.1.

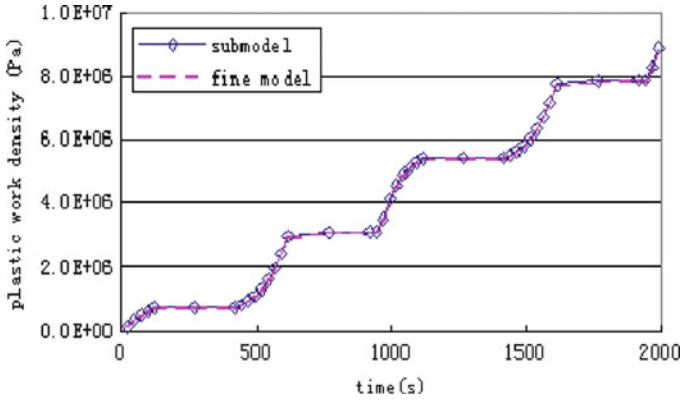

Fig. 5.11 Plastic work density for nonunderfill FCOB

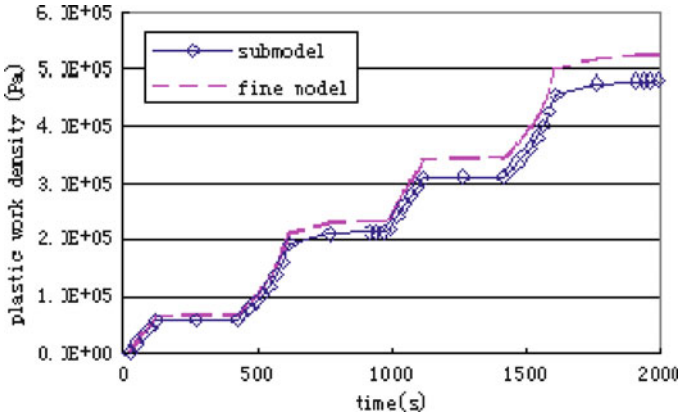

Fig. 5.12 Plastic work density for underfilled FCOB

Table 5.1 Submodel to 3D fine model comparisons

Items		Elements	Nodes	Comp. time (Min)	Result file (Mb)
Submodel	Coarse (1)	900	1,216	12	113
	Submodel (2)	5,084	5,664	84	650
Fine 3D model (3)		22,409	24,896	671	2,730
Factor (3)/(1 + 2)		3.74	3.62	6.99	3.58

5.4 3D Global–Local-Beam Modeling Technique

5.4.1 Introduction

FE modeling of an electronic assembly subjected to TC can employ symmetry boundary condition. Vibration and drop analysis need a full model of the assembly because of nonsymmetry in out-of-plane displacement. A full detailed model of a BGA or FCOB assembly, which includes numerous solder joints and many modules, is difficult to model. The submodeling technique mentioned earlier can reduce the FE mesh complexity, but can be still too complex with many components. In this section, a two-level global–local technique is introduced, which is named global–local-beam (GLB) technique in order to distinguish from submodel method. The key technique in this method is the use of simple elements, such as beam elements with effective stiffness matrix, to represent solder joints, and by doing this, the number of elements needed to model the entire structure can be reduced. This method consists of three main steps given as following:

1. Stiffness extraction analysis of a single solder joint
   In this step, a typical solder joint is modeled using detailed three-dimensional solid elements in order to establish its effective mechanical properties. A unit displacement in the *X*, *Y,* and *Z* direction and a unit rotation about *X*, *Y*, and *Z* direction are applied at the top and bottom surfaces of the solder joint, respectively. The reaction forces at each node of two ends of solder joint were calculated by FEA and summed together to get the total force in *X*, *Y,* and *Z* directions and moments around them. The relation between the displacements and reaction force shows the stiffness matrix of solder joint. This stiffness matrix is used in the deformation analysis of the entire structure.
2. Deformation analysis of the entire structure
   Solder joints, which connect the SMT modules to the PCB, are modeled as two-node beam elements with effective stiffness matrix established in step 1. The other parts of assembly are modeled as solid or shell elements. Then deformation caused by thermal or mechanical loading is calculated by FEA. The weakest solder joint can be detected by examining deformation of the entire structure. Usually, the relative deformations between two nodes of the beam elements are used as an index to determine the weakest solder joint.
3. Stress strain analysis of solder joint
   The weakest solder joint is modeled like the mesh used in stiffness extraction analysis of a single solder joint in the first step. Displacements calculated in the second step are applied at two ends of the solder joint model as boundary conditions. The translational displacements can be applied at the top and bottom surfaces of the detailed solder joint model directly. The rotational displacements are modified to the translational displacements considering the location of each node on the surfaces.

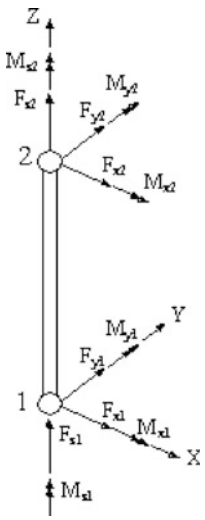

Fig. 5.13 Schematics of two-node element

5.4.2 Equivalent Beam Stiffness Analysis

Figure 5.13 shows a two-node beam element, which has 12 DOFs, three translational, and three rotational at each end, marked by node 1 and 2. The relation between the generalized nodal force vector $\{F\}$ and the generalized nodal displacement vector $\{u\}$ of beam is expressed in matrix form as following:

$$\{F\} = \{K\}\{u\} \tag{5.1}$$

$$\{F\} = [F_{x1} \quad F_{y1} \quad F_{z1} \quad M_{x1} \quad M_{y1} \quad M_{z1} \quad F_{x2} \quad F_{y2} \quad F_{z2} \quad M_{x2} \quad M_{y2} \quad M_{z2}]^{\mathrm{T}} \tag{5.2}$$

$$\{u\} = [u_{x1} \quad u_{y1} \quad u_{z1} \quad \theta_{x1} \quad \theta_{y1} \quad \theta_{z1} \quad u_{x2} \quad u_{y2} \quad u_{z2} \quad \theta_{x2} \quad \theta_{y2} \quad \theta_{z2}]^{\mathrm{T}} \tag{5.3}$$

where $[K]$ is the stiffness matrix of two-node beam. F_{ij} in (5.2) means a nodal force in the i-th direction at the j-th node and M_{ij} means a nodal moment around the i-th direction axis at the j-th node.

The u_{ij} in (5.3) means a translational displacement in the i-th direction at the j-th node and θ_{ij} means a rotational displacement around the i-th direction axis at the j-th node.

According to the beam theory [18], the stiffness matrix of a beam element corresponding to X, Y directions can be expressed as

$$\begin{Bmatrix} M_{x1} \\ M_{x2} \end{Bmatrix} = \begin{bmatrix} B & D \\ D & B \end{bmatrix} \begin{Bmatrix} \theta_{x1} \\ \theta_{x2} \end{Bmatrix} \tag{5.4}$$

$$\begin{Bmatrix} M_{y1} \\ M_{y2} \end{Bmatrix} = \begin{bmatrix} A & C \\ C & A \end{bmatrix} \begin{Bmatrix} \theta_{y1} \\ \theta_{y2} \end{Bmatrix} \tag{5.5}$$

in which

$$B = \frac{4EI_x}{L}, \quad D = \frac{2EI_x}{L}, \quad A = \frac{4EI_y}{L}, \quad C = \frac{2EI_y}{L}$$

where I and E are the moment of inertia and elastic modulus, respectively. L is the length of the beam. The torsional stiffness with respect to Z direction can be expressed as

$$\begin{Bmatrix} M_{z1} \\ M_{z2} \end{Bmatrix} = \frac{JG}{L} \begin{bmatrix} 1 & -1 \\ -1 & 1 \end{bmatrix} \begin{Bmatrix} \theta_{z1} \\ \theta_{z2} \end{Bmatrix} = \begin{bmatrix} Q & -Q \\ -Q & Q \end{bmatrix} \begin{Bmatrix} \theta_{z1} \\ \theta_{z2} \end{Bmatrix} \tag{5.6}$$

where J and G are polar moment of inertia and shear elastic modulus, respectively. The axial stiffness can be expressed as

$$\begin{Bmatrix} F_{z1} \\ F_{z2} \end{Bmatrix} = \frac{EA}{L} \begin{bmatrix} 1 & -1 \\ -1 & 1 \end{bmatrix} \begin{Bmatrix} u_{z1} \\ u_{z2} \end{Bmatrix} = \begin{bmatrix} H & -H \\ -H & H \end{bmatrix} \begin{Bmatrix} u_{z1} \\ u_{z2} \end{Bmatrix} \tag{5.7}$$

where A is the cross-section area. Combining (5.5)–(5.7) yields

$$\begin{Bmatrix} M_{x1} \\ M_{y1} \\ F_{z1} \\ M_{z1} \\ M_{x2} \\ M_{y2} \\ F_{z2} \\ M_{z2} \end{Bmatrix} = \begin{bmatrix} B & 0 & 0 & 0 & D & 0 & 0 & 0 \\ 0 & A & 0 & 0 & 0 & C & 0 & 0 \\ 0 & 0 & H & 0 & 0 & 0 & -H & 0 \\ 0 & 0 & 0 & Q & 0 & 0 & 0 & -Q \\ D & 0 & 0 & 0 & B & 0 & 0 & 0 \\ 0 & C & 0 & 0 & 0 & A & 0 & 0 \\ 0 & 0 & -H & 0 & 0 & 0 & H & 0 \\ 0 & 0 & 0 & -Q & 0 & 0 & 0 & Q \end{bmatrix} \begin{Bmatrix} \theta_{x1} \\ \theta_{y1} \\ u_{z1} \\ \theta_{z1} \\ \theta_{x2} \\ \theta_{y2} \\ u_{z2} \\ \theta_{z2} \end{Bmatrix} \tag{5.8}$$

or

$$\{\overline{F}\} = [S_l]\{\overline{u}\} \tag{5.9}$$

As Fig. 5.14 illustrates, the following relationships can be derived by summing moments at two ends 1 and 2:

$$\begin{aligned} &\sum M_{x1} = 0 = M_{x1} + M_{x2} - F_{y2}L \\ &F_{y2} = \frac{M_{x1} + M_{x2}}{L} \end{aligned} \tag{5.10}$$

$$\begin{aligned} &\sum M_{x2} = 0 = M_{x1} + M_{x2} + F_{y1}L \\ &F_{y1} = \frac{-M_{x1} - M_{x2}}{L} \end{aligned} \tag{5.11}$$

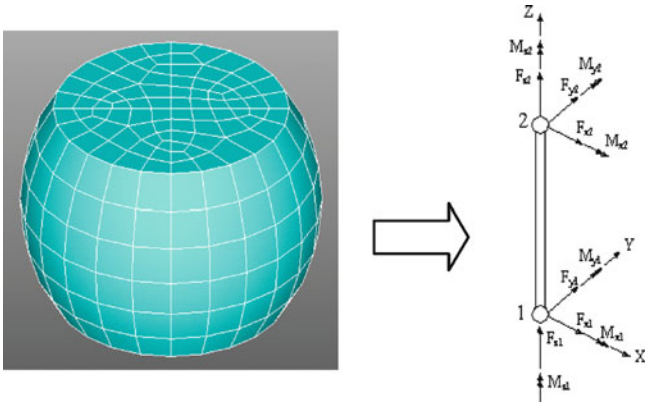

Fig. 5.14 FE model of a solder ball and its simple two-node beam element

$$\sum M_{y1} = 0 = M_{y1} + M_{y2} + F_{x2}L$$
$$F_{x2} = \frac{-M_{y1} - M_{y2}}{L} \tag{5.12}$$

$$\sum M_{y2} = 0 = M_{y1} + M_{y2} - F_{x1}L$$
$$F_{x1} = \frac{M_{y1} + M_{y2}}{L} \tag{5.13}$$

Rewriting (5.10)–(5.13) in matrix form yields

$$\{F\} = \begin{Bmatrix} F_{x1} \\ F_{y1} \\ F_{z1} \\ M_{x1} \\ M_{y1} \\ M_{z1} \\ F_{x2} \\ F_{y2} \\ F_{z2} \\ M_{x2} \\ M_{y2} \\ M_{z2} \end{Bmatrix} = \frac{1}{L} \begin{bmatrix} 0 & 1 & 0 & 0 & 0 & 1 & 0 & 0 \\ -1 & 0 & 0 & 0 & -1 & 0 & 0 & 0 \\ 0 & 0 & L & 0 & 0 & 0 & 0 & 0 \\ L & 0 & 0 & 0 & 0 & 0 & 0 & 0 \\ 0 & L & 0 & 0 & 0 & 0 & 0 & 0 \\ 0 & 0 & 0 & L & 0 & 0 & 0 & 0 \\ 0 & -1 & 0 & 0 & 0 & -1 & 0 & 0 \\ 1 & 0 & 0 & 0 & 1 & 0 & 0 & 0 \\ 0 & 0 & 0 & 0 & 0 & 0 & L & 0 \\ 0 & 0 & 0 & 0 & L & 0 & 0 & 0 \\ 0 & 0 & 0 & 0 & 0 & L & 0 & 0 \\ 0 & 0 & 0 & 0 & 0 & 0 & 0 & L \end{bmatrix} \begin{Bmatrix} M_{x1} \\ M_{y1} \\ F_{z1} \\ M_{z1} \\ M_{x2} \\ M_{y2} \\ F_{z2} \\ M_{z2} \end{Bmatrix} = [S] \begin{Bmatrix} M_{x1} \\ M_{y1} \\ F_{z1} \\ M_{z1} \\ M_{x2} \\ M_{y2} \\ F_{z2} \\ M_{z2} \end{Bmatrix} \tag{5.14}$$

Substituting (5.9) into (5.14) yields

$$\{F\} = [S][S_I][S]^T\{u\} = [K]\{u\} \tag{5.15}$$

$$[K] = \begin{bmatrix}
\frac{2(A+C)}{L^2} & 0 & 0 & 0 & \frac{A+C}{L} & 0 & \frac{-2(A+C)}{L^2} & 0 & 0 & 0 & \frac{A+C}{L} & 0 \\
0 & \frac{2(B+D)}{L^2} & 0 & \frac{-(B+D)}{L} & 0 & 0 & 0 & \frac{-2(B+D)}{L^2} & 0 & \frac{-(B+D)}{L} & 0 & 0 \\
0 & 0 & H & 0 & 0 & 0 & 0 & 0 & -H & 0 & 0 & 0 \\
0 & \frac{-(B+D)}{L} & 0 & B & 0 & 0 & 0 & \frac{B+D}{L} & 0 & D & 0 & 0 \\
\frac{A+C}{L} & 0 & 0 & 0 & A & 0 & \frac{-(A+C)}{L} & 0 & 0 & 0 & C & 0 \\
0 & 0 & 0 & 0 & 0 & Q & 0 & 0 & 0 & 0 & 0 & -Q \\
\frac{-2(A+C)}{L^2} & 0 & 0 & 0 & \frac{-(A+C)}{L} & 0 & \frac{2(A+C)}{L^2} & 0 & 0 & 0 & \frac{-(A+C)}{L} & 0 \\
0 & \frac{-2(B+D)}{L^2} & 0 & \frac{B+D}{L} & 0 & 0 & 0 & \frac{2(B+D)}{L^2} & 0 & \frac{B+D}{L} & 0 & 0 \\
0 & 0 & -H & 0 & 0 & 0 & 0 & 0 & H & 0 & 0 & 0 \\
0 & \frac{-(B+D)}{L} & 0 & D & 0 & 0 & 0 & \frac{B+D}{L} & 0 & B & 0 & 0 \\
\frac{A+C}{L} & 0 & 0 & 0 & C & 0 & \frac{-(A+C)}{L} & 0 & 0 & 0 & A & 0 \\
0 & 0 & 0 & 0 & 0 & -Q & 0 & 0 & 0 & 0 & 0 & Q
\end{bmatrix}$$

We can easily find that the stiffness matrix $[K]$ is symmetric matrix. The simple upper triangle form of $[K]$ can be rewritten as following:

$$[K] = \begin{bmatrix}
S_{11} & 0 & 0 & 0 & S_{15} & 0 & -S_{11} & 0 & 0 & 0 & S_{15} & 0 \\
 & S_{22} & 0 & -S_{24} & 0 & 0 & 0 & -S_{22} & 0 & -S_{24} & 0 & 0 \\
 & & H & 0 & 0 & 0 & 0 & 0 & -H & 0 & 0 & 0 \\
 & & & B & 0 & 0 & 0 & S_{24} & 0 & D & 0 & 0 \\
 & & & & A & 0 & -S_{15} & 0 & 0 & 0 & C & 0 \\
 & & & & & Q & 0 & 0 & 0 & 0 & 0 & -Q \\
 & & & & & & S_{11} & 0 & 0 & 0 & -S_{15} & 0 \\
 & & & & & & & S_{22} & 0 & S_{24} & 0 & 0 \\
 & & \text{sym} & & & & & & H & 0 & 0 & 0 \\
 & & & & & & & & & B & 0 & 0 \\
 & & & & & & & & & & A & 0 \\
 & & & & & & & & & & & Q
\end{bmatrix} \tag{5.16}$$

where $S_{11} = \frac{2(A+C)}{L^2}$, $S_{15} = \frac{A+C}{L}$, $S_{22} = \frac{2(B+D)}{L^2}$, $S_{24} = \frac{B+D}{L}$

When the cross section of the beam is axisymmetric or square, yields $A = B$, $C = D$, then $S_{11} = S_{22}$, $S_{15} = S_{24}$.

The solder joint can be replaced by a simple two-node beam element shown in Fig. 5.14. In order to extract the stiffness of the solder joint, unit translational and unit rotational are applied on the surface of the solder joint as a boundary condition. Here 10^{-6} m and 10^{-6} rad were selected as unit translational and unit rotational then the reactions are amplified to obtain the stiffness matrix of the solder joint. The 1 m and 1 rad were not selected as unit displacements because these values are far greater than the geometry of the solder joint, thus lead to some errors in stiffness extraction analysis due to distortion. Therefore, a boundary value problem, which is subjected to $\{u\} = \{10^{-6}, 0, 0, \ldots 0\}^{\mathrm{T}}$, is solved by using FEA. From the solutions the generalized forces imposed at two end surfaces can be obtained, and these generalized forces form first column or first row elements in the stiffness matrix of

the solder joint. By means of same process, when 12 different boundary value problems with unit displacement are solved, all the terms in the stiffness can be obtained. When the original stiffness matrix is obtained, then modify it according to the form of [K] in (5.16).

5.4.3 Deformation Analysis of the Entire Structure

In this process, the solder joints, which connect the chip to the PCB, are modeled as two-node beam elements with the effective stiffness matrix established in above analysis. Chip and PCB can be modeled as solid or shell elements. In this study, two types of elements are used to model chip and PCB in order to find which model is more accurate, by means of results comparison between simple model and fine 3D model. The temperature range is selected as loading form to validate the feasibility of global–local beam element method.

In the ANSYS software, MATRIX27 element can represent this beam element with effective stiffness matrix. MATRIX27 represents an arbitrary element whose geometry is undefined but whose elastic kinematic response can be specified by stiffness, damping, or mass coefficients. In this project, only stiffness coefficients are considered. The element is defined by two nodes and matrix coefficients. The stiffness matrix constants are input as real constants in simulation. The matrix is assumed to relate two nodes, each with six degrees of freedom: translations in the nodal x, y, and z directions and rotations about the nodal x, y, and z axes.

5.4.4 Stress Strain Analysis of Solder Joint

After the deformation analysis mentioned above, the weakest solder joint should be selected as the one which has the largest stress. In the present approach, the relative deformations between two nodes of the beam elements are used as an index to determine the weakest solder joint. Relative shear deformation, longitudinal extension, and rotation are considered to select the weakest solder joint. After determining the weakest solder joint, the nodal displacements at both ends of the beam element are applied to the detailed model as prescribed displacement boundary condition. For the thermal load case, the stress distribution can be obtained from the detailed solder joint 3D elements. Figure 5.15 shows the comparison of maximum Von Mises stress in the solder joint. It can be seen that solid model used in global–local model can give rise to more accurate result than shell model. The difference induced by global–local solid model is about 24% compared to the full 3D model. The difference induced by global–local shell model is very large, 40%, and this error is not acceptable for reliability analysis of the solder joint.

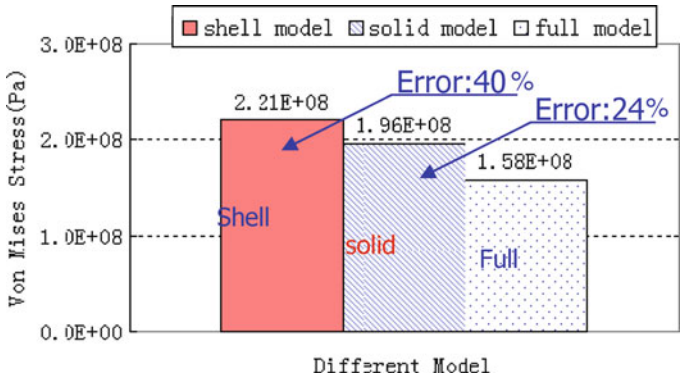

Fig. 5.15 Von Mises stress comparison for different model

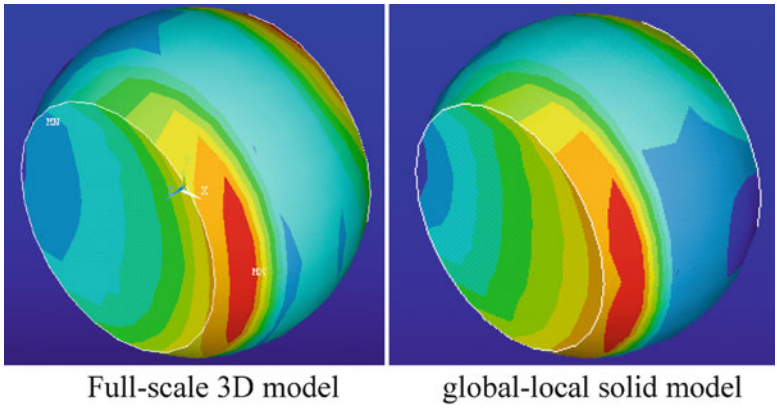

Fig. 5.16 Von Mises stress distribution comparison

In order to further verify the data validation from the solid element used in GLB model, the Von Mises stress distribution of the whole solder joint is compared between GLB model and full 3D model and the result is shown in Fig. 5.16. It can be seen clearly that the stress distribution is similar between two methods.

From above analysis, some conclusions can be drawn. Firstly, the GLB model is a more simple simulation method than submodeling technology because the solder joint is only replaced by one two-node beam element with effective stiffness, thus leading to more error using the GLB model than submodel. Secondly, in GLB model technique, using solid elements to simulate the components except solder joint in electronic assemblies can obtain more accurate results than using shell element.

5.5 Case Study I: Pb-Free and Pb-Based Solders

5.5.1 Anand Viscoplastic Model

The viscoplastic Anand model is widely used for electronic solder applications in FEA of thermo-mechanical behavior of solders [5, 19] the Anand model is expressed by a flow and three evolution equations below.

Flow equation

$$\frac{d\varepsilon_p}{dt} = A\left[\sinh\left(\frac{\xi\sigma}{s}\right)\right]^{1/m} e^{(-Q)/kT} \tag{5.17}$$

Evolution Equations

$$\frac{ds}{dt} = \left\{h_0(|B|)^a \frac{B}{|B|}\right\} = \frac{d\varepsilon_p}{dt} \tag{5.18}$$

$$B = 1 - \frac{s}{s^*} \tag{5.19}$$

$$s^* = \hat{s}\left(\frac{1}{A}\frac{d\varepsilon_p}{dt}e^{Q/kT}\right)^n \tag{5.20}$$

There are nine constants to be curve-fitted to the Anand model. ANSYS has an option for viscoplastic analysis using Anand's model to describe rate-dependent material behavior with large strain solid, Visco107 element, for three-dimensional large strain solid. When using Anand's model, nine material constants from C1 to C9 are required.

5.5.2 Low Cycle Fatigue Models for Solder Joint

The Coffin–Manson model has been used to relate low cycle fatigue life (N_f) for solder materials with the plastic strain range ($\Delta\varepsilon_p$),

$$N_f{}^m \Delta\varepsilon_p = C \tag{5.21}$$

where, m is the fatigue exponent and C is the fatigue ductility coefficient. For 63Sn–37Pb refer to Shi et al. [20] and for SAC tested at 125°C and 0.001 Hz, m and C are 0.853 and 9.2, respectively.

Morrow's energy-based model is often used to predict the low cycle fatigue life. The prediction fatigue life in terms of plastic work density can be expressed as follows:

$$N_{\mathrm{f}}^{n} W_{\mathrm{p}} = A \tag{5.22}$$

where n and A are material constants. For eutectic 63Sn–37Pb solder refer to Shi et al. [21] and for SAC tested at 125°C and 0.001 Hz, n is 0.897 and A is 311.7.

Darveaux [5] proposed that the calculated strain energy density increases as element size in the solder joint decreases. Hence a volume technique was used to reduce this sensitivity to meshing. The averaged viscoplastic work density accumulated per cycle for the interface elements, ΔW_{ave}, can be calculated by the following equation:

$$\Delta W_{ave} = \frac{\sum \Delta W V}{\sum \Delta V} \tag{5.23}$$

where $\Delta W$is the viscoplastic work density per cycle of each element, and V is the volume of each element. The values of ΔW and V can be obtained in ANSYS simulation and are important parameters in the calculation of fatigue life.

5.5.3 *Implementation of Pb-Free and Pb-Based Solder Anand Model*

The Pb-free solders Sn–3.8Ag–0.7Cu, Sn–0.7Cu, and 96.5Sn–3.5Ag are widely used for solder connection. Comparison between Pb-based and Pb-free solders is made. Some Pb-based solders, including high-Pb solders such as 92.5Pb–5Sn–2.5Ag, 97.5Pb–2.5Sn and near eutectic Pb–Sn solders such as 60Sn–40Pb, 62Sn–36Pb–2Ag were investigated. The specimen studied is the same as that shown in Fig. 5.5. The submodeling technique was used for simulation of the FCOB solder joints. The Anand's model derived in this project for Sn–3.8Ag–0.7Cu and Sn–0.7Cu solders and other reported solders were used in the ANSYS FEA program. The nine parameters in the Anand model for different solder alloys are listed in Table 5.2. In FEA simulation, thermal cycle loading (−40°C to +125°C) shown in Fig. 5.10 was used and underfill was considered with temperature-dependent elastic modulus.

Plastic strain energy density, or plastic work density, was compared for different solder joints and shown in Fig. 5.17. A volume technique was used to calculate averaged plastic work density accumulated per cycle for the top interface elements by (5.23). It can be seen from Fig. 5.17 that plastic work density accumulated per cycle is similar for near eutectic solder of 60Sn–40Pb and 62Sn–36Pb–2Ag. The

Table 5.2 Anand model constants for different solder alloys

Parameters	62Sn36Pb2Ag	92.5Pb5Sn2.5Ag	60Sn40Pb	96.5Sn3.5Ag	97.5Pb2.5Sn	95.5Sn3.8Ag0.7Cu[a]	Sn0.7Cu[a]
S_0 (MPa)	12.41	33.07	56.33	39.09	15.09	37.1	33.8
Q/k (°K)	9,400	11,010	10,830	8,900	15,583	6656	5276
A	4.00E + 06	1.05E + 05	1.49E + 07	2.23E + 04	3.25E + 12	65.92	9875
ξ	1.5	7	11	6	7	8	2
m	0.303	0.241	0.303	0.182	0.143	0.346	0.176
ho (MPa)	1,379	1,432	2,640.75	3,321.15	1,787.02	86442.8	61987.3
$\hat{s}$ (MPa)	13.79	41.63	80.42	73.81	72.73	80.8	65.2
n	0.07	0.002	0.0231	0.018	0.00437	0.0002	0.003
a	1.3	1.3	1.34	1.82	3.73	1.29	1.03

[a] New data

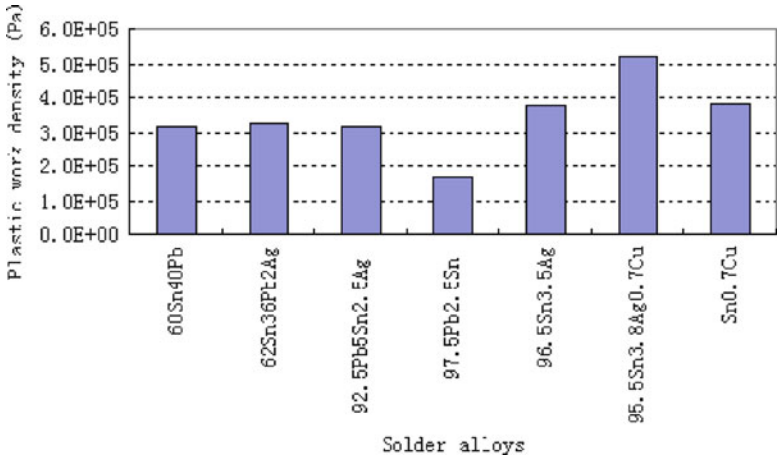

Fig. 5.17 Plastic work density comparisons for different solder joints

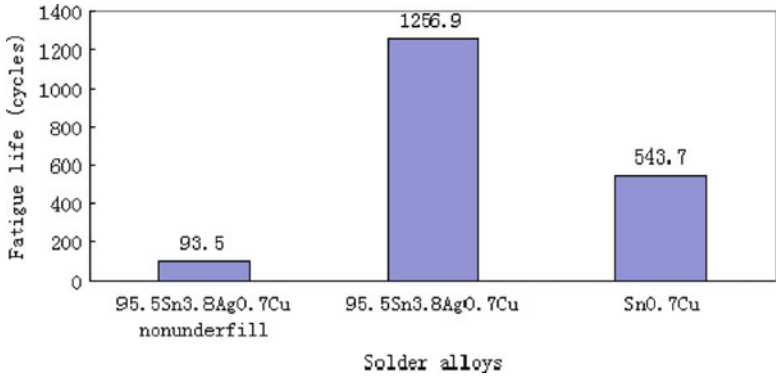

Fig. 5.18 Life comparisons for Sn0.7Cu and 95.5Sn–3.8Ag–0.7Cu solder joints

high-Pb solder, 97.5Pb–2.5Sn, has the lowest plastic work density. Pb-free solders have higher plastic work density.

Plastic work density accumulated per cycle is usually selected as a parameter to predict the solder joint life using Morrow's energy-based model shown in (5.22). The fatigue life was calculated for lead-free solder of 95.5Sn–3.8Ag–0.7Cu and Sn–0.7Cu. Figure 5.18 shows the fatigue life comparison for 95.5Sn–3.8Ag–0.7Cu and Sn–0.7Cu solder. It can be seen that the fatigue life of 95.5Sn–3.8Ag–0.7Cu solder is longer than that of Sn0.7Cu solder. The effect of nonunderfill and underfill FCOB on fatigue life of 95.5Sn–3.8Ag–0.7Cu solder joints is significant. The fatigue life of solder joints increases by more than ten times when underfill is used.

5.6 Case Study II: PBGA Assembly with 95.5Sn–3.8Ag–0.7Cu Solder Joints

Finite Element Analysis is used extensively in solving thermo-mechanical problems in the electronic packaging industry. The temperature profile loading is based on the temperature profile used in the experimental work. A 2D plane strain model is used to model the Micro-BGA shown in Fig. 5.19, with the materials defined in Table 5.3.

The elements of the solder ball with the furthest distance from the neutral point (DNP) were refined for detailed study of the solder joint deformation. The usual 2D symmetry boundary condition was applied in the *x*-direction, and one node was restricted in the *y*-direction to prevent free body translation and rotation. The finite element model employs the Anand viscoplastic model for 95.5Sn–3.8Ag–0.7Cu solder and viscoelastic properties for the Micro-BGA mold compound. A 2D rate-dependent material behavior with large strain solid, VISCO 108 element, was defined in ANSYS to represent the viscoplastic deformation of solder.

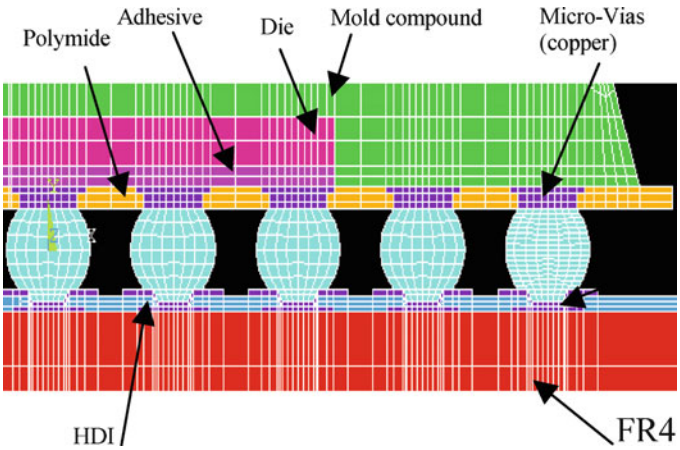

Fig. 5.19 2-D Finite Element Model of Micro-BGA solder joints

Table 5.3 Constitutive models for Micro-BGA materials

Material	Constitutive model	Source
Silicon Die	Elastic-isotropic	[23]
Polyimide	Elastic-isotropic	Vendors data
Mold	Viscoelastic-isotropic	[23]
Copper Pad	Elastic-isotropic	[23]
HDI	Elastic-isotropic	Vendors data
PCB	Temp-dependent elastic, isotropic	[23]
Die adhesive	Temp-dependent elastic, isotropic	[23]
Sn–3.8Ag–0.7Cu Solder	Viscoplastic	Curve-fitted

The solder joint is subjected to a complex state of multiaxial stress–strain response during thermal cycling, and the equivalent stress–strain concept is required to represent the multiaxial state of stress and strains in the solder joints. From the experimental results, the interface between the solder and silicon chip is the sensitive region to failure. And the solder joint fatigue failure is due to the cyclic plastic and creep strain damage leading to crack initiation and propagation. Hence, the plastic work or inelastic energy density ΔWave is extracted as a fatigue failure parameter at the top layer of the solder elements. This method seeks to output the plastic work, ΔWave, and averaging it across the elements along the solder joint interface where the crack propagates. This area averaging technique reduces the sensitivity to meshing.

$$\Delta W_{ave} = \frac{\sum \Delta W \cdot V}{\sum V}$$

The energy density outputted from FEA is 0.33 MPa. Energy-based Morrow's model given in (5.22) can be used to predict the fatigue life for Sn–Ag–Cu solder joint. The Morrow's model constants, $n = 0.897$ and $A = 311.7$ here were used. The predicted fatigue life is 2,056 cycles.

$$N_{\mathrm{f}}^{n} W_p = A$$

Using the Morrow's life prediction model, the predicted fatigue life cycles of 2,056 is within 2× of the MTTF of 3,177 cycles from test result.

References

1. Clough RW (1960) The finite element method in plane stress analysis. Proceedings, American society of civil engineers, 2nd conference on electronic computation, Pittsburgh, Pennsylvania, 23, pp 345–378
2. Desai CS, Abel JF (1987) Introduction to the finite element method-a numerical method for engineering analysis. CBS Publishers & Distributors, India
3. Ansys Version 7.0 Manual (2002). Ansys Inc.
4. Pang JHJ, Chong DYR, Low TH (2001) Thermal cycling analysis of flip-chip solder joint reliability. IEEE Trans Components Packaging Technol 24(4):705–712
5. Darveaux R (2000) Effect of simulation methodology on solder joint crack growth correlation. 50th Electronic components and technology conference, Las Vegas, Nevada, 21–24 May 2000, pp 1048–1058
6. Pang JHL, Seetoh CW, Wang ZP (2000) CBGA solder joint reliability evaluation based on elastic-plastic-creep analysis. J Electron Packaging 122:255–261
7. Anderson T, Guven EM (1999) The necessity of reexamining previous life prediction analyses of solder joints in electronic packages. 49th Electronic components and technology conference, pp 1010–1014
8. Yao Q, Qu J (1999) Three-dimensional versus two-dimensional finite element modeling of flip-chip packages. J Electron Packaging 121:196–201

9. Pang JHL, Low TH, Xiong BS, Che FX (2003) Design for reliability (DFR) methodology for electronic packaging assemblies. Proceedings of 5th EPTC conference, Singapore, 10–12 December 2003, pp 470–478
10. Cheng HC, Chiang KN, Lee MH (1998) An effective approach for three-dimensional finite element analysis of ball grid array typed packages. J Electron Packaging 120:129–134
11. Yu Q, Shiratori M, Wang SB (1993) Stress analysis of surface-mount assembly by an influence function method. Advances in electronic packaging, ASME international electronic conference, EEP-vol 4–1, Binghamton, New York, 29 September–2 October
12. Anderson T, Barut A, Guven I, Madenci E (2000) Revisit of life-prediction model for solder joints. 50th Electronic components and technology conference, Las Vegas, Nevada, 21–24 May 2000
13. Gustafsson G, Guven I, Kradinov V, Madenci E (2000) Finite element modeling of BGA packages for life prediction. 50th Electronic components and technology conference, Las Vegas, Nevada, 21–24 May 2000
14. Zhu J (1999) Three-dimensional effects of solder joints in micro-scale BGA assembly. J Electron Packaging 121:297–302
15. Zhu J, Quander S, Reinikainen T (2001) Global/local modeling for PWB mechanical loading. 51th Electronic components and technology conference, Orlando, FL, USA, 29 May–1 June
16. Saito N, Sasaki K, Hata N (1999) Effective stress and displacement analysis method for area-array structures. Advances in electronic packaging, ASME international electronic conference, EEP-vol 26–1
17. Yang QJ, et al (1999). Vibration reliability analysis of a PBGA assembly under foundation excitations. Advances in electronic packaging, ASME international electronic conference, EEP-vol 26–1
18. Cheng FY (2001) Matrix analysis of structural dynamics: applications and earthquake engineering. Marcel Dekker, New York
19. Cheng ZN, Wang GZ, Chen L, Wilde J, Becker K (2000) Viscoplastic Anand model for solder alloys and its application. Soldering & Surface Mount Technol 12(2):31–36
20. Shi XQ, Pang HLJ, Zhou W, Wang ZP (2000) Low cycle fatigue analysis of temperature and frequency effects in eutectic solder alloy. Int J fatigue 22(3):217–228
21. Shi XQ, Pang HLJ, Zhou W, Wang ZP (1999) A modified energy-based low cycle fatigue model for eutectic solder alloy. Scr Mater 41(3):289–296
22. Pang JHL, Low TH, Che FX (2004) Lead free 95.5Sn-3.8Ag-0.7Cu solder joint reliability analysis of Micro-BGA assembly. Proceedings of ITherm 2004 conference, Las Vegas, 1–4 June 2004
23. Amagai M (1999) Chip scale package (CSP) solder joint reliability and modeling. Microelectron Reliab 39:463–477

Chapter 6
Thermo-Mechanical Reliability Test and Analysis

Abstract Chapter 6 reports on solder joint reliability test case studies for thermal cycling tests. Thermal cycling test and FEA of lead-free solder PCB assemblies for BGA and FCOB test specimens were evaluated to determine the Weibull cumulative failure distribution. Finite element modeling and simulation of this reliability test was employed to predict the solder joint reliability performance. Experimental study was conducted on lead-free 95.5Sn–3.8Ag–0.7Cu soldered assemblies provided by Solectron Technology [8]. The test variables include different packages (PBGA, PQFP) and different PCB board surface finishes on copper pads (Cu-OSP, ENIG, and Im-Ag). FEA modeling of the PBGA assembly with 95.5Sn–3.8Ag–0.7Cu solder joints and fatigue analysis was applied to predict the solder joint mean-time-to-failure life cycles. Failure analysis investigation on intermetallic compound or IMC layer growth subject to isothermal aging, thermal cycling, and thermal shock aging experiments were conducted to correlate IMC layer growth properties in lead-free 95.5Sn–3.8Ag–0.7Cu solder joint specimens. Highly Accelerated Life Test (HALT) approaches were also developed for lead-free 95.5Sn–3.8Ag–0.7Cu soldered PCB assemblies.

6.1 Accelerated Testing and Reliability Engineering

The reliability of a packaged microelectronic system is related to the probability that it will be operational within acceptable limits for a given period of time [1]. The design for reliability knowledge triangle is shown in Fig. 6.1. It can be seen that three parts are needed for DFR of electronic packaging: reliability test, FEA modeling and simulation, and fatigue life prediction model. Reliability test is an important part in DFR of electronic packaging because it can be used to verify the results of FEA modeling and fatigue life prediction analysis. Reliability test provide the actual failure mechanism of special design of electronic package.

J.H.L. Pang, *Lead Free Solder: Mechanics and Reliability*,
DOI 10.1007/978-1-4614-0463-7_6,

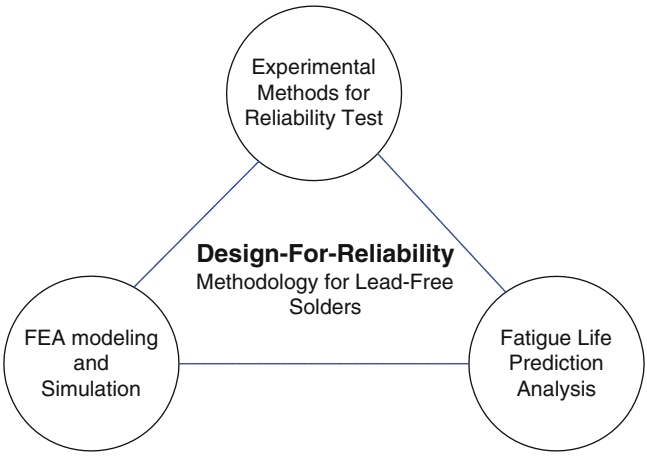

Fig. 6.1 Design for reliability (DFR) knowledge triangle

Electronic products may be subjected to different types of loading, such as thermal cycling (TC) or thermal shock (TS), vibration, and drop impact loading. Failure mechanisms for electronic solders include creep, low-cycle fatigue, high-cycle fatigue, and brittle fracture. In SMT assemblies, the solder joint in the electronic assembly is often the weakest link and solder joint reliability becomes even more important with further minimization. The solder joint is particularly prone to fatigue failure due to temperature cycling and mechanical loading [2].

In real service condition, the failure of solder joints in electronic assemblies is expected to precipitate after the warranty period for electronic products. It is not practical to obtain reliability test data for service condition, as it would take too long to test and collect failure data. Reliability testing often employs accelerated stress testing (AST). Reliability tests are aimed at revealing and understanding the physics of failure. Another objective of accelerated tests is to accumulate representative failure statistics [3]. Accelerated tests use elevated stress levels and/or higher stress-cycle frequency to precipitate failures over a much shorter time. Typical accelerating stresses are temperature, mechanical load, thermal cycling, and vibration. Stress loading includes: constant stress, step stress, progressive stress, and random stress [4]. Such tests can facilitate physics of failure reliability tests that are cost effective, shorten the product process, and improve long-term product reliability. Highly Accelerated Life Tests (HALTs) are carried out to obtain, as soon as possible, the preliminary information about the reliability of products and the principal physics of their failures. The HALTs are conducted with a smaller number of samples.

Temperature cycling or thermal cycling is very common loading for electronic products. In order to assess the reliability of electronic package subjected to thermal cycling loading, the accelerated thermal cycling reliability test is often used. When accelerated thermal cycling (ATC) tests were carried out, the acceleration

factor (AF) given by Norris and Landzberg [5] has been used to relate test conditions to field conditions.

$$\mathrm{AF} = \left(\frac{\Delta T_{\mathrm{t}}}{\Delta T_f}\right)^{1.9} \left(\frac{f_{\mathrm{f}}}{f_{\mathrm{t}}}\right)^{1/3} \exp\left[1414\left(\frac{1}{T_{\max .\mathrm{f}}} - \frac{1}{T_{\max .\mathrm{t}}}\right)\right], \tag{6.1}$$

where ΔT_{t}, ΔT_{f} are temperature ranges at test and field conditions; f_{t}, f_{f} are the cyclic frequencies at test and field conditions; $T_{\max.\mathrm{t}}$, $T_{\max.\mathrm{f}}$ are the highest temperatures in Kelvin at test and field conditions, respectively.

Life distribution model is a statistic model that is a theoretical population model used to describe the lifetime of a component/product/system and is defined as the cumulative distribution function $F(t)$ for the population [6]. The life distribution model $F(t)$ has two useful interpretations:

- $F(t)$ is the probability a random unit drawn from the population fails by t hours (or cycles).
- $F(t)$ is the fraction of all units in the population, which fails by t hours (or cycles).

It is defined as:

$$F(t) = F(s \le t) = \int_{-\infty}^{t} f(s)\mathrm{d}s, \tag{6.2}$$

where $f(t)$ is probability density function.

The Weibull life distribution model is widely used for solder joint reliability investigations. For two-parameter Weibull distribution, the failure density function can be written as

$$f(t) = \frac{\beta}{\eta}\left(\frac{t}{\eta}\right)^{\beta-1} \exp\left[-\left(\frac{t}{\eta}\right)^{\beta}\right], \tag{6.3}$$

where β is called a shape factor because it measures how the failure frequency is distributed around the average lifetime. η is called the lifetime parameter because it gives the time at which 63.2% of the devices failed. So the failure function can be obtained.

$$F(t) = \int_{0}^{t} f(\tau)\mathrm{d}\tau = 1 - \exp\left[-\left(\frac{t}{\eta}\right)^{\beta}\right] \tag{6.4}$$

The reliability function corresponding to this failure function can be obtained

$$R(t) = 1 - F(t) = \exp\left[-\left(\frac{t}{\eta}\right)^{\beta}\right] \tag{6.5}$$

and the failure rate can be calculated.

$$h(t) = \frac{f(t)}{R(t)} \tag{6.6}$$

When the life distribution model is available, the mean time to failure can be calculated by the following equation:

$$\text{MTTF} = \int_0^\infty tf(t)\mathrm{d}t = \eta \cdot \Gamma\left(\frac{1}{\beta} + 1\right) \tag{6.7}$$

The Weibull probability plot was used to determine whether the data could fit to the Weibull distribution model. Then the parameters β and η were estimated by fitting the test results to the Weibull distribution model.

6.2 Temperature Cycling Test and Analysis

The two common ATC tests used for solder joint reliability conducting in industry are the thermal cycling (TC) (JESD22-A104-B) [7] and thermal shock (TS) (JESD22-A106-A) [8] tests. TC has a ramp rate varying from 8°C/min to 33°C/min, whereas TS condition has ramp rate between 33°C/min and 55°C/min. Dwell time is included at the cycle extremes to allow for creep and stress relaxation process to take place. Table 6.1 shows the temperature cycling test conditions according to JESD22-A104-A standard. Different temperature ranges are shown in Table 6.2 for different service environments for electronic products.

The thermal cycling test is modeled using finite element analysis to study the failure mechanism of solder joint. Figure 6.2 shows a similar modeling methodology for TC and TS test. The methodology requires (a) Finite element analysis employing temperature and strain rate-dependent properties for solder; (b) solder fatigue model compensating for frequency and temperature effects in order to model the correct trend in TC and TS test results; (c) solder joint reliability test results for validating the TC and TS modeling and fatigue life prediction results.

Table 6.1 Temperature cycling test conditions

Test condition	Nominal TS(min) (°C) with tolerances	Nominal TS(max) (°C) with tolerances
A	−55(+0, −10)	+85(+10, −0)
B	−55(+0, −10)	+125(+15, −0)
C	−65(+0, −10)	+150(+15, −0)
G	−40(+0, −10)	+125(+15, −0)
H	−55(+0, −10)	+150(+15, −0)
I	−40(+0, −10)	+115(+15, −0)
J	−0(+0, −10)	+100(+15, −0)
K	−0(+0, −10)	+125(+15, −0)
L	−55(+0, −10)	+110(+15, −0)
M	−40(+0, −10)	+150(+15, −0)

Table 6.2 Thermal environments for electronic products

Use condition	Thermal excursion (°C)
Consumer electronics	0 to 60
Telecommunications	−40 to 85
Commercial aircraft	−55 to 95
Military aircraft	−55 to125
Space	−40 to 85
Automotive-passenger	−55 to 65
Automotive-under the hood	−55 to 150

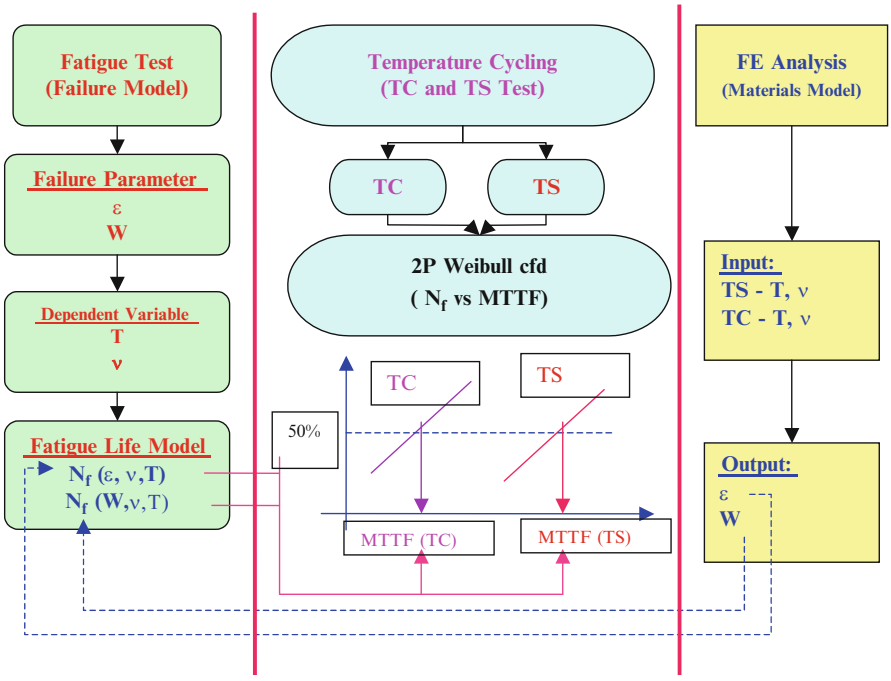

Fig. 6.2 DFR modeling methodology for TC and TS tests

6.3 TC and TS Tests for 96.5 Sn–3.5Ag Solder Bumped FCOB Assembly

Thermo-mechanical failures are the most common cause of failure in an electronic assembly. The temperature loading arises from ATC test or service environment. Due to difference of the thermal expansion between the different materials of the package, the package will deform and result in stresses and strains generated and ultimately cause failure. Since solder is the weakest material in the assembly, the

Table 6.3 Thermal profiles for TS and TC tests conditions

Test	T_{max} (°C)	T_{min} (°C)	Ramp rate (°C/min)	Dwell time (min)	Cycle time (min)
TS	+125	−55	~50	5	17
TC	+125	−40	~30	15	60

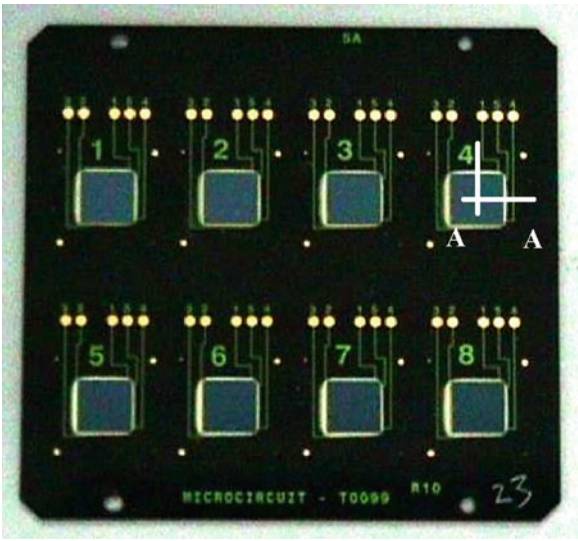

Fig. 6.3 FCOB test vehicle

likely cause of failure is expected in the solder joint. Temperature cycling tests by slow TC or faster TS tests are widely used for quantifying the solder joint reliability performance.

Thermal cycling and thermal shock tests for FCOB were conducted in a three-zone temperature cycling chamber. The TC loading has a cycle time of 60 min while the TS loading has a cycle time of 17 min. The thermal profile for the TS and TC tests are given in Table 6.3. The solder interconnections are connected via daisy chains and used for in-situ resistance monitoring. Failure of the FCOB solder joint was defined when the resistance value exceeding 300Ω (i.e., an open joint or resistance) in this study.

Prior to testing, the FCOB assemblies were screened using scanning acoustic microscope and electrical continuity check. Figure 6.3 shows the FCOB assembly test vehicle. Time zero resistance measurements were taken only after the samples were prebaked for 24 h at 125°C. Only the outer row solder joints are monitored by four daisy chains. The failed units were cross-sectioned to identify the failure location and the failure mode. From the SEM analysis, as shown in Fig. 6.4, the observed failure mode is solder fatigue cracking, where the crack propagation path is along the top solder joint, below the UBM layer.

The test results are presented using a two-parameter Weibull analysis and plotted in Fig. 6.5. The first failure, MTTF and Beta, or slope is given in Table 6.4 for both

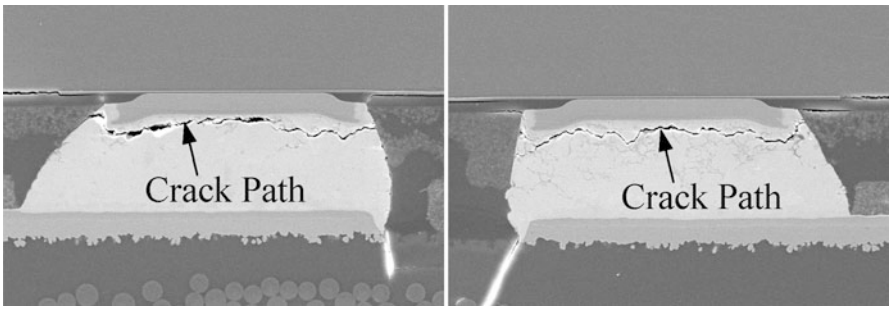

Fig. 6.4 SEM picture 96.5Sn–3.5Ag FCOB solder failure

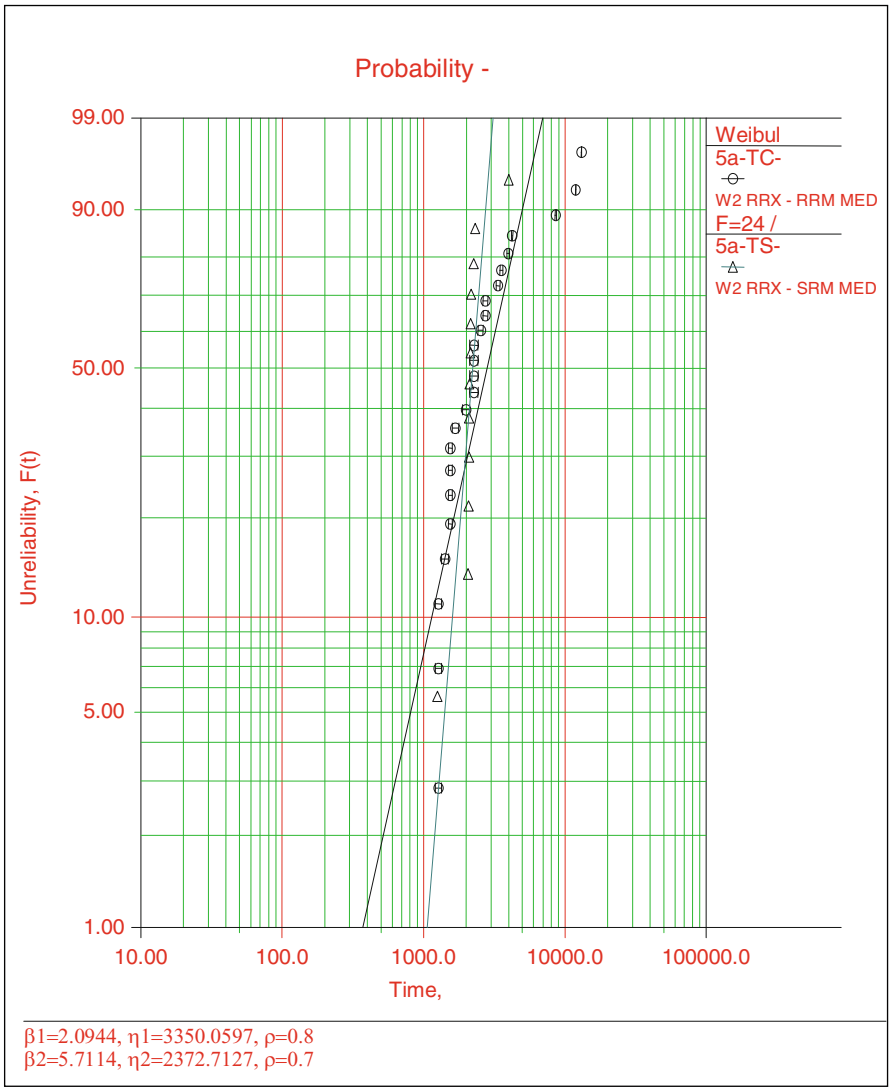

Fig. 6.5 Weibull plot of TC and TS test condition

Table 6.4 TS and TC test results

	1st failure	Beta/slope	MTTF
TS	1,255	5.71	2,226
TC	1,271	2.09	2,813

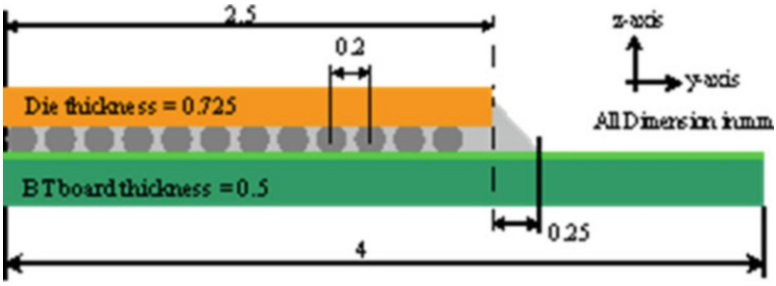

Fig. 6.6 Planer dimension of the FCOB assembly

the TC and TS test condition. The table shows that the test results for the TS condition are very close to that of the TC condition.

6.3.1 FEA Modeling of FCOB with 96.5 Sn–3.5Ag Solder Joints

Finite element method is applied to investigate the flip chip solder joint reliability modeling. The implementation of this FE simulation involves five main input parameters such as: (a) material property, (b) geometry, (c) boundary condition, (d) element type, and (e) initial and loading condition. After which, the computed results are used for assessing the solder joint reliability. The modeling methodology and procedure used are consistent throughout the various models developed in this work. The following assumptions are made prior to modeling: (a) The FCOB assembly is stress free at initial condition, (b) Temperature on the FCOB assembly is uniform during temperature cycling and transient effect is not considered, (c) Perfect adhesion at all material interfaces, and (d) FCOB assembly modeled is free of voids, delaminations, and defects. 3D models are developed to capture all the material components in a FCOB assembly. The planer dimension of the FCOB assembly is shown in Fig. 6.6. Its detail flip chip joint geometry is measured from a cross-sectioned specimen and implemented in the FEA, as shown in Fig. 6.7. The constitutive models for various materials in the FCOB assembly are summarized in Table 6.5.

The solder is modeled as a separate constitutive model in ANSYS, taking into account the time-independent plasticity and the time-dependent creep. This phenomenological model can separate the different deformation behaviors in solder by analyzing the plastic and creep behavior.

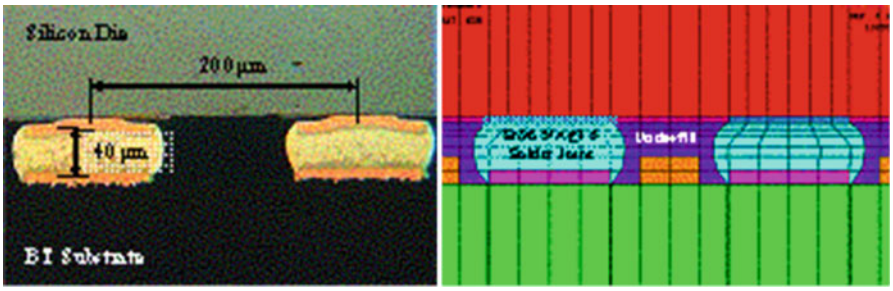

Fig. 6.7 Detail flip chip solder joint structure in the FE model

Table 6.5 Thermo-mechanical constitutive models and Element Types used for FCOB

Material	Constitutive
Silicon die	Elastic-isotropic
Cr-Cu UBM	Elastic-isotropic
Cu Pad	Elastic-isotropic
BCB	Elastic-isotropic
Solder mask	Temp-dependent elastic-isotropic
BT substrate	Temp-dependent elastic-orthotropic
Underfill	Temp-dependent elastic-isotropic
Sn96.5–Ag3.5 solder	Elastic-plastic-creep

The total strain of an elastic-plastic-creep analysis can be expressed as the sum of elastic strain ε_{el}, time-independent plastic strain ε_p, and steady state creep strain ε_c given in (6.8).

$$\varepsilon_{total} = \varepsilon_{el} + \varepsilon_p + \varepsilon_c \tag{6.8}$$

The elastic modulus of 96.5Sn–3.5Ag solder given in (6.9), is fitted with its mean loading rates from 0.64 MPa/s to 51 MPa/s [9]. The solder response is assumed to exhibit elastic and perfectly plastic behavior after yielding. The plastic deformation is characterized by nonrecoverable strain and occurs when stresses exceed the yield point of solder. Hence, the temperature-dependent yield stress given in (6.10) is fitted from its three different nominal strain rates of 5E−5 to 5E−3 s^{-1} [9] to determine the yield state condition. Hence, a strain rate value of 1E−5 to 1E−3 s^{-1} is used to simulate the solder joint strain rate response under a temperature cyclic loading condition.

$$E(\text{MPa}) = 92295 - 149.7 \times T \tag{6.9}$$

$$\sigma_y(\text{MPa}) = 200.45 - 0.7756T + 0.0007T^2 \tag{6.10}$$

Table 6.6 ANSYS input for implicit creep analysis

Solder alloy	C1	C2	C3	C4
Sn96.5–Ag3.5	5E-6	1	11	9,601

ANSYS creep analysis employs an implicit time integration method, which has provisions for including temperature-dependent constants, and simultaneous modeling of creep and kinematics hardening plasticity. The experimental steady state creep behavior of 96.5Sn–3.5Ag flip chip solder joint specimen by Wiese [11, 12] is given in (6.11). This equation is then rewritten into (6.12), which is in the form of input for implicit creep model (TBOPT = 10 for 96.5Sn–3.5Ag solder) in ANSYS [10]. The constants C1, C2, C3, and C4 are given in Table 6.6.

$$\delta\varepsilon/\ \delta t = A(\sigma/B)^n \exp(-Q/\mathrm{k}T) \tag{6.11}$$

$$\mathrm{d}\varepsilon/\mathrm{d}t = \mathrm{C1}(\mathrm{C2}\sigma)^{\mathrm{C3}} \exp(-\mathrm{C4}/T) \tag{6.12}$$

Boundary conditions are typically set to describe the symmetry planes and set at the bottom corner of the structure to prevent free rotation in space. However, in the 3D-slice model, addition boundary condition is required; this is applied at the opposite edge of the two symmetry planes, which is shown in Fig. 6.8. The purpose of this boundary condition is to couple the nodes at the edge and constraint to only out-of-plane movement during thermal loading condition. Figure 6.8 shows the applied boundary conditions in a 3D-slice and 3D-octant models.

The solder joint is subjected to a complex state of multiaxial stress–strain response during thermal cycling, and the equivalent stress–strain concept is required to represent the multiaxial state of stress and strains in the solder joints. From the experimental results, the interface between the solder and silicon chip is the sensitive region to failure. And the solder joint fatigue failure is due to the cyclic plastic and creep strain damage leading to crack initiation and propagation. Hence, the accumulated equivalent inelastic strain is extracted from the finite element analysis as a fatigue parameter, at the top layer of the solder.

It is found that the elemental results are more dependent on the mesh size than the nodal results. Therefore, the failure parameter is calculated from the nodal point solution. However, the existence of singularities or large gradients at the free edges, abrupt change of geometry, or sharp corners of the solder joints make this consideration critical. The inelastic strain in the strain concentration area is very sensitive to the local mesh density. To minimize the mesh sensitivity and stress–strain singularity, element volume averaging technique is introduced in this flip chip solder joint modeling. This will effectively characterize the inelastic strain response at the critical solder element layer by averaging these values among the selected elements at a designated time step. Figure 6.9 shows the fatigue parameter extracted at a nodal location point of the critical solder joint. It also shows the top solder element layer taken from the critical solder joint at the outer most row to

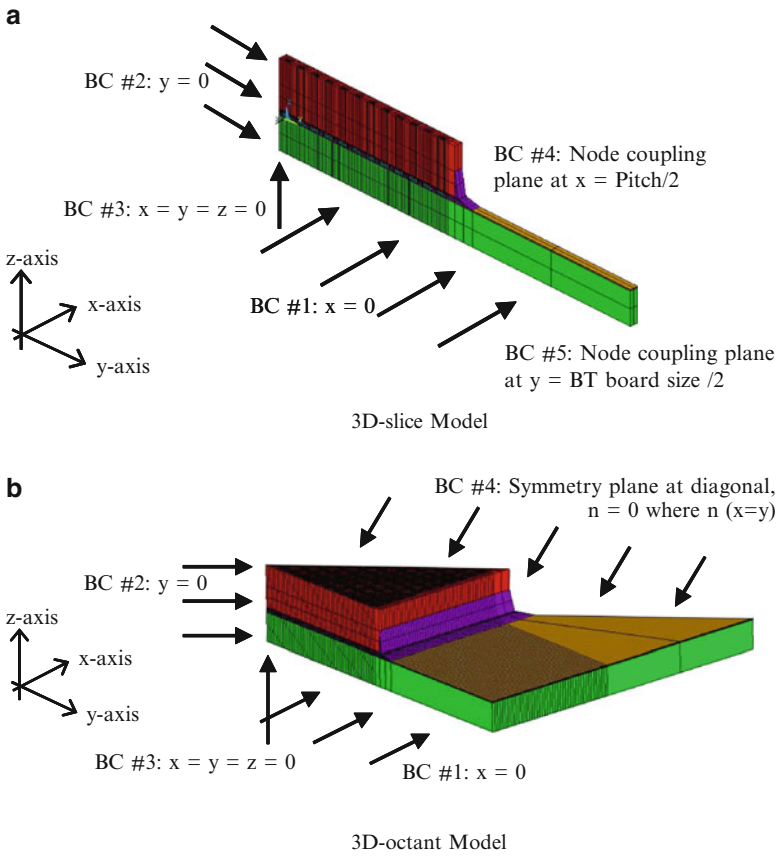

Fig. 6.8 Boundary conditions for the FCOB assembly. (**a**) 3D-slice model. (**b**) 3D-octant model

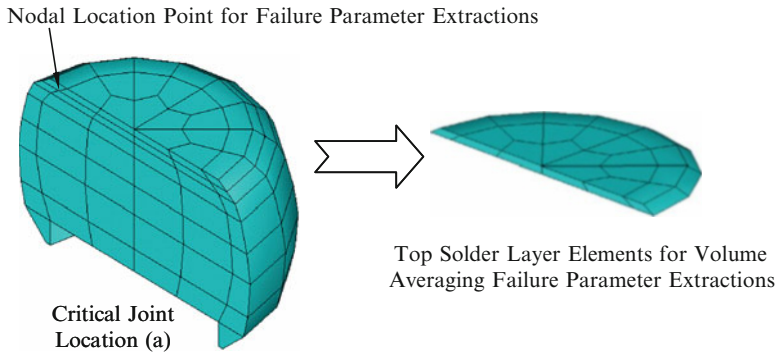

Fig. 6.9 Fatigue failure parameter extraction

characterize the failure/fatigue parameters by volume averaging method at the last thermal cycle. The equations of the element volume averaging calculation are described in (6.13) and (6.14). The accumulated equivalent inelastic strain per cycle is calculated from (6.15), and then substituted into the fatigue model to estimate the solder joint fatigue life.

Accumulated equivalent

$$\Delta\varepsilon_{\text{pl}} \text{ per cycle} = \left[\sum \Delta\varepsilon_{\text{pl}} \times V\right] \Big/ \sum V \tag{6.13}$$

Accumulated equivalent

$$\Delta\varepsilon_{\text{crp}} \text{ per cycle} = \left[\sum \Delta\varepsilon_{\text{crp}} \times V\right] \Big/ \sum V \tag{6.14}$$

$$\Delta\varepsilon_{pl} + \Delta\varepsilon_{\text{crp}} = \Delta\varepsilon_{\text{Inelastic}} \tag{6.15}$$

The life prediction model of 96.5Sn–3.5Ag solder is taken from the published work by Kanchanomai et al. [13]. Kanchanomai et al. conducted their low cycle fatigue test on several Sn–Ag system solders using a noncontact strain controlled system at 20°C, with a constant frequency of 0.1 Hz. Their failure in the solder fatigue test is defined as 25% reduction of maximum tensile load instead of 50%, which is recommended by ASTM [14], and commonly used by the researchers in their low cycle solder fatigue testing. This is because, solder fatigue lifetime corresponding to this failure criterion of 50% load changed is often beyond the onset of solder softening acceleration.

Equation (6.16) shows the Coffin–Mansion type of fatigue model for the 96.5Sn–3.5Ag solder alloy.

$$N_f = 27.63\Delta\varepsilon_{\text{inelastic}}{}^{-1.08} \tag{6.16}$$

In this work, the FEA results are compared between 3D-slice model and 3D-octant model. The solder fatigue parameters that extracted from a 3D-slice and -octant models are shown in Fig. 6.10, with the location notation of (1) and (2). Its modeling results are presented in Table 6.7.

From Table 6.7, FE result generated using a 3D-slice model calculated the lowest inelastic strain value, which predicted a higher fatigue life as compared to a 3D-octant model. If comparing the fatigue life predicted at the same joint location (1) of 3D-slice and -octant models, the difference is only about 5%. In 3D-octant model, the maximum inelastic strain is located at the outer most diagonal joint [joint location (2)]; however, the differences in the life predicted, at joint location (1) and (2) is less than 6%. The major difference in simulations for both models employed is their computing time and space. The 3D-octant structure required an enormous number of elements, hence this will demand a huge computing space and longer time for analysis, as compared to 3D-slice structure.

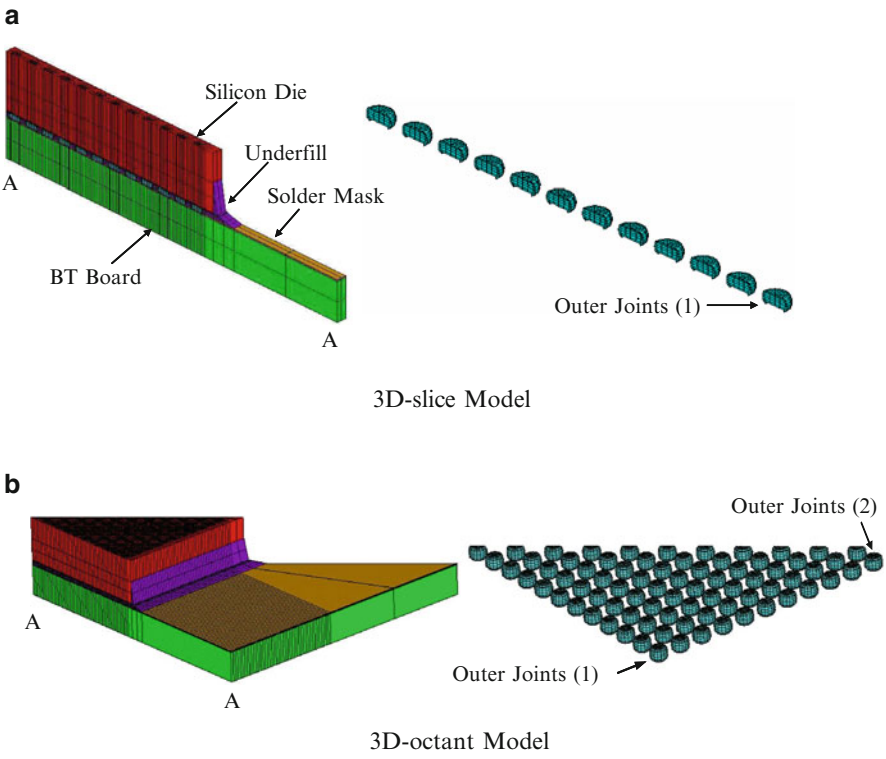

Fig. 6.10 (**a**) 3D-slice and (**b**) 3D-octant models of FCOB assembly

Table 6.7 Element volume averaging results of 3D-slice and 3D-octant model

3D-model	$\Delta\varepsilon_{pl}$	$\Delta\varepsilon_{crp}$	$\Delta\varepsilon_{Inelastic}$	N_f	Computing space
Slice (1)	7.11E−3	19.02E−3	26.13E−3	1,416	~0.1
Octant (1)	7.09E−3	20.30E−3	27.39E−3	1,346	1.0
Octant (2)	7.66E−3	21.19E−3	28.85E−3	1,272	1.0

6.4 Thermal Cycling Test for Pb-Free 95.5 Sn–3.8Ag–0.7Cu Solder Joints

The test specimen is shown in Fig. 6.11. Four different components, BGA316, PQFP208, PQFP176, and TSSOP48, are mounted on the FR4 PCB using lead-free solder of Sn–3.8Ag–0.7Cu. Three different finishes are used on PCB surface, say, Ni/Au, Immersion Ag, and OSP finish. For each board surface finish, six specimens were tested.

A total of 18 test boards were tested under thermal cycling condition. Thermal cycling tests for lead-free solder specimen were conducted in a three-zone

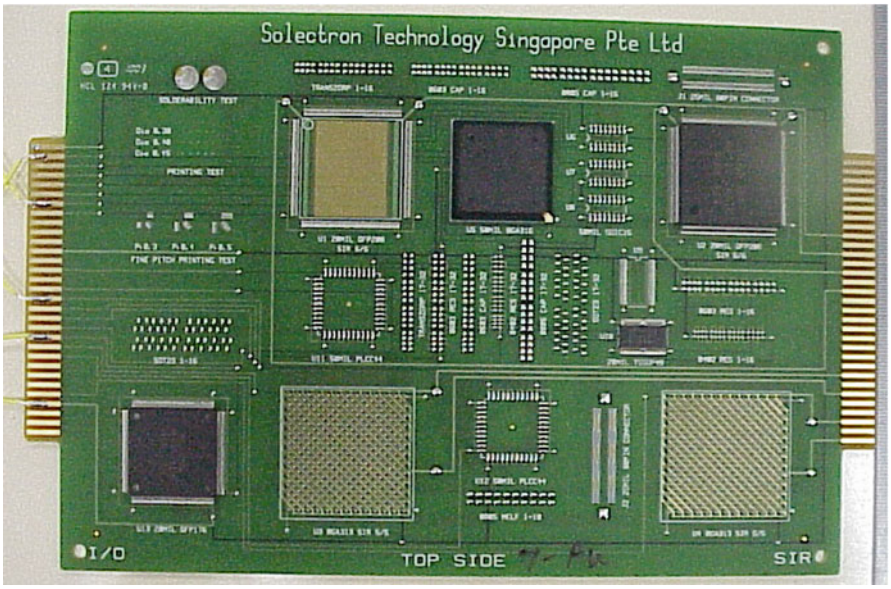

Fig. 6.11 Lead-free solder assembly specimen

Table 6.8 Thermal profiles for TS and TC tests conditions

Test	T_{max} (°C)	T_{min} (°C)	Ramp rate (°C/min)	Dwell time (min)	Cycle time (min)
TC	+125	−40	11	15	60

Table 6.9 Test result and Weibull parameter for BGA316 component

	Ni/Au	Ag	OSP
BGA316 test result	2,745	1,048	1,236
	3,053	1,309	1,680
	2,131	1,347	2,661
	2,892	1,432	2,987
	2,972	2,127	1,931
Beta	7.7	4.4	3
MTTF	2,741	1,439	2,105

temperature cycling chamber. The TC loading has a cycle time of 60 min. The thermal profile for TC tests are given in Table 6.8.

The solder interconnections are connected via daisy chains and used for in-situ resistance monitoring. Failure of the solder joint was defined when the resistance value exceeded 300Ω (i.e., an open joint or resistance) in this study. Only one daisy chain for each component connects all the solder joints. The test is stopped after 3,400 cycles.

The test results are listed in Table 6.9. It can be seen that all BGA components failed after test. For PQFP208, Ni/Au finished component has not failed after 3,400

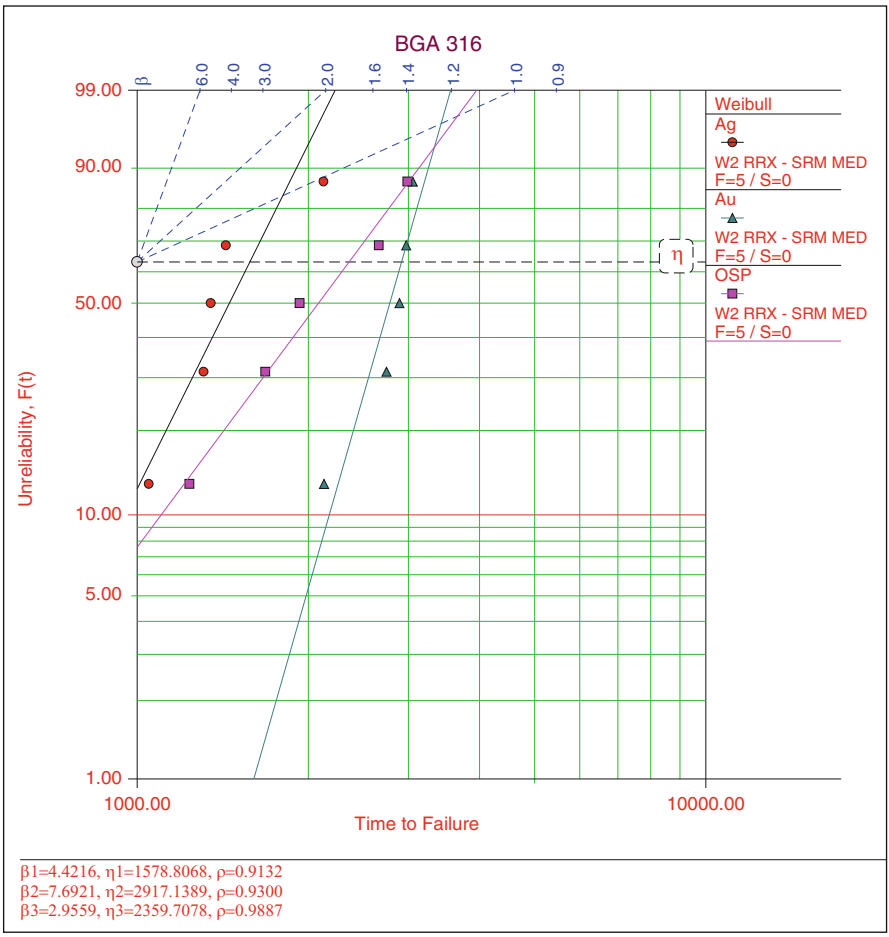

Fig. 6.12 Weibull plot for BGA 316 component with three surface finishes

TC cycles test. For PQFP176, failure occurred for the component with OSP finish. For TSSOP 48, no failure occurred for all components with different finishes. It was shown from test results that small components are safer than large ones subjected to thermal cycling loading; components with Ni/Au finish exhibit more fatigue life than components with Ag or OSP finish; fatigue life of BGA component exhibits more sensitivity to thermal cycling load than that of PQFP component. The fatigue failure result data for BGA component with different finishes and PQFP 208 component with OSP finish are enough to plot two-parameter Weibull distribution curve. The Weibull plot for BGA component is shown in Fig. 6.12 and PQFP208 with OSP finish in Fig. 6.13. The Weibull parameters, such as mean-time-to-failure (MTTF) and slope, are listed in Table 6.9. The large slope value means that the first-time-to-failure (FTTF), MTTF and all the failure data are closed so that the failure

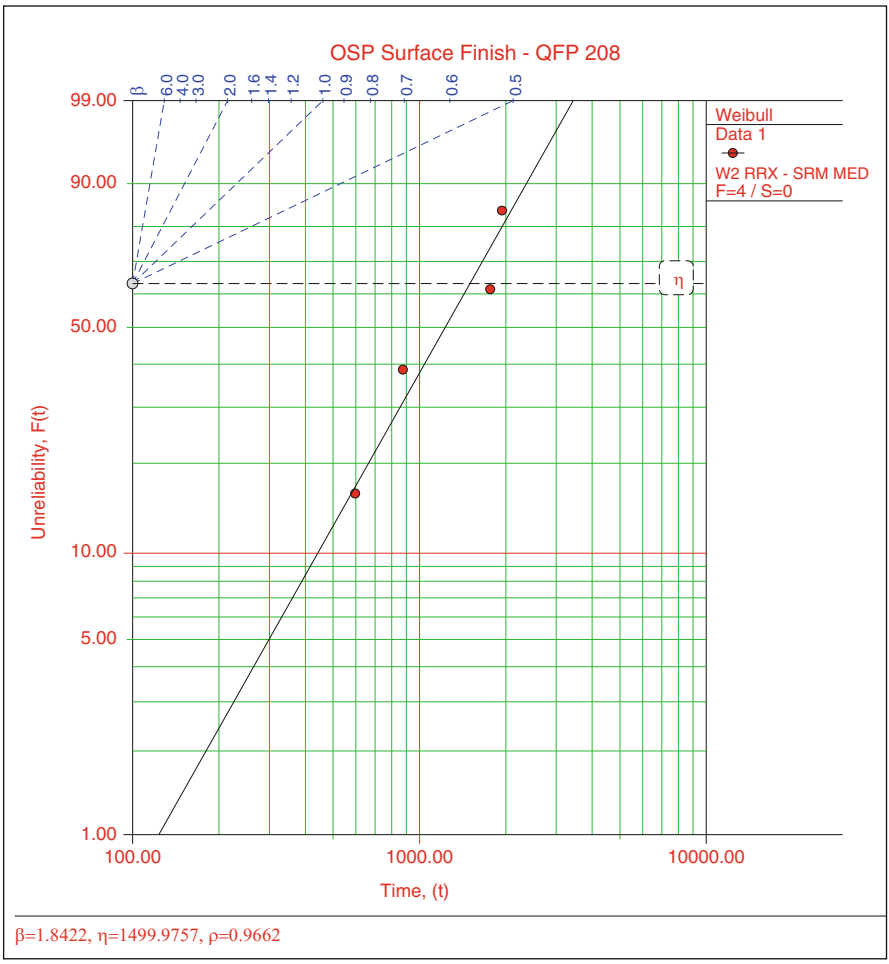

Fig. 6.13 Weibull plot for PQFP208 component with OSP surface finish

data are closed to MTTF. The small slope value means that the failure data are scattered.

Finite element method is applied to investigate the lead-free PBGA solder joint reliability modeling. The PBGA component geometry is measured from a cross-sectioned specimen and implemented in the FEA. Because of significant geometry mismatch among different materials and many solder balls, the submodeling method is used in FEA model in order to obtain more accurate result. The quarter model is used for global model due to symmetric geometry and boundary condition shown in Fig. 6.14. The constitutive models for various materials in the BGA assembly are summarized in Table 6.10. The Anand viscoplastic model was used for solder joint and the plastic work density is a very important parameter for energy-based fatigue life prediction model. Three thermal cycles are used in FEA simulation.

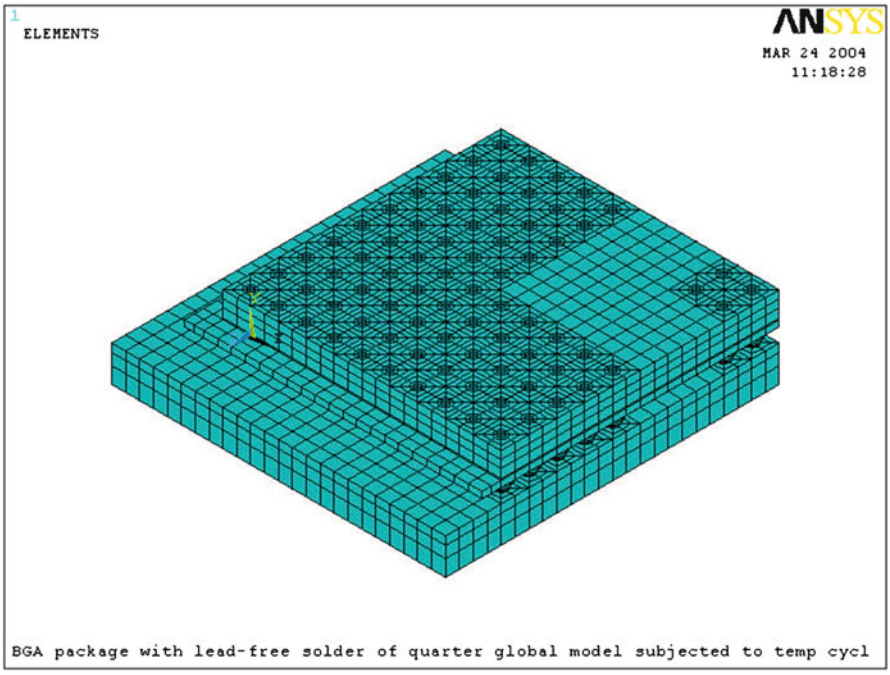

Fig. 6.14 Global quarter model of PBGA component

Table 6.10 PBGA Assembly materials and models used

Material	Constitutive
Silicon die	Temperature-dependent Elastic-isotropic
Die adhesive	Elastic-isotropic
Cu pad	Elastic-bilinear kinematic hardening plastic
BT substrate	Elastic-orthotropic
FR4 PCB	Elastic-orthotropic
Mold compound	Elastic-isotropic
Sn–3.8Ag–0.7Cu solder	Viscoplastic (Anand's model)

Figure 6.15 shows the plastic work density result for global model. It can be seen that the critical solder joint is located under the die corner due to large CTE mismatch. The die side interface exhibits more critical than PCB board side one. Therefore, the subsequent analysis of fatigue life would be focused on die side interface. The submodel is shown in Fig. 6.16 selecting from the critical solder joint closed to die corner.

It is noted that plastic work density in stress concentration area is very sensitive to the mesh density and position as shown in Fig. 6.17. To minimize the mesh sensitivity, element volume averaging technique is introduced in this study. However, how to select suitable elements for volume-averaged results is very

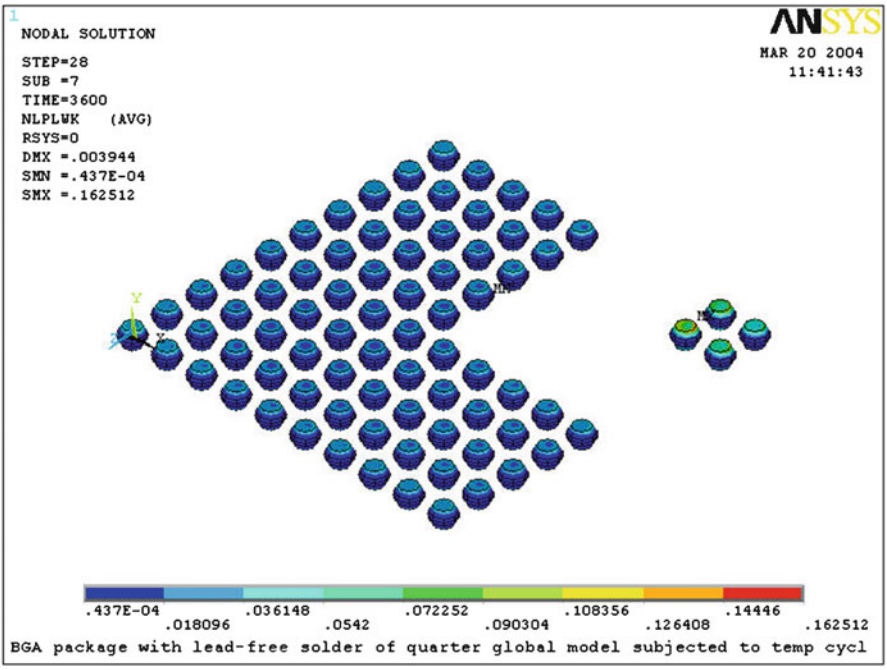

Fig. 6.15 Plastic work density result for solder joint of global model

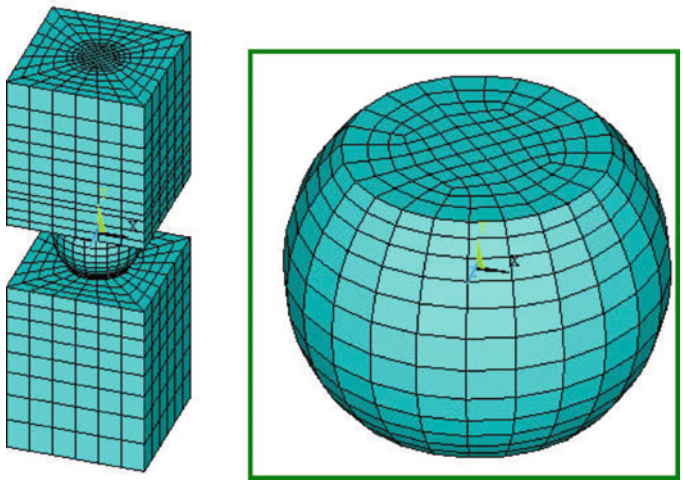

Fig. 6.16 Submodel including one critical BGA solder joint

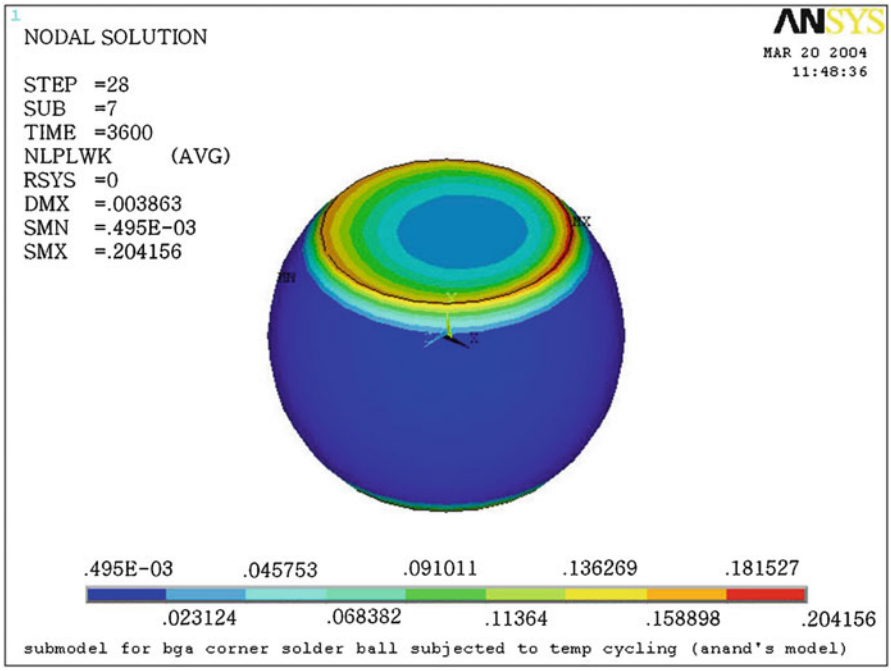

Fig. 6.17 Plastic work density result sensitive to location

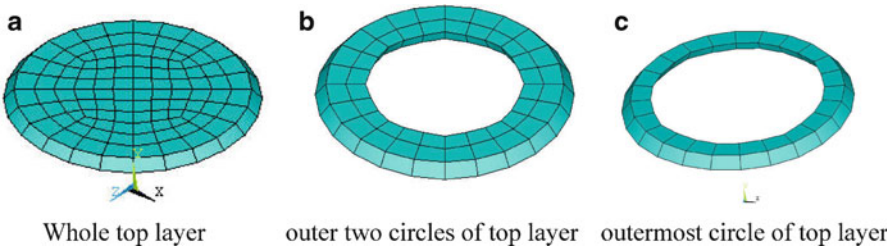

Fig. 6.18 Different averaged volumes

important and it can affect the fatigue result significantly. In this study, different methods are used to compare with test result. Figure 6.18 shows the fatigue parameter extracted at different locations of solder joint interface element layer under the die. The element volume averaging calculation of accumulated plastic work density per cycle is calculated from (6.17) and then substituted into the fatigue model shown in (6.18) shown in Fig. 6.19 to estimate the solder joint fatigue life.

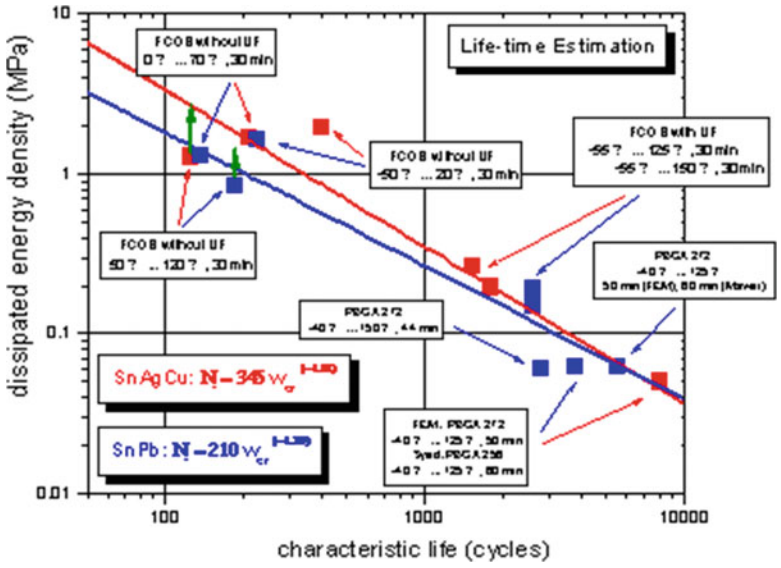

Fig. 6.19 Energy-based model for lead-free and lead–tin solder joints [15]

Table 6.11 Element volume averaging results of 3D-slice and 3D-octant model

Volume	ΔW_p	N_f
Whole top layer	0.172	2,081
Outer two circle of top layer	0.228	1,634
Outermost circle of top layer	0.243	1,460

Accumulated plastic work density per cycle

$$\Delta W_p = \left[\sum \Delta W_p \times V\right] / \Sigma V \tag{6.17}$$

Energy-based fatigue model [15]

$$N_f = 345 W_p^{(-1.02)} \tag{6.18}$$

Table 6.11 given the fatigue life prediction base on (6.18) for different averaged-volume method. It can be seen that the life prediction is sensitive to the element location. During thermal cycling test, the crack always initiates at the outer area of interface between solder and die due to stress concentration on this area. Then, the crack propagates along the interface so that the stress concentration area will move toward the interface center. Therefore, the whole top layer averaged parameter will

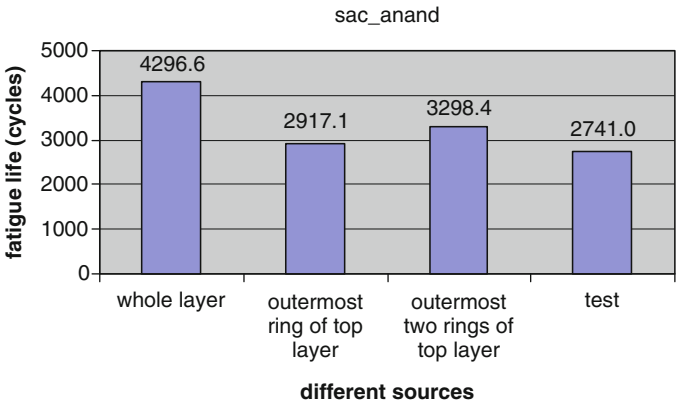

Fig. 6.20 Fatigue life comparison for different FE output methods

underestimate the plastic strain energy density and overestimate the fatigue life accordingly. The averaged parameter located on outer circle elements is appropriate for fatigue life prediction.

Equation (6.18) is obtained by combining component fatigue test data and FEA analysis result. The fatigue life is derived from component level solder joint thermal cycling fatigue test, and plastic strain energy density is derived from the FEA analysis result based on volume-averaged technique for top layer element of die side. Therefore, the fatigue life prediction using whole top layer volume-averaged data results in closed fatigue life (2,081 cycles) compared to test result (2,741 cycles for Ni/Au surface finish) based on (6.18).

In thermal cycling test, temperature changes from −40°C to 125°C with 1 h per cycle. The isothermal tension test condition is required closing to thermal cycling test. The highest temperature and strain rate in thermal cycling test have significant effect on solder joint fatigue failure. According to the above condition, the isothermal test condition is selected as at temperature 125°C with 0.001 Hz of frequency. The material constant m and C for Sn–3.8Ag–0.7Cu solder are 0.897 and 311.7 MPa, respectively [16, 17] obtained from isothermal test. Figure 6.20 shows the fatigue life prediction for different methods using material constants from bulk solder isothermal fatigue test result.

It can be seen that fatigue life is overestimated when volume averaging the whole top layer plastic strain energy density compared to testing result by using material fatigue constant from isothermal bulk material fatigue test result. Using the outermost ring of top layer as averaged volume can lead to ideal fatigue life result compared to test result when using material fatigue constant from isothermal bulk material fatigue test result. The stress strain is closed to uniform at cross section of bulk solder material during tension fatigue test. From FEA analysis result, the stress strain distributed on top layer is sensitive to position and the difference is very large

between outer ring and center of top layer. The crack will initial around outer ring due to higher stress at outer ring of top layer. So selecting the outer ring of top layer is desirable for volume average.

6.5 Thermal Aging Effects on Pb-Free 95.5 Sn–3.8Ag–0.7Cu Solder Joint Reliability

The morphology and growth of interfacial IMC compounds between 95.5Sn–3.8Ag–0.7Cu Pb-free solders and Nickel/Gold (Ni/Au) surface finish was studied on a BGA solder joint specimen. Digital imaging techniques were employed in the measurement of the average IMC growth thickness. The IMC growth behavior subjected to isothermal aging exposure at 125°C, thermal cycling, and thermal shock with an upper soak temperature of 125°C are compared.

The solder joint specimen consists of a single BGA 95.5Sn–3.8Ag–0.7Cu solder ball, soldered between two FR4 substrate materials as shown in Fig. 6.21. The Ni/Au surface finish on copper pad has a nickel (Ni) layer thickness of 5 μm and a gold (Au) flash thickness of submicron. The copper pad thickness is 30 μm. The FR4 substrate specimen pieces have dimensions of 12 × 3 × 0.5 mm. The specimen pieces are placed on a template for soldering. No-clean flux was applied onto the copper pad and a solder sphere is placed on top of the flux and reflowed on one side as shown in Fig. 6.21. After the first reflow, another fluxed FR-4 piece is placed onto the template and the reflowed piece is flipped over a second FR-4 piece and

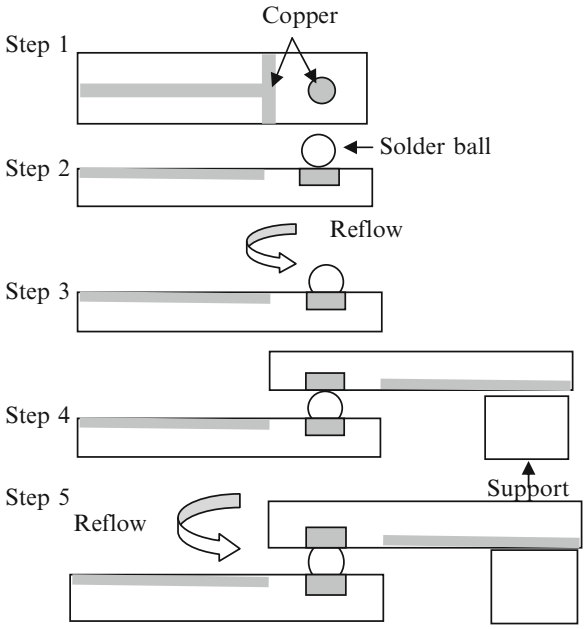

Fig. 6.21 Fabrication process for solder joint specimen

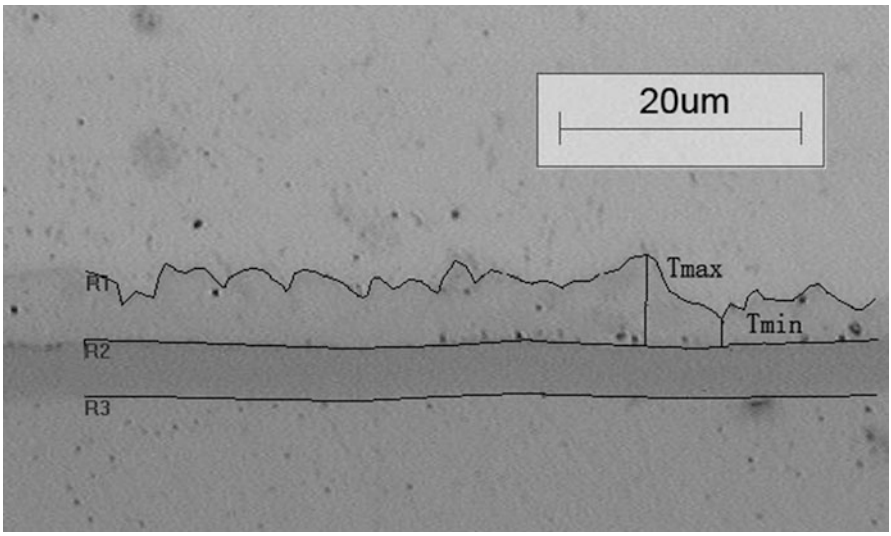

Fig. 6.22 Digital imaging techniques to measure the average IMC thickness

reflowed for a second time to form a lap shear specimen. The solder reflow profile with a peak temperature of 250°C was used in the fabrication.

Isothermal aging at 125°C, Thermal Cycling (TC), and Thermal Shock (TS) were used for solid state IMC growth studies. Isothermal aging at 125°C was carried out in a thermal chamber for 47, 119, 167, 262 h. The TC profile is −40°C to +125°C with a cycle time of 56 min, a ramp rate of 12.7°C/min and hold time of 15 min. The TS profile is −55°C to +125°C with a cycle time of 17 min, a ramp rate of 51.4°C/min and hold time of 5 min. The solder joints were subjected to TC and TS aging for 500, 1,000, and 2,000 cycles. The exposure time is equal to the total dwell time spent at the high temperature soak period for the TC and TS profile, respectively.

After thermal aging, the lap shear specimens were mounted, cross-sectioned, polished for optical microscope investigation. Then they were etched (5% HNO_3 + 95% methanol) and observed by a JOEL JSM-5410LV Scanning Electron Microscopy (SEM) under an accelerated voltage 20 kV. At the same time, Energy dispersed X-ray (EDX) was used to identify the material elements present in each selected area in the solder joint. Digital imaging techniques were employed in the measurement of the average IMC growth thickness shown in Fig. 6.22. Two polylines R1, R2 were created manually along the edge of the IMC by using the tracing tool. Then the average distance between the two polylines will be given automatically. The thickness results were defined by spatial calibration. The minimum and maximum distance between the two lines will also be marked in the image.

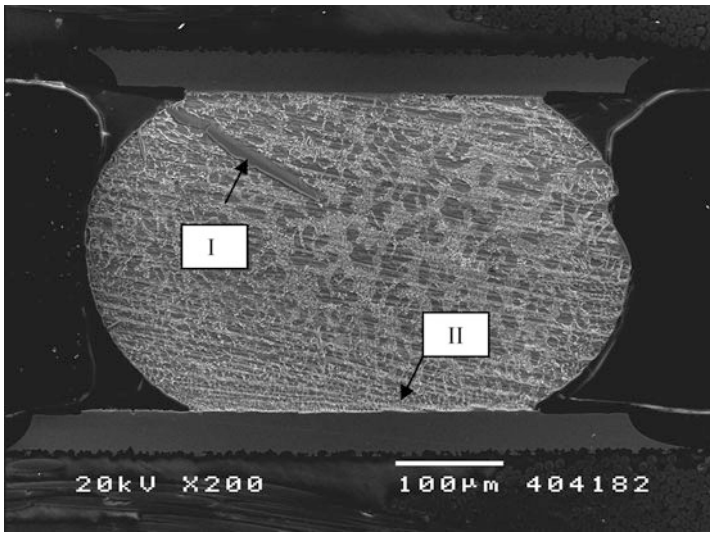

Fig. 6.23 Microstructure of Sn–3.8Ag–0.7Cu solder joint after reflow

The features of the microstructure and IMCs formed after reflow was observed by SEM. Energy dispersed X-ray (EDX) was used to identify the material elements present in the solder joint. Low magnification image of the whole solder joint is shown as Fig. 6.23 and the region of interest indicated by (I) and (II) will be discussed further. The microstructure of the solder joint after reflow typically consist of globular Sn rich phases surrounded by small Ag_3Sn phases, and Cu_6Sn_5 are also present. Some large Ag_3Sn IMC rods are formed in the solder, and can be as long as 100 µm or more. The enlarged images of the region (I) and (II) are shown in Figs. 6.24 and 6.25, together with the EDX spectrums.

Region (II) in Fig. 6.25 shows the morphology of solder/nickel interface, which is the enlarged image of region (II) in Fig. 6.23. EDX analysis was used to identify the traces of respective elements noted at the IMC layer. The darker phase above the IMC is the Sn-rich phase whereas the lighter features are Ag_3Sn and some Cu_6Sn_5 precipitates. The Ni metallization layer is approximately 5-µm thick. The darker phase below the Ni layer is the copper pad.

IMC formation between solder and Ni/Au surface finish on copper pad and its subsequent growth can have a serious consequence on the solder joint reliability performance. The Cu pad metallization is made up of a thin layer of gold (Au) for oxidation protection on top of a Nickel (Ni) layer acting as a diffusion barrier preventing a diffusion couple between the Sn-rich solder and copper (Cu) pad. The gold layer diffuses readily into the solder during reflow. Under such combinations, the intermetallic compounds formed between Sn–Ag–Cu solder and Ni/Au surface finish on Cu pad could be a ternary $(Cu–Ni)_6Sn_5$ and/or a complex quad, $(Cu–Ni–Au)_6Sn_5$ intermetallic compounds, if Au goes into IMC formation during the wetting and aging process.

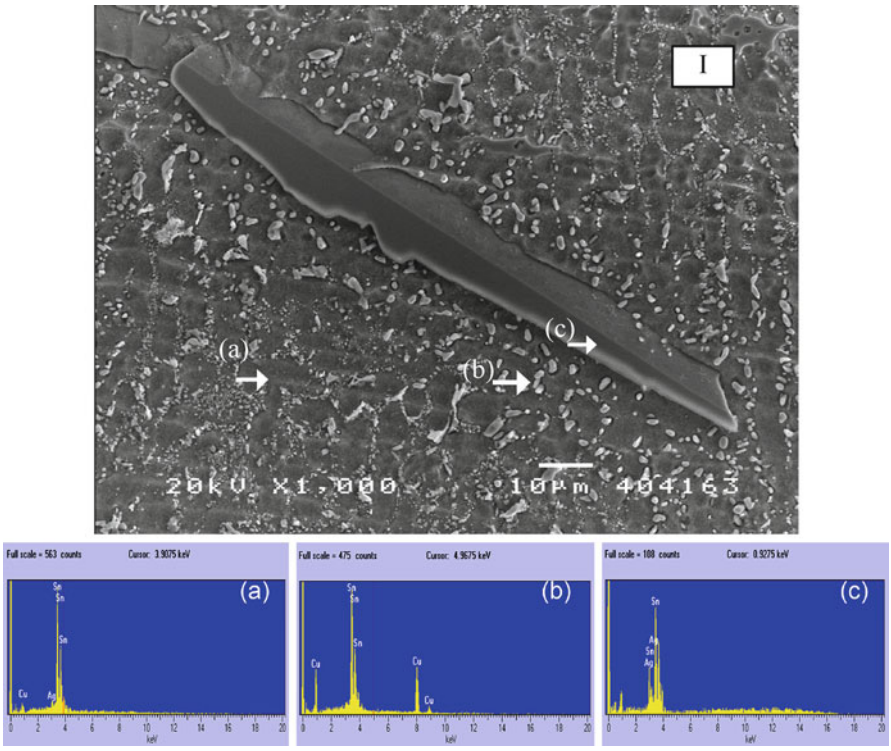

Fig. 6.24 The IMC and EDX features in the solder joint, plot I in Fig. 6.28. (**a**) Sn-rich; (**b**) Cu_6Sn_5; (**c**)Ag_3Sn

Solder joints are subjected to thermal cycling exposure due to cyclic environment thermal excursions and/or electronic equipment power on–off cycles. Therefore it is important to understand the effects of thermal cycling aging on the microstructure and IMC growth of solder joints subject to controlled thermal cycling exposure. A comparison of the morphology and the average IMC thickness on the interface were performed between isothermal aging, TC, and TS aging.

After isothermal aging for 47, 119, 167, 262 h, the interface morphology were captured by optical microscopy. The measurements of the Cu–Ni–Sn IMC thickness were processed from the optical microscope images rather than SEM images. The Cu–Ni–Sn IMC on the solder/nickel interface are needle-like structures and are readily observed on the optical images of a cross-sectioned surface. The Cu–Ni–Sn IMC details are not readily observed on the SEM image of a cross-sectioned surface. By etching away the solder, the Cu–Ni–Sn IMC details on the surface and behind it can be seen as shown in Fig. 6.26. When using the digital imaging technique with such SEM image, higher average IMC layer thickness will be computed. Thus, optical images were used to determine the IMC layer thickness in this study.

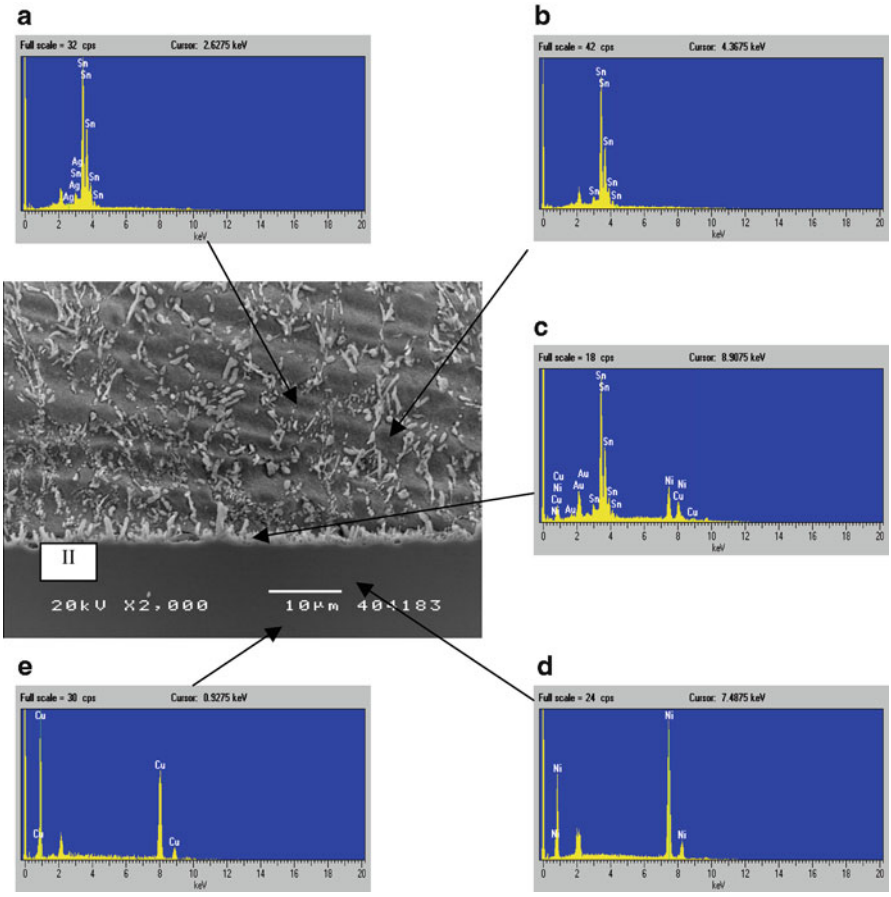

Fig. 6.25 IMC and EDX features at the Solder/Nickel interface, plot II in Fig. 6.23. (**a**) Ag_3Sn IMC; (**b**) Sn-rich; (**c**) Cu–Ni–Sn IMC; (**d**) Ni metallization layer; (**e**) Cu pad

The IMC morphology after 0, 119, and 262 h of isothermal aging at 125°C were noted to grow and coarsen. After reflow (i.e., at 0 h), the IMC on the solder/nickel interface are irregular and grow in needle like manner. After 119 h of aging, coalescence of the IMC needles leads to lateral thickening and ripening. After 262 h of aging, the IMC layer growth is planar in nature. For the TC and TS aging experiments, the IMC growth phases are similar to the isothermal aging case. However, the IMC growth rate for TC and TS aging were much higher than that for isothermal aging at 125°C.

In order to simplify the comparison, the IMC growth was assumed to be volume diffusion controlled, that is, the growth rate is proportional with the square root of time. The IMC thickness, x_t, subject to the aging time can be described by (6.19), where D, is the temperature-dependent coefficient, x_0, is the initial IMC thickness.

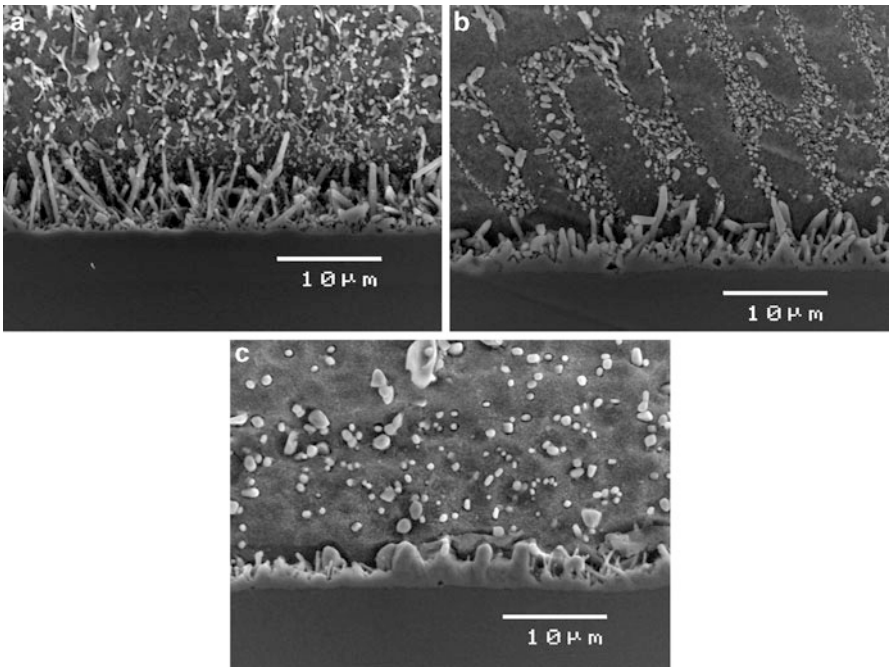

Fig. 6.26 IMC morphology change subject to isothermal aging (SEM image). (**a**) 0 h; (**b**) 119 h; (**c**) 262 h

$$x_t = \sqrt{Dt} + x_0 \tag{6.19}$$

For TC and TS aging, the "effective aging time", t_{eff}, is defined as the total accumulated dwell time at the upper soak temperature of 125°C. It is reasonable to assume that the upper soak temperature segments at 125°C of the temperature cycles contribute mainly to the IMC layer growth for TC and TS aging compared to isothermal aging at 125°C. For TS aging between −55°C to 125°C, the cycle time is 17 min and the dwell time at the upper soak temperature is 5 min. Thus the t_{eff} at the upper soak temperature of 125°C after 2,000 cycles of TS aging is 10,000 min or 166.7 h.

The IMC growth behavior measured for TC, TS, and Isothermal aging at 125°C are plotted in Fig. 6.27. It is interesting to note that the IMC growth rate for TS aging is higher than TC aging. Both IMC growth rate behavior for TS and TC aging is also faster than Isothermal aging at 125°C. The coefficient $\sqrt{D}$ for isothermal aging, TC, and TS aging are 0.0816, 0.1032, and 0.1778, respectively.

The "equivalent isothermal aging time" t_{eq} was then calculated for each of the TC and TS aging condition, based on their respective IMC thickness and the coefficient $\sqrt{D}$ for isothermal aging. The formula used to calculate t_{eq} is derived

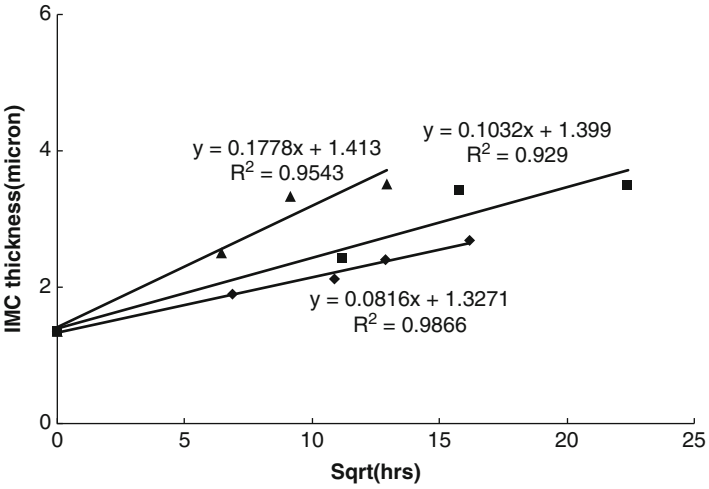

Fig. 6.27 Comparison of IMC data for TC, TS, and isothermal aging at 125°C. (*filled diamond*) ISO 125, (*filled square*) TC, (*filled triangle*) TS

Table 6.12 Equivalent isothermal aging time considering the IMC growth for TC and TS

Process condition	Effective time t_{eff} (h)	IMC thickness x_t (μm)	Equivalent isothermal time t_{eq} (h)	Accelerated factor $K = t_{eq}/t_{eff}$
500 TC	125	2.42	172	1.376
1,000 TC	250	3.42	643	2.572
2,000 TC	500	3.5	694	1.388
500 TS	41.7	2.1	84	2.01
1,000 TS	83.3	2.61	238	2.85
2,000 TS	166.7	2.93	375	2.24

from (6.19), in which D_{iso} is the square of 0.0816 or 6.66×10^{-3}, and the average initial IMC thickness, x_0, is taken as 1.35 μm.

$$t_{eq} = \frac{1}{D_{iso}}(x_t - x_0)^2 \tag{6.20}$$

The "equivalent isothermal aging time" can quantitatively represent the accelerated effect of TC and TS aging compared to isothermal aging. For example, after 2,000 cycles of TC aging, the total dwell time at 125°C, t_{eff} is 30,000 min or 500 h. The IMC thickness accumulated after 2,000 cycles is 3.5 μm. To obtain such an IMC thickness by isothermal aging, it will need a longer equivalent time of 694 h, which is calculated by (6.20). And the accelerated factor K is defined as the t_{eq} divided by t_{eff}, or as expressed in (6.21). For TC at 2,000 cycles, the accelerated factor is 1.39.

$$K = \frac{1}{D_{\text{iso}} t_{eff}} (x_t - x_0)^2 \tag{6.21}$$

The t_{eq} and the accelerated factor for each TC and TS aging were calculated and shown in Table 6.12. After 2,000 cycles of TC and TS aging, the factor is about 1.388 and 2.24 respectively. This suggests that both TC and TS aging accelerate the growth of IMC layer compared to isothermal aging at 125°C. This may be due to higher thermal stresses generated from nonisothermal TC and TS aging conditions. The effect of TS aging on IMC growth rate is greater than TC aging, suggests that stress relaxation in the solder joint is not as pronounced in TS aging compared to TC aging, which has a longer cycle time and soak period. However, isothermal aging at 125°C allows for extensive stress relaxation in the solder joint, giving lower stress, and hence lower IMC growth rate compared to both TC and TS aging.

6.6 Highly Accelerated Life Test

Accelerated tests can be divided, from the standpoint of their objectives, into three major types: product development/verification tests, qualification tests, and ALTs and HALTs. The difference between the ALTs and HALTs is that the HALTs are carried out to obtain, as soon as possible, the preliminary information about the reliability of products, and the principal physics of their failures. The HALTs are conducted with a smaller number of samples and at higher acceleration factors than ALTs. Accelerated tests can be performed at any level, such as part level, component level, module level, equipment level, and system level. Usually, if the reliability characteristics of all the components are known from the ALTs or HALTs, then the reliability characteristics of the equipment or the system can be evaluated theoretically, and often with sufficient accuracy.

6.6.1 HALT Test Strategy for Pb-Free Solder Joint Assembly

The test specimen is same as the specimen shown in Fig. 6.11, including three different surface finishes listed in Table 6.13. The test strategy would include two AST tests; Base-line Product Test and Highly accelerated Stress Screening Test (HASS), which would be elaborated further.

Table 6.13 Specimens of HALT test

Reliability test methods (number of boards)	Halt
Surface finish	
OSP	1
Ni/Au	1
Immersion Ag	1

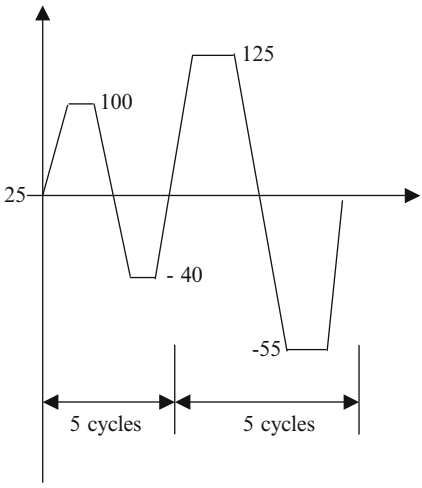

Fig. 6.28 Thermal shock profile

6.6.1.1 AST Test I: Base-Line Product Test

In order to verify robust product design margins, one must perform a series of base-lining experiments in which stress levels applied to the product are incrementally increased until either a target robust design stress level is achieved or an operational or destruct limit is defined. Testing above the destruct limit may cause unrealistic damage to the product (e.g., exceed the glass transition temperature (T_g) of the FR-4). The screening profile will start from a least damaging (storage temperature) to the most damaging (combined temperature and vibration) profile. The experiment seeks to determine the capabilities of the HALT chamber to uncover weak links in the electronic assemblies in a time much shorter.

(a) Storage Temperature
The HASS profile will start with the High Temperature Storage Temperature (150°C) – JEDEC Standard (Condition B), test duration of 1 h following which the Low Temperature Storage Temperature at −40°C, test duration of 1 h. This storage temperature or stabilization bake is used to uncover infant mortality.

(b) Thermal Shock Stress
Figure 6.28 shows the TC test profile including two different conditions: one is from −40 to 100°C, the other is from −55 to 125°C.

(c) Vibration Step Stress
In this vibration step stress, a step tickle vibration of 5 Grms with a dwell time of 10 min is introduced. The purpose of this mild vibration is to ensure that the parts still function after each high-level vibration is completed. A frequency range of 0–2,000 Hz was used as it will generally precipitate most of the latent defects of IC packages. A limitation of 28 Grms was used before proceeding to the next test. Figure 6.29 shows the profile for the vibration step stress.

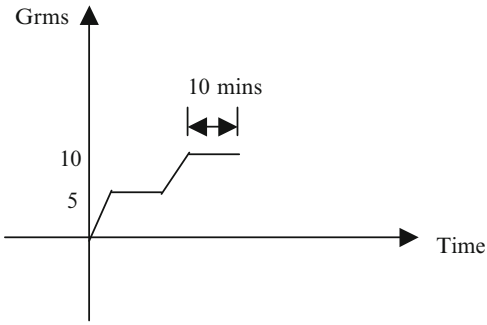

Fig. 6.29 Vibration step stress test

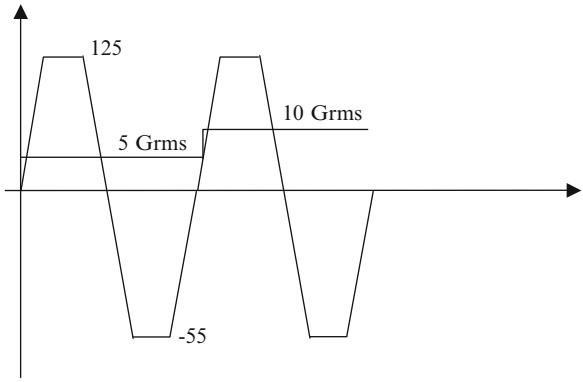

Fig. 6.30 Temperature and vibration test

(d) Combine Thermal Cycling and Vibration
The final step to ruggedize a product is to combine all the stresses, which were previously used. For the temperature cycling profile, the temperature range of −55 to 125°C shown in Fig. 6.30 was used. Each thermal cycle will have a vibration dwell of a multiple of 5 Grms. The test will stop when the vibration reaches 28 Grms.

6.6.2 HASS Test Setup and Analysis

6.6.2.1 AST Test II: Highly Accelerated Stress Screening Profile

AST Test I is used early in the product life cycle for fault finding. After the product goes into production, it will not be feasible to conduct the test as it is very time consuming. Therefore a HASS test profile as shown in the Fig. 6.31 is used as a means to screen products from defects.

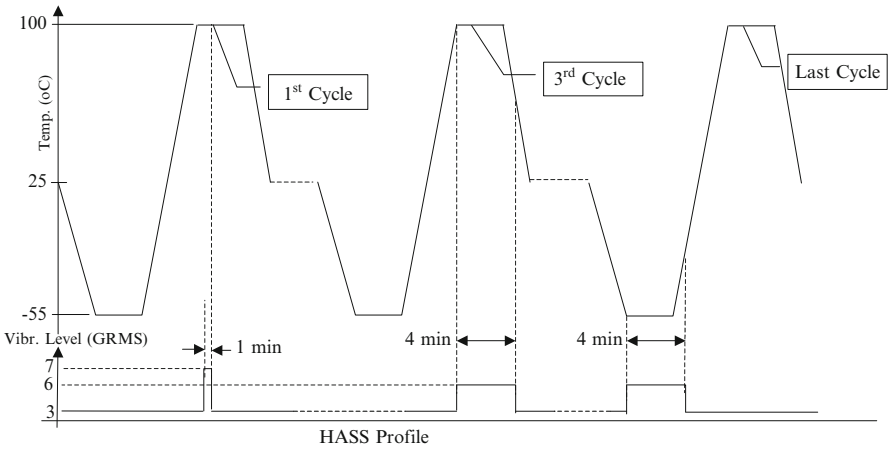

Fig. 6.31 HASS test profile

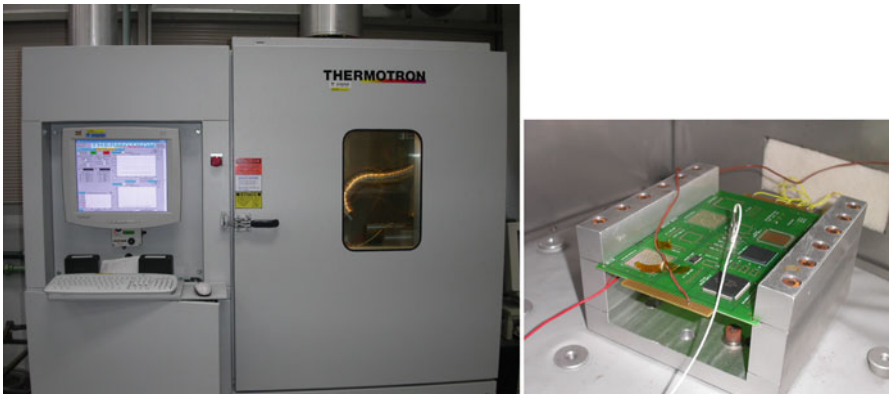

Fig. 6.32 Thermotron AST test facility and HALT/HASS test setup

The HASS test setup is shown in Fig. 6.32, and clamped–clamped boundary condition is used. The event detector is used to measure the resistance change of daisy chain. The failure criteria is defined as the resistance change of 300 Ω. The QFP208 component with Ag finish fails after one block of HASS test. Other components did not fail after one block of HASS test. Although, the QFP component is known to have better thermal fatigue performance than BGA, but the combined thermal cycling and random vibration condition cause the QFP to fail earlier than the BGA due to the compliant connection of the QFP to the PCB board.

Temperature cycling under thermal cycling (TC) and thermal shock (TS) loading for FCOB assembly with Pb-free 96.5Sn–3.5Ag solder joints was reported [18].

Full 3D and 3D strip FEA models were able to predict the solder joint fatigue life with satisfactory agreement with test result [17].

Thermal cycling test of Pb-free 95.5Sn–3.8Ag–0.7Cu soldered assemblies for PBGA, PQFP, and TSSOP surface-mounted devices with three different PCB surface finish conditions were conducted. The test results show that the PBGA devices are more prone to thermal cycling failures compared to the leaded devices like PQFP.

Weibull failure analysis of the PBGA with three different surface finishes used gave a MTTF life of 1,439 cycles for Im-Ag, 2,105 cycles for Cu-OSP, and 2,741 cycles for Ni/Au respectively. Finite element analysis modeling and simulation of the PBGA assembly predicted fatigue lives of 1,460–2,081 cycles, depending on the volume averaging techniques used. This falls within the range of MTTF lives for the three different surface finishes tested.

Highly Accelerated Life Test and HASS test methodologies were developed for Pb-free soldered assemblies to provide another alternative reliability assessment tool for understanding reliability failures in board-level soldered assemblies.

Thermal aging studies for isothermal, thermal cycling, and thermal shock exposure on IMC growth behavior has contributed new finding on faster IMC growth rates for Thermal shock loading compared to thermal cycling and isothermal aging. A framework for correlating the IMC growth behavior for TS and TC to isothermal aging behavior was proposed [19].

References

1. Tummala RR (2001) Fundamentals of microsystems packaging. McGraw Hill, New York
2. Lau JH (1993) Thermal stress and strain in microelectronics packaging. Van Nostrand Reinhold, New York
3. Suhir E (2002) Accelerated life testing (ALT) in microelectronics and photonics: its role, attributes, challenges, pitfalls, and interaction with qualification tests. J Electron Packaging 124:281–291
4. Nelson W (1990) Accelerated testing: statistical models, test plans, and data analyses. Willey, New York
5. Norris KC, Landzberg AH (1969) Reliability of controlled collapse interconnections. IBM J Res Dev 13:266–271
6. Lau JH, Pao YH (1996) Solder joint reliability of BGA, CSP, flip chip, and fine pitch SMT assemblies. McGraw-Hill, New York
7. JEDEC Standard (2000) JESD22-A104-B, Temperature Cycling. July 2000
8. JEDEC Standard (1995) JESD22-A106-A, Temperature shock. April 1995
9. Microelectronics packaging material database, Purdue University, Center for Information & Numerical Data Analysis & Synthesis (CINDAS)
10. ANSYS User Manual (V7.0) (2000). Singapore, 2002
11. Wiese S, Schubert A, Walter H, Dudek R, Feustel F, Meusel E, Michel B (2001) Constitutive behavior of lead-free solders vs. lead-containing solders – experimentals on bulk specimens and flip chip joint. Proceedings of 51st ECTC, Las Vegas, Nevada, May 2001
12. Wiese S Wolter K-J (2003) Microstructure and creep behavior of eutectic SnAg and SnAgCu solders. Proceedings of 4th EuroSime, Aix-en Provence, France, April 2003

13. Kanchanomai C, Yamamota S, Miyashita Y, Mutoh Y, McEvily AJ (2002) Low cycle fatigue test for solders using non-contact digital image measurement system. Int J Fatigue 24:57–67
14. The American Society for Testings & Materials Standards, ASTM E606: Standard practice for strain-controlled fatigue testing
15. Pang J, Schubert A (2002) Lead free solder materials and reliability performance. 4th Electronic packaging technology conference Short course, Grand Copthorne Waterfront Hotel, Singapore, 10 Dec 2002
16. Pang JHL, Low TH, Xiong BS, Che FX (2003) Design for reliability (DFR) methodology for electronic packaging assemblies. Proceedings of 5th EPTC conference, Singapore, 10–12 Dec 2003, pp 470–478
17. Pang JHL, Low TH, Che FX (2004) Lead free 95.5Sn-3.8Ag-0.7Cu solder joint reliability analysis of Micro-BGA assembly. Proceedings of ITherm 2004 conference, Las Vegas, June 1–4, 2004
18. Pang JHL, Yeo A, Low TH (2004) Lead free 95Sn-3.5Ag flip chip solder joint reliability analysis. Proceedings of ITherm 2004 conference, Las Vegas, June 1–4 2004
19. Pang JHL, Xu L, Shi XQ, Zhou W, Ngoh SL (2004) Intermetallic growth studies on Sn-Ag-Cu lead-free solder joints. Invited paper, TMS annual meeting, 15–18 March 2004, Phase stability, phase transformation, and reactive phase formation in electronic materials III. J Electron Mater

Chapter 7
Dynamic Mechanical Reliability Test and Analysis

Abstract Chapter 7 focuses on vibration and drop impact test investigation. Experimental testing and FEA of the vibration mode and frequency for clamped–clamped PCB assemblies were compared. Constant amplitude vibration fatigue tests were conducted for the FCOB assemblies and test data were developed for 3G, 5G, and 10G respectively. Variable amplitude vibration fatigue tests for an increasing block loading of 3G-to-5G-to-10G repeated loading was conducted to develop cumulative damage index (CDI) vibration fatigue analysis methods using board-level fatigue data and solder material-level fatigue data. The Global–Local Sub-modeling technique developed was used in a quasi-static vibration fatigue analysis method for predicting the vibration fatigue life of the block loading test results. Impact drop testing is increasingly employed by many electronic product manufacturers to evaluate the product reliability to accidental or repeated drop events. Impact drop test and solder joint reliability investigations for Pb-based and Pb-free soldered assemblies were investigated. Explicit dynamic FEA modeling and simulation of the board-level drop test were used to predict the transient vibration deformation and acceleration from the drop test result. Dynamic stress strain analysis of the solder joints reveals fairly high plastic strain range generated and fatigue life prediction confirms the low cycle fatigue failure mechanism.

Electronic products are subjected to vibration loading during transportation and handling operations. The vibration loads are generally very low and screening vibration tests on a sample of the product are routinely conducted. However, for high reliability electronic applications, where the electronic soldered assemblies are mounted on an automotive, military, or aircraft moving platform, vibration fatigue tests are required. Another challenging reliability problem for soldered electronic assemblies is in the portable electronics sector (i.e., hand phone), where design for reliability against accidental drops is a highly competitive selling point. Drop impact tests are often conducted to study the drop-induced failures in soldered board-level assemblies and product level. In this chapter, vibration, drop test, and analysis for board-level soldered assemblies are reported.

J.H.L. Pang, *Lead Free Solder: Mechanics and Reliability*,
DOI 10.1007/978-1-4614-0463-7_7,

7.1 Vibration Test and Analysis

Electronic equipment can be subjected to many different forms of vibration loading over a wide frequency range and acceleration levels [1]. The simplest form of periodic motion is harmonic motion, which is usually represented by a continuous sine wave on a plot of displacement versus time, and this type of vibration is often selected for testing electronic equipment. For vibration analysis, vibration mode and natural frequency of the vibrating body must be determined. The first harmonic mode often has the greatest displacement amplitude and usually the greatest displacement-induced stresses. Vibration-induced stress can usually lead to fatigue failure for electronic assemblies. Vibration fatigue failure of solder joints is often assessed for reliability using high cycle fatigue model, which is represented by an *S–N* curve. A specimen *G–N* curve, acceleration versus fatigue life, was determined based on vibration test results. Modal analysis using FEA for surface-mounted components on a printed circuit board (PCB) was conducted [2]. Model analyses using different models were performed. Two-level global-local modeling approach [3–5] gave accurate results compared to test results. The analyses by Basaran [6, 7], Chandaroy [8] and Zhao et al. [9] show that solder joints respond elastically mainly at room temperature vibration loading.

A flip chip on board (FCOB) assembly was selected for vibration test to analyze the dynamic response of the FCOB to sinusoidal vibration. The specimen and chip number are shown in Fig. 7.1. Six larger flip chip modules of 8.5 × 8.5 × 0.65 mm ($L \times W \times H$) silicon die with 388 I/Os and six smaller flip chip modules of 3.5 × 3.5 × 0.65 mm ($L \times W \times H$) silicon die with 48 I/Os were mounted on the PWB assembly, which is made of FR-4 of 185 × 150 × 1.13 mm ($L \times W \times H$) in size. The solder joints are eutectic 63Sn/37Pb solder with a diameter of 0.16 mm, ball pitch of 0.35 mm, and standoff height of 0.1 mm. A total of four test boards were tested to different acceleration levels to assess the reliability of FCOB assembly subjecting to constant G-level and block G-level loading. Board 1 for varying amplitude test, including 3G, 5G, and 10G (G is gravity acceleration) blocks, Board 2, 3, 4 for constant 3G, 5G, 10G level vibration tests, respectively.

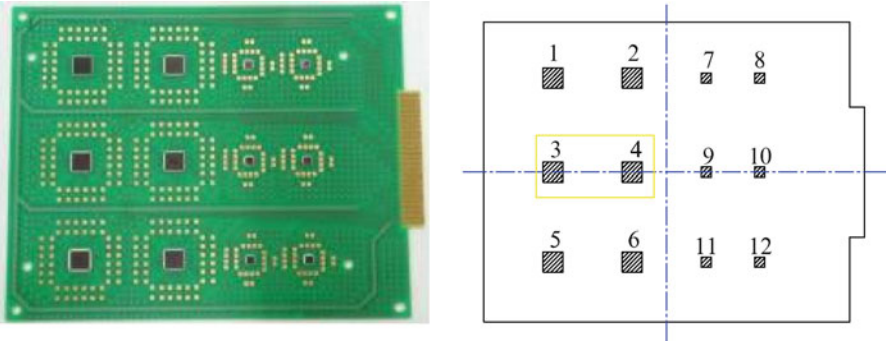

Fig. 7.1 FCOB assembly schematics and silicon chip number

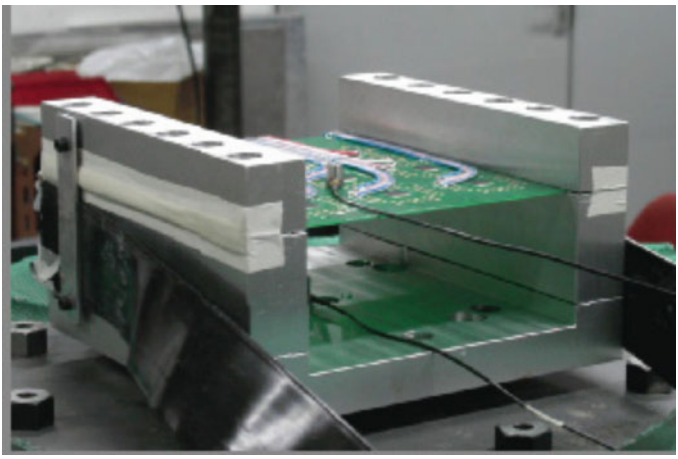

Fig. 7.2 Setup of the vibration test

Vibration tests of specimens were accomplished by using electrodynamic shaker and vibration control software. Two accelerometers were used in the test to determine the dynamic response of the specimen subjected to vibration, one for fixture and the other for PWB, thus the vibration transmissibility of the PWB can be determined when evaluated at different acceleration levels. In order to minimize the effect of the accelerometer's mass on the specimen, a miniature accelerometer (2 g of mass) was adopted. The specimen was clamped along two long opposite sides using aluminum fixture, which was bolted to the shaker header. This gives a clamped–clamped boundary condition for the specimen. The resistance change of the connecting loops to the solder joints was used to determine the failure of the solder joints. There are three loops for each larger flip chip, except for chip 6, with outer, middle, and inner loops. There is only one outer loop for each smaller chip and chip 6. A total of 22 loops were monitored simultaneously by the monitoring device called the Event Detector during vibration test. The threshold of the Event Detector was preset before the test. Any resistance change exceeding a preset threshold with minimum duration of 0.1 μs can be detected by the Event Detector. In general, 50% increase of resistance was used as a rule to determine the threshold setting. Figure 7.2 shows the setup of the vibration test.

The resonance frequency-scanning test was conducted first with sweep sine from 20 Hz to 1,000 Hz. The first order natural frequency of 194 Hz is determined by scanning test. The transmissibility of the specimen can be estimated using the following formula

$$T = \frac{G_{out}}{G_{in}}, \tag{7.1}$$

where G_{out} is the maximum acceleration measured at the center of the specimen, and G_{in} is the acceleration amplitude of the sinusoidal excitation.

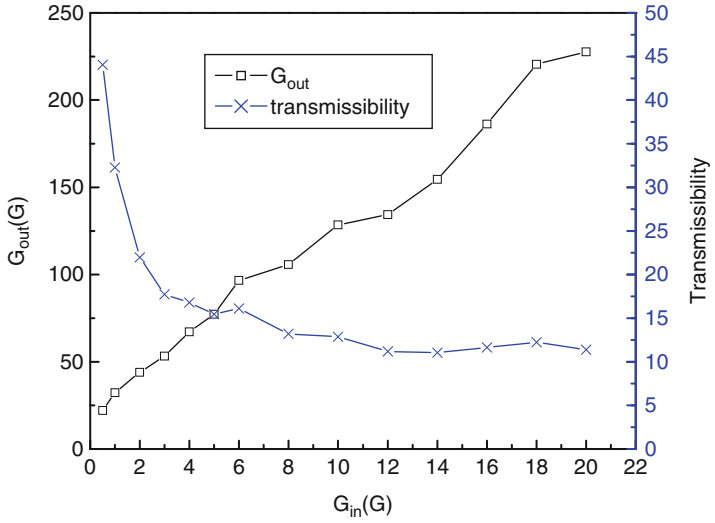

Fig. 7.3 Nonlinear relationship between G_{in} and G_{out}

According to Meirovitch [10], for a linear vibration system, its transmissibility should remain constant regardless of the any change in the input. However, the varying transmissibility, T, at different acceleration input was observed in test as shown in Fig. 7.3. The FCOB assembly under the out-of-plane sinusoidal excitation is not a linear vibration system. Yang et al. [11] showed that the PBGA assembly under out-of-plane vibration has similar nonlinear vibration effect.

The sweep frequency range was 10% around the fundamental resonance frequency, that is, from 175 to 215 Hz. For the varying block G-level vibration test, 3G, 5G, 10G level vibration tests were conducted in turn for each acceleration level of 5 h for same specimen. Constant G level vibration tests at 3G, 5G, and 10G were conducted for 200, 100, 36 h, respectively. Resistance change larger than 50% of initial resistance would be considered as a failure and recorded by the Event Detector, which continuously monitored the resistance of each daisy chain loop. The vibration cycles to failure were calculated based on the failure time recorded by the Event Detector and the average frequency of the sweep sinusoidal excitation. The test results for outer chains on the large chips are given in Fig. 7.4 and satisfy two-parameter Weibull distribution well. No failure results were obtained for the small chips components.

Table 7.1 shows the Weibull parameters together with the MTTF and first time to failure (FTTF) for three different G level tests. It can be seen from the table that the fatigue life reduces rapidly with increase of sinusoidal vibration acceleration amplitude.

From test results, a plot of G-level versus fatigue life can be obtained as shown in Fig. 7.5. In log-log scale, the liner relationship is clear. The fatigue model can be obtained based on G_{in}–N curve for FCOB assembly used in this study as expressed in the following equation

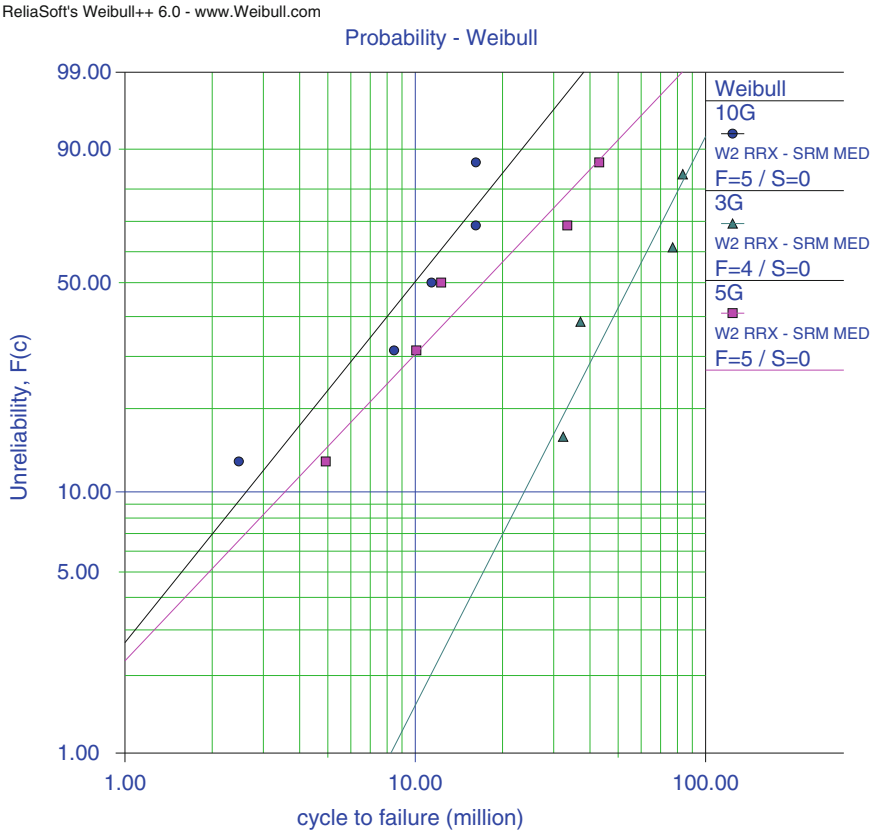

Fig. 7.4 Weibull plots of test results for different G_{in}

Table 7.1 Weibull parameters, MTTF and FTTF

G_{in}	$\eta(10^6)$	β	MTTF(10^6)	FTTF(10^6)
3G	65.30	2.22	57.84	32.30
5G	23.28	1.20	21.91	4.93
10G	12.89	1.41	11.73	2.47

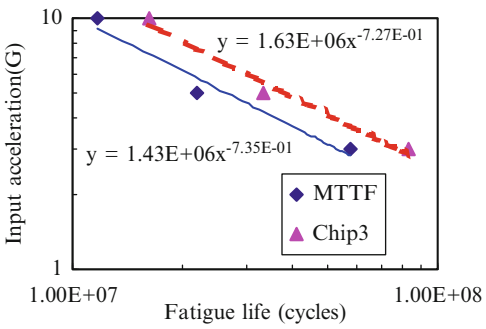

Fig. 7.5 Plot of input G-level versus fatigue life

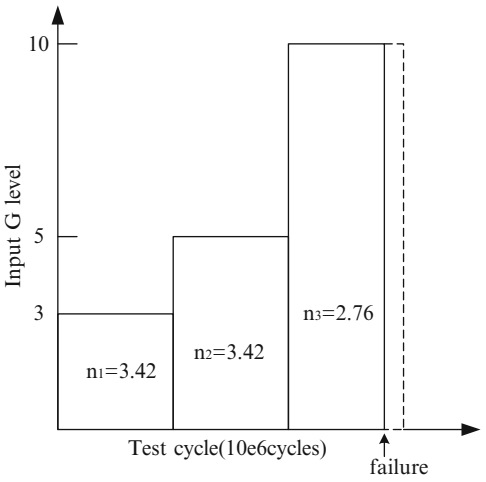

Fig. 7.6 Schematic of block G-level test for chip 3

$$\begin{aligned} A &= 1.43\mathrm{e}^6 N^{-0.735} \text{ for } MTTF \\ A &= 1.63\mathrm{e}^6 N^{-0.727} \text{ for chip 3,} \end{aligned} \tag{7.2}$$

where A is input, G, N is fatigue life. Therefore, (7.2) can be used to predict fatigue life of FCOB assemblies subjected to different G-level input vibration tests.

For the electronic assembly subjected to different blocks of acceleration level (G-level) vibration test, the fatigue damage due to each acceleration level can be superimposed using the linear superposition method by Miner's law [12]. Miner's cumulative fatigue damage ratio is based on an analysis method that sums up the ratio of the actual number of fatigue cycles (n) accumulated in a specific element, in different environments, divided by the number of fatigue cycles (N) required to produce a fatigue failure in the same specific element in the same environment. When the ratios are added together, a sum of 1.0 or greater means that the fatigue life has been used up and should fail. The cumulative damage index (CDI) using Miner's cumulative damage law, assuming a linear summation given by

$$\mathrm{CDI} = D_{\text{total}} = \sum_{i=1}^{n} \frac{n_i}{N_i} \tag{7.3}$$

Failure is assumed to occur at a more conservative value, such as $D_{\text{total}} = 0.7$. For the varying G-level test, chip 3 and 4 were selected for the CDI analysis. The values of n_i are obtained from the varying G-level test result as shown in Fig. 7.6 for chip 3 and Fig. 7.7 for chip 4 while N_i values are equal to MTTF shown in Table 7.1. Substituting the data shown in Figs. 7.6 and 7.7 into (7.3), the CDI can be obtained:

$$\mathrm{CDI}_{\text{chip3}} = \frac{n_1}{N_1} + \frac{n_2}{N_2} + \frac{n_3}{N_3} = \frac{3.42}{57.84} + \frac{3.42}{21.91} + \frac{2.76}{11.73} = 0.451$$

$$\mathrm{CDI}_{\text{chip 4}} = \frac{n_1}{N_1} + \frac{n_2}{N_2} + \frac{n_3}{N_3} = \frac{6.84}{57.84} + \frac{6.84}{21.91} + \frac{3.65}{11.73} = 0.742$$

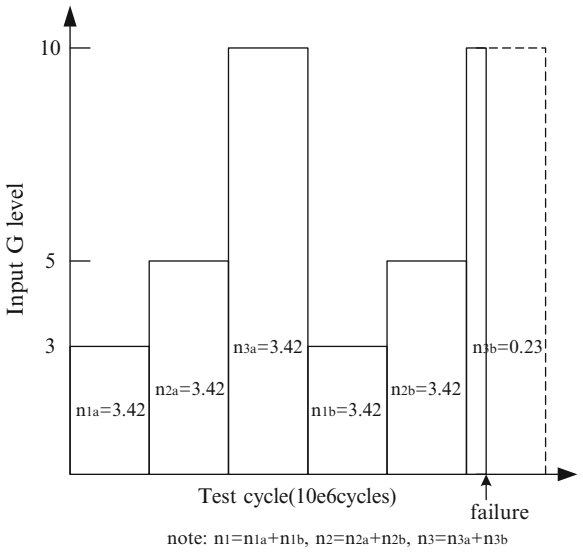

Fig. 7.7 Schematic of block G-level test for chip 4

From CDI values for chip 3 and 4, when the CDI was 0.451 and 0.742 for outer chain of chip 3 and 4, the failure occurred in these two chips, respectively. Using the CDI of unity is unconservative and a safety factor of 3 is recommended.

7.2 Finite Element Analysis for Vibration Test

Because the natural frequencies and mode shapes are very important parameters in the design of a structure for dynamic loading conditions, modal analysis to determine these parameters was conducted firstly. PWB was modeled as shell element in FE modal analysis. The clamped–clamped boundary condition was simulated according to the testing condition. First, the bare PWB without Flip Chip components attached was simulated for modal analysis to study the different variables effect such as material properties, element size. The FE model of the bear PWB is shown in Fig. 7.8. Table 7.2 shows the natural frequency results of first three modes for bare PWB when considering different variables. The element size has a very slight effect on the natural frequency of the bare PWB. In the subsequent analysis, the 5 × 5 mm shell element size was used. Actually, the FR-4 PWB has the orthotropic material properties. However, it can be seen from Table 7.2 that the effect of the orthotropic material properties on the natural frequencies is very slight so that the effect can be neglected.

In order to verify that a good approximation of PWB modal response can be made by considering the PWB as a bare unpopulated thin plate, four detailed modal analyses were conducted. In case 1, the Flip Chip components mounted on the PWB were modeled as distributed masses on the PWB. In case 2, the Flip Chip

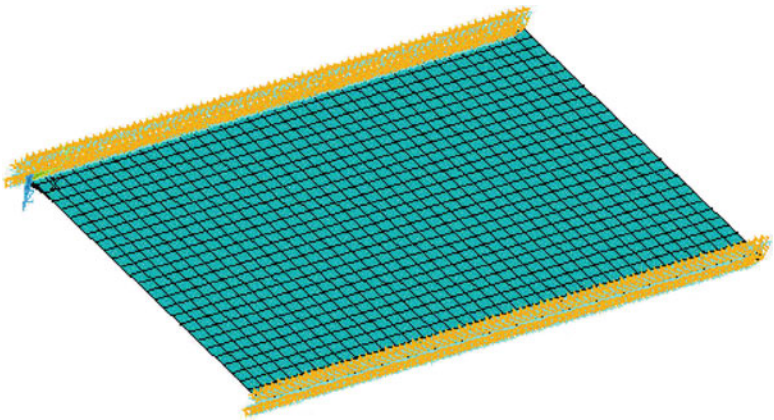

Fig. 7.8 Finite element model of bare PWB

Table 7.2 Natural frequency for bare PWB modal analysis

No.	E (GPa)	v	f1	f2	f3	Element size (mm × mm)
1	22	0.28	208	232	324	2.5 × 2.5
2	22	0.28	208	232	323	5 × 5
3	22	0.28	208	232	322	7.5 × 7.5
4	22	0.28	208	232	322	10 × 10
5	$E_x = 22$ $E_y = 22$ $E_z = 10$	$v_{xy} = 0.28$ $v_{yz} = 0.11$ $v_{zx} = 0.12$	208	232	322	5 × 5

components were modeled as concentrated masses at the center locations of the components on the PWB. In case 3, the Flip Chip components were modeled as solid part of the pure chip without considering the effects of the solder joint and underfill. In case 4, the IC chips were modeled as shell and the solder joints were modeled as effective two-node beam elements with equivalent stiffness of solder joint [5]. According to Steinberg [1], the fundamental resonance frequency for a PWB with the Clamped–Clamped boundary condition can be obtained from the following equation

$$f_n = \frac{3.55}{a^2}\sqrt{\frac{D}{\rho}}, \tag{7.4}$$

where

$$D = \frac{Eh^3}{12(1-\mu^2)}, \quad \rho = \frac{\text{Mass}}{\text{Area}},$$

$E = 22{,}000$ N/mm^2, (Young's modulus),
$\mu = 0.28$, (Poisson's ratio),

Table 7.3 Comparison of the natural frequencies results

Mode	Bare PWB	Case 1	Case 2	Case 3	Case 4	Eq. (7.4)	Test
1	208	206	206	209	201	209	194
2	232	231	231	234	213		
3	323	321	321	326	272		

$h = 1.13$ mm, (thickness of the PWB),
$a = 140$ mm, (free side length of the PWB), and
$\rho = 2.147$ kg/m$^{2.}$

Table 7.3 shows the first three order frequencies of the PWB obtained from different methods. The frequencies obtained from case 1 and case 2 were slightly less than those from bare PWB because only the masses increased for the PWB while the stiffness did not change for PWB. It can be seen from Table 7.3 that the results of modal analysis have a good agreement among FEA, test and theory. Therefore, for PWB with Flip Chip assembly, a good approximation of PWB modal response can be made by considering the PWB as a bare unpopulated thin plate. The increase in stiffness of PWB due to the mounting of the components is offset by the increase in total mass the populated PWB. The same approximation can introduce more error for PWB with BGA assemblies because the contribution of the masses and stiffness of the BGA modules for PWB could not be ignored as the BGA modules have the larger volume and mass compared with Flip Chip modules. The first natural frequency obtained by case 4 has better agreement with the testing results.

A quasi-static analysis method was developed to calculate the stress strain behavior of the solder joints, which can be used for fatigue life prediction using high cycle fatigue model. The dynamic loading due to vibration was replaced by effective static loading in this method. According to Newton's second law, the pressure acting on the PWB or component can be obtained

$$p = \frac{F}{A} = \frac{mG_{\text{out}}}{A} = \frac{\rho v G_{\text{out}}}{A} = \rho t G_{\text{out}} g, \tag{7.5}$$

where m, ρ, v, A, t are mass, density, volume, area, thickness of PWB, or chip i, respectively. G_{out} is output acceleration in G (acceleration of gravity).

For constant G-level test, the pressure loading can be obtained from (7.4) and (7.5) when transmissibility is known. It is observed that transmissibility is not a constant value along transverse locations. The transmissibility was measured only for half of the PWB due to symmetry. Eight locations uniformly distributed shown in the Fig. 7.9 were selected to measure transmissibility of the PWB subjected to vibration. Figure 7.10 shows the transmissibility result for different locations at fundamental resonance frequency for 10G input test, and that a linear relationship between transmissibility and location is clear.

Sub-modeling technique was used in this quasi-static analysis because it is difficult to take board level simulation using full 3D model. Figure 7.11 shows the brief procedure for sub-modeling technique. For the whole model, only two

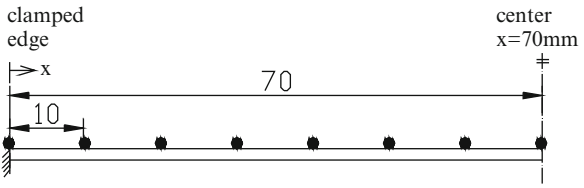

Fig. 7.9 Schematic of the location of the measured point

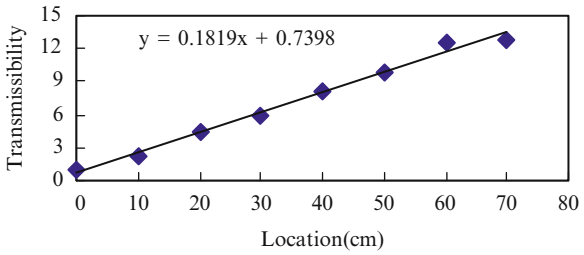

Fig. 7.10 Transmissibility at natural frequency for 10G test

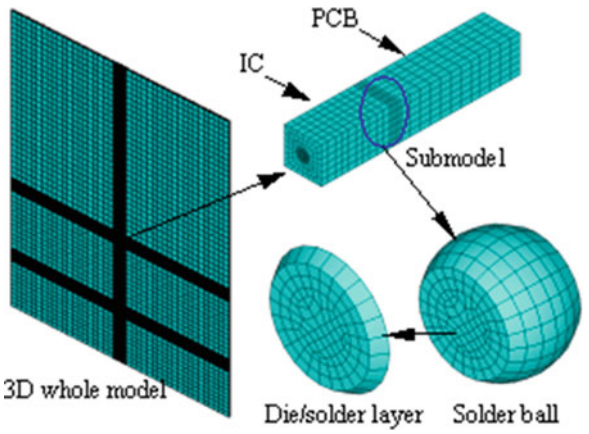

Fig. 7.11 Sub-modeling technique for vibration stress analysis

large chips numbered 3 and 4 shown in Fig. 7.1 distributed on center of PWB were selected and clamped–clamped boundary condition along two opposite longer sides was used. Elastic-plastic analysis for solder joint was used and no plastic strain occurs from result. The stress strain distribution for two chips was almost same, so only chip 3 was used for analysis. The outmost corner solder joint has the maximum stress, which means the first failure will occur in the outmost corner solder joint. Thus, sub-model was used to simulate the outmost solder joint. The stress-based high cycle fatigue approach was used to predict the fatigue life of component as shown below:

$$\sigma_{\mathrm{a}} = \sigma_{\mathrm{f}}{}'(2N_{\mathrm{f}})^{b}, \tag{7.6}$$

where σ_a = stress amplitude,

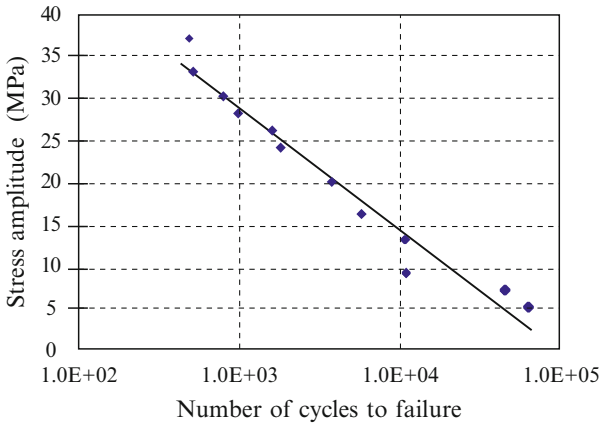

Fig. 7.12 High cycle fatigue S-logN curve for solder [13]

σ_f' = fatigue strength coefficient,
b = fatigue strength exponent, and
$2N_f$ = reversals of failure (1 reversal = 1/2 cycle).

For eutectic Pb/Sn solder, the material constant σ_f' and b can be determined by curve fitting shown in Fig. 7.12 using testing data by Yao et al. [13] and they are 177.1 MPa and −0.2427, respectively. For multi-axes stress situation, the equivalent von Mises stress is used to output the state of stress in the solder joint.

$$\sigma_{\text{eff}} = \frac{1}{\sqrt{2}}\sqrt{(\sigma_1 - \sigma_2)^2 + (\sigma_2 - \sigma_3)^2 + (\sigma_3 - \sigma_1)^2} \tag{7.7}$$

In order to minimize the effect of stress concentration, the volume-weight method was used to calculate the equivalent von Mises stress for the die/solder interface layer in which the failure commonly occurs first for FCOB assembly. Volume-weight average stress can be obtained by

$$\sigma_{ave} = \frac{\sum \sigma \cdot V}{\sum V} \tag{7.8}$$

Then fatigue life can be determined by (7.8) when stress amplitude was known. The frequency range from 175 to 215 Hz was used for vibration test. Different transmissibility occurs at different frequencies as shown in Fig. 7.13. Therefore, specimen was subjected to different effective pressures with different slop triangle distribution at utmost location during test. Miner's law shown in (7.3) was used and fatigue life can be predicted combining with (7.6). In this study, CDI of 0.5 was used. The fatigue life result comparisons between quasi-static method and testing for chip 3 are listed in Table 7.4. It can be seen that the quasi-static can give reasonable fatigue life prediction result compared to testing result, especially for lower G-level vibration test. By imitating *S–N* curve, the *G–N* curve can be

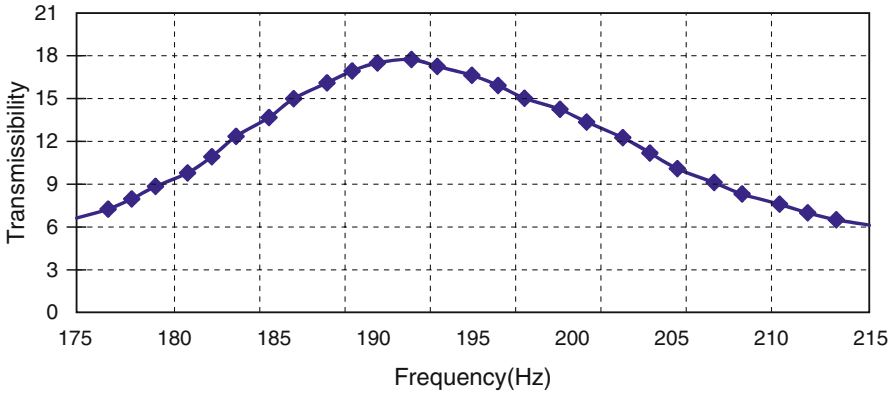

Fig. 7.13 Transmissibility versus frequency for 3G test

Table 7.4 Fatigue life comparisons for chip 3

G level	Test (1)	Prediction (2)	Factor (2/1)
3	8.34E + 07	1.10E + 08	1.32
5	3.34E + 07	2.57E + 07	0.77
10	1.62E + 07	2.61E + 06	0.16

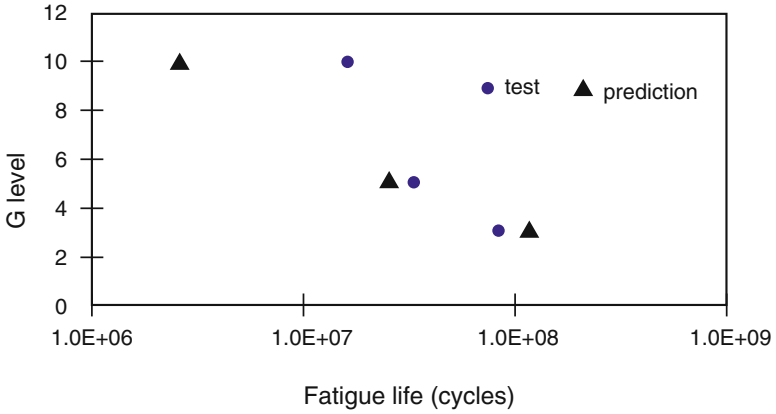

Fig. 7.14 G-N curve for different methods

obtained based on fatigue life result for different G-level test as shown in Fig. 7.14. Different CDI values were used to predict the flip chip solder joint fatigue life in order to investigate the CDI effect. The factor is defined as the ratio of fatigue cycles predicted by FEA to experimental fatigue cycles. Different factors corresponding to four CDI values of 1, 0.7, 0.5, and 0.33 were calculated and shown in Fig. 7.15. It can be seen that fatigue life prediction has a good agreement with test data for 5G vibration test.

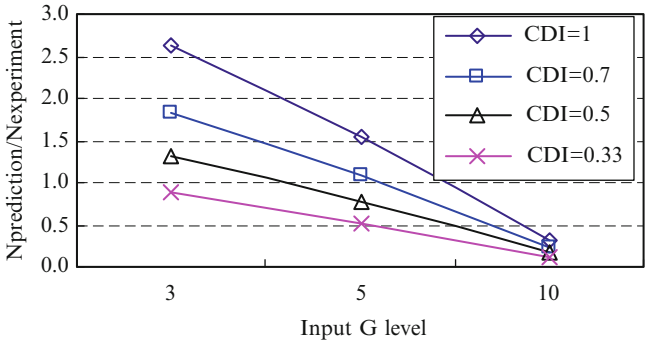

Fig. 7.15 CDI effect on fatigue life prediction

7.3 Drop Impact Test and FEA Modeling

Portable electronic devices like personal digital assistant (PDA) and mobile hand phone have to be designed to withstand drops. In these devices, flip chips are widely used to reduce weight and mounting size. Impact and drop studies of flip chip solder joints reliability are emerging research interests. The flip chip solder joints are subjected to operating conditions and accidental drop causing short-time stress from impact loading. Drop tests are often substituted in qualification testing of microelectronic devices by shock tests. In order to adequately mimic the drop test conditions, a short-term external acceleration is applied and should be well below the fundamental period of system's free vibrations. Otherwise, the response of the system can result in substantially higher curvatures and accelerations than that occurring during drop tests [14]. In the drop test, the measured maximum acceleration is often used as a criterion of the strength of structure in microelectronic products. The maximum acceleration of PCB board can reach to more than 1,000G when subjected to drop impact, but the displacement and strain of the PCB is relatively small. It is well known, however, that it is the maximum stress, not the maximum acceleration, which is responsible for the dynamic strength of a structure [15]. The dynamic reliability of portable electronic equipment relates to several external and product factors, which affect the forces and accelerations during impact [16] drop height, housing material, weight, shape, orientation at impact, and surface onto which it drops. Most drop heights used in the industry are 1 and 1.5 m. Yu et al. [17] show that the horizontal impact case of PCB is the most dangerous case for reliability of solder joints. The first order mode vibration is more dominant in dynamic fracture of solder joints than higher modes. There are mainly three types of drop tests in the electronic industry: (1) free fall product level; (2) free fall board level; and (3) controlled pulse drop at board level. Board level drop test is convenient to characterize the solder joint performance, as it is more controllable than product level drop test. Some researchers [18–20] have conducted board level drop tests to understand the response of solder joint to impact loading.

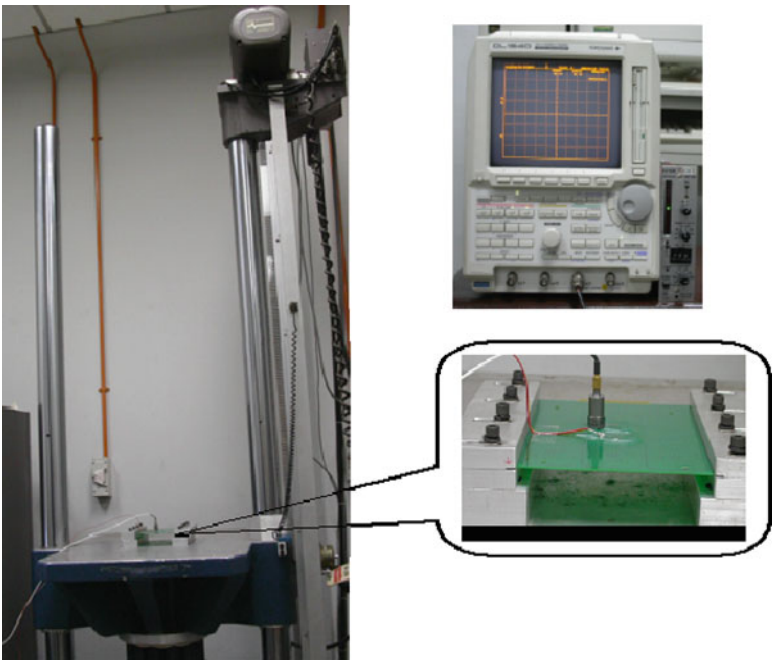

Fig. 7.16 Drop test setup and fixed specimen

Some researchers [21, 22] have conducted product level drop tests due to real drop events. In this study, free fall board level drop test was conducted.

In this study, FCOB assembly shown in Fig. 7.2 was selected for drop test to analyze the dynamic response of the FCOB to drop impact loading. The Lansmont Model 65/81-shock test machine is used to provide the free-fall drop test of board-level mounted with the flip chip packages. This machine can provide two types of shock pulse: half sine pulse and trapezoid pulse. The half sine pulse will be chosen for the excitation of the impact. The acceleration level of the half sine pulse is related to the drop height and mount of the felt pads. The duration of the pulse is adjustable, somewhat, by the addition or subtraction of the felt pads. The drop machine and specimen are shown in Fig. 7.16.

The drop table is an aluminum weldment with an assembled mass of approximately 190.5 kg. It has a 650 × 810 mm top-mounting surface, which is drilled and fitted with threaded inserts for test specimen mounting. The specimen of PCB with flip chip packages is attached to a metal table through aluminum fixture shown in Fig. 7.16. During impact, the longitudinal stress wave will travel in the table, when the wave travels into the PCB, it turns into the bending wave. The propagation velocity of the longitudinal stress wave in the table and fixture can be expressed as [23]

$$C_{\mathrm{L}} = \sqrt{\frac{E}{\rho}}, \tag{7.9}$$

Fig. 7.17 Marks on the specimen and fixture

where E is the Young's modulus and ρ is the density of the material. The velocity of the bending wave in the specimen may be expressed as

$$C_b = \frac{\pi\gamma}{L}, \tag{7.10}$$

where $\gamma = \sqrt{D/\rho_a}$, D is the flexural modulus $Eh^3/12$, h is thickness of specimen, $\rho_a = \rho h$ is the area density of specimen, and L is the length of the free edge.

Usually, in the drop test, impact force, accelerations, drop velocity, and strains are measured. In this test, the strain gages and accelerometer affixed to the surface of the PCB desired location are used to measure the dynamic strain and acceleration of the specimen shown in Fig. 7.17. This specimen has the fundamental frequency of 195 Hz determined by the vibration test, which is equivalent to period of the 5.1 ms.

After every five drop tests, the continuity of the functional daisy chain net was checked using a multimeter. Failure criterion was electrical open of the daisy chain net. During the drop test, a high-speed camera was used to capture the images of the specimen movements. This camera has an ability to record up to 4,500 frames per second for immediate playback so that the image storage of extremely rapid events such as drop can be accurately carried out. Based on the results obtained by the high-speed camera, the position and shape of the specimen can be obtained. Furthermore, the velocities, accelerations, and flections of the specimen can be calculated by using the fundamental data of displacement. Before the drop test, some marks are attached on the specimen, which can make the data recorded easily by high-speed camera, shown in Fig. 7.17. Mark 4 is a reference point attached on the fixture, and Marks 1, 2, and 3 are located on the left side, center point, and right side of specimen edge, respectively.

In the first drop test, four felt pads were placed on the base surface to prevent metal-to-metal impact. The drop height is 1 m. The vertical relative displacements obtained from the high-speed camera are shown in Fig. 7.18. The data for a period of 20 ms were extracted for analysis. These relative displacements represent the displacement differences between the marks on specimen and mark on fixture. It can be seen from Fig. 7.18 that the motion of the specimen during the drop test is similar to the simple harmonic motion and maximum deflection along the specimen occurs at almost the same time, suggesting the existence of a dominant fundamental deformation mode. The vibration displacement range (2 × amplitude) of the center point marked by No. 2 shown in Fig. 7.18 is about 4.9 mm approximately. It can be

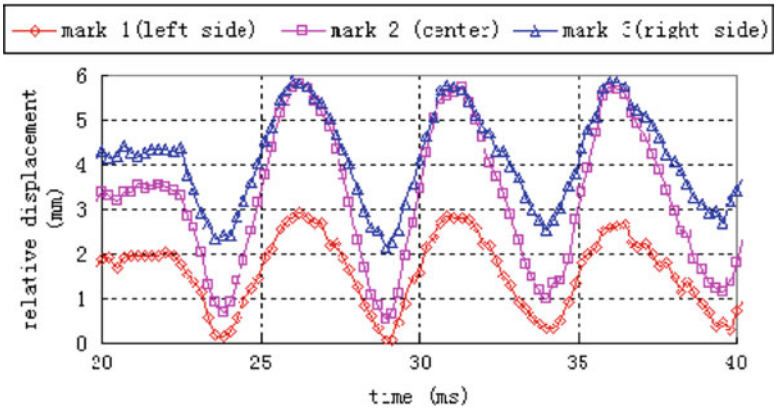

Fig. 7.18 Relative displacement of the specimen (camera)

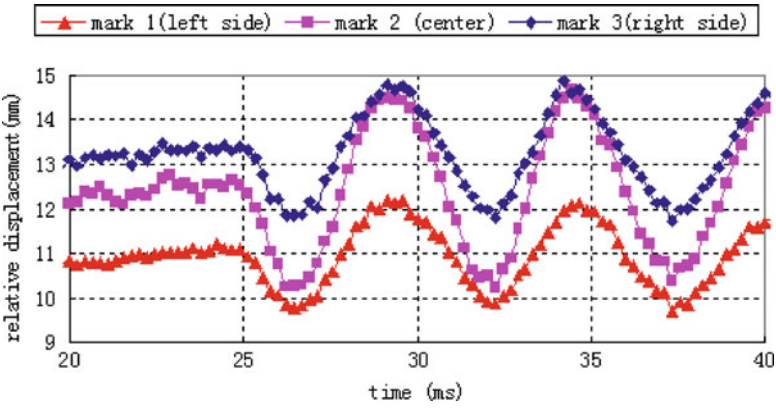

Fig. 7.19 Relative displacement of the specimen with wooden plate on drop base

seen from Fig. 7.18 that the vibration period of the specimen during and after impact is about 5.4 ms. This is equivalent to the frequency of 185 Hz and is close to the theoretical fundamental frequency of the PCB specimen of 195 Hz, for the first vibration mode shape under clamped–clamped condition tested.

A wooden plate was placed above the felt pads in order to vary the effect of the impact surface on the dynamic response of the specimen. The relative displacement of the specimen is shown in Fig. 7.19. The vibration displacement range of the center point of the specimen is equal to 4.4 mm and a vibration period of the specimen is about 5.7 ms. Compared with the results shown in Figs. 7.18 and 7.19, it is obvious that the wooden plate reduces the maximum vibration displacement and increases vibration period of the specimen, thus the maximum acceleration of the specimen will be reduced.

The acceleration of the specimen calculated from the data recorded by high-speed camera is shown in Fig. 7.20. It can be seen that the maximum acceleration occurs at

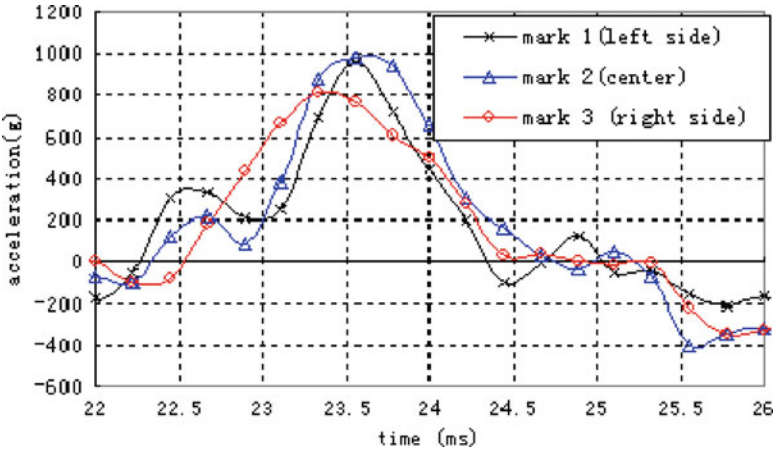

Fig. 7.20 Acceleration of the specimen (camera)

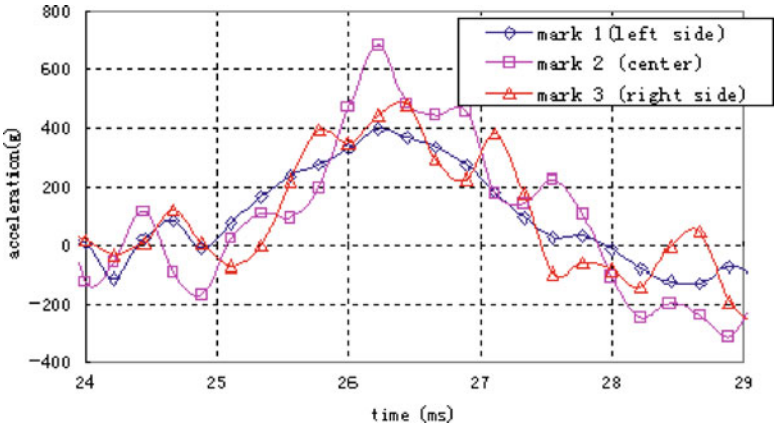

Fig. 7.21 Acceleration of the specimen (accelerometer)

the center of the specimen and the acceleration has a value of 981G. The relationship of the acceleration and time presents a half-sine shape and the duration of the impact is 2.5 ms. In addition, the acceleration can be measured directly by the accelerometer, and the results are shown in Fig. 7.21. Comparison with the results by camera shown in Fig. 7.20 and the accelerometer result in Fig. 7.21, the acceleration of the center point of the specimen has a magnitude of 980G and duration of 2.5 ms. The acceleration of the drop table is also measured during the impact period and is shown in Fig. 7.21. According to (7.9), the stress wave propagation velocity of the table reaches to 5,090 m/s, so the transition of the wave in the table is very fast and impact wave can travel through table to specimen in 0.06 ms. Therefore, the maximum accelerations of the specimen and drop table almost occur in the same

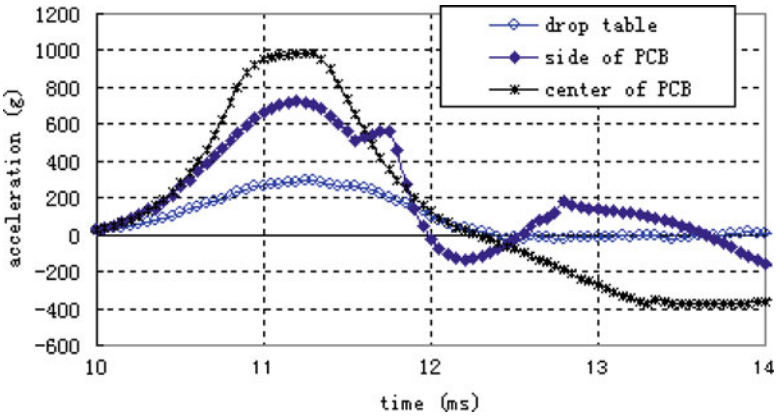

Fig. 7.22 Acceleration of the specimen with wooden plate on drop base

time, as can be validated from Fig. 7.21. It can be seen that the acceleration of the center point of the PCB specimen has a higher G magnitude compared to that of the side of the PCB and the drop table. Note that transient vibration of the PCB specimen continues even after the table approaches a stable state.

Figure 7.22 shows accelerations of specimen when a wooden plate was placed on the drop base. It can be seen that the maximum acceleration reduces to 700G for the center point and half-sine shape has a bigger duration of 3 ms compared with those results shown in Fig. 7.20 without wooden plate. Therefore, the soft drop base would reduce the maximum acceleration during impact and extend the duration of impact.

After more than 30 drops, no failure of solder joint was found based on the resistance measured. The FCOB assembly has good impact drop solder joint reliability performance due to underfill encapsulation. Other SMT assemblies, such as PBGA, CBGA, QFP, and TSOP board level assemblies may not be so resistant to drop impact tests.

The combination of numerical simulation and testing is the best approach to obtain failure analysis to understand the dynamic response of the electronic assembly on impact loading. It is a significant advantage for numerical simulation that it can pick up complete mechanical information at any location of analyzed object. Impact response is a typically transient phenomenon. In transient analysis with FEA, there are two basic algorithms for time integration methods: implicit and explicit methods. ANSYS has a LS-DYNA module for explicit-based problems and was selected for the simulation of the impact problem in this study. It has suitable element type, material model, and contact surface definition capabilities.

In the analysis, the specimen, fixture, table, and impact base are all simulated. The detailed model is shown in Fig. 7.23. Assume a rigid behavior for the drop base and bilinear kinematic hardening plasticity for the table, fixture, and specimen. The table and fixture are modeled using solid element, specimen using shell, and base using rigid shell. Some important information of the element, material properties is listed in the

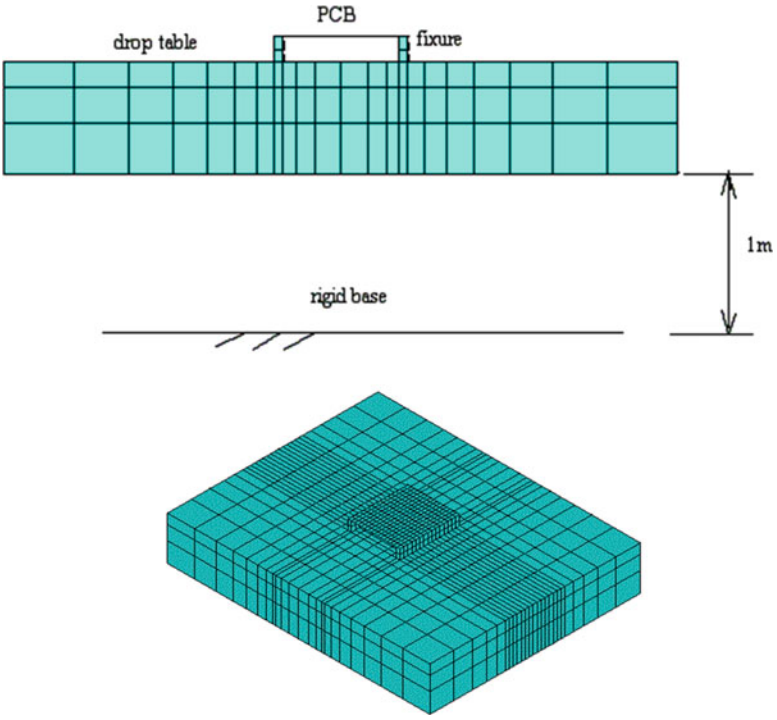

Fig. 7.23 Impact model and meshed fall part

Table 7.5 Element types and material properties of the model

Components	Table and fixture	Specimen	Drop base
Element type	Solid 164	Shell 163	Shell 163(rigid)
Density (kg/m^3)	2,700	1,900	7,800
Elastic modulus (GPa)	70	22	200
Poisson ratio	0.346	0.28	0.25

Table 7.5. A total of 1,921 elements and 2,836 nodes are included in this analysis. The simulation time is 50 ms, and 500 substeps are involved during this simulation period. During the free fall stage, the table and specimen is simply accelerating due to gravity. To save CPU time, apply an initial velocity of 4.43 m/s to simulate the free drop height of 1 m. 4.43 m/s is an approximation derived using $v = \sqrt{2gh}$, where v is the final velocity, g is the acceleration due to gravity, and h is the displacement of 1 m.

In order to interpret the dynamic response of the specimen on the drop test conveniently, some labels are marked in the Fig. 7.24 for specimen shell. Label C presents a central line, which also is a symmetric axis of the specimen shell. Label L1 and R1 present the outmost left line and right line, respectively, and they are symmetric about central line labeled mark C. The line labeled L2, located the middle position between line of L1 and line of C, is symmetric to the line labeled R2 about central line.

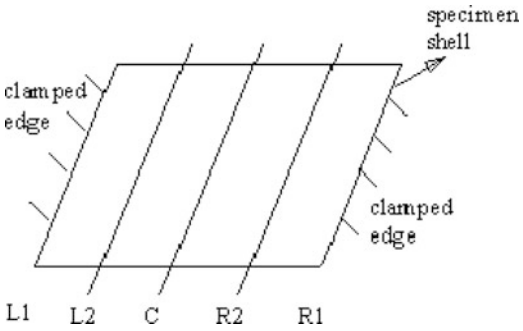

Fig. 7.24 Labels on the specimen

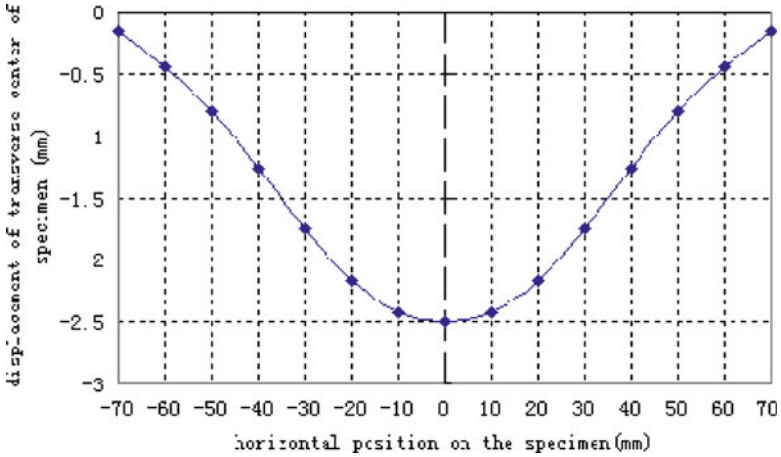

Fig. 7.25 Maximum relative displacement of the specimen

From the results, it was found that the specimen vibrates in the form of first order mode shape, so the displacements, velocities, and accelerations at the symmetric location of specimen have the similar trends and magnitude.

The deformation along the transverse direction of the specimen is shown in Fig. 7.25. It can be seen that the deformation is symmetric about the central line and this deformation shape is consistent with the first vibration mode. The maximum displacement of the center is about 2.5 mm, which agrees well with the result obtained by high-speed camera.

The symmetric deformation of the specimen during drop test can also be validated from the rotational angle shown in Fig. 7.26. It can be seen that the vibration shape of the specimen after impact exhibits the first vibration mode shape. For this type of drop test, we can consider that certain period vibration is induced by the impact force. Thus, drop test problem can be considered a transient vibration problem. It can be seen that the rotation angle decreases with the time increasing

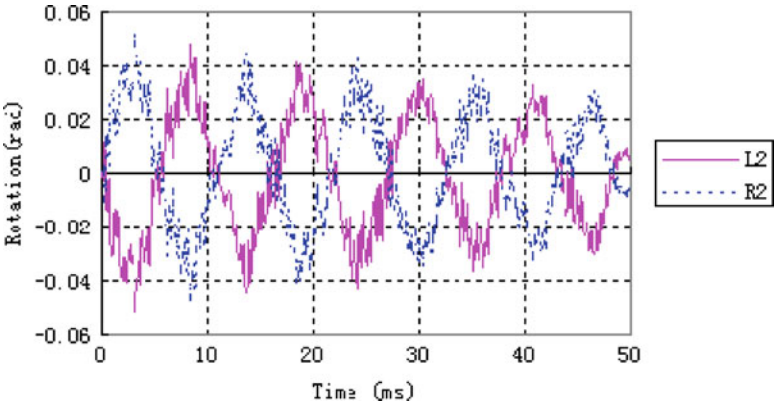

Fig. 7.26 Rotation angle of the specimen about horizontal axis

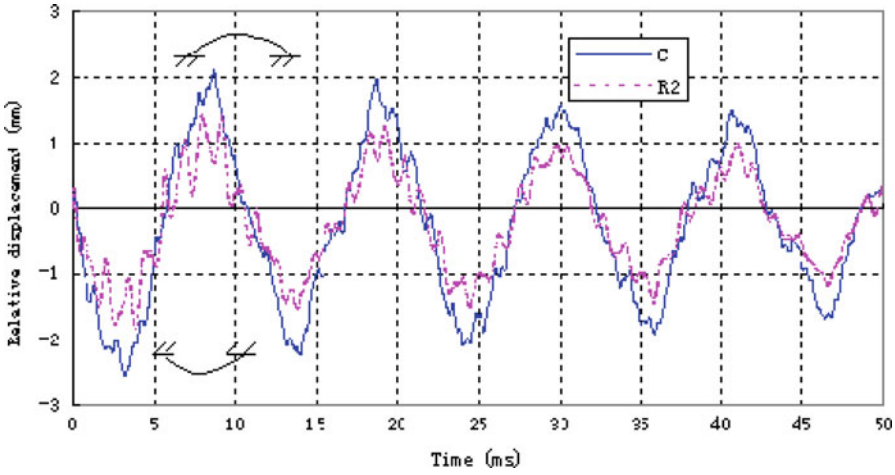

Fig. 7.27 Relative displacement–time relation of specimen

due to air damping. The vibration period of 10 ms can be obtained from Fig. 7.27, which is larger than that from high-speed camera.

The acceleration results of FEA are shown in the Fig. 7.28. The maximum acceleration of the specimen is 1,400G approximately, which is higher than the real maximum acceleration of 980G measured by the accelerometer during the drop test because of the effect of the rigid base used in the FEA. Taking the drop base as a rigid body without considering the effect of the felt pads induces the difference between the measured results and simulation. Further modeling study is needed to obtain more accurate simulation results for acceleration.

The simulation of the drop base as rigid body leads to overestimation of the acceleration at the center of the board compared to the measured response.

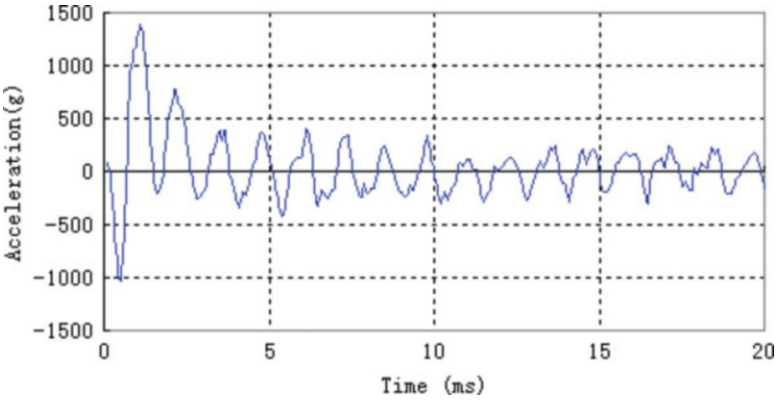

Fig. 7.28 Acceleration–time relationship of the center point on specimen

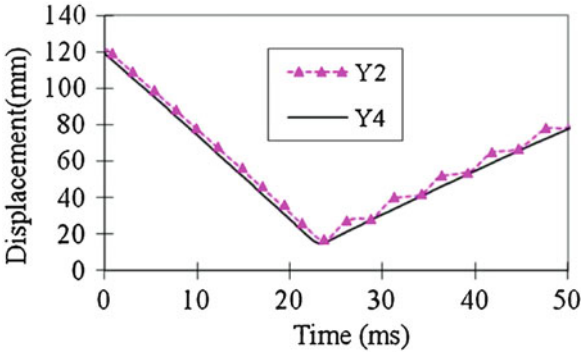

Fig. 7.29 Location of mark 2 and 4 measured by camera

The displacement period of the first transient cycle of the specimen agrees with first order vibration mode frequency for the clamped–clamped board. The vibration amplitude has good agreement with measured result, as the vibration amplitude is less sensitive to drop base impact condition compared to acceleration.

After drop impact, the transient vibration occurs. In order to find the stress strain behavior of solder joint, the component including solder joint must be modeled in FEA simulation. In this study, hybrid model was used to calculate the stress–strain behavior of FCOB solder joints subjected to impact loading. This method simulates the FCOB assembly without considering whole drop table, drop base, and fixture. The displacement of fixture measured by high-speed camera (see Fig. 7.29) was considered as the input boundary condition, applied along the fixed edges of specimen.

Explicit finite element analysis for FCOB assembly was conducted using LS-DYNA. In order to reduce the simulation time, only one large component near the board center numbered 4 was considered and mass scaling technique was used.

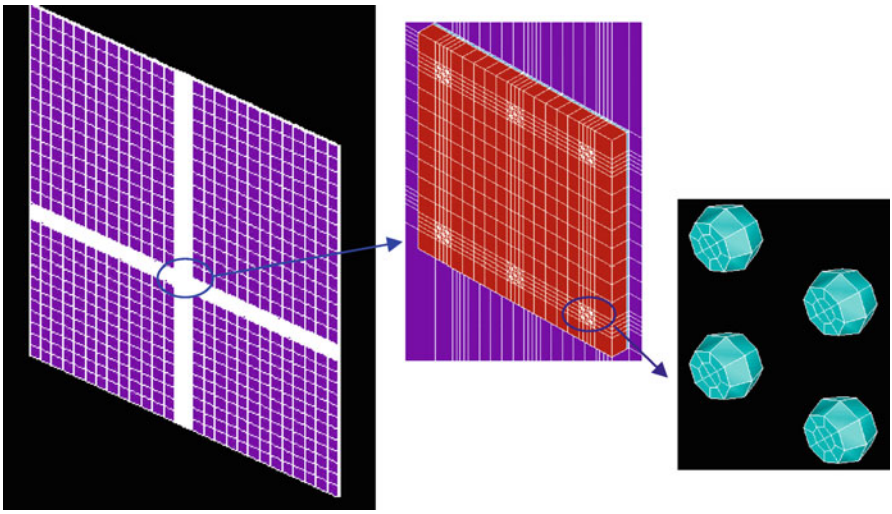

Fig. 7.30 FE model for FCOB assembly

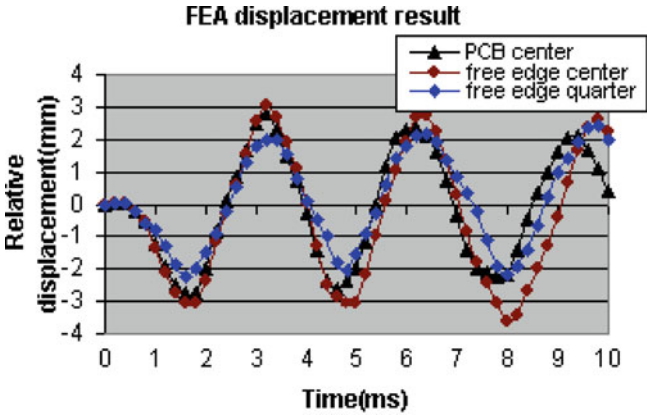

Fig. 7.31 FEA displacement result for drop test

Four different materials are considered in this simulation, including FR-4 PWB board, underfill, eutectic Sn/Pb solder, and silicon chip. Solder material was modeled as bilinear plastic behavior based on data derived from impact testing of solder. Figure 7.30 shows the FEA model for drop test simulation; corner solder balls are simulated in this model due to their critical location.

The displacement FEA result is shown in Fig. 7.31 for three points of PWB center, free edge center, and free edge quarter. Free edge center and free edge quarter in FEA result are corresponded to mark 2 and mark 3, as shown in Fig. 7.17, respectively. Comparing FEA result with testing result, it can be seen the relative displacement amplitude and vibration period has good agreement. Figure 7.32 shows the displacement and acceleration change with time on specimen center.

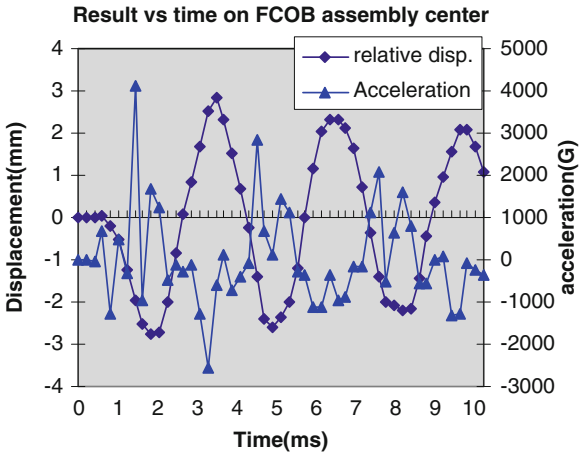

Fig. 7.32 Acceleration, displacement versus time

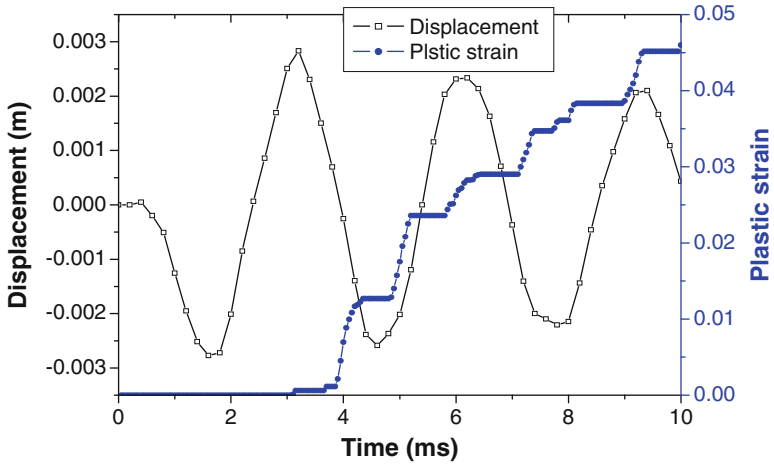

Fig. 7.33 Plastic strain, displacement versus time

It can be seen that the positive acceleration occurs when specimen bends down while the negative acceleration occurs when specimen bends up. The acceleration value calculated from FEA is slightly higher than that from the test result.

Figure 7.33 shows the plastic strain and displacement comparison with respect to time for one critical element of corner solder joint. It can be seen that when PWB first bent down no plastic deformation occurred. When PWB first got its peak bending-up point, plastic deformation occurred. Therefore, from this point, the cyclic plastic strain is calculated, and plastic strain of 0.02764 for first cycle and 0.01692 for second cycle are estimated. The cyclic plastic strain becomes lower with time due to damping.

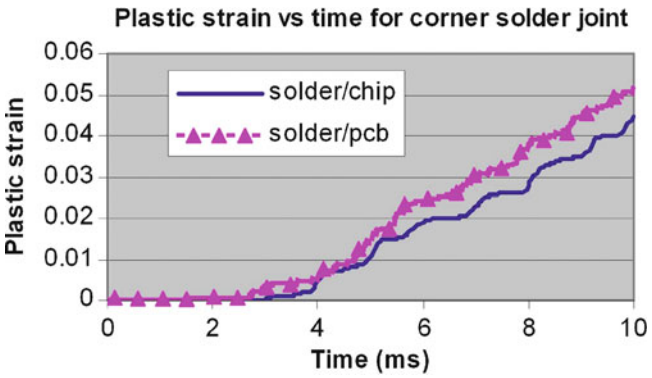

Fig. 7.34 Plastic strains of outmost corner solder joint

The volume-average method for plastic strain was used for the outermost corner elements of the corner solder joint because the plastic strain was very location-dependent. Figure 7.34 shows the volume-average plastic strain for outmost corner solder joint. It can be seen that the plastic strain on the solder/PWB side is more than that on the solder/chip side because PWB board flexure and inertial force have significant effect on solder material deformation near the PWB side while the board flexure effect is slighter for solder material deformation near the chip side than that near the PWB side.

When the plastic strain is obtained, the fatigue life of solder joint can be predicted based on the fatigue failure model such as Coffin–Manson model, which was used for lower cycle fatigue behavior of eutectic solder as shown below:

$$N_{\mathrm{f}}{}^{m}\Delta\varepsilon_{p} = C, \tag{7.11}$$

where C and m are material constants, which can be determined by polynomial expression fitting from temperature-dependent experimental data given by Shi et al. [24]. Using room temperature, $T = 25$, and frequency of 1 Hz obtain $m = 0.727$ and $C = 2.033$. There is a need for a suitable drop fatigue model. Tentatively, the Coffin–Manson model was used for drop fatigue life prediction. A time period of 10 ms was used for drop test analysis to calculate the solder joint drop plastic strain. The plastic strain equal to 0.0512 computed from solder/PWB side as shown in Fig. 7.34. The fatigue life, N_{f}, is equal to 158 drops. This means that after 158 drops from a drop height of 1 m, the solder joint on the FCOB assembly is subjected to plastic strain cycling due to the impact loading and is expected to fail by fatigue.

7.3.1 Drop Test for Pb-Free 95.5Sn–3.8Ag–0.7Cu Soldered Assembly

In this drop test, bare PCB and populated PCB were selected as drop specimens. For populated PCB specimen, one BGA, one QFP, and one TSSOP component are mounted on PCB board. For BGA component, three different surface finishes, such

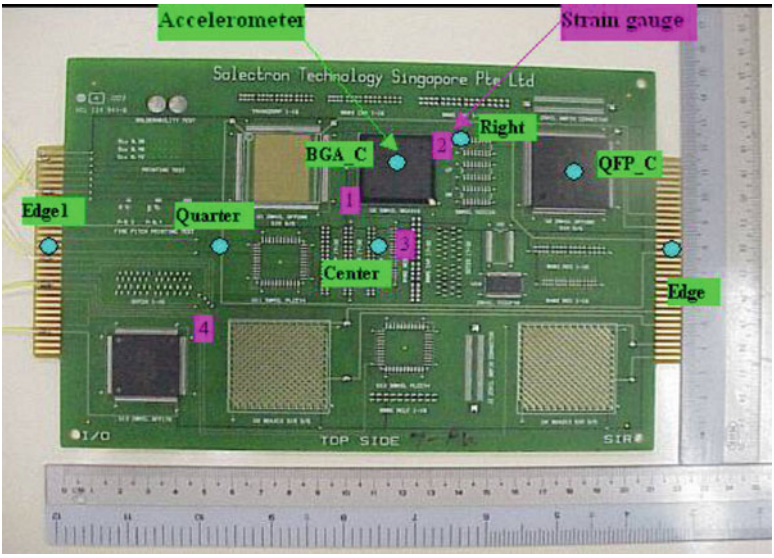

Fig. 7.35 Pb-free solder test board and measurement points

as Ag, Au, and OSP, are used. In the drop test, accelerometers and strain gauges were used to measure the dynamic response of the specimen subjected to drop loading. Figure 7.35 shows the locations of measurement. For bare PCB drop test, all four strain gauges were used, accelerations just on center and right location were measured, and four different drop heights were selected. For populated PCB specimen, all seven locations were selected for acceleration measurement and only strain gauge 1 and 2 near the BGA component were used. One-meter drop height for populated PCB specimen is fixed. For two different PCB specimens, the clamped–clamped boundary condition along the longer edge was used.

In populated PCB drop test, only 1 m-drop height was selected. Thirty drops were conducted for each surface-finishing component such as silver, gold, and OSP surface finishing. Figure 7.36 shows the acceleration comparison of PCB center for different surface finishing. Different surface finishing effect on acceleration can be ignored because it hardly affects the populated PCB structure, stiffness, and mass. Different surface finishing, however, can affect the fatigue failure of solder joint due to different interface material properties for different surface finishes. In this populated PCB drop test, seven different locations as shown in Fig. 7.36 were selected to measure the acceleration response. Figure 7.36 shows the acceleration of different locations for Ag surface finishing. Other surface finishes have almost same results. It can be seen from Fig. 7.37 that the largest acceleration will occur at PCB-free edge center. The acceleration on the QFP center is slightly more than that on BGA center because the location of the QFP center is closer to the free edge than location of BGA center. Thus can provide the guide to prevent the high acceleration of component mounted on PCB by arranging its location for clamped–clamped boundary condition.

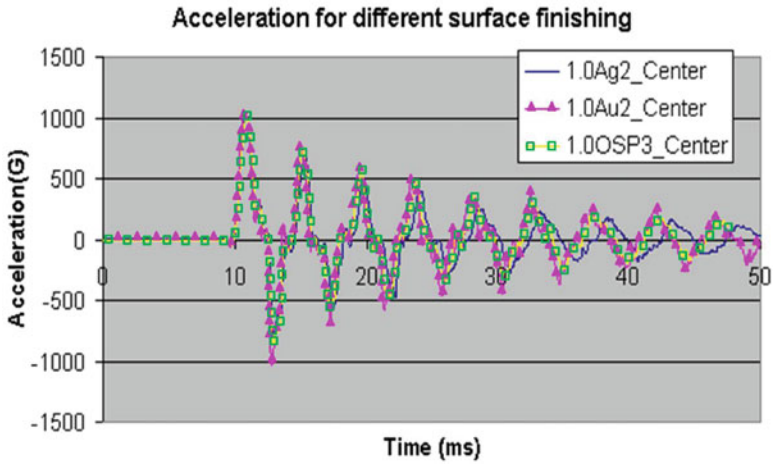

Fig. 7.36 Acceleration of PCB center for different surface finish

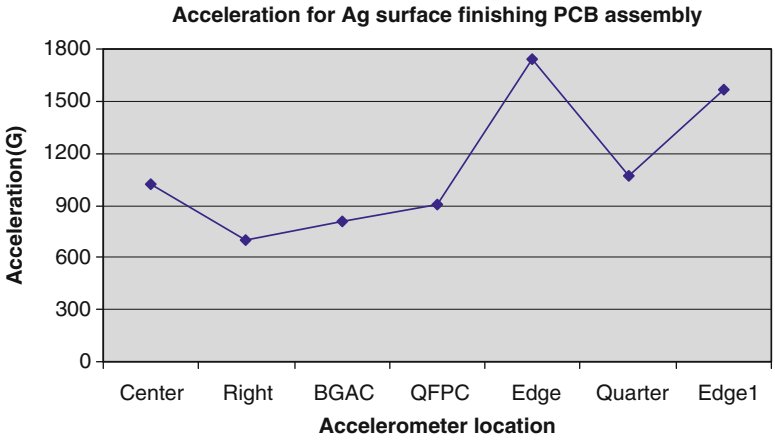

Fig. 7.37 Acceleration of different locations

In the populated PCB drop test, strain gauge 1 and 2 near the BGA corner as shown in Fig. 7.35 were used to measure the strain response of BGA component location. Figure 7.38 shows the strain result for three repeated measurements and the repeatability is consistent. In the drop test, the location of the accelerometer is changed after every five drops. The accelerometer has the mass of 2.4 g and this additional mass will affect the strain value when the accelerometer location varies. Figure 7.39 shows the effect of the accelerometer on the strain magnitude. It can be seen that the effect of accelerometer mass on strain of strain gauge1 is evident when accelerometer lay on the BGA center because of the added mass near the strain guage1 while the other locations effect is very slight.

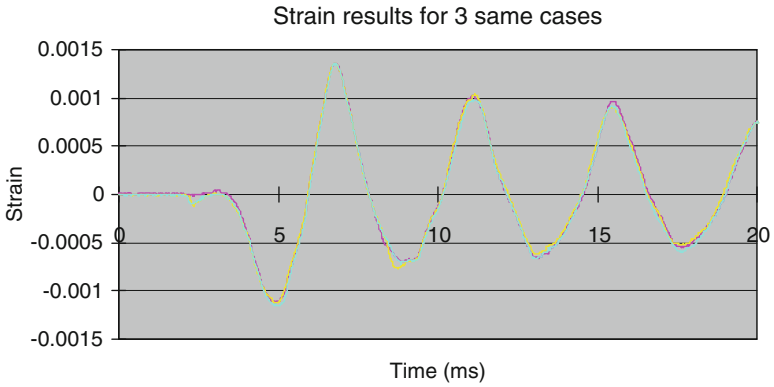

Fig. 7.38 Repeatability of strain measurement

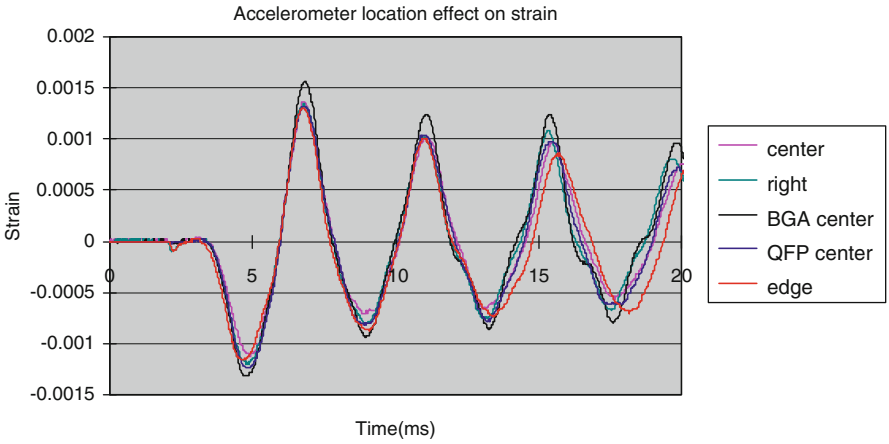

Fig. 7.39 Effect of accelerometer location on the strain

Figure 7.40 shows the strain comparison between strain gauge 1 and strain gauge 2 as shown in Fig. 7.35. It can be seen that the strain varies with position of PCB significantly and the strain magnitude becomes lower with time due to damping. Figure 7.41 shows the strain of strain gauge 1 for different surface finishing. It can be seen that the strain for the Au surface finishing is larger than that of others at the first PCB bending down while the strain will be almost same at subsequent PCB motion. Gold surface finishing PCB assembly indicates lower stiffness than other surface finishes when PCB is subjected to drop loading.

Reliability test for vibration fatigue was conducted for FCOB assembly with eutectic 63Sn–37Pb solder joints. Two methods of vibration fatigue analysis were developed using the G-level based *G–N* fatigue curve data for the FCOB assembly and the stress–life, *S–N* fatigue curve data for eutectic 63Sn–37Pb solder [25, 26].

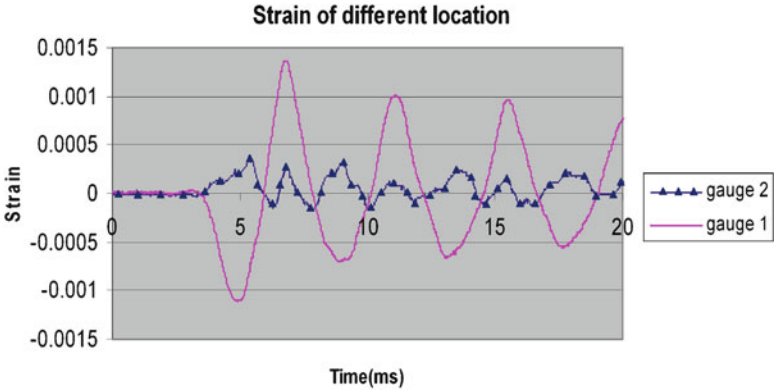

Fig. 7.40 Strain for different locations

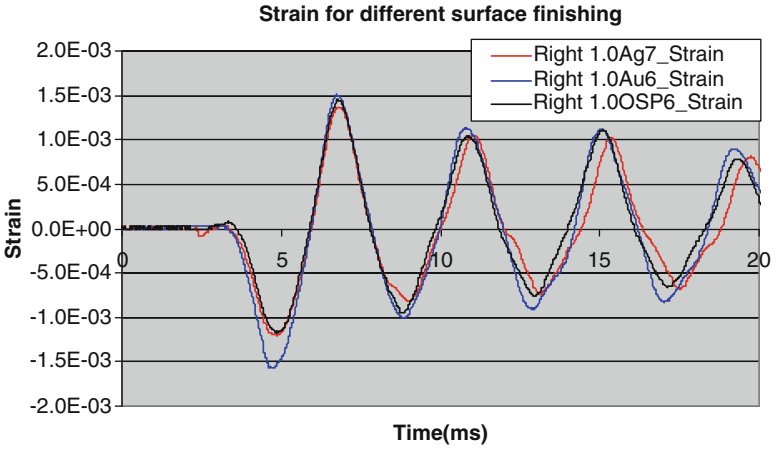

Fig. 7.41 Strain comparison for different boards

Drop impact test studies on the FCOB assembly with 63Sn–37Pb solder and Pb-free 95.5Sn–3.8Ag–0.7Cu soldered assemblies were conducted. Experimental measurements of the board-level displacement, acceleration, and strain responses were made. No failure was recorded after 30 drops from a 1-m height on the drop test machine [27].

Finite element analysis using the explicit dynamic analysis with LS-DYNA was able to model and simulate the board level deformation and acceleration characteristics. Stress and strain analysis of the solder joint was investigated for the FCOB assembly with 63Sn–37Pb solder and the predicted failure was estimated at 158 drops [26, 28].

References

1. Steinberg DS (1998) Vibration analysis for electronic equipment. Wiley, New York
2. Barker DB, Chen YS, Dasgupta A (1993) Estimating the vibration fatigue life of quad leaded surface mount components. J Electron Packaging 115:195–200
3. Pitarresi JM, Akanda A (1993) Random vibration response of a surface mount lead/solder joint. ASME international electronic conference, EEP, vol 4–1, Advances in electronic packaging, pp 207–215
4. Lee SB, Ham SJ (1999) Fatigue life assessment of bump type solder joint under vibration environment. ASME international electronic conference, EEP, vol 26–1, Advances in electronic packaging, pp 699–704
5. Yang QJ, Lim GH, Pang HLJ et al (1999) Vibration reliability analysis of a pbga assembly under foundation excitations. ASME international electronic conference, EEP, vol 26–1, Advances in electronic packaging, pp 705–711
6. Basaran C, Chandaroy R (1999) Nonlinear dynamic analysis of surface mount interconnects: Part I-theory. J Electron Packaging 121:8–11
7. Basaran C, Chandaroy R (1999) Nonlinear dynamic analysis of surface mount interconnects: Part II-application. J Electron Packaging 121:12–17
8. Chandaroy R, Basaran C (1999) Damage mechanics of surface mount technology solder joints under concurrent thermal and dynamic loading. J Electron Packaging 121:61–68
9. Zhao Y, Basaran C, Cartwright A, Dishongh T (2000) Thermomechanical behavior of micron scale solder joints under dynamic loads. Mech Mater 32:161–173
10. Meirovitch L (1986) Elements of vibration analysis. McGraw-Hill, New York
11. Yang QJ, Wang ZP, Lim GH et al (2002) Reliability of PBGA assemblies under out-of-plane vibration excitation. IEEE Trans Component Packaging Technol 25:293–300
12. Miner MA (1945) Cumulative fatigue damage. ASME J Appl Mech 12(3):A159–A164
13. Yao QZ, Qu JM, Wu SX (1999) Solder fatigue life in two chip scale packages. Proceedings of IEEE-IMAPS international symposium on microelectronics, Chicago, IL, October 1999, pp 563–570
14. Suhir E (2002) Could shock test adequately mimic drop test conditions? J Electron Packaging 24:170–177
15. Weaver W Jr, Timoshenko SP, Young DH (1990) Vibration problems in engineering. Wiley, New York
16. Sidharth V, Gannamani R, Zhang ML (2000) Characterization of a novel fine-pitch ball grid array package for flash memory application. Proceedings of 50th electronic components and technology conference, pp 353–357
17. Yu Q, Kikuchi H, Ikeda S, Shiratori M, Kakino M, Fujiwara N (2002) Dynamic behavior of electronics package and impact reliability of BGA solder joints. Proceedings of intersociety conference on thermal phenomena, pp 953–960
18. Xie DJ, Arra M, Yi S, Rooney D (2003) Solder joint behavior of area array packages in board level drop for handheld devices. Proceedings of 53rd of electronic component and technology conference, pp 130–135
19. Tee TY, Ng HS, Lim CT, Pek E, Zhong ZW (2003) Board level drop test and simulation of TFBGA packages for telecommunication applications. Proceedings of 53rd of electronic component and technology conference, pp 121–129
20. Masazumi M, Toyoda Y, Tajima T (2003) High solder joint reliability with lead free solders. Proceedings of 53rd of Electronic component and technology conference, pp 317–322
21. Zhu LP (2003) modeling technique for reliability assessment of portable electronic product subjected to drop impact loads. Proceedings of 53rd of electronic component and technology conference, pp 100–104
22. Lim CT, Ang CW, Tan LB, Seah SKW, Wong EH (2003) Drop impact survey of portable electronic products. Proceedings of 53rd of electronic component and technology conference, pp 113–120

23. Johnson W (1972) Impact strength of material. Edward Arnold, London
24. Shi XQ, Pang HLJ, Zhuo W, Wang ZP (2000) Low cycle fatigue analysis of temperature and frequency effects in eutectic solder alloy. Int J Fatigue 22:217–228
25. Che FX, Pang HLJ, Wong FL, Lim GH, Low TH (2003) Vibration fatigue test and analysis for flip chip solder joints. Proceedings of 5th EPTC conference, Singapore, 10–12 Dec 2003, pp 107–113
26. Pang JHL, Che FX, Low TH (2004) Vibration fatigue analysis for FCOB solder joints. Proceedings of 54th ECTC conference, Las Vegas, June 1–4 2004
27. Wang YQ, Low KH, Che FX, Pang HLJ, Yeo SP (2003) Modeling and simulation of printed circuit board drop test. Proceedings of 5th EPTC conference, Singapore, 10–12 Dec 2003, pp 263–268
28. Pang JHL, Low TH, Xiong BS, Che FX (2003) Design For reliability (DFR) methodology for electronic packaging assemblies. Proceedings of 5th EPTC conference, Singapore, 10–12 Dec 2003, pp 470–478

Chapter 8
Thermal Cycling Aging Effects on Board-Level Drop Test Result

Abstract Chapter 8 deals with Board-Level Drop Test and reports on the effects of thermal cycling aging on board level drop reliability for lead-free SnAgCu (SAC) in fine pitch ball grid array (FPBGA) packages. The drop life was observed before and after thermal cycling aging. Comparison of SAC/ENIG packages to SAC/OSP packages was investigated. Thermal cycling (TC) aging subject to −40°C to +125°C causes concurrent degradation of the solder joints and result in IMC growth and thermal fatigue damage. The IMC growth, as well as the void/crack formation subject to thermal cycling aging will affect the long-term solder joint reliability performance. It can also affect the impact shock reliability as thicker IMC layer causes brittle fracture failure.

The effect of thermal cycling aging on board-level drop reliability for lead-free SnAgCu (SAC) in fine pitch ball grid array (FPBGA) packages is studied in this chapter. The drop life was observed before and after thermal cycling aging. Comparison of SAC/ENIG package to SAC/OSP package was investigated.

8.1 Background

In accelerated thermal cycling (ATC) tests, the cyclic excursions of temperatures between −40°C and +125°C cause concurrent degradation of the solder joints and result in IMC growth [1] and thermal fatigue damage. The IMC growth, as well as the void/crack formation subject to isothermal aging and thermal cycling aging, is expected to affect the long-term solder joint reliability performance. It can also affect the impact shock reliability as thicker IMC layer cause brittle fracture failure. The growing use of portable electronic devices such as cell phone and PDA has led to increased concerns on drop impact-related failures in electronic assemblies. The studies on impact drop test on lead-free solder joint reliability have been reported [2–7]. Brittle fracture of IMC caused by dynamic loading, such as impact shock, is

J.H.L. Pang, *Lead Free Solder: Mechanics and Reliability*,
DOI 10.1007/978-1-4614-0463-7_8,

the dominant failure mode [7]. During service of electronic products, the solder joint is exposed to thermal aging before accidental drop impact occurs. The solder joints are subjected to thermo-mechanical induced stress-strains leading to solder fatigue degradation. Board-level drop impact test and finite elements modeling have been reported [7–9]. The effect of IMC growth and presence of Kirkendall void formation subject to thermal aging has been reported [10–13]. For the portable electronic products, it is necessary to test the drop impact reliability after a period of usage.

The effect of thermal cycling aging on drop impact reliability has been investigated. A 15 × 15-mm fine-pitch BGA (FPBGA) with 324 I/O was subject to drop test. Lead-free SAC with either organic solderability preservative (OSP) or electroless nickel immersion gold (ENIG) surface finishes was used. Interfacial IMCs, Kirkendall voids formation, and interconnect failure mode are studied subject to TC aging. Kirkendall voids were observed with Ar^+ sputtering etching. The failure sites and mechanism were then examined and correlated with IMC and void formation.

8.2 Experiment Procedures

8.2.1 Test Setup and Measurement

The Lansmont test machine was used to provide the drop impact load for board-level FPBGA soldered assemblies. A half sine g-input shock pulse on the drop table is calibrated to drop height and the felt pads on drop base to give the required g-input pulse and time duration. The drop machine structure consists of a steel base, two solid chrome plated guide rods, drop table, and hoist positioning system as shown in Fig. 8.1. The aluminum-welded table has an assembled mass of 190.5 kg.

The experiment matrix and sample aging condition are given in Table 8.1. The test specimen with seven mounted FPBGA (324 I/O) units soldered onto the printed circuit board are shown in Fig. 8.2. The test board (1 mm thick) either has OSP on copper pads (Cu-OSP) or ENIG, or NiAu, surface finish. The FPBGA package is daisy chained, with full interconnection failure monitoring of the solder joint. Multiple fault isolations pads are designed-in for the purpose of easy identification of failure distribution.

Thermal cycling aging was conducted with TC profile of −40°C to +125°C. The cycle time was 1 h, where 15 min at upper soak and lower soak temperature, respectively. Isothermal aging at 125°C and 150°C was also conducted for comparison. After 0, 500, 1,000, and 1,500 cycles, the test boards were taken out from TC chamber for board-level drop impact tests. The test board was screw mounted to the drop table at four corners with the units facing downwards.

The drop height was set at 1.0 m with the impact base surface covered with felt pad. The drop orientation is in the horizontal plane with packages in a face-down position. The test PCB was screwed onto the drop table at four support pin locations (see Fig. 8.3). During the test, the drop table is raised and dropped from the desired

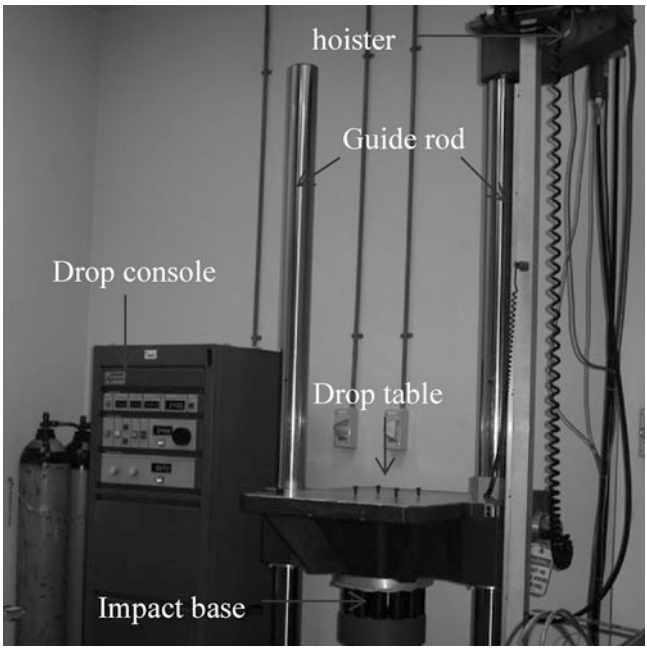

Fig. 8.1 Drop impact test vehicle and setup

Table 8.1 FPBGA specimen and thermal aging condition

Solder joint	Aging temperature (°C)	Aging time
SAC/Cu-OSP	−40 ~ 125 (TC)	500, 1,000, 1,500 TCs
SAC/ENIG	−40 ~ 125 (TC)	500, 1,000, 1,500 TCs
SAC/Cu-OSP	125, 150	0, 120, 240, 360 h
SAC/ENIG	125, 150	0, 120, 240, 360 h

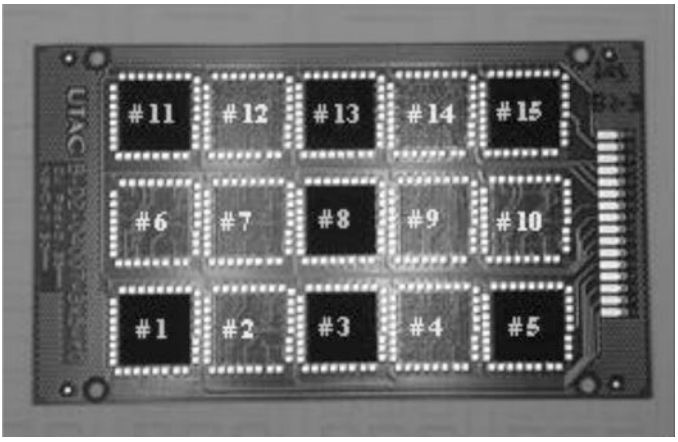

Fig. 8.2 PCB test board (77 × 132mm) with 15 × 15mm FPBGA packages

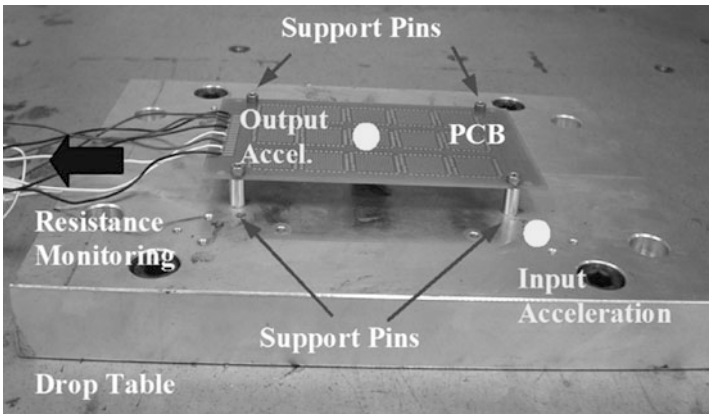

Fig. 8.3 Drop test fixture with PCB mounted

height (1 m). Upon impact, the drop responses of interest is the shock g-level (G-input) experienced by the drop table and the PCB (G-output) and the bending strain experienced at the center the PCB. The static and dynamic resistances of the daisy-chained solder joints were recorded. The peak G-input shock pulse of the drop table was about 690 g in the form of a half-sine wave with a 2-ms period. An accelerometer was mounted on the drop table near to the fixture to measure the input acceleration (G-input). For drop test consistency and repeatability, drop responses of input/output acceleration and PCB strain were monitored.

8.2.2 Dynamic Response and Failure Detection

The dynamic measurement method used for monitoring resistance of daisy-chained solder assembly in real-time during drop impact is shown in Fig. 8.4. A constant resistor, R_0, is placed in series with the daisy chain resistance of R_x, and connected to a DC power supply. The oscilloscope was used to measure the dynamic voltage drop on daisy chain loop. The dynamic resistance of solder joints, R_x, can be expressed as:

$$R_x = \frac{R_0 V_x}{U - V_x}, \tag{8.1}$$

where U is the voltage of the DC power supply and 1.8 V was used in this test, V_x is the dynamic voltage of daisy chain measured by oscilloscope, and R_0 is the constant resistance of 10Ω used in this test. When $V_x \to U$, $R_x \to \infty$ (implies an open circuit), it indicates the critical solder joint has failed. Three solder joint daisy-chained current loops for components labeled "A", "B", and "C" as shown in Fig. 8.4 were monitored by three oscilloscope channels for one test board.

In a drop test, it is common to observe that the solder joint crack opens up resulting in a resistance discontinuity and closes back to resume electrical

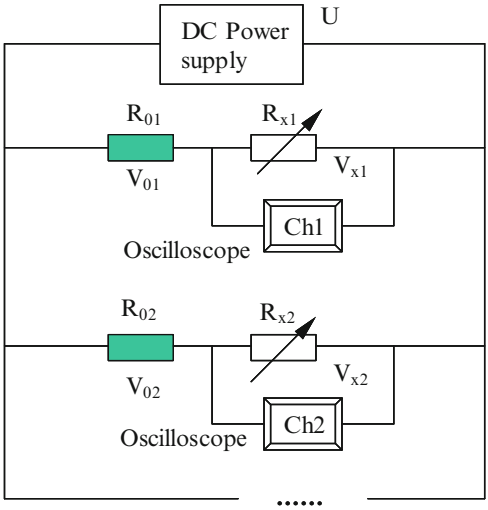

Fig. 8.4 Dynamic resistance measurement setup

continuity. The upward/downward deflection of the PCB leads to the opening/closing mode of the crack, which is known as an intermittent solder joint failure. When the crack becomes larger and cannot close back after the impact test, a permanent solder joint failure is recorded. In this study, the permanent solder joint failure is identified as the failure criteria.

8.2.3 Failure Characterization

After TC aging and drop test, the specimens were cross sectioned and observed by Scanning Electron Microscopy (SEM) under an accelerated voltage of 15 kV and backscattered electron mode (BSE). The IMC layer at the interface was examined at high resolution. Characterization of IMC thickness and Kirkendall voids after thermal cycling was conducted. The specimen was cross sectioned and polished, and then it was etched by Ar^+ sputtering with an R.F. magnetron sputtering equipment. After the chamber was evacuated to 10^{-6} Pa, argon was introduced to maintain working pressure. The specimens were etched by Ar^+ for 10 min with a power of 120 W.

8.3 Board-Level Drop Characterization

8.3.1 Drop Impact Lifetime Comparison Before and After TC Aging

The resistance of daisy-chained solder joints was monitored during thermal aging. The drop lifetime was monitored by the change of dynamic resistance for the daisy-chained

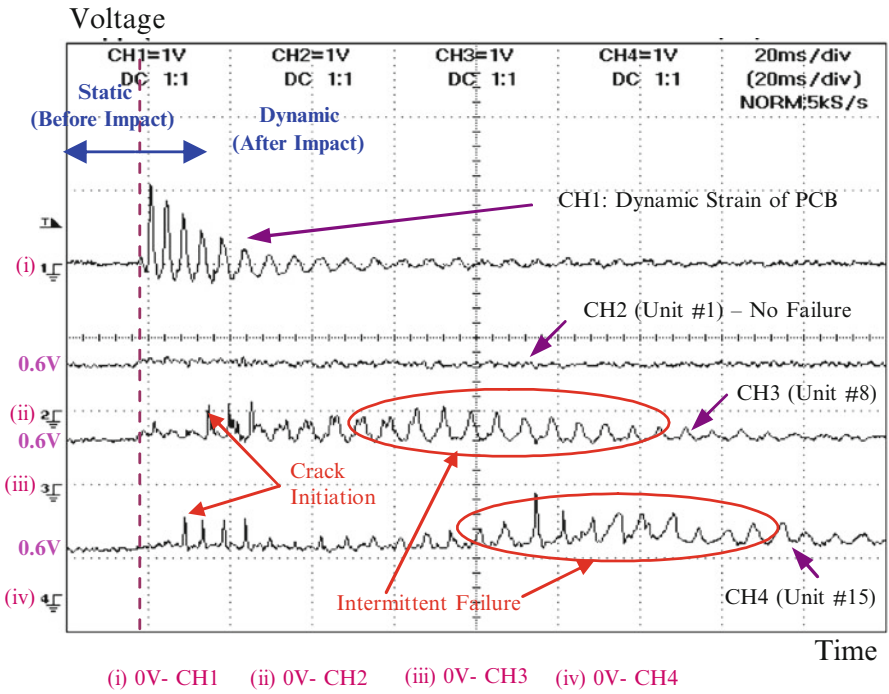

Fig. 8.5 Typical dynamic responses for drop test

solder joints in real-time during drop impact. During drop test, the solder joints resistance (or "voltage") for the FPBGA packages and PCB bending strain was captured. A typical response is showed in Fig. 8.5. It can be divided into two regions, before impact (static) and after impact (dynamic). Test result for as reflowed board after a certain number of drops is used for illustration. Channel 1 is used for dynamic strain measurement at the PCB center upon impact. Channels 2, 3, and 4 are measuring the dynamic voltages of package units 1, 8, and 15, respectively. Before impact, the PCB strain is zero while the static solder joint resistance is similar to the value measured by manual probing. Each package location has its own zero-reference voltage and initial voltage reading as indicated. With reference to channel 3 (unit 8), a peak voltage was registered after impact, indicating that an initial failure in a solder joint has occurred. The following fluctuation in peaks constituted with the upward/downward flexing of the PCB and shows the opening/closing mode of the cracking behavior. When flexing of the board has ended, static resistance measurement by manual probing was not able to register any discontinuity. This observation describes the intermittent solder joint failure. At subsequent drops, unit 8 would register fluctuation in voltage reading and finally the discontinuity was confirmed by manually probing with an open circuit being measured, thus implying that the solder joint has opened permanent.

The drop test was conducted until all the units on the board had failed. The average number of drop cycles to initial failure after each thermal condition was

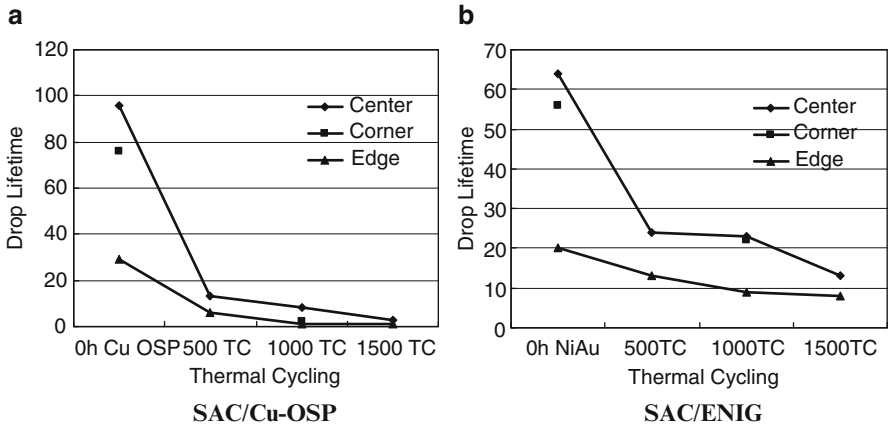

Fig. 8.6 Board level drop lifetime before and after thermal cycling aging. (**a**) SAC/Cu-OSP. (**b**) SAC/ENIG

recorded as the drop impact lifetime. Average drop impact lifetime vs. thermal aging for SAC/Cu-OSP and SAC/ENIG is plotted in Fig. 8.6a, b.

For the FPBGA assembly on board, the units are classified into three groups due to their location and symmetry of the board: (1) Edge units C3 and C13, which have the shortest lifetime; (2) Center units C8 and; (3) Corner units C1, C5, C11, and C15. It can be seen from Fig. 8.6 that the drop lifetime decreased significantly after thermal aging conditioning followed by drop test. For all the units in this study, drop lifetime could decrease by more than 50% only after 500 cycles of TC aging or 120 h isothermal aging. This is even more significant after longer thermal aging time. For SAC/Cu-OSP after 1,000 and 1,500 cycles of TC, or after isothermal aging of 240 and 390 h, the drop impact lifetime reduced down to five drops or even worse.

For as reflowed specimens, take unit C3 and C13 as examples, as shown in Fig. 8.7. The drop lifetime for SAC/Cu-OSP (29 drops) is better than SAC/ENIG (21 drops). This is reasonable as needle-like IMC (SAC/ENIG) is not as resistant to IMC fracture as scallop IMC layer (SAC/Cu-OSP). The failure crack morphology is characterized in the following sections. For the drop lifetime performance of different surface finish, however, SAC/ENIG seems to be better than SAC/Cu-OSP after thermal cycling aging. The drop impact lifetime significantly decreased from 29 to 6 for SAC/Cu-OSP, after only 500 TC aging. After 1,000 and 1,500 cycles of TC aging, the specimen can only endure one drop before failure occur. The drop lifetimes for SAC/ENIG after 500, 1,000, and 1,500 were 13, 9, and 8, respectively and were obviously better than SAC/Cu-OSP.

8.3.2 Characterization of Failure Modes

The drop impact failure was characterized from both plane-view and cross-section observation. For plane-view observation, dye penetration was used to mark the

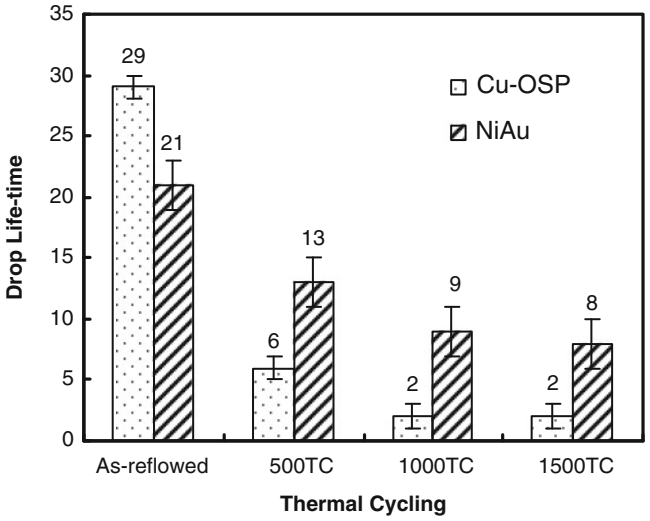

Fig. 8.7 Drop lifetime for unit C3 and C13 before and after TC aging

failure site. Blue ink 35 vol.% + ethanol 65% was used as a dye-penetration solution. The FPBGA unit was then pilled off from the board, the marked failure site display purple-blue color under optical microscope. Among the 324 BGA I/Os in one unit, the typical drop impact failure occurred at the corner or edge of the unit. The solder joints failure distribution across the PCB is, however, location dependant. Due to pure bending mode in location (2) or C8, joints at corner of the package failed as a result. Damage by shock wave transmission through the support pins was evidently demonstrated for units in group (3), where joints at the package corner had failed. For group I, failure was registered at left and right rows of the package. The failure location mapping was preformed after all units in a single board had failed. Thus it may have failed to capture the first solder joint crack occurring at the corner of the package. The subsequent drop cycles resulted in adjacent joints to fail. The failure distribution was similar for all test specimens.

For all of the tested boards with the two different PCB surface finishes (Cu-OSP and ENIG) and thermal aging profiles, it showed that the drop impact failure occurred at multiple locations. Four types of possible solder joint failure were detected after drop impact, as shown in Fig. 8.8. They are; (1) IMC failure between SAC/Cu pad at the PCB side, as shown in Fig. 8.8a, where solder joint is detached from the pad through the IMC interface. The IMC failure is the dominant failure mode in this study. (2) Pad/substrate failure at the PCB side, as shown in Fig. 8.8b, the copper pad is totally detached from the resin substrate; the fibers in PCB could be clearly seen in plane-view. (3) IMC/solder failure at the component side, as shown in Fig. 8.8c, in which the solder ball was left at the board side, the crack could be either in the IMC or in the solder near the interface. (4) Copper trace failure, as shown in

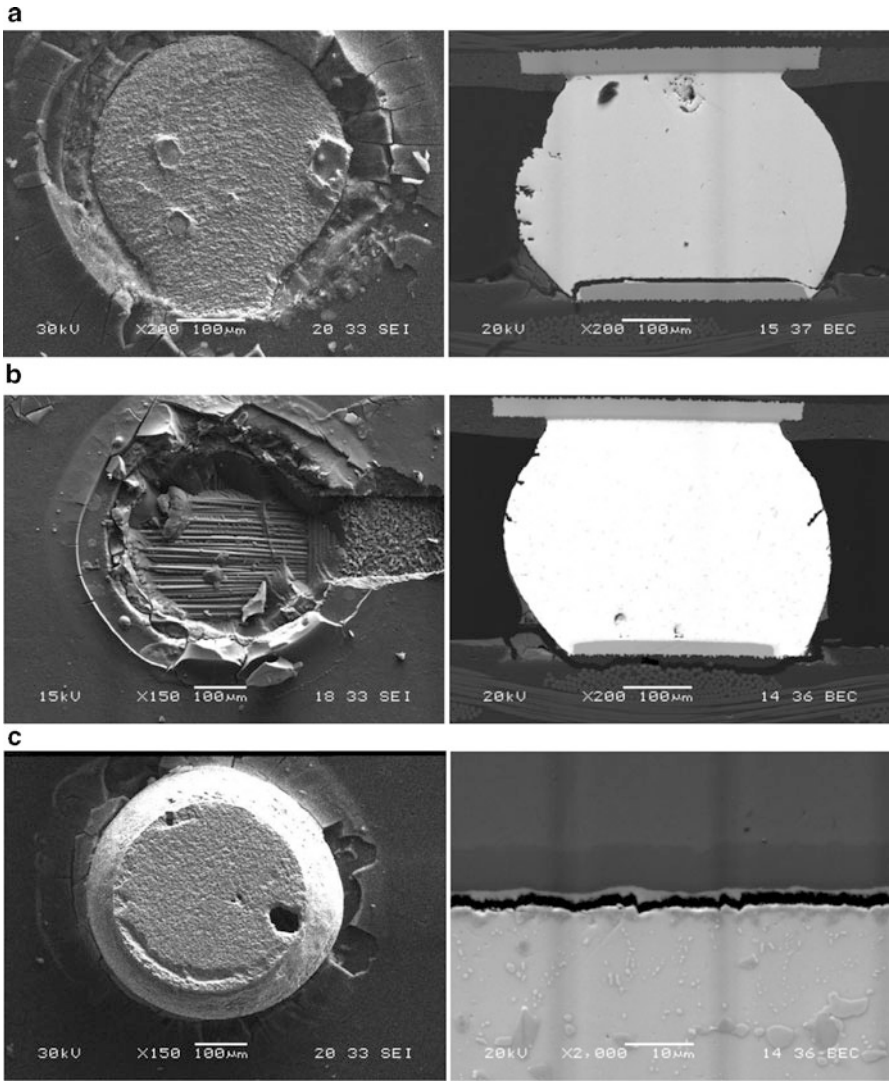

Fig. 8.8 Solder joint failure modes subject to drop impact. (**a**) IMC failure between SAC/Cu pad at the PCB side. (**b**) Pad/resin failure at the PCB side. (**c**) IMC/solder failure at the component side. (**d**) Copper trace failure

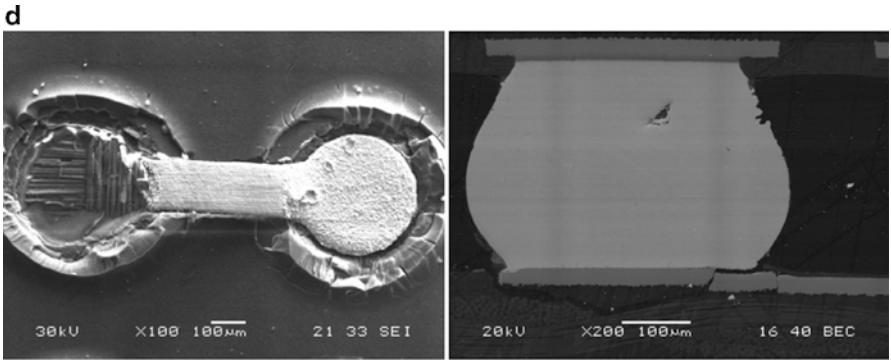

Fig. 8.8 (continued)

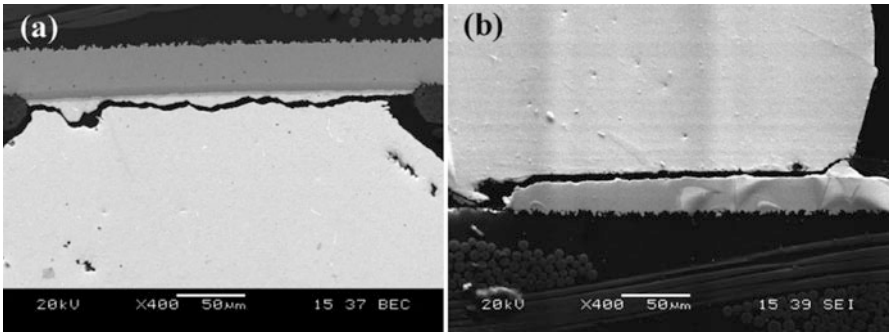

Fig. 8.9 Solder joint failure subject to (**a**) TC, failure in SAC solder near component interface and (**b**) Drop impact, failure in IMC at PCB side

Fig. 8.8d, where it can be seen that the copper trace broken must be accompanied with the Pad/substrate open. When the copper pad is detached from substrate, the dog-bone shaped copper trace would be easily broken at the route of one end.

The solder joint failure mode subject to TC aging was reported [14–16]. The typical fatigue failure after TC aging occurred in the SAC solder near the component interface, as shown in Fig. 8.9a, the location of solder joint failure was typically at the outmost component corner or die corner. After 500 to 1,500 cycles of TC aging, the crack in solder joint is expected to propagate already, which could affect the drop reliability significantly. However, the failure site after drop impact test was not where the thermal fatigue crack initiated. The dominant failure is still the brittle failure of IMC, at IMC layer on the SAC/Cu pad at board side, as shown in Fig. 8.9b. The solder ball was totally separated from the copper pad.

8.4 IMC Failure Analysis

8.4.1 Drop Impact Crack Propagation

In this section, the first type of drop impact failure, IMC failure between SAC/Cu pads were observed under high resolution SEM (BSE mode) for SAC/Cu-OSP and SAC/ENIG test board. The drop tests were conducted after different TC aging time. Figure 8.10a–d shows the enlarged drop impact failure interface for the SAC/Cu-OSP specimens with 0, 500 1,000, or 1,500 TC aging. Although all the four failures occurred in the IMC, the location of the crack path is different. For as reflowed specimen shown in Fig. 8.10a, the crack path is random in the Cu_6Sn_5 IMC, either near the Cu–Cu_6Sn_5 interface, or near the SAC–Cu_6Sn_5 interface, or in the middle of Cu_6Sn_5. For the specimen after 500 TCs as shown in Fig. 8.10b, a dominant crack can be seen in the Cu_6Sn_5 IMC, while quite a lot inclined tiny cracks exist. These tiny cracks stopped at the interface of IMC and copper pad. After 1,000 TC aging, the crack became very close to the IMC–copper interface, where the Cu_3Sn grows during TC aging. The crack is flatter compared to the as-reflowed condition and 500 cycles TC aging specimens. This is even more significant for the specimen after 1,500 cycles of TC aging, as shown in Fig. 8.10c; the crack propagates merely through the bottom Cu–IMC interface.

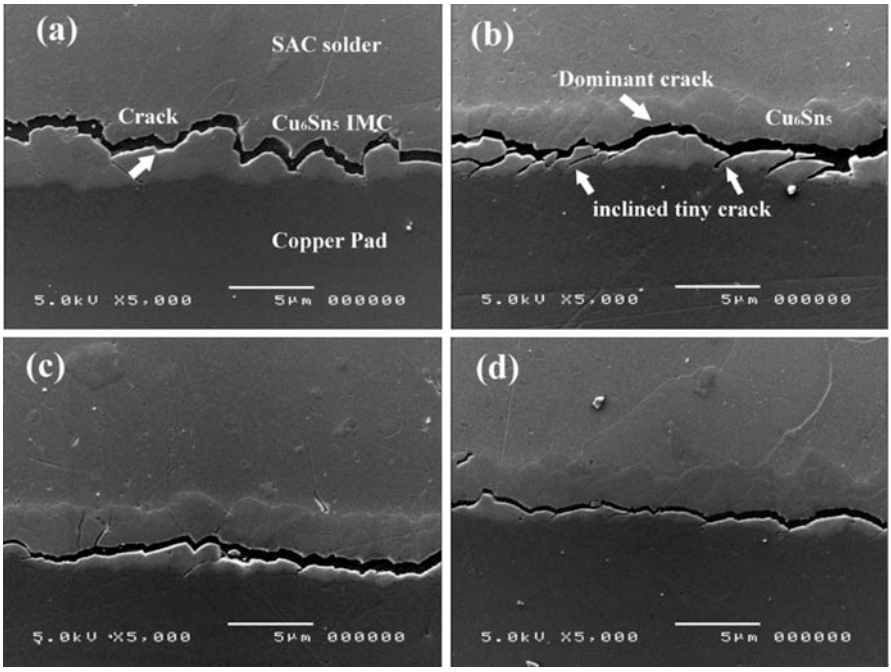

Fig. 8.10 SAC solder to copper pad interface after drop impact test for (**a**) as-reflowed, (**b**) 500 TC, (**c**) 1,000 TC, and (**d**) 1,500 TC

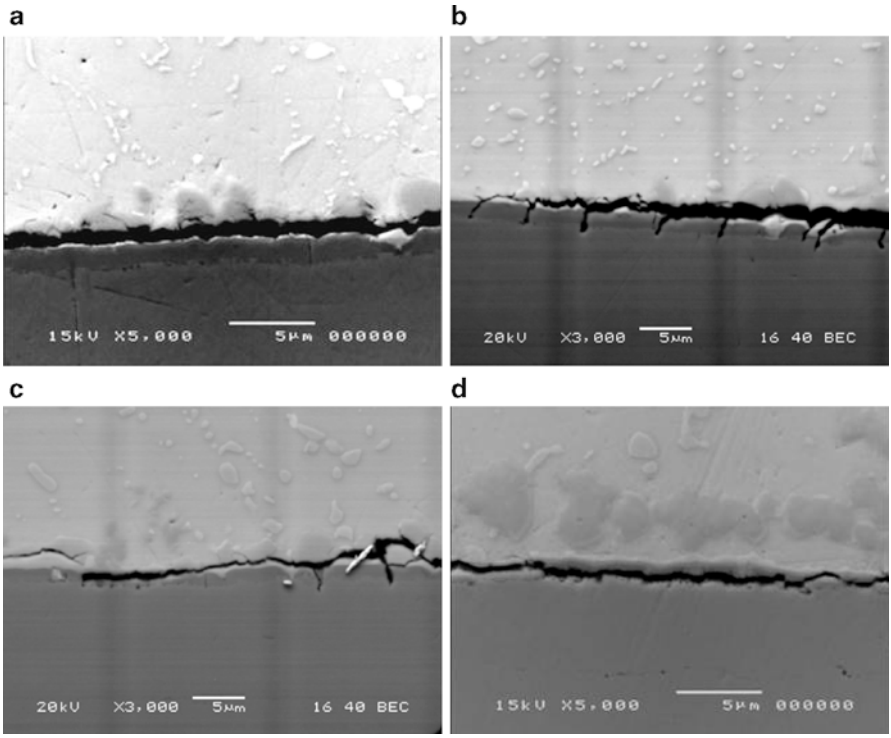

Fig. 8.11 SAC solder to ENIG interface after drop impact test for (**a**) as-reflowed, (**b**) TC 500, (**c**) TC 1,000, and (**d**) TC 1,500.

The drop impact failure interface for the SAC/ENIG specimens after 0, 500, 1,000, or 1,500 cycles of TC aging is given in Fig. 8.11a–d. For as reflowed specimen shown in Fig. 8.11a, the crack occurred at the interface between IMC and Ni(P) layer. This is different from SAC/Cu–OSP which has scallop IMC layer. The ternary needle-like NiCuSn IMC did not form a compact layer at the interface. After 500 TCs, the dominant crack was again at the IMC–Ni(P) interface. It is noted that vertical crack features penetrated the Ni(P) layer and stopped at the interface of Ni(P) and copper pad. This indicates that the Ni(P) layer exhibit brittle fracture weakness. After 1,000 cycles of TC aging, the Ni(P) layer was further consumed and the crack was at the IMC–Ni(P) interface. The Ni(P) layer became very thin at some locations, and voids can be seen as shown in Fig. 8.11c. During TC aging, NiCuSn ternary IMC grow in thickness but it may not be in planner-like. Spalling of IMC could be seen, as shown in Fig. 8.11d, after 1,500 cycles of TC aging. The Ni (P) layer degraded, as the crack forms at the interface of Ni(P) and Copper pad. The interface microstructure requires further characterization for both SAC/Cu-OSP and SAC/ENIG after TC aging to examine why the crack paths change and how the IMC growth affects the solder joint strength.

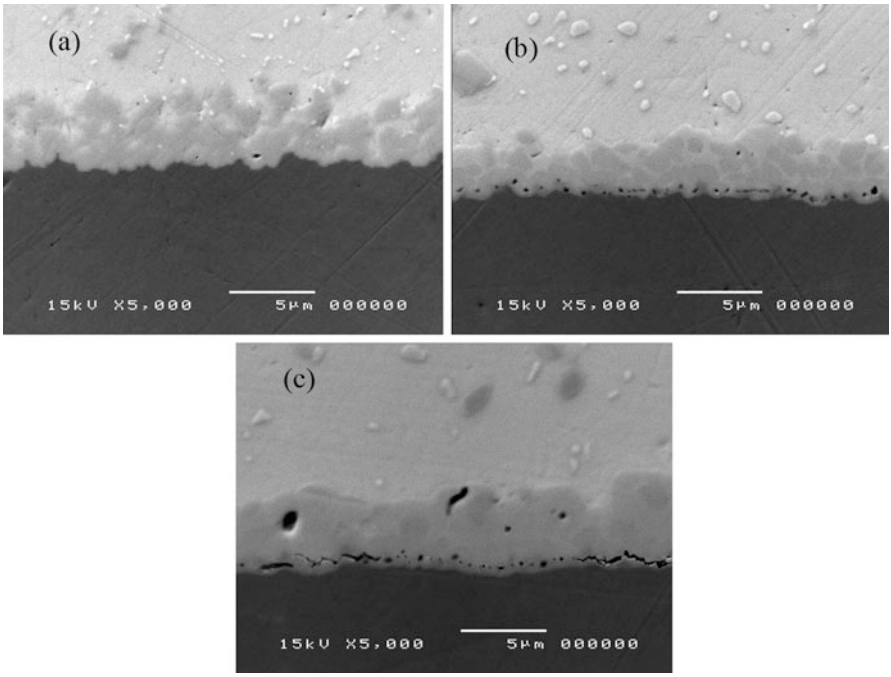

Fig. 8.12 SAC solder to copper pad interface after Ar^+ sputtering etch (**a**) as reflowed specimen, (**b**) TC 500 Kirkendall voids formed and occupied about 10% of the interface, and (**c**) TC 1,000, growth of Kirkendall voids is noted, micro-crack could be seen at the interface

8.4.2 Kirkendall Voids Characterization

During TC aging, solid state Cu–Sn interdiffusion process continues to grow the IMC layer. Earlier studies [11–16] reported the formation of Kirkendall voids in the Cu–Cu_3Sn interface and Cu_3Sn compound layer when the SAC/Cu solder joints were subject to isothermal aging. For the two elements, Cu was the dominant diffusing species through Cu_3Sn and Cu_6Sn_5. In the Cu-SAC solder reaction couple, the diffusing Cu atoms arrive at Cu_3Sn–Cu_6Sn_5 and Cu_6Sn_5–solder interfaces and result in the growth of both IMC layers. Because of the unbalanced Cu–Sn interdiffusion through interface, atomic-level vacancies left by the migrating Cu atoms on the bare Cu side are not filled by Sn atoms. These vacancies coalesce into the so-called Kirkendall voids.

However, the voids were so small that they would be smeared with the normal mechanical polishing process and cannot be seen in typical SEM pictures. The SEM pictures reported by Chiu and Zeng [11] were taken from samples cross-sectioned by Focused Ion Beam (FIB). In this study, Ar^+ ion sputtering was used to reveal the tiny Kirkendall voids. The formation and growth of the Kirkendall voids at the Cu–solder interface after TC aging are shown in Fig. 8.12.

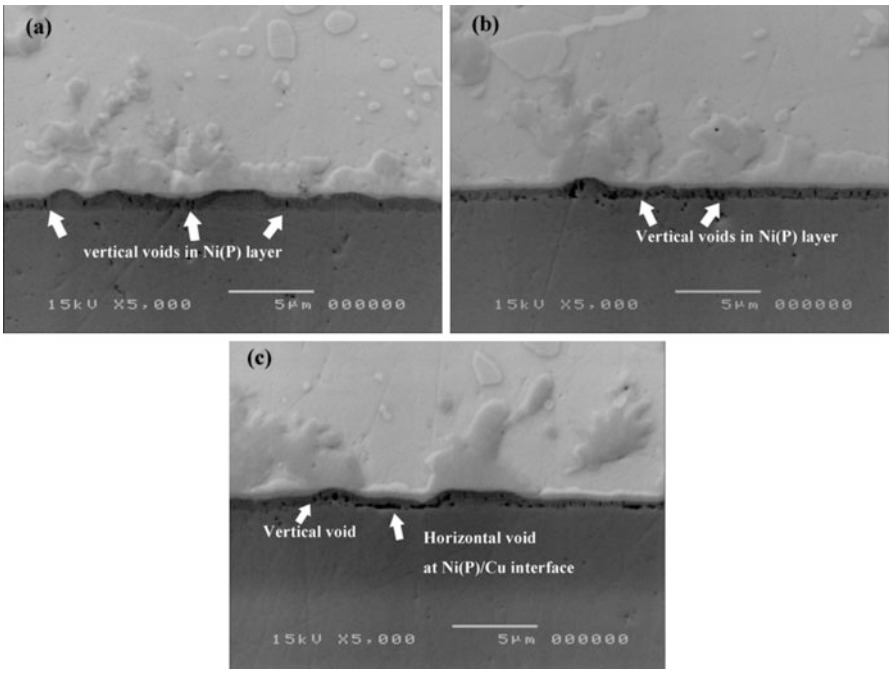

Fig. 8.13 SAC solder to ENIG interface after Ar^+ sputtering etch (**a**) TC 500, (**b**) TC 1,000 vertical voids could be seen in Ni(P) layer, and (**c**) TC 1,500, horizontal void developed at Ni (P)–Cu interface

For as reflowed specimen shown in Fig. 8.12a, no voids could be seen at the interface. While after 500 TCs, it can be seen that many Kirkendall voids were formed at the Cu–IMC interface, where Cu_3Sn is located. It occupied about 20% of the interface length, shown in Fig. 8.12b. The density of the voids area further increases as the thermal aging increased to 1,000 cycles of aging. As shown in Fig. 8.12c, the voids coalesced and generated micro-cracks at the interface. This voiding process seems to develop faster than the case isothermal aging at 125 C reported by Chiu [11]. Dynamic recrystallization at the Solder–Cu_6Sn_5 interface could accelerate the interdiffusion of Cu atoms. The unbalanced Cu–Sn interdiffusion through the interface is significant, and Kirkendall voiding process under TC aging is more serious than isothermal aging.

The growth of Kirkendall voids explain why the TC aging effect on drop impact durability reduced significantly for SAC/Cu-OSP soldered assemblies. At the submicron level, the voids form near the Cu–IMC interface and coalesce during TC aging. Cracks propagate more readily at the interface than in the IMC layer. Thus the morphology of the crack path becomes flatter after TC aging and the drop impact lifetime decreased significantly.

The SAC–Ni(P) interfacial microstructure after TC aging was observed in SEM BSE mode after Ar^+ sputtering. Figure 8.13a–c showed the images for TC aging

after 500, 1,000, and 1,500 cycles, respectively. Voids were found in the Ni(P) layer after 500 cycles of TC aging. These voids had rod shape and were perpendicular to the Ni(P) layer, or called vertical void in contrast to the horizontal voids, which is parallel to the Ni(P) layer. This is consistent with the observation shown in Fig. 8.13b, c, where quite a lot of vertical cracks were found in Ni(P) layer. After 1,000 cycles of TC aging, the Ni layer became thinner and there were more vertical voids formed. After 1,500 cycles of TC aging, layered horizontal void formed at the interface of Cu/Ni(P). Compared with crack propagation shown in Fig. 8.13d, it is clear that these horizontal voids degraded the Ni/Cu layer joint strength. From the above characterization of interfacial void after Ar^+ sputtering, we can see the effect of TC on the interfacial voiding process and subsequently drop impact lifetime. Although both BGA units with SAC/Cu-OSP and SAC/ENIG solder joint showed good drop impact reliability before TC aging, their performance after TC are not acceptable.

Thermal cycling aging shows significant effect on board-level drop reliability for SAC-soldered FPBGA packages in this study. SAC/ENIG packages exhibit longer drop impact life after thermal aging than that of SAC/OSP. Kirkendall voids formation and solder joint failure mode are characterized by SEM after Ar^+ sputtering. It was found that growth of Kirkendall voids and IMC significantly weakened the solder joint interface with TC aging. Drop impact crack path locations changed from the IMC to the IMC–Cu interface. For SAC/ENIG specimen, vertical and horizontal voids in Ni(P) layer were found after TC aging; drop impact crack propagates between Ni(P)–Cu pad interface along the horizontal voids.

References

1. Pang JHL, Xu LH, Shi XQ et al (2004) Intermetallic growth studies on Sn-Ag-Cu lead-free solder joints. J Electron Mater 33(10):1219–1226
2. Liu YL (2006) Lead-free chip scale packages: assembly and drop test reliability. IEEE Trans Electron Packaging Manufacturing 29(1):1–9
3. Lai YS, Yang PF, Yeh CL (2006) Experimental studies of board-level reliability of chip-scale packages subjected to JEDEC drop test condition. Microelectron Reliab 46(2–4):645–650
4. Chong DYR, Che FX, Pang JHL et al (2008) Evaluation on influencing factors of board-level drop reliability for chip scale packages (Fine-Pitch ball grid array). IEEE Trans Advanced Packaging 31(1):66–75
5. Chong DYR, Che FX, Pang JHL et al (2006) Drop impact reliability testing for lead-free and lead-based soldered IC packages. Microelectron Reliab 46(7):1160–1171
6. Wong EH, Mai YW, Seah SKW (2005) Board level drop impact – Fundamental and parametric analysis. J Electron Packaging 127(4):496–502
7. Wong EH (2005) Drop impact: fundamentals & impact characterisation of solder joints. In: 55th Electronic Components & Technology Conference, vols 1 and 2, 2005 Proceedings. IEEE, New York, pp 1202–1209
8. Gu J, Lim CT, Tay AAO (2005) Simulation of mechanical response of solder joints under drop impact using equivalent layer models. In: 55th Electronic Components & Technology Conference, vols 1 and 2, 2005. IEEE, New York, pp 491–498

9. Alajoki M, Nguyen L, Kivilahti J (2005) Drop test reliability of wafer level chip scale packages. In: 55th Electronic Components & Technology Conference, vols 1 and 2, 2005 Proceedings. IEEE, New York, pp 637–644
10. Pang JHL, Low TH, Luhua X et al (2004) Thermal cycling aging effects on Sn–Ag–Cu solder joint microstructure, IMC and strength. Thin Solid Films 462–463:370–375
11. Chiu TC, Zeng K (2004) Effect of thermal aging on board level drop reliability for Pb-free BGA packages. In: 54th Electronic Components & Technology Conference, vols 1 and 2, Proceedings. IEEE, New York, pp 1256–1262
12. Mei ZQ, Sunwoo AJ, Morris JW (1992) Analysis of low-temperature intermetallic growth in copper-tin diffusion couples. Metall Trans A-Phys Metall Mater Sci 23(3):857–864
13. Xu LH, Pang JHL (2005) Interfacial IMC and Kirkendall void on SAC solder joints subject to thermal cycling. In: Proceedings of the 7th Electronics Packaging Technology Conference, vols 1 and 2, 2005, Singapore. IEEE, New York, pp 863–867
14. Chang TC, Wang MC, Hon MH (2003) Crystal growth of the intermetallic compounds at the Sn-9Zn-xAg/Cu interface during isothermal aging. J Cryst Growth 252(1–3):401–412
15. Chang JL, Janz D, Kempe W et al (2005) Degradation of Sn-Ag-Cu heat-sink attachment during thermal shock cycling. Soldering Surface Mount Technol 17(4):10–16
16. Xu LH, Pang JHL, Che FX (2008) Impact of thermal cycling on Sn-Ag-Cu solder joints and board-level drop reliability. J Electron Mater 37(6):880–886

Erratum to: Theory on Mechanics of Solder Materials

Erratum to:
J. H. L. Pang, *Lead Free Solder: Mechanics and Reliability*,
https://doi.org/10.1007/978-1-4614-0463-7_2

The chapter was inadvertently published with a parameter missing in Table 2.1, h0: 921.48 is incorrect, this is now corrected to h0: 92148.

The Table 2.1 has been updated in the chapter.

The updated online version of this chapter can be found at
https://doi.org/10.1007/978-1-4614-0463-7_2

J. H. L. Pang, *Lead Free Solder: Mechanics and Reliability*,
https://doi.org/10.1007/978-1-4614-0463-7_9

Index

J.H.L. Pang, *Lead Free Solder: Mechanics and Reliability*,
DOI 10.1007/978-1-4614-0463-7, © Springer Science+Business Media, LLC 2012